Università Politecnica delle Marche
Scuola di Dottorato di Ricerca in Scienze dell'Ingegneria
Curriculum in Ingegneria Civile, Ambientale, Edile e Architettura

---

Static and dynamic response of RC beams strengthened with NSM C/GFRP rods

Ph.D. Dissertation of:

Maria Vittoria Vecchietti

Advisor:

Prof. Roberto Capozucca

XXXIV edition - new series

Università Politecnica delle Marche
Dipartimento di Ingegneria Civile, Edile e Architettura
Via Brecce Bianche — 60131 - Ancona, Italy

Abstract

The Near-Surface Mounted (NSM) strengthening technique has proven, in recent years, as a valid alternative to the conventional strengthening methods, like the externally bonded (EB) technique. In the last two decades its potential and its advantages, as well as its applications, has been studied, trying to optimize the construction system and the parameters that influence it. However, it is interesting to deepen the topic both in static, highlighting the non-conservation of the flat section, due to the bond-slip effect between FRP rod and resin, which, for simplification has never been taken into consideration by analytical models proposed in literature, both in dynamic key, which allows, by studying the trend of proper frequencies of vibration, to understand the effectiveness of the reinforcement and how different types of damage affect it.

Therefore, in this research work, static and dynamic tests were performed on RC beams strengthened with NSM CFRP and GFRP rods, which still need to be investigated. The aim of the research is to analyze the effects of different types of strengthening.

Bending tests with cycles of loading until failure are carried out, these tests allowed to define the behavior of beam specimens, even in presence of damage, and to generate different damage degrees, due to cracking of concrete. At each step of load, dynamic analysis, by free vibration test, allows monitoring the effectiveness of the reinforcement at different damage degrees. Failure modes of beam models are also analyzed.

A comparison between the responses of the unreinforced and reinforced models is presented; the behavior of beam specimens was also analyzed by theoretical models.

In the end, a finite element analysis of beam models has been developed, in order to validate the results obtained by the experimental research.

Keywords: NSM technique; RC beams; CFRP and GFRP rods; static and dynamic tests; damage degrees; FE analysis.

Contents

List of Figures

List of Tables

List of Symbols

A	area of the cross section of the beam
b	base of the cross section of the beam
h	height of the cross section of the beam
E	elastic modulus
I	moment of inertia
EI	flexural stiffness
L	length of the beam
ρ	density
f	frequency value
λ	eigenvalue
M	moment value
P	experimental load value
χ	curvature of midspan section
ε	strain value
δ	deflection at midspan
x	depth of neutral axis
k	stiffness
c	compliance
m	mass
D	damage degree
μ	ductility of section
k_1, k_2	strain lag value
r	index of vibration mode
s	index of strained steel rebar
s,1	index of upper steel rebar
s,2	index of lower steel rebar
c	index of compressed concrete
FRP	index of FRP rod
cr	index of phase I, cracking
y	index of phase II, yielding
u	index of ultimate phase
i	index of damage degree
f	index of failure
exp	index of experimental value
th	index of theoretical value

List of Abbreviations

RC	Reinforced Concrete
FRP	Fiber Reinforced Polymers
GFRP	Glass Fiber Reinforced Polymers
CFRP	Carbon Fiber Reinforced Polymers
AFRP	Aramid Fiber Reinforced Polymers
BFRP	Basalt Fiber Reinforced Polymers
GP	General Performance
HP	High Performance
HT	High Tensile
IM	Intermediate Modulus
HM	High Modulus
UHM	Ultra-High Modulus
NSM	Near Surface Mounted
EBR	Externally Bonded Reinforcements
EB	Externally Bonded
NDT	Non-Destructive Testing
SHM	Structural Health Monitoring
FEM	Finite Element Model

Chapter 1. Introduction

1.1. General

FRP material with remarkable characteristics such as the appropriate ratio of strength to weight, high resistance of corrosion, and admirable degree of durability is one of the most utilized innovative materials in techniques to increase the ultimate sustainable load capacity of existing reinforced concrete structures [1,2,3]. Strengthening reinforced concrete structures with FRP is categorized into two major techniques, including externally bonded reinforcement (EBR) and near-surface mounted reinforcement (NSM).
For the last several decades FRP composites have been widely used as strengthening and retrofitting materials, during this period innumerable studies concerning the most effective factors on the overall performance of strengthening reinforced concrete structures with FRP materials, either for shear or flexural strengthening have been conducted via various methods including analytical, numerical, and experimental methods [4-14].

In this work, the NSM reinforcement technique, which consists in inserting bars or sheets of composite material inside grooves specifically cut in the concrete cover of the structural element is studied in-depth [15,16]. This technique is also compared with the EBR technique, which is less effective, mainly due to the premature delamination of the fabric in composite material [17-19]. Instead with NSM method, because of embedding process, NSM FRP bars have a much stronger bond to the concrete than externally bonded FRP laminates, so the tensile strength of the former can be more fully utilized than that of the latter. However, this improved bond effectiveness does not preclude the possibility of debonding failure of NSM FRP bars, and indeed debonding is still a likely failure mode in RC members strengthened with NSM FRP bars [20,21].

To avoid this type of failure, it is necessary to ensure adequate adhesion between the reinforcement bars and the concrete [22,26]. Many factors can influence the adhesion mechanism such as: the bond length; the diameter of the bars used; the type of FRP material used; the surface configuration of the bars and the size of the grooves [22,24-27].

Investigation and theoretical studies have been developed regarding the bond behavior of FRP rods in RC elements [24,26,28,29]; on one hand, direct pull-out tests may be adequate for describing bond mechanism, defining a bond-slip relation, on the other hand bending tests allow to define failure modes in NSM strengthened RC elements.

In addition to these two just mentioned methods, another one can be added to fully study the behavior of FRP strengthened RC elements.
Recently, various non-destructive testing (NDT) and structural health monitoring (SHM) approaches have been increasingly and widely incorporated to improve the safety of structures by precise damage detection, identification, and visualization.
The research was carried out also using vibration-based methods, that belong to the most popular and widely used damage detection techniques for decades [30-37] and they are still intensively developed [38].
Changes in modal parameters, such as natural frequencies, mode shapes, or damping coefficients, make it possible to monitor the condition of structures: the basic concept is that the dynamic characteristics of a structure are functions of its physical properties, therefore a change caused by any damage modifies its dynamic response [39,40].

1.2. Objectives and Scopes

In view of above, the main objective of this work is the assessment of the performance of RC beams strengthened using composite materials applying NSM technique, through experimentation and numerical simulation, through experimental static and dynamic tests. The main objectives of this research program are:

- Validation of NSM strengthening method, using different FRP strengthening materials, analyzing static response of specimens under bending loads;
- Examination of failure mode of the specimens, in order to observe the conservation of adhesion between concrete and resin or between FRP and resin, until failure of specimens;
- Use of vibration tests as additional non-destructive method to control the damage condition of beams, how the type of reinforcement affects the performance of the tested elements.

The project undertaken at the Polytechnic University of Marche was sponsored by the research funds provided by the university.
The content of the thesis is covered in eight chapters including this introduction.

Chapter 2 is a review of historical background concepts and previous work regarding the strengthening of reinforced concrete structures using fiber-reinforced composite materials (FRP). Firstly, an introduction to FRP materials was made, describing the main materials used and their mechanical characteristics. Then, an overview about the different strengthening technique and typical failure mechanism, both EB technique and NSM technique, used for the specimen's object of this work, have been addressed.

Chapter 3 reports a comprehensive literature review about the problem of adhesion, and the parameters that can influence it are discussed. A theoretical evaluation, present in literature, relating to local adhesion-sliding behavior is also reported.

In Chapter 4 the four RC beams specimens un-strengthened and strengthened with FRP rods are presented. Indications relating to the beam models designed are provided; the characteristics of the materials used are defined.
This section also contains the theoretical treatment of dynamic problem of vibration of the beam as a continuous system, as well as the theoretical static calculation of the beam subject to bending, following the theory of structural engineering.

In Chapter 5, the experimental campaign carried out during this research program is presented, the methods of carrying out the static and dynamic tests and the relative instruments used are described.
A short outline on the experimental modal analysis techniques, also used in this research work, is exposed. These techniques allow to experimentally obtain information on the dynamic behavior of a structure, such as natural frequencies and modal forms, through the measurement of the response of the same to a known excitation. The results obtained from the static tests and the dynamic tests of the experimental campaign are also reported and analyzed.
The results of the static tests concern the response of the beam models in terms of load-deflection, load-strain of the principal materials, moment-curvature, and high-strain at each loading-unloading cycle; the static behavior of each beam model, strengthening and not, is defined.
The results of the dynamic tests concern the frequency response functions in terms of acceleration, therefore the values of the natural frequencies at each state of damage relating to the first four modes of vibration.

In Chapter 6 comparisons between the results obtained are made: the experimental static results are compared with theoretical ones, in terms of deformation, a value of strain lag experimentally determined is proposed.

From dynamic tests, experimental results are compared with the theoretical ones, variations in percentage of natural frequencies at each state of damage relating to the first four modes of vibration with respect to the initial condition and with respect

to the condition of previous damage were calculated and exposed. The dynamic response of each beam model at the different damage levels, therefore the effectiveness of the reinforcement technique and the effects of the of damage, are evaluated.

Chapter 7 deals with the modeling developed with Ansys software for the beam models in question. In fact, a dynamic analysis on finite element beam models was carried out to validate the results obtained experimentally for each level of damage. In particular, the procedure followed for the modeling is reported: the creation of the finite element geometry; the choice of the types of elements; modeling of materials; the definition of the mesh; the application of loads and restraints. Then the results of the dynamic analysis are displayed: the modal forms; the values of the natural vibration frequencies; the absolute and relative percentage variations in frequency, calculated for each level of damage by assigning an elastic modulus evaluated starting from the experimental frequency data. In the end, data are compared with those obtained from laboratory tests.
The last chapter, Chapter 8, summarizes the main conclusion that can be drown from this thesis.

Chapter 2. Properties and applications of FRP in strengthening of RC structures

2.1. Introduction

A significant portion of existing structures is in urgent need of strengthening and rehabilitation because of deterioration due to natural causes or increased loading or due to exceptional actions such as earthquakes. Even the evolution of the legislation makes these buildings structurally inadequate and functionally obsolete.
The strengthening or repairing techniques are typically more convenient than new constructions, for this reason retrofit systems have been explored to extend service life and to improve performance of these structures. Fiber reinforced polymer (FRP) systems have shown great potential for such applications and have acknowledged significant interest recently. FRP is a composite material, i.e. a material made from two or more constituent materials with significantly different physical or chemical properties that, when combined, produce a material with characteristics different from the individual ones. In general, a composite material signifies two or more materials, which are combined on a macroscopic scale to form a useful third material [41]. FRP material systems are composed of fibers embedded in a polymeric matrix, which protects the load carrying fiber component of composite.
The most attractive characteristics of FRP in retrofit applications and some areas of construction are the ease of installation, high-strength, and lightweight properties, however FRP engineering structural components must possess not only sufficient strength and stiffness properties to resist the full superimposed and self-weight loads to which the structures are exposed but also the relevant in-service and physical characteristics required to function in the environmental conditions.
The first uses of FRP date back to 1975 in Russia, where it was used as reinforcement bars, later in Europe around 1980 [42]. At the same time in the United States, FRP composites were considered as a mainstream building material. In 1990s, composite materials became popular in Japan, where in 1996 the first design guidelines for FRP in the strengthening of RC structures were announced [43,44]. Later the use of composite materials commenced to expand worldwide.
In the next paragraphs the main characteristics of composite materials and the strengthening techniques of existing reinforced concrete members, in particular of RC beams, object of this dissertation, are expounded.

2.2. General Aspects on FRP Materials

As already mentioned, the FRP is a composite material consisting of two connected phases, polymer matrix and fiber, working in different ways. The polymer composite derives its mechanical characteristics wholly from those of the fibre and the quality of the fibre/matrix interface. In Figure 2.1 is shown the classification of composite materials, in particular of FRPs.

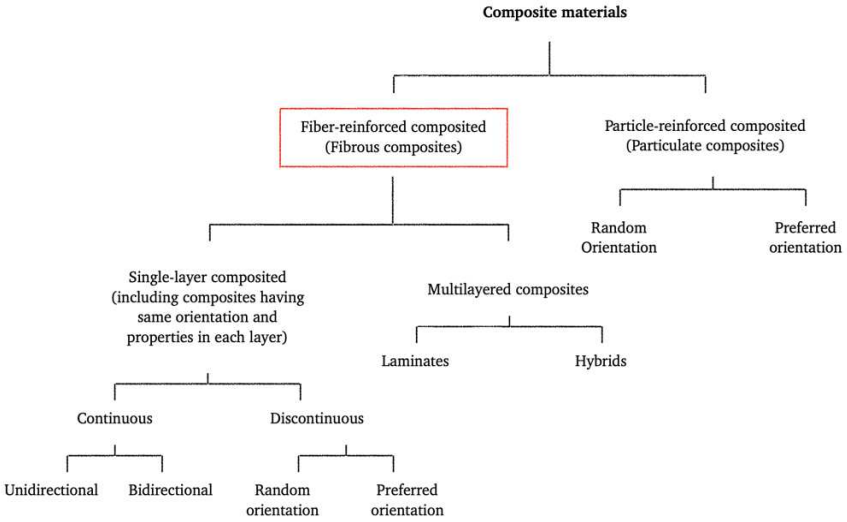

Figure 2.1 – Classification of composite materials

Talking about the individual constituent materials of the composite, the vinyl-esters, the epoxies and the polyesters are the thermosetting matrices which are most utilized for composite structural members, while a wide range of amorphous and crystalline polymer materials can be used to form fibres.
From a morphological point of view, the reinforcement systems made with FRP materials are distinguished in:

- Preformed systems (pre-cured): bars, sheets and strips produced in the factory by pultrusion, or other production processes and subsequently glued in situ on the element to be reinforced;
- Systems impregnated in situ (wet lay-up): sheets or fabrics of single or multi-directional fibers impregnated with a resin that can also act as an adhesive with the substrate concerned;
- Pre-impregnated systems (pre-preg): sheets or fabrics of single or multi-directional fibers pre-impregnated with partially polymerized resin and glued to the substrate to be reinforced with (or without) the use of additional resins.

In the construction industry the most common fibres are made from carbon fiber, to produce CFRP, glass fiber, to produce GFRP, basalt fiber, to produce BFRP and aramid fiber, to produce AFRP. AFRP is not a popular structural bar because of low compressive strength regardless of fiber alignment direction and high charge; its

main use is for ballistic-resistant fabrics. CFRP exhibit the highest resistance to fatigue and creep failure than other FRP materials, while GFRP is the cheapest material of all structural FRPs. Figure 2.2 illustrates the overall comparison between FRP materials and steel reinforcements based on stress-strain behavior. As can be seen from the figure, FRP reinforcements exhibit a linear elastic behavior before failure because of their poor plasticity and brittle nature.

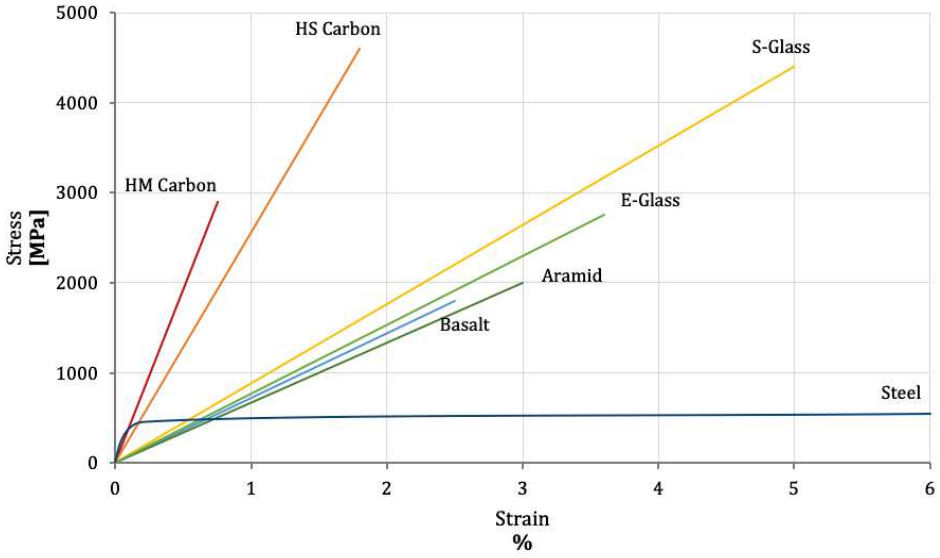

Figure 2.2 – Comparison of FRP materials with steel

The selection of strengthening materials generally depends on the types of materials used in the existing structure, strength requirements, environmental conditions, availability and costs. CFRP and GFRP, the most popular FRP material in civil field and those used in this research program, are reviewed in detail in the sequent section.

2.2.1. Typical Materials

Carbon fibers have diameters limited between 5 and 10 µm, the fibers are comprised of carbon atoms that bond both in crystals. Variations during the fiber manufacturing process allow to produce carbon with different characteristics; based on Young's modulus, carbon fibers can be classified into two macro families: General Performance (GP), High Performance (HP).
Carbon fibers belonging to GP category are characterized by low values of Young's modulus (<200 GPa); fibers belonging to HP category are divided in other sub-categories:

– High Tensile Strenght (HT), with standard values of Young's modulus (150 ÷300 GPa) and high values of tensile strength (>3000 MPa);

- Intermediate Modulus (IM), with standard values of Young's modulus (150 ÷300 GPa);
- High Modulus (HM), with high values of Young's modulus (300÷400 GPa);
- Ultra High Modulus (UHM), with very high values of Young's modulus (>400 GPa).

The mechanical behavior of a part produced in carbon fiber is characterized by the quantity of resin used as impregnating material. The higher the quantity of resin contained, the lower the mechanical quality of the product will be.
This is a consequence of the fact that the resin used in the impregnation of the fibers, once catalysis and hardening has taken place, assumes a "cushioning" behavior. Furthermore, a greater amount of resin also means a smaller amount of fiber used.
When comparing two parts in CFRP having the same shape, size and weight, the one with the highest resin content will be characterized by greater elasticity and less stiffness, therefore with qualitatively lower mechanical characteristics.
In general, comparing CFRP with steel, CFRP has an ultra-elastic modulus similar to steel, but is 5 times lighter and 8 times to 10 times more tensile resistant than conventional steel. Carbon fibers possess extremely high tensile strength and strength-to-weight ratio (20% the mass of steel) and because of its high stiffness is usually selected over GFRP to improve the strength in concrete structures.
GFRP is a sort of plastic compound that uses glass fiber constituent to increase the stiffness and strength of plastics. These fibers exhibit isotropic behavior – the physical properties do not depend on the direction in which the material itself is analyzed – and have an amorphous structure – a solid structure is defined as amorphous if there is no long-range order in the positions of the atoms or molecules that constitute it. GFRP also has extremely high strength-to-weight ratio, low weights of 9.67 kg/m^2 to 19.52 kg/m^2, as well as high resistance to corrosion. The types of glass fibers differ from each other for the quantity and type of oxides they contain and are the following:

- E type, where E stands for Electric, given its great characteristic of electrical resistivity; it has an elastic modulus lower than 80 GPa, excellent mechanical characteristic with breaking stresses up to 3.5 GPa; it is the cheapest type of fiber;
- S type S, where S stands for Strenght, therefore they are fibers characterized by high mechanical resistance, elastic modulus up to 90 GPa and tensile strength up to 4.5 GPa; it is the most expensive type of fiber;
- C Type, where C stands for Corrosion, a type of fiber characterized by greater resistance to corrosion and high temperatures;
- M type, where M stands for Modulus, a type of fiber characterized by a high elastic modulus up to 115 GPa;
- D type D, where D stands for Dielectric, a type of fiber characterized by a high dielectric constant, used for electronic applications;

– L type, where L stands for Light, type of fiber that is used for radiation protection, X-ray protective clothing is made.

The torsion capacity of CFRP beam elements is more advantageous for strengthening than that of GFRP beam elements, however CFRP-strengthened beams rapidly fail once reaching the ultimate point, whereas GFRP-strengthened beams exhibit residual strength for a considerable duration after peaking. Lastly, CFRP is more expensive than GFRP.

The main characteristics of carbon and glass fiber in comparison are shown in Table 2.1

Table 2.1 – Typical properties of C/GFRP

	Tensile Strength (GPa)	**Young's modulus** (GPa)	**Density** (g/cm^3)	**Typical diameter** (μm)	**Extension to break** (%)	**Cost**
HM Carbon	2.4-3.4	380-400	1.85-1.9	5-10	0.5-0.8	High
HS Carbon	4.1-5.1	230-280	1.75	5-10	1.6-1.73	High
E Glass	2-3.5	70-80	2.5-2.6	10	3.5-4.5	Very low
S Glass	4-4.8	85	2.4-2.5	10	4.5-5.5	Low

Hybrid FRPs also exist, they comprise a combination on CFRP and GFRP: carbon fiber provides high tensile strength, while glass fiber helps to lower the cost of the product.

Therefore, the composite material is composed of fiber that affords the strength and carries the applied loads, and the matrix, generally a polymer resin, that guarantees the consistency of the fibers, re-transition of applied loads to the fibers, and defense of fibers from exterior environment.

The most typical resins are thermosetting and thermoplastic polymer.

Most of thermosetting resins used on composites are Polyester, Vinylester and Epoxy. They display suitable thermal constancy and resistance to chemical and endure low creep and stress reduction. All these types of resins are used with glass fiber, while the expensive and performing carbon fiber is combined only with epoxy resin, which is equally high-performance and expensive. In Figure 2.3 a comparison between Polyester, Vinylester and Epoxy is shown.

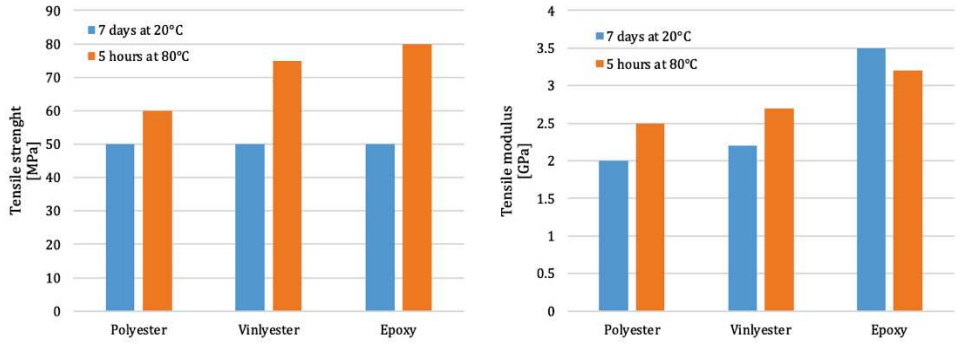

Figure 2.3 – Comparison of thermosetting resins

Focusing on epoxy resin, this type of resin comprises epoxy and hardener components that are mixed in requisite proportions in accordance with the manufacturer's specification. Epoxies should have high glass transition temperatures to withstand elevated temperatures and should be durable to adapt to critical environment and loading condition. They have unit weights of 1.1 kg/m^3 to 1.4 kg/m^3 and weights per unit surface area of approximately 0.5 kg/m^3. Epoxies are applied along the treated surface of RC elements and FRP sheets/strips are directly applied along the indicated space. They are sometimes injected into RC members through drilled holes for crack repair or FRP anchor strip insertion when NSM strengthening techniques are applied. Epoxy resins have tensile strengths of 30-90 MPa, maximum elongation at failure of 0.9-4.5%, and elastic modulus of 1.1-6 GPa. The required epoxy curing period are ranging from 3 days to 14 days at temperature 16-23°C.
Thermoplastic polymer instead is not applicable to be used for civil engineering resolution on account of its low creep and thermal resistance.
Adhesives can also be used for installation of certain types of FRP reinforcement, such as pultruse foils. The most appropriate choice of the adhesive and the type of surface treatment to be carried out before the application must be made according to the nature of the substrate of the structure to be repaired (steel, c.a., masonry or wood) and the reinforcement material. There are many types of natural and synthetic adhesives, the most suitable for FRP reinforcements are epoxy resin-based adhesives.

2.3. Main strengthening techniques

The main reasons why RC beams are strengthened using FRPs are the increasing of flexural strength, shear strength, fatigue life, seismic resistance, and impact or blast resistance. All these goals can be achieved through techniques involve the use of externally bonded (EB) laminates, near-surface mounted (NSM) bars or strips, or mechanical anchorage systems. The externally bonded (EB) FRP method has become a prevailing technique over the last two decades [15,16]. In the past ten

years, as a promising alternative to the EB FRP method, the near- surface mounted (NSM) FRP strengthening technique has attracted increasing worldwide attention [17-19].
EB FRP strengthening method consist in using wet lay-up sheets bonded to the faces of the beam; it can be performed with the desired number of strengthening layers on the beams in any configuration, such as side bonding, U-wrapping, or fully wrapping. Instead in NSM technique strips, or bars, can be inserted into grooves cut along tension faces of the beams and covered with concrete or adhesive layers with sufficient thickness.
The NSM FRP method owns many advantages over the EB FRP method:
– Surface preparation is no longer required;
– Better protection of the FRP reinforcement by the concrete cover;
– Higher bonding efficiency.
De Lorenzis and Teng [15] provided a detailed and critical review of the research available to them at the time on the strengthening NSM FRP technique. Their review covered various aspects like the reinforcement material, groove filler, groove dimensions, groove position and constructional aspects, that are all important construction parameters, which can influence the bond performance and therefore the structural behavior. They also outlined the main research needs for more extensive applications of this strengthening technique and identified an important issue to examined: the bond behavior between NSM FRP and concrete.
After De Lorenzis and Teng work [15], a significant amount of research has been conducted, including experimental, theoretical and numerical studies into the behavior of concrete structural members strengthened with NSM FRPs.

2.3.1. Flexural strengthening

A significant number of experimental studies have also been conducted on RC beams strengthened in flexure with NSM CFRP strips in the past two decades [22,45-47]. The application of FRP reinforcement in correspondence of tensile edge on a bent concrete element, gives an increase in the flexural strength. The existing experimental studies on NSM CFRP RC beams generally show a significant enhancement of the flexural capacity of the strengthened RC beam. Hassan [48] investigated the performance of various NSM FRP reinforcing bars and strips, as well as externally bonded FRP sheets on small-scale concrete beams and slabs. Test results showed that using NSM CFRP reinforcing bars increased the strength by 36%. Using NSM CFRP strips increased the strength by 43% in comparison with an increase of only 11% using the axial stiffness used as externally bonded strips due to peeling failure of the strips. Hassan reported that the efficiency of using FRP reinforcing bars as NSM reinforcement is controlled by the bond characteristics of the reinforcing bars in addition to the bond between the epoxy adhesive material and the surrounding concrete in groove. Such behavior has been confirmed and

reported by other research. De Lorenzis and Nanni [24] found that the maximum tensile strain in the CFRP and GFRP bars used as NSM reinforcement did not exceed 33 and 60% of the rupture strain of the bars at failure. Hassan reported that such a limiting value is highly dependent on the configuration and the ratio of the steel reinforcement inside the concrete beam as well as on the stress level at the concrete-epoxy interface. The exact amount of enhancement depends on the amount of FRP, the steel reinforcement ratio and the failure mode, among others. Compared to the results of RC beams strengthened with externally bonded FRP plates a much higher utilization of the tensile capacity of the FRP was observed in NSM CFRP RC beams [45,46,49,50]. El-Hacha and Rizkalla [45], testing simply supported T-beams reinforced with different FRP reinforcements (CFRP bars and strips as well as GFRP thermoplastic strips), found that NSM FRP reinforcements significantly increased the ultimate load-carrying capacity of the beams, the ultimate strength of strengthened beams with NSM CFRP strips was governed by tensile rupture strength of CFRP strips, while in the case of NSM CFRP reinforcing bars, FRP-epoxy-split failure was the dominant mode of failure as a result of high tensile stresses at the CFRP reinforcing bar-epoxy interface.
Kotynia [51,52] has focused her research on RC beams strengthened with NSM CFRP strips varying the depth of the CFRP strips, thickness of the concrete cover, amount of longitudinal steel reinforcement, percentage of CFRP reinforcement and strength of concrete and found the higher was NSM CFRP ratio the lower was limit strain during its debonding and the strain utilization of the FRP.
Barros and other [53,54] have studied reinforced concrete beams reinforced with a variable number of CFRP strips and with different steel reinforcement ratios. Test results showed an almost double increase in load bearing capacity; in addition, the significant increase in the yield strength of steel and the cracking load of concrete for reinforced beams demonstrates the greater efficiency of the NSM technique compared to the EBR technique

In general, it can be said FRP reinforced members are over-reinforced, that means, the proportion of FRP bar to concrete is larger than the balanced ratio; hence, concrete crushing of the member controls the failure mode [55]. The flexural strength of FRP material is determined using ACI 440 similar to ACI 318 because of rebars do not yield similar to steel bars [55-57].
For the evaluation of flexural strength of a reinforced section using FRP system, the following assumptions are made:

- The deformations on the FRP and on concrete are directly proportional to the distance from the neutral axis (conservation of plane sections);
- Perfect adhesion between the external FRP reinforcement and concrete;
- The shear deformation inside the adhesive layer is neglected as the adhesive layer is cery thin with small variations in its thickness;
- The maximum usable deformation in concrete is 0.0033;

– FRP reinforcement has a constitutive linear elastic behavior up to failure.

This hypothesis may not faithfully reproduce the actual behavior of the strengthened element. For this reason, a resistance reduction coefficient is applied to compensate the discrepancies.

The design bending strength, ϕM_n, is obtained from the nominal strength of the structural element, M_n, multiplied by the reduction coefficient ϕ. The approach taken by this guide follows the philosophy of ACI 318-05. A strength reduction factor given by (2.1) should be used, where ε_t is the net tensile strain in the extreme tension steel at nominal strength and ε_{sy} is the yielding strain of steel reinforcements, as defined in ACI 318-05.

$$\phi = \begin{cases} 0.90 \; for \; \varepsilon_t \geq 0.005 \\ 0.65 + \dfrac{0.25(\varepsilon_t - \varepsilon_{sy})}{0.005 - \varepsilon_{sy}} for \; \varepsilon_{sy} < \varepsilon_t < 0.005 \\ 0.65 \; for \; \varepsilon_t \leq \varepsilon_{sy} \end{cases} \quad (2.1)$$

This means to set a reduction factor at 0.90 for ductile section and 0.65 for brittle sections where the steel does not yield and provides a linear transition for the reduction factor between the two extremes.

Figure 2.4 illustrates the internal strain and stress distribution for a rectangular section under flexure at the ultimate limit state both for EB and NSM strengthening methods. The calculation procedure used to arrive at the ultimate strength should satisfy strain compatibility and force equilibrium and should consider the governing mode of failure.

An additional reduction factor for FRP,ψ_f, is applied to the flexural-strength contribution of the FRP reinforcement. The recommended value of ψ_f is 0.85. This reduction factor for the strength contribution of FRP reinforcement is based on the experimentally calibrated statistical properties of the flexural strength.

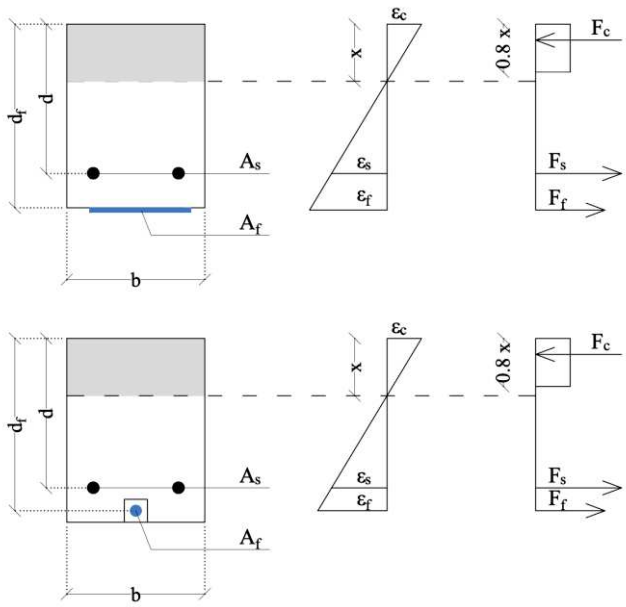

Figure 2.4 – Distribution of stress and strain in RC elements with flexural strengthening

2.3.2. Shear strengthening

The shear capacity of beams with insufficient shear reinforcement or cracked concrete must be increased. EB FRP systems have been successfully used in the shear strengthening of RC beams over the past few years. Additional FRP web reinforcements can be applied as shear reinforcements with vertical, inclined, side-bonded, U-wrapped or anchored configurations to beams through the EB technique. The EB FRP strengthening technique has been proven to increase the shear strength of RC beams, and its effectiveness under corresponding loading conditions depends on the types and orientations of FRP reinforcements [58].
Through NSM technique it is also possible to obtain a significant shear reinforcement of RC elements; reinforcement bars are inserted inside grooves cut on the sides of the element, inclined respect to the axis of the beam; the reinforcements are arranged orthogonally to the beam axis, or in any case to the intended direction of the shear cracks. The experimental results available show that the rectangular section of FRP reinforcements guarantees greater effectiveness at the ultimate shear capacity, due to the greater ratio between the reinforcement-concrete adhesion perimeter and the cross-sectional area of the reinforcement, as well as the greater confinement provided by the concrete around the reinforcement itself [59].
De Lorenzis and Nanni [60] proved the effectiveness of shear strengthening testing eight RC beams strengthened with CFRP rods varying spacing of the rods, strengthening pattern, end anchorage of the rods, and presence of internal steel shear

reinforcement. They found an increase in capacity of 106% in absence of stirrups, and of 35% in the specimens with steel stirrups.
Barros and Dias [61] tested beams of different sizes without internal stirrups: some beams reinforced with CFRP strips applied according to the NSM technique with different inclinations, others reinforced with an equivalent amount of externally applied FRP shear reinforcement (EBR). The increase in resistance measured varies from 22 to 77% and in all cases is greater than the increase obtained with the external reinforcement technique.
Nanni et al. [62] reported the results of the test conducted on a single full-scale beam, of a bridge, reinforced in shear with CFRP strips applied according to the NSM technique; the beam reaches failure due to bending.
Furthermore, experimental research has also shown that the effectiveness of shear reinforcement according to the NSM technique depends mainly on the following parameters: percentage and orientation of the FRP reinforcement; strength of concrete and percentage of internal steel stirrups. The application of shear reinforcement often concerns elements in reinforced concrete already cracked; however, the experimental tests have shown that the main difference in the behavior of beams with or without cracks lies in the loss of initial stiffness compared to un-damaged beams [63]. In these beams the effectiveness of FRP reinforcements begins immediately after the crack opening process; on the contrary, in non-cracked beams it occurs only when the shear crack has formed: however, the already existing crack does not affect the effectiveness of the NSM shear reinforcement technique in terms of load-bearing capacity and final deflection.

2.4. Analysis of failure of FRP-strengthened RC beams

The effectiveness of strengthening could be reflected by the failure mode of strengthened structures. Most strengthened structures are expected to undergo ductile failure with the maximum utilization of strain capacity. EB FRP could help change the failure mode of RC structures from brittle failure to ductile failure under static and dynamic loading [64].
The failure zones of RC beams strengthened by EB FRP are shown in Figure 2.5 [65]. This failure mechanism has also been described in several studies [66]. The most common failure associated with beams strengthened with EB FRP is debonding.

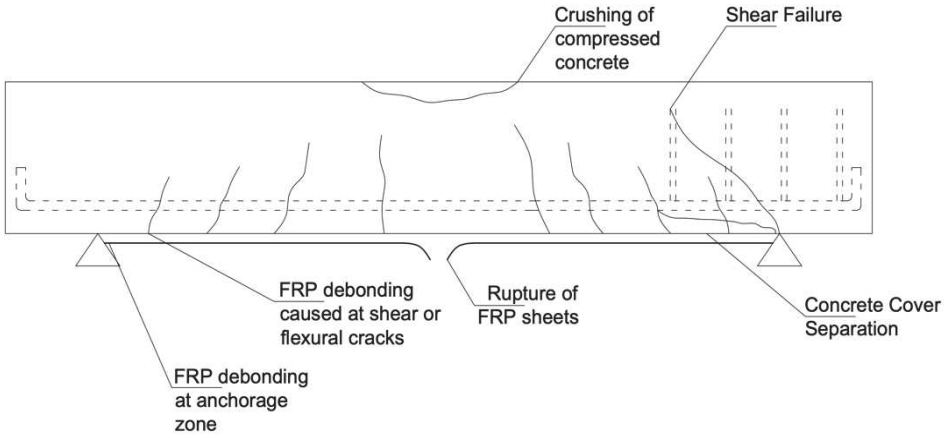

Figure 2.5 – Typical failure mode of a RC beam strengthened by EB FRP

The NSM strengthening technique could delay the debonding failure of FRP, this mechanism can be classified into several types, which will be described in the following paragraph.

2.4.1. Debonding failure

As anticipated, one of the most commonly reported disadvantages of the FRP strengthening system is its brittle debonding failure mode.
Observing the bond-free-end slip relationships (i.e. the trend of end slip on the NSM bar) for RC beams strengthened with NSM CFRP bar, Hassan and Rizkalla [25] tried to explain bond mechanism identifying two main stages:

Stage I: represents the initial bond provided by chemical adhesion. At this stage no slip occurs.

Stage II: represents break of the chemical adhesion and transfer of bond forces by mechanical friction provided by the lugs of the bars. At this stage, bearing stresses in concrete epoxy are developed and induced transverse micro cracks at the tips of the lugs allowing the bar to slip. Later in this stage, a significant increase of bearing forces accompanied by numerous internal cracks around the deformed CFRP bars took place causing debonding failure.
In the context of simply supported NSM FRP RC beams, debonding failure modes are likely to occur both at the ends of NSM FRP strips or bars and in the maximum moment region. Debonding may occurs in the form of interfacial debonding, that occurs at or near a bi-material interface, and in the form of separation of concrete cover where the concrete cover containing the NSM FRP reinforcements. The term "debonding" refers to both interfacial debonding failure and cover separation failure; that is, it refers to all failure modes where the composite action between the

FRP and the concrete beam is not maintained. In the experimental studies of NSM CFRP RC beams, in addition to the two conventional failure modes of RC beams, namely, flexural failure by crushing of compressive concrete [51,67,68] and flexural failure by rupture of FRP [25,45], the following debonding failure modes have been reported [69]:

– Intermediate crack (IC) induced debonding failure. In this failure mode, the debonding of FRP starts from the maximum moment region and propagates to one of FRP ends. Figure 2.6 depicts a typical schematic fractures of the IC debonding failure. In IC interfacial debonding (Figure 2.6-a) the debonding happens between FRP rod and the surrounding concrete (more accurately, in the thin concrete layer adjacent to the adhesive layer), instead in IC cover separation failure (Figure 2.6-b the FRP rod together with the concrete cover is detached from the beam starting from the maximum moment region, with a major crack travelling on the plane of the steel tension bars;

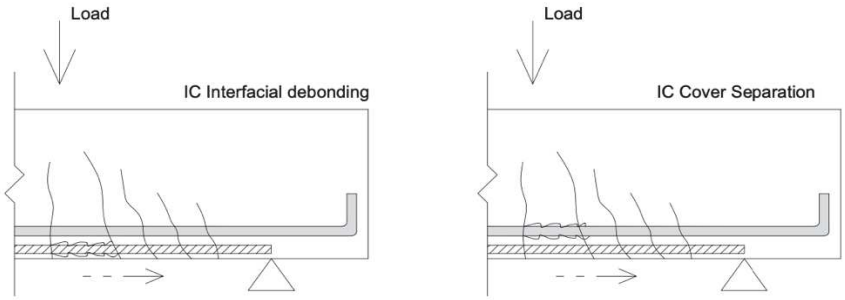

(a) *(b)*

Figure 2.6 – Scheme of Interfacial Debonding

– End debonding failure [20,25,53,54,70]. In this failure mode, the debonding of the FRP rod starts from one end of the FRP and propagates to the mid-span of the beam. This failure mode is mainly due to the high interfacial shear and normal stresses caused by the abrupt termination of FRP element. Figure 2.7 depicts a typical schematic fractures of end debonding failure. As in the previous case, the end debonding failure can happens into two different ways: end interfacial debonding (Figure 2.7-a) and end cover separation (Figure 2.7-b).

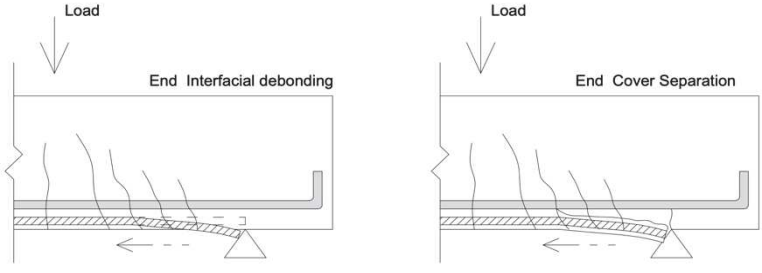

(a) *(b)*

Figure 2.7 – Scheme of End Debonding

End interfacial debonding and end cover separation are quite similar to their correspondent's IC interfacial debonding and IC cover separation respectively, except for the starting point of debonding.
Between interfacial debonding and cover separation there are differences from the point of view of the intrinsic failure mechanism: the interfacial debonding failure interests the FRP-to-concrete interface, so the debonding strength is thus mainly controlled by the material and interfacial properties on/near such interfaces. Instead, the cover separation failure happens on the horizontal plane of tension steel bars with both concrete cover and FRP detached from the RC beam, therefore the strength is mainly controlled by steel bars. In the next chapter, which is entirely dedicated to the adherence mechanism, the debonding failure will be resumed and detailed from the mechanical point of view.

The most common failure mode among the above debonding failure modes for NSM FRP RC beams is cover separation (i.e. IC cover separation and end cover separation). Possible reasons for this phenomenon include:
– the strong bond between NSM FRP and resin makes the interfacial debonding failure less likely;
– the large radial stresses, exerted by the steel tension bars to the surrounding concrete during their tension process [4], it plays an important role in accelerating the cracking in the concrete along the level of steel tension bars.

Nevertheless, interfacial debonding is also an important debonding failure mode, especially for NSM FRP-strengthened RC beams with a relatively large beam width [71].
The key concept of maintaining bond between NSM rods and concrete and/or adhesive resin until failure of beam ensures the availability of NSM strengthening. Considerations on NSM FRP strengthening can be elaborated from the results of experimental investigation using pull-out tests on concrete specimens with G/CFRP rods, in order to evaluate the local bond stress-slip relationship controlling numerically developed strategies.
In the next chapter, the issue of adherence between FRP and adhesive and the safety checks against the delamination mechanism will be explored.

2.4.2. Rupture of FRP

The high strength of concrete–adhesive bonds, the effective utilization of stress, and the inferior quality of fibers within high-strength concrete and internal steel could induce the occurrence of FRP rupture as ultimate failure. The most common failure experienced by strengthened RC beams with full wrapping is FRP rupture after localized debonding, which may be ascribed to the effective utilization of strain [72]. EB FRP systems with fibers in the horizontal and vertical directions show higher strain utilization than EB FRP systems with fibers in the vertical direction. Nevertheless, debonding occurs when fibers tear under failure load. FRP

rupture occurs because of the development of excessive diagonal shear cracks under peak load when a partially side-wrapped shear strengthening system is used in RC beams under ultimate loading. These ruptures occur in the strong direction parallel to fiber alignment. The maximum FRP rupture strain is obtained in the horizontal direction for the beam strengthened with a single layer of CFRP sheet instead of a double layer sheet. The allowable strain in FRP is approximately 10%–25% of the rupture strain [73]. Multiple layers of FRP can reduce the possible utilization of strain and the brittle rupture of FRP layers at levels below their effective stress. Anchors can prevent premature fracture effectively with the help of effective bond stress distribution along the width of concrete.

2.4.3. Influence of anchorage system

The overall performance of EB wrapping and NSM strengthening is dependent on the bonding between the FRP and concrete, consequently numerous researchers studied the use of different methods to eliminate debonding as a mode of failure (mechanical anchors, sheets wrapped at ends…). The presence of an end anchorage system on FRP-strengthened beams can prevent debonding failure in partially wrapped FRP-strengthened beams and increase capacity [74]. Anchorage can increase strain levels in FRP before failure. The use of the appropriate types of anchorages increased strength by up to 95% and reduced slip level [75]. Given the presence of the anchor system, the chance of debonding reduces stress concentration along the anchor zone in most cases. Therefore, primary failure occurs in the form of FRP rupture with concrete crushing or with partial or full debonding [76]. In NSM FRP-strengthened beams the location of NSM strips controls stress distribution and crack patterns within the anchorage zone. NSM strips along the side of the beam could better enhance the utilization of FRP strain than NSM strips along the bottom of the beam [49] because the bottom NSM strip-strengthened beam fails through concrete cover separation at the anchorage zone.
By now metallic and non-metallic anchorage measures have been investigated in experimental tests. The metallic anchorage measures suffer from two types of disadvantages: the difficulty of installation and the poor resistance to corrosion. Therefore, non-metallic anchorage systems are more attractive than the previous. The studies on the use of FRP U-jackets as anchorage measures for NSM FRP bars in FRP-strengthened RC beams have been rather limited. These limited existing studies, however, have revealed that FRP U-jackets are quite effective in both postponing the end debonding of the beam and enhancing the ductility of the beam.

In this chapter, the literature available on the main reinforcement systems with FRP materials for RC beams has been briefly treated, mainly focusing on topics pertaining to the research in this thesis. From the review emerges that the NSM FRP strengthening method in the flexural strengthening of RC beams is much more efficient than the EB FRP method.

In conclusion failure modes of strengthened RC specimens of beam are reviewed: several experimental studies have been conducted on NSM CFRP RC beams, which have led to identify four debonding failure modes. Concrete cover separation has been found to be more often than interfacial debonding in NSM FRP RC beams.
The review presented in this chapter also suggests that using U-shaped FRP jackets for end-anchorage of NSM FRP strips or bars was shown to enhance the strengthening efficiency. However, this method has not been deeply investigate.

Chapter 3. Bond Analysis

3.1. Introduction

In strengthening reinforced concrete elements with composite materials, the role of adherence between concrete and FRP assumes great importance as it guarantees the effectiveness of the NSM consolidation method. In addition, the mechanism of rupture by delamination (loss of adhesion) is of brittle type, therefore following the criterion of hierarchy of resistances, this crisis mechanism must not precede the collapse by bending or cutting of the reinforced element.
The loss of adhesion between composite and concrete may concern sheets or fabrics applied to the intrados of reinforced concrete beams for bending reinforcement, and on the side faces for shear reinforcement, but also rods inserted into grooves, as in the case of the NSM technique.
In principle, therefore, delamination can occur between adhesive and concrete, between adhesive and composite or within the composite itself (for example between layers of woven fabric with different inclination angles of the fibers).
In the case of reinforcements placed correctly in place, since the adhesive resistance is generally much higher than the tensile strength of the concrete, delamination always takes place inside the latter with the removal of a layer of material, whose thickness can vary from a few millimeters up to affect the entire concrete cover of the reinforcing bars.
Understanding the real behavior of NSM FRP reinforcement is fundamental for an adequate use of this strengthening technique.
In this chapter theoretical bond analysis for evaluating strain data and shear stress-slip laws, present in literature, are reported and discussed; in one case the theoretical model is supported by an experimental investigation using pull-out tests on concrete specimens with C/GFRP rods, whose results are shown.
In closing, the construction parameters that can influence the bond and therefore the structural behavior, as well as the safety checks against delamination or the evaluation of the maximum transmissible force from the concrete to reinforcement and the evaluation of the tangential and normal stresses mobilized at the concrete-FRP interface are reported.

3.2. Theoretical model of bond adhesion

Hassan and Rizkalla [21] simultaneously with tests on 8 R.C. T-beams strengthened with NSM CFRP bars, developed an analytical model in order to evaluate the development length of NSM FRP bars of different configurations and type of fibers. In the proposed approach two simplifying hypotheses are admitted:

– friction coefficient $\mu = 1/\tan\beta$ is constant, even though it actually changes during the loading process (with β is the inclination of the force with respect to the axis of the bar);
– the radial pressure distribution is uniform, although the pressures on the thicker concrete substrate are higher than those on the thinner cover.

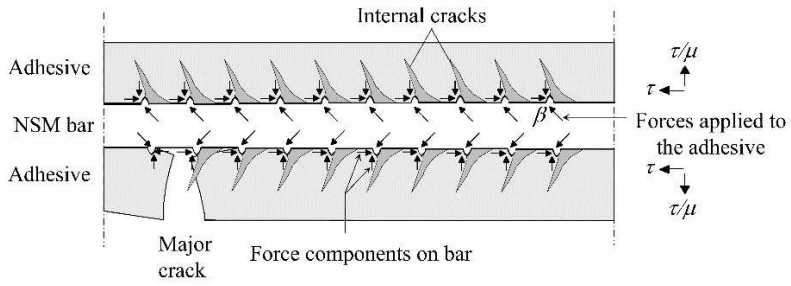

Figure 3.1 – Forces between the NSM bars and adhesive proposed in Hassan and Rizkalla research [21]

In this case the adhesion bond for ribbed circular section bars is controlled by tensile stresses in the epoxy resin cover and surrounding concrete.
L. De Lorenzis [77] assumed $\gamma = 45°$ that means $\mu = \frac{1}{\tan\gamma} = 1$, while T.K. Hassan and S. Rizkalla determine it by relying on ASTM G115-98 [78] (i.e. $\mu = 0.5$).
For ribbed circular section bars, T.K. Hassan and S. Rizkalla proposed a finite element model to describe the crisis mechanism for splitting the epoxy resin cover. They provided two formulas to predict the tangential resistance values of adhesion at the epoxy resin-concrete and bar-epoxy resin interface. The tangential adhesion resistance is therefore the lesser of the two, that is
$\tau_{max} = min\{\tau_{\max epoxy-concrete}, \tau_{\max bar-epoxy}\}$.
The two forumula are:

$$\tau_{\max epoxy-concrete} = \frac{f_{ct}\,\mu}{G_1} \qquad (3.1)$$

$$\tau_{\max bar-epoxy} = max\left\{\frac{f_{at}\mu}{G_2}, \frac{f_{at}\mu}{G'_2}\right\} \qquad (3.2)$$

Where f_{ct} and f_{at} are respectively the tensile strength of concrete and epoxy resin, and G_1, G_2, G'_2 are coefficients evaluated by finite element analysis.

The coefficients G_1, G_2, G'_2 depend on the ratio of thickness of the epoxy resin cover, to the diameter of the bar and the width of the groove to the diameter of the bar.
For G_1, G_2, G'_2 special diagrams have been developed (Figure 3.2).

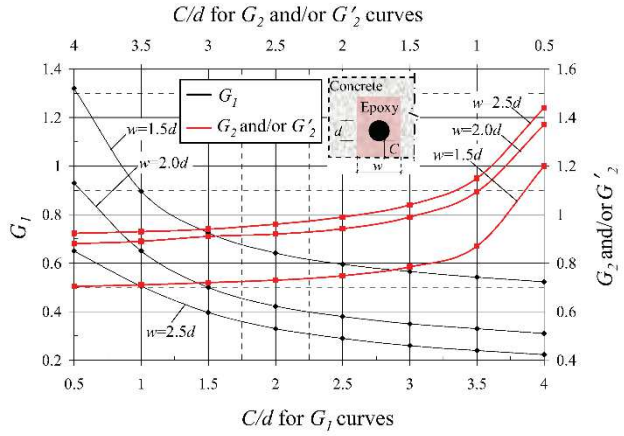

Figure 3.2 – Design chart for the development length of NSM FRP bars, proposed in Hassan and Rizkalla research [21]

Therefore τ_{max} varies between $0.77\mu f_{ct}$ e $1.72\mu f_{ct}$, which are very low values compared to the test results reported by L. De Lorenzis. It should be noted that the tangential adhesion resistance in this model is the value of the adhesion tension corresponding to the opening of cracks in the epoxy resin or concrete. A two-dimensional elastic stress analysis was conducted by L. De Lorenzis [79], to determine the adhesion tension corresponding to the cracking of the epoxy resin cover. However, no equation for the tangential adhesion resistance has been proposed.
Concerning the tangential adhesion resistance for NSM laminae, some formulas have been proposed by M. Blaschko [80] and by T.K. Hassan and S. Rizkalla. M. Blaschko formula is:

$$\tau_{max} = 0.2\,(a'_e)^{\frac{1}{4}} \cdot f_{av} \qquad (3.3)$$

Where f_{av} is the shear strength of the epoxy resin.
T.K. Hassan and S. Rizkalla [21] formula is:

$$\tau_{max} = \frac{f'_c\, f_{ct}}{f'_c + f_{ct}} \qquad (3.4)$$

where f'_c e f_{ct} are respectively the cylindrical compressive and tensile strength of the concrete. The two formulas relate the tangential adhesion resistance with different parameters, in line with their own experimental observations: M. Blaschko considered the crisis for achieving the cohesive shear strength of the epoxy resin and the effect of a_e', while T.K. Hassan and S. Rizkalla observed the crisis for achieving the cohesive shear strength of the concrete. M. Blaschko's formula was calibrated with pull-out test results, while T.K. Hassan and S. Rizkalla derives from

Mohr's circle for pure shear stress state, which, used in finite element modeling, gave delamination load predictions in good agreement with bending test results.
E. Cosenza et al. [81] presented a synthesis of the adhesion properties of FRP bars used as internal reinforcement, obtaining a tangential adhesion strength of 2.74 MPa for sandblasted bars and 11.61 MPa for ribbed bars and 11.90 MPa for wound bars spiral.
The diagrams of bond law (τ-s) have been deduced through experimental tests by L. De Lorenzis [79] for different types of circular section bars, and by J.M. Sena-Cruz and J.A.O. Barros [82] for NSM foils. L. De Lorenzis reported three different types of adhesion bond.

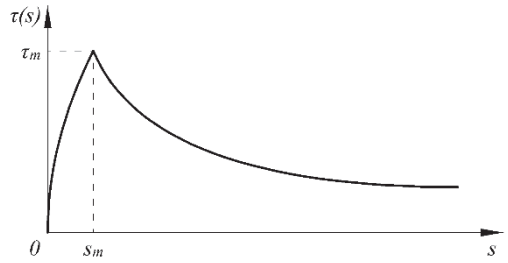

Figure 3.3 – Diagram of bond law τ-s behavior of Type I

$$\tau(s) = \tau_m \cdot \left(\frac{s}{s_m}\right)^{\alpha} = C \cdot s^{\alpha} \text{ with } 0 \le s \le s_m \text{ and } 0 < \alpha \le 1 \quad (3.5)$$

$$\tau(s) = \tau_m \cdot \left(\frac{s}{s_m}\right)^{\alpha'} = C \cdot s^{\alpha'} \text{ with } s \ge s_m \text{and } \alpha' < 0 \quad (3.6)$$

Found for:
- bars with circular section for CS-I crises;
- ribbed circular section bars for SP crises;
- NSM sheets for ID crisis.

Figure 3.4 – Diagram of bond law τ-s behavior of Type II

$$\tau(s) = \tau_m \cdot \left(\frac{s}{s_m}\right)^{\alpha} = C \cdot s^{\alpha} \text{ with } 0 \le s \le s_m \text{ and } 0 < \alpha \le 1 \quad (3.7)$$

$$\tau(s) = \tau_f \text{ with } s \ge s_m \quad (3.8)$$

Found for ribbed and spiral wound circular section bars for SP crises.

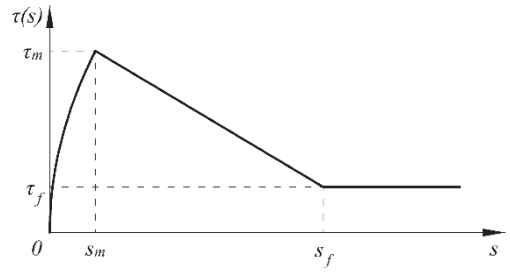

Figure 3.5 – Diagram of bond law τ-s behavior of Type III

$$\tau(s) = \tau_m \cdot \left(\frac{s}{s_m}\right)^{\alpha} = C \cdot s^{\alpha} \text{ with } 0 \le s \le s_m \text{ and } 0 < \alpha \le 1 \quad (3.9)$$

$$\tau(s) = \left(\frac{\tau_f - \tau_m}{s_f - s_m} \cdot (s - s_m)\right) + \tau_m \text{ with } s_m \le s \le s_f \quad (3.10)$$

$$\tau(s) = \tau_f \text{ with } s \ge s_f \quad (3.11)$$

Found for sandblasted circular section bars
With τ_m peak adherence stress, s_m slip relative to peak adherence stress τ_f residual friction adhesion stress, s_f slip relative to residual friction adhesion stress.
The maximum tension that can be supported by an NSM bar with a sufficiently long anchor length is given by

$$\sigma_{max} = \sqrt{2E_b \frac{\sum_b}{A_b} G_f} \quad (3.12)$$

With $G_f = \int_0^{\infty} \tau(s)ds$ fracture energy and A_b, Σ_b, E_b, respectively the area of the FRP bar section, the perimeter of the FRP bar section and the elastic modulus of the FRP bar. If σ_{max} is lower than the tensile strength of the FRP bar, the total capacity of the reinforcement cannot be developed regardless of the extension of the anchoring length.

The effective anchorage length is defined as the one at which the tension σ_{max} develops and beyond which, a further increase in the anchorage length does not produce any benefit. If the stress σ_{max} is greater than the tensile strength of the bar, the total capacity of the reinforcement can be developed, and the corresponding anchor length value is called the "development length".
Usually for bonds of adhesion for which the fracture energy G_f has a finite value, the total capacity of the reinforcement cannot be developed, consequently the development length cannot be calculated, as opposed to the effective anchor length.
It is important to note that while the tangential resistance of adhesion τ_{max} determines the breaking load for elements with short reinforcement, the breaking load for elements with long reinforcement, depend more on the type of adhesion bond, in particular of its descending post-peak branch which controls the ability to redistribute stresses along the length anchor.

3.2.1. Capozucca's elastic model

R. Capozucca developed an elastic model to analyse bond behaviour of NSM C/GFRP rods which allows to obtain data to compare with pull-out tests results [23,83]. It can be assumed that the elastic behaviour is maintained up to failure. Slip function *s(z)* represents the displacement of the FRP rod point along its axis. The theoretical analysis is based on the definition of the system's total potential energy and on the search function *s(z)* which determines the minimum of energy. The elastic strain energy of the FRP rod is equal to:

$$L_{FRP} = \frac{1}{2}\int_0^{l_b}\int_{A_b} \sigma(z)\cdot\varepsilon(z)dA_b\cdot dz \tag{3.13}$$

Where A_b is the area of the GFRP rod section and l_b is the bonded length. Being $\varepsilon(z) = \frac{ds(z)}{dz}, \sigma(z) = E_b\cdot\varepsilon(z)$, with E_b rod's Young's modulus, the following is obtained:

$$\begin{aligned} L_{FRP} &= \frac{1}{2}\int_0^{l_b}\int_{A_b} E_b\cdot\left(\frac{ds(z)}{dz}\right)^2 dA_b\cdot dz \\ &= \frac{1}{2}\int_0^{l_b} E_b\cdot A_b\cdot(s'(z))^2\cdot dz \end{aligned} \tag{3.14}$$

The elastic strain energy of the adhesive-resin is expressed by the following:

$$L_{epoxy} = \frac{1}{2}\int_0^{l_b}\tau(z)\cdot s(z)\cdot\sum_g\cdot dz \tag{3.15}$$

Where: Σ_g is the perimeter of the groove in contact with the epoxy resin. Being $\tau(z) = G_e\cdot\gamma(z)$ with G_e shear modulus of adhesive, and $\gamma(z) = \frac{s(z)}{t}$ shear strain of adhesive, the following is obtained:

$$L_{epoxy} = \frac{1}{2}\int_0^{l_b} G_e\cdot\frac{s(z)^2}{t}\cdot\sum_g\cdot dz \tag{3.16}$$

Assuming the following value as stiffness of adhesive:

$$K_e = \frac{G_e\cdot\sum_g}{t} \tag{3.17}$$

Hence, the following is had:

$$L_{epoxy} = \frac{1}{2}\int_0^{l_b} K_e\cdot s(z)^2\cdot dz \tag{3.18}$$

The external work values can be expressed as:

$$L_F = -F\cdot s(z = l_b) \tag{3.19}$$

Total potential energy results to be:

$$E_{PT} = \int_0^{l_b} \frac{1}{2}\left(E_b A_b \cdot \left(s'(z)\right)^2 + K_e \cdot s(z)^2\right) dz - F \cdot s(z = l_b) \quad (3.20)$$

For the principle of the least energy, function *s(z)* is sought E_{PT} *(z, s(z), s'(z))*, through the following equation:

$$\frac{\delta}{\delta s(z)} E_{PT}(z, s(z), s'(z)) = 0 \quad (3.21)$$

Assuming

$$f\left(z, s(z), s'(z)\right) = \frac{1}{2}\left(E_b \cdot A_b \cdot \left(s'(z)\right)^2 + K_e \cdot s(z)^2\right) \quad (3.22)$$

Hence:

$$\delta E_{PT} = \delta\left(\int_0^{l_b} f \cdot dz\right) + \delta(-F \cdot s(z = l_b)) \quad (3.23)$$

Being $\delta s(0) = \delta s(l_b) = 0$ the energy's first variation is given by:

$$\delta E_{PT} = \delta\left(\int_0^{l_b} f \cdot dz\right) = \int_0^{l_b} \left(\frac{\partial f}{\partial s} - \frac{d}{dz}\left(\frac{\partial f}{\partial s'}\right)\right) \cdot ds \cdot dz \quad (3.24)$$

Becoming null:

$$\frac{\partial f}{\partial s} - \frac{d}{dz}\left(\frac{\partial f}{\partial s'}\right) = 0 \quad (3.25)$$

Where

$$\frac{\partial f}{\partial s} = K_e \cdot s(z)$$
$$\frac{d}{dz}\left(\frac{\partial f}{\partial s}\right) = E_b A_b \cdot s''(z) \quad (3.26)$$

The following differential equation is thus had:

$$s''(z) - \left(\frac{K_e}{E_b \cdot A_b}\right) \cdot s(z) = 0 \quad (3.27)$$

By introducing the coefficient $\xi^2 = \frac{K_e}{E_b \cdot A_b}$, the slip function may be obtained from (3.27) which becomes:

$$s''(z) - \xi^2 \cdot s(z) = 0 \quad (3.28)$$

The solution of (3.28) is of the type:

$$s(z) = C_1 \cdot \cosh(\xi \cdot z) + C_2 \cdot \sinh(\xi \cdot z) \quad (3.29)$$

Assuming the following boundary conditions:

$$\begin{cases} \varepsilon(z = 0) = 0 \\ \varepsilon(z = l_b) = \dfrac{F}{E_b \cdot A_b} \end{cases} \quad (3.30)$$

The following two constants are obtained:

$$C_1 = \frac{F}{\xi \cdot E_b \cdot A_b} \cdot \frac{1}{\sinh(\xi \cdot l_b)}$$
$$C_2 = 0 \quad (3.31)$$

And, finally, the expression of the function *s(z)* sought:

$$s(z) = \frac{F}{\xi \cdot E_b \cdot A_b} \cdot \frac{\cosh(\xi \cdot z)}{\sinh(\xi \cdot l_b)} \quad (3.32)$$

Strain distribution may be evaluated by:

$$\varepsilon(z) = \frac{\sigma(z)}{E_b} \cdot \frac{\sinh(\xi \cdot z)}{\sinh(\xi \cdot l_b)} \quad (3.33)$$

Considering the equilibrium of a GFRP rod of length *dz* subjected to tensile stress, σ, and shear stress, τ, the following expression is had:

$$\tau(z) = \frac{A_b}{\Sigma_b} \cdot E_b \cdot \xi^2 \cdot s(z) = K \cdot s(z) \quad (3.34)$$

Where the coefficient K is given by $K = \frac{A_b}{\Sigma_b} \cdot E_b \cdot \xi^2 = \frac{K_e}{\Sigma_b}$. For circular rod of diameter d_b, assuming, for the perimeter $\Sigma_b = \frac{3}{4} \cdot (w_g \cdot \pi)$, where w_g is the width of the groove, we obtain:

$$K_e = \frac{3}{2} \cdot \pi \cdot \frac{w_g}{w_g - d_b} \cdot G_e \quad (3.35)$$

To validate this elastic model, experimental pull-out tests are carried out: the results of the experimental pull-out tests are compared to those obtained by the elastic model. In the next paragraph the method of execution of the tests, the samples used are described and the results obtained are shown.

3.3. Experimental Pull-out tests

The most common types of adhesion tests used for NSM reinforcement are direct pull-out tests and pull-out tests on beams subject to bending.
Pull-out tests on beams subject to bending have several practical disadvantages. Direct pull-out tests avoid the drawbacks of pull-out tests on beams subject to bending. L. De Lorenzis et al. [84] have introduced a C-shaped block, in which a single NSM bar has been placed at the center of gravity of the block, however the dimensions of the specimen must be specifically designed, for each type of groove. Furthermore, this configuration is not suitable for studying edge effects, due to the presence of the two flanges.

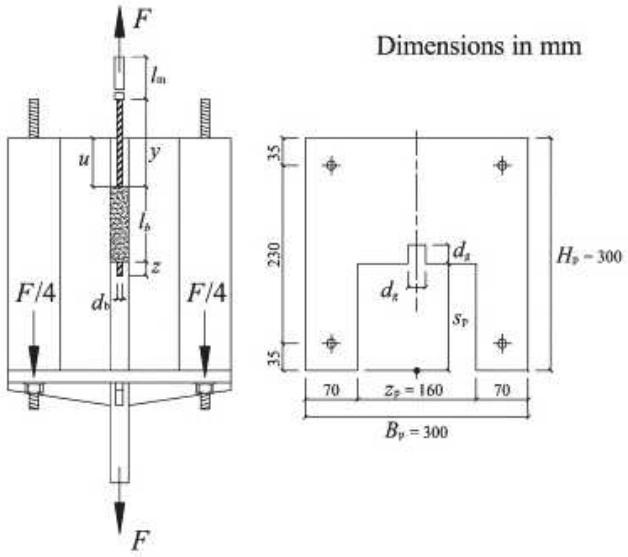

Figure 3.6 – C-shaped block for pull-out tests by L. De Lorenzis et al. [84]

There are three methods for obtaining adhesion bond diagrams:

- Approximate them with those that relate the average adhesion tension, with the sliding of the loaded end or the free end or the average of the two (method adopted for specimens with short anchoring length);
- Obtain the adhesion stresses from measurements of the free-end creep and from measurements of the deformation in discrete points, along the anchor length (method adopted for specimens with long anchor length);
- Calibrate the unknown parameters of the adhesion bond, the shape of which must be known or assumed a priori, starting from the measurements of the sliding of the free end and the loaded end.

Each of the methods has its advantages and disadvantages. The first method does not require the use of strain gauges, which simplifies the preparation of the specimens and does not alter the adhesion properties between the bar and the epoxy. However, the anchor length must be long enough to ensure the specimen is representative.
The obtained adhesion bond diagram represents the average performance of the specimen anchor length.
The second method is more expensive and alters the bar-epoxy resin interface to some extent but has the advantage that the adhesion performance can be studied for a longer and therefore more representative section. The bond bond diagram can be obtained for each load level or alternatively at each measurement point. More data is obtained with this method.

The third method allows to obtain the adhesion bond, for specimens with long anchor length, without the need to measure the deformations. The disadvantages are the shape of the adhesion bond must be known in advance and the precision of the inferred equation can be compromised if the assumed form is inappropriate.
In all cases, the specimen must be carefully designed to ensure that the specimen size does not significantly affect the loading and seizure modes. In addition, the anchored part of the bar should start at an adequate distance from the end of the specimen, to avoid a cone crack in the concrete.

R. Capozucca [23,28] developed pull-out tests out on RC elements with circular CFRP rods and circular GFRP rods inserted into a groove. The pull-out tests shown below are of the direct type, i.e. the specimen consists of a concrete block with a square or rectangular section composite bar inserted inside, this facilitates the control of the sliding and the performance of the test itself. In this case, compressive stresses acting on the concrete block at the loaded end react to the tensile force applied to the bar.
The dimensions of RC specimens built for the pull-out test's rods were: 150 mm x 150 mm in section and 400 mm in length for circular GFRP and CFRP rods. Tests are conducted considering different rod bond length l_b= 200 mm, 250 mm and 300 mm.
The FRP rod's main properties are shown in Table 3.1, while the properties of the concrete and the steel bars are shown in Table 3.2. Epoxy resin having tensile resistance f_{EP} ~ 8 MPa and Young's modulus E_{EP} ~ 95 $\cdot 10^3$ MPa was used for anchoring the rods. Strains were recorded using strain gauges located at different end points along the FRP rod surface, placed at 50 mm intervals. An LVDT was also used to measure displacements at the rod's free end during loading. It is observed that typical failure is on the interface between rod and groove-filling material, for CFRP strengthened specimens, while in the others failure occur cause of reaching of GFRP rod's tensile strength.

Table 3.1 – Geometric and mechanical data of FRP rods

	Diameter d_b/ Section a_b x b_b	**Tensile Strength f_{FRP}**	**Young's Modulus E_{FRP}**
	(mm)	(MPa)	(MPa)
GFRP circular rod	9.53	760	$40.8 \cdot 10^3$
CFRP circular rod	8	1700	$124 \cdot 10^3$

Table 3.2 – Properties of concrete and steel reinforced

Concrete			**Steel**	
Compressive Strength f_c	**Tensile Strength f_{ct}**	**Young's modulus E_c**	**Yield Strength f_y**	**Young's modulus E_s**
(MPa)	(MPa)	(MPa)	(MPa)	(MPa)
34.86	2.24	$34 \cdot 10^3$	528	$200 \cdot 10^3$

The bond mechanism between NSM FRP rod – resin – concrete is investigated below via elastic analysis. In Figure 3.7 the experimental specimen samples subjected to the pull-out test are shown.

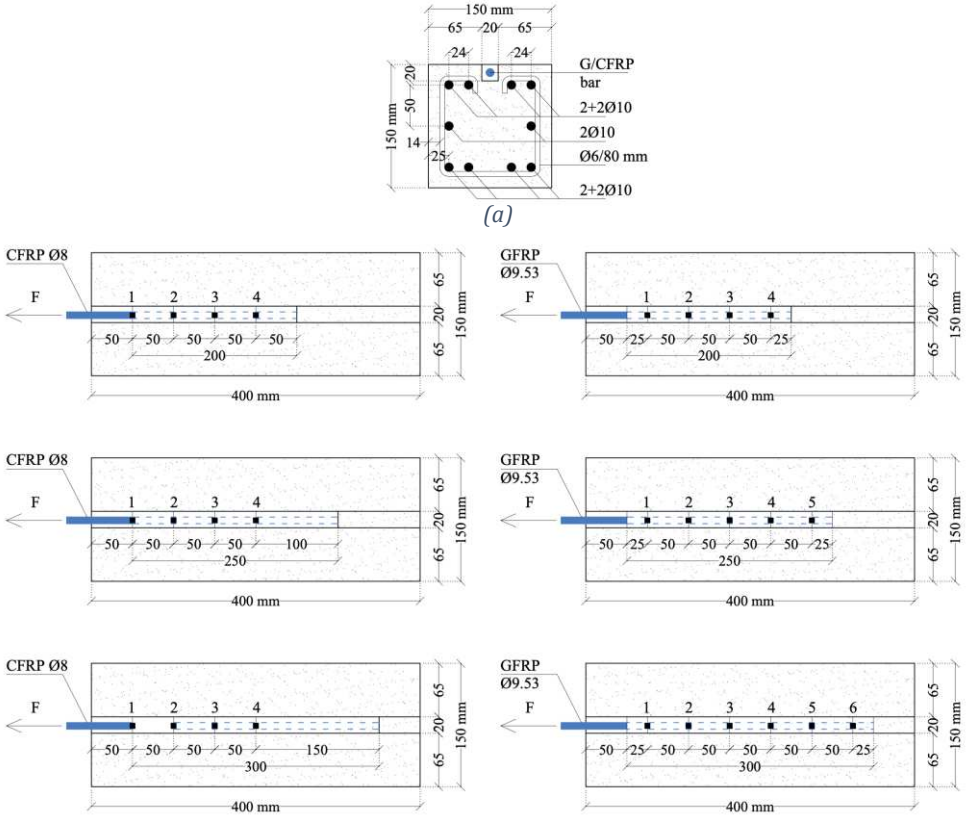

Figure 3.7 – Specimens of pull-out test (a) cross section of RC specimens reinforced with C/GFRP circular rods; (b) specimens reinforced with CFRP circular rods with different anchorage length and location of strain gauges on points 1,…,4; (c) specimens reinforced with GFRP rods with different anchorage length and location of strain gauges on points 1,…,6

In Figure 3.8 the results of experimental pull-out tests are compared to those obtained by the elastic model.

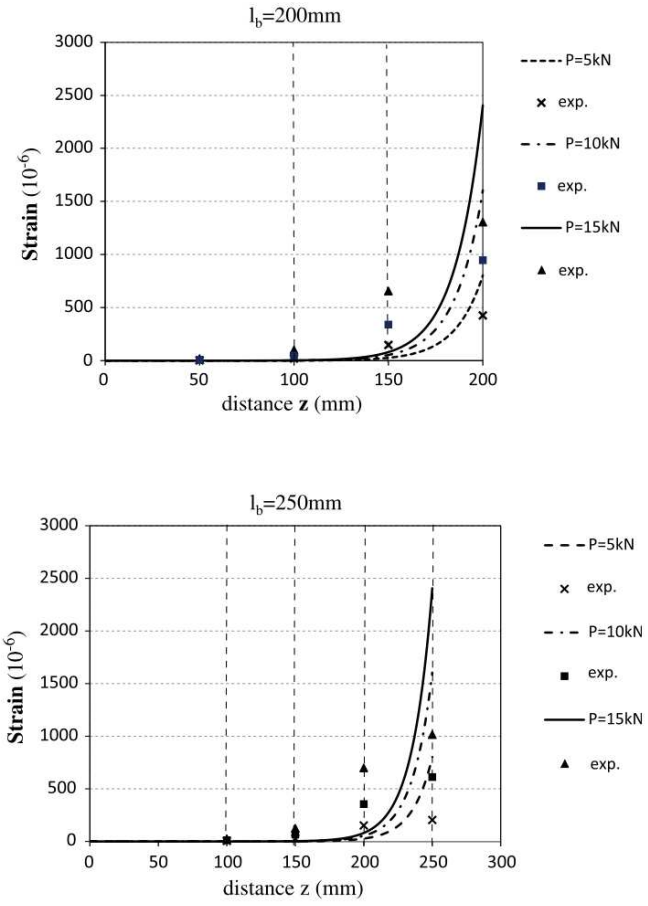
l_b=200mm
Strain (10^{-6})
distance **z** (mm)
P=5kN
exp.
P=10kN
exp.
P=15kN
exp.
l_b=250mm
Strain (10^{-6})
distance z (mm)
P=5kN
exp.
P=10kN
exp.
P=15kN
exp.

(a)

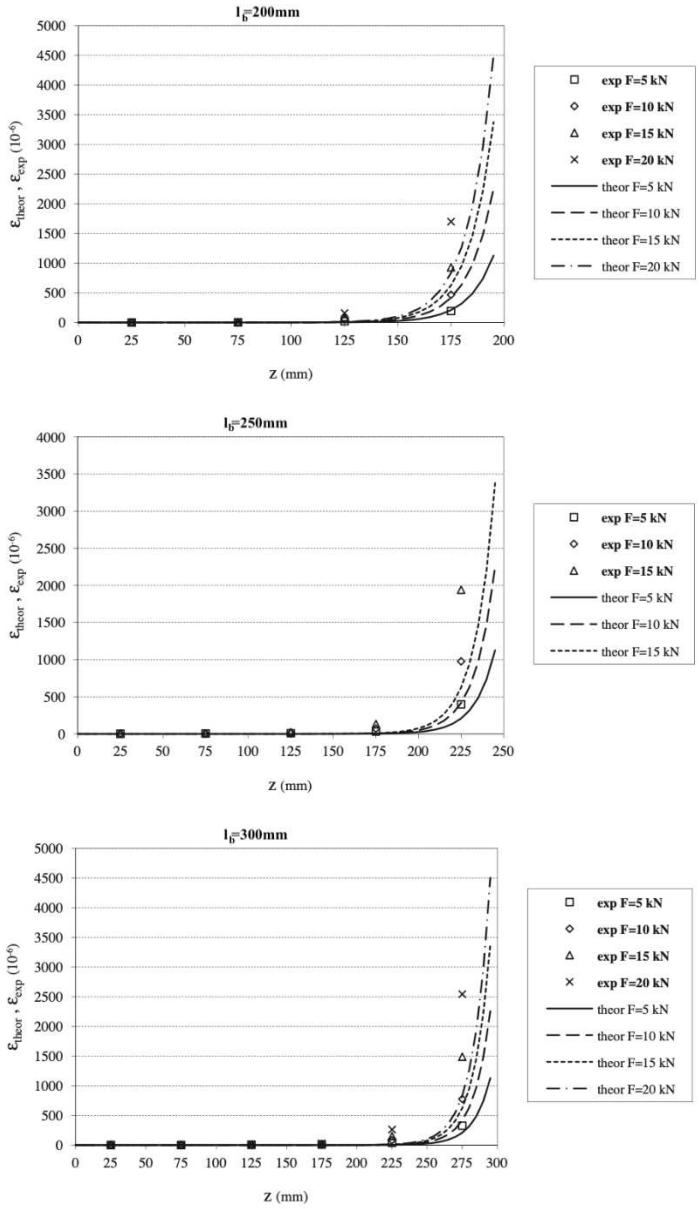

(b)

Figure 3.8 – Comparisons of theoretical and experimental strains vs length of pull-out tests results: (a) for specimens with CFRP; (b) for specimens with GFRP

Diagrams show a good fit between the experimental and theoretical data; therefore, the theoretical model is valid for the describing the adhesion mechanism which strongly depend on the adhesives 'elastic modulus.

Another result from pull-out tests is that bond between FRP rod-resin-concrete is maintained until failure of specimen, that occurs with the reaching of the tensile strength of the rod, for GFRP, and on the interface between rod and groove-filling

material for CFRP. Capozucca also found that over a $3.5 \cdot 10^{-3}$value of strain, bond-slip effects reduce the capacity of steel reinforced beams.

3.4. Parameters that influence the adhesion mechanism

In literature, many works describe the factors affecting bond mechanism in NSM strengthening. The main construction parameters that can affect adherence and therefore structural behavior are:

- dimensions of section rods (nominal diameter d_b, for circular section bars, thickness t_b and high h_b for rectangular section bars);
- groove width w_g and groove depth d_g,
- distance a_g between two adjacent grooves;
- distance a_e between a groove and the edge of the beam.

I.A. Sharaky et al. [27], based on experiments carried out, state that if epoxy resin is used as filler, the delamination load increases as the size of the groove increases, while if cement mortar is used it decreases. For this reason, the size of the groove appears to be a secondary factor as regards the delamination load, which mainly depends on the properties of the filler. Furthermore, it has been observed, by I.A. Sharaky et al. [27], that the delamination load increases as the w_g width of the groove increases, regardless of the properties and surface treatment of the FRP bars.

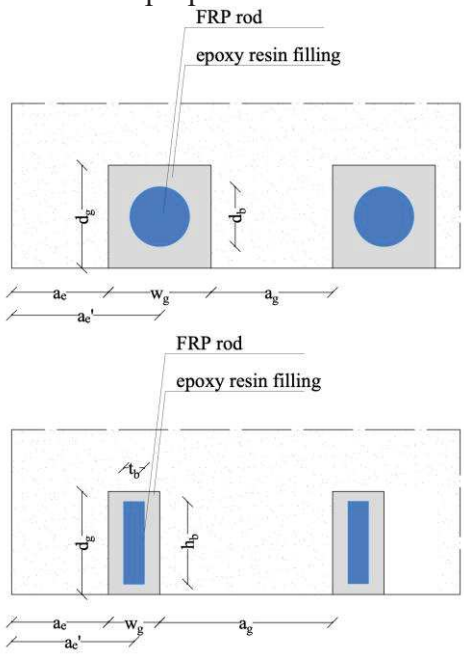

Figure 3.9 – Construction parameters that influence adherence

For circular section bars, L. De Lorenzis [77], based on the results of the adhesion tests on elements with square grooves (w_g=d_g) defining k=w_g/d_b, proposed a

minimum value of $k=1.5$ for smooth or lightly sandblasted bars and a minimum value of $k=2.0$ for ribbed bars.
R. Parretti and A. Nanni [85] suggest w_g and d_g must not be inferior to 1.5 d_b.
L. De Lorenzis [77], based on a simplified analytical model, for ribbed circular section bars, found that the breaking load of the epoxy resin cover decreases as the width-depth ratio of the groove increases w_g/d_g, (for a given depth d_g),
but the delamination load remains substantially unchanged. This result was confirmed by T.K. Hassan and S. Rizkalla [21] through finite element modeling. It has also been found that the tensile stresses in concrete decrease as the width of the groove w_g increases, which implies a higher concrete cracking load (but not necessarily a higher delamination load). Based on finite element models, for ribbed circular section bars, T.K. Hassan and S. Rizkalla [21] suggest minimum values of a_g and a_e respectively equal to $2d_b$ and $4d_b$, regardless of the width of the groove w_g. However, one of the beams tested by L. De Lorenzis [77], reinforced with spiral wound bars with $a_g = 30\ mm \approx 1.8\ w_g \approx 1.8\ d_g \approx 3.6\ d_b$ and $a_g = 69\ mm \approx 4.3\ w_g \approx 4.3\ d_g \approx 8.6\ d_b$, reaches the crisis due to delamination of the NSM bars, which involve the detachment of the concrete cover of the longitudinal reinforcements along the edges. This test, therefore, suggests that the minimum recommended values of a_g and a_e are not sufficient to eliminate interactions between an NSM bar and the edge of a beam.
For NSM foils, M. Blaschko [80] suggested that the depth d_g and the width of the groove w_g should be about 3 mm larger, respectively, than the height h_b and thickness t_b of the foil, to obtain an adhesive layer thickness of approx 1÷2 mm. Parretti and Nanni [85] suggest that the minimum width of a groove w_g should not be less than $3t_b$ and the minimum depth must not be less than $1.5h_b$.
T.K. Hassan and S. Rizkalla [21] through finite element modeling, found that the delamination load of an NSM sheet increases with increasing width of groove w_g. By keeping the groove depth d_g constant, an increase in the groove width w_g implies a greater interface surface between the epoxy resin and the concrete. This implies a greater delamination load, if we assume that delamination occurs due to the achievement of the cohesive shear strength of the concrete, at the epoxy resin-concrete interface.
Based on tests on NSM foils, M. Blaschko indicated a minimum value of $a_e' = a_e + w_g/2$ of about 20 mm necessary to avoid breaking the edge of the beam. For values of a_e' larger than 30 mm no cracks have formed in the concrete. Furthermore, M. Blaschko, suggested that a_e' must be the greater of: 30 mm and the maximum size of the aggregates. During the tests, a_e' influences the adhesion behavior up to the maximum studied value of 150 mm, beyond which it is assumed that there are no further influences.

I.A. Sharaky et al. [27] performed pull-out tests on specimens with grooves of different shapes: with U-shaped cross section, trapezoidal, with teeth to favor interlocking mechanisms. Specimens with CFRP NSM bars and with trapezoidal

grooves, with the same perimeter, show less creep at the delamination load than those with square grooves. For specimens with NSM GFRP bars, the shape of the groove shows no significant effects for the initial load levels, instead at the delamination load, the slip is greater for the specimens with U-grooves, trapezoidal and with teeth to favor mechanisms interlocking, compared to specimens with square grooves.

3.5. Failure modes

On the basis of what is stated in the previous paragraph, it can be summarized that the relevant construction parameters that can influence the adhesion and therefore the structural behavior of the NSM strengthened reinforced concrete element are:
- dimensions and shape of the section and surface configuration of the bars;
- width and depth of the grooves;
- distance between two adjacent grooves;
- distance between a groove and the edge of the beam;
- tensile and shear strengths of concrete;
- type of filler for the grooves;
- degree of roughness of the surface of the grooves.

The adhesion performance of a FRP bar depends on the design, the manufacturing process, the mechanical properties of the bar itself and the environmental conditions.
In a bar anchored in concrete, the adhesion stress can be transferred by:
- adhesion resistance of the interface also called chemical bond;
- frictional resistance to sliding of the interface;
- interlocking mechanisms due to the irregularity of the interface.

The methods and mechanisms that lead to the loss of adhesion of the NSM bars are many; in paragraph 2.4.1, these have already been exhibited according to the area in which the mechanism occurs, here are resumed and deepened from the mechanical point of view:
- delamination at the bar-epoxy resin interface (Interfacial debonding), this mechanism can occur at the interface level (ID-I) or due to achievement of cohesive shear strength of the resin (ID-C);
- delamination at the concrete-epoxy resin interface (concrete cover separation) this mechanism can occur at the interface level (CS-I) or to achieve the cohesive shear strength of the concrete (CS-C);
- splitting of epoxy resin cover without involving the concrete (SP-E) or with the formation of cracks along inclined planes in the surrounding concrete (SP-C1);

– not visible from the outside with formation of cracks along inclined planes in the surrounding concrete (SP-C2) or with fracture in the concrete of the edge of the beam (SP-ED).

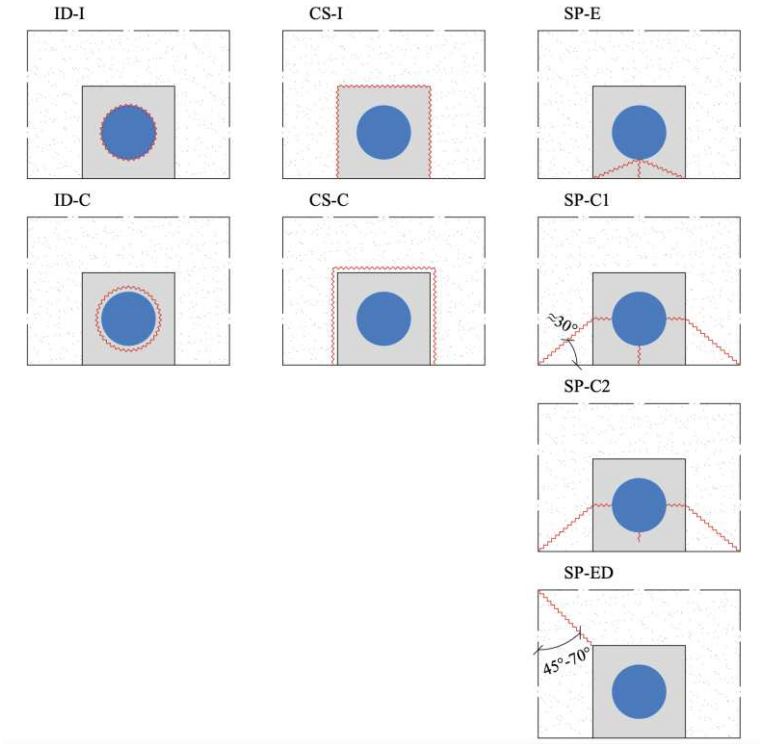

Figure 3.10 – Mechanisms that lead to loss of adhesion

The interfacial debonding failure interests the FRP-to-concrete interface, so the debonding strength is thus mainly controlled by the material and interfacial properties on / near such interfaces: the delamination at the bar-epoxy interface at the interface (ID- I) is critical for smooth or slightly rough bars, i.e. when the roughness of the bar is unable to generate interlocking mechanisms between the bar and the epoxy resin. For round bars, this mode becomes critical if the dimensions of the groove are large enough to avoid splitting of the epoxy resin cover. For epoxy resins and concretes of moderate resistance, L. De Lorenzis and Nanni [24] have estimated that for smooth or slightly rough circular cross-section bars, a value of $k = w_g/d_b = 1.5$ is sufficient to avoid the splitting of the epoxy resin covering.
For circular cross-section bars, fractures of the epoxy resin cover produced by the radial components of the adhesion stresses, can accelerate the occurrence of delamination at the bar-epoxy interface at the interface (ID-I).
Delamination at the bar-epoxy interface to achieve the cohesive shear strength of the resin (ID-C) was observed for NSM sheets with a rough surface. This mode occurs when the shear strength of the epoxy is exceeded. Delamination phenomena

inside the bar itself, even if theoretically possible, have never been observed. Unlike the case of FRP ribbed bars used as internal reinforcement in concrete, the truncation of the ribs of ribbed bars has never been observed. However, in some tests conducted by L. De Lorenzis et al. [84], the surface of the ribbed bars was found damaged after the loss of adhesion, indicating that this could be an upper limit of the delamination mode.
Delamination at the epoxy-concrete interface at the interface (CS-I) has been found to be critical for elements manufactured to already have grooves. For spirally wound bars or ribbed bars with slightly accentuated ribs and for pre-prepared grooves, this was found to be the critical delamination mode, independent of the value of $k = w_g/d_b$.
For ribbed bars with very accentuated ribs this mode was critical only for values of higher k and a minimum value (equal to about 2.0 for ribbed bars fixed with epoxy resin), for lower k values, the loss of adhesion occurs due to splitting of the epoxy resin cover.
The delamination at the epoxy resin-concrete interface to achieve the cohesive shear strength of the concrete (CS-C), has never been observed in the adhesion tests, but was found in bending tests on beams within the reinforced region or at the ends of the bars. Epoxy roofing splitting is critical for circular, ribbed or spiral-wound bars.
The mechanism that leads to the splitting of the epoxy resin cover for the NSM system is similar to that for the bars used as internal reinforcement to the concrete. The tensile strength of epoxy resin is an order of magnitude greater than that of concrete, but the thickness of the epoxy cover, for NSM FRP reinforcement, is an order of magnitude less than the thickness of the concrete cover of an element in furthermore, the longitudinal steel reinforcement of r.c. beams benefits from the confinement effects due to shear reinforcement, which are not available for NSM longitudinal reinforcement, unless there is some form of external containment (e.g. FRP U-jackets used for shear reinforcement).
The splitting of the epoxy resin cover without involvement of the concrete (SP-E) occurs when $k = w_g/d_b$ it is very low (for example k = 1.12 ÷ 1.18) and the crisis is limited to the epoxy resin covering and causes little damage in the surrounding concrete.
The splitting of the epoxy resin roofing with the formation of cracks according to inclined planes in the surrounding concrete (SP-C1), occurs for values of $k = w_g/d_b$ higher. It has been observed that the cracking planes in the concrete are inclined approximately 30 ° with respect to the horizontal.
The splitting of the epoxy resin cover, not visible from the outside, with the formation of cracks along inclined planes in the surrounding concrete (SP-C2), occurs for high groove depths and / or when the tensile strength ratio of the concrete-epoxy is small.
The splitting of the epoxy resin roofing with concrete fracture of the beam edge (SP-ED), occurs when the NSM bar is close to the edge of the beam, i.e. for $a_e' = a_e +$

$w_g/2 < 20mm$. It has been observed that the crack planes in concrete have an angle of inclination with respect to the vertical which varies between 45 ° and 70 °.
The strength associated with the SP-ED mode should strongly depend on the tensile strength of the epoxy, while the strengths associated with the SP-C1 and SP-C2 mode should strongly depend on the tensile strength of the concrete. In all cases, the tangential adhesion resistance should increase with the thickness of the NSM bar cover (that is with the depth d_g of the groove). However, for $d_g > 2d_b$ the increase in adhesion tensions begins to decrease and the SP-C2 mode replaces the SP-C1.
In all types of tests, the average adhesion shear stress normally decreases as the anchor length increases, this depends on the non-uniform distribution of stresses. Tangential adhesion resistance refers to the maximum value of adhesion tension that the interface can withstand. Tangential adhesion resistance can be evaluated by processing deformation (and / or creep) measurements.
Several authors have studied the tangential adhesion resistance of NSM systems, this allows to make the following observations:

- the tangential resistance of adhesion associated with the crisis due to splitting (for ribbed bars), as expected, is greater if the depth of the groove is greater and if the ribs of the bars are not very accentuated;
- the tangential adhesion resistance associated with the ID-I mode, wich was observed for bars with a sandblasted surface, is not affected by the size of the grooves and is less than that for ribbed bars;
- the tangential adhesion strength of NSM sheets is comparable to that of spirally wound bars (in two out of three test series).

L. De Lorenzis et al. [84], reported the tangential adhesion resistance values, based on tests performed by them and others, on specimens with different types of bars.

Table 3.3 – Tangential adhesion resistance of NSM circular section rods from research word of L. De Lorenzis et al. [84]

Type	Superficial configuration	Filler for grooves	Tangential adhesion resistance (MPa)
CFRP	Sand blasted	Epoxy resin	8,6
CFRP	Sand blasted	Epoxy resin	9,7
CFRP	Ribbed	Epoxy resin	11,2
CFRP	Ribbed	Epoxy resin	15,4
CFRP	Ribbed	Epoxy resin	16,6
GFRP	Ribbed	Epoxy resin	9,1
GFRP	Ribbed	Epoxy resin	10
GFRP	Ribbed	Epoxy resin	12,5
CFRP	Spiral-wound and coated with sand	Epoxy resin	18
CFRP	Spiral-wound and coated with sand	Epoxy resin	20,8
CFRP	Spiral-wound and coated with sand	Epoxy resin	21,9

For EC-I mode, L. De Lorenzis et al., observed that the bar surface configuration did not have a significant effect on the adhesion behavior and the difference in tangential adhesion resistance between ribbed and spiral wound bars, it is essentially due to the different diameters and therefore to the different dimension

of the groove for a given value of $k = w_g/d_b$ Furthermore, it has been found that the tangential resistance of adhesion decreases as the size of the groove increases.

Chapter 4. Experimental model of NSM strengthened RC beams

4.1. Introduction

During this research work four beam models, first in their initial and un-damage condition and then strengthened with NSM FRP rods, are analysed, and therefore presented in this chapter.

In the first section, the description of the tested specimens and the mechanical characterization of the materials used in the experimental campaign are exposed.
In order to properly analyze the behavior of the beam models, the theoretical behavior, both static and dynamic was deepened: the second section deals with the dynamic problem of vibration of the beam intended as a continuous system, theoretical frequencies were also calculated according to the Euler Bernoulli approach in the two constraint conditions in which the specimens were tested; in the last section the theoretical analysis of RC beam sections under bending loading was developed and reported.

4.2. Introduction to experimental tested beam model

4.2.1. Tested Specimens

The four specimens tested were cast with the same dimensions and same steel bars. These are characterized by a cross-section of 120·160 mm and length of 2200 mm; the steel reinforcements consist in four longitudinal steel bars of 10 mm diameter and stirrups of 6 mm diameter, opened at the bottom, to obtain a groove with adequate dimensions for the insertion of FRP reinforcement and ensure its effectivness. The wheelbase of stirrups is 60mm at ends and 130mm at midspan, like shown in Figure 4.1.

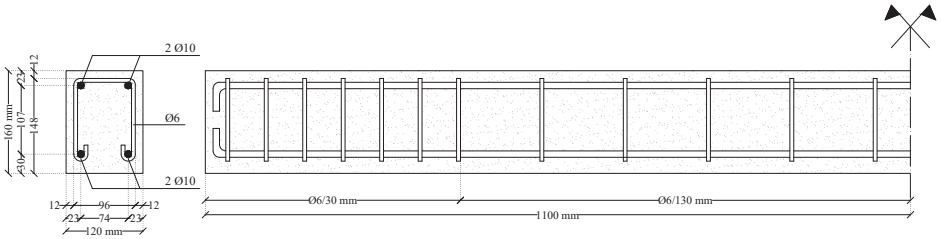

Figure 4.1 – Longitudinal and transverse section of RC beam specimens in the un-strengthened condition

After the first experimental tests, useful for characterizing the behavior of the beams in their initial configuration, a groove of 20·20 mm was created at the bottom of four specimens, for the entire length, to locate an NSM reinforcement bar: a GFRP bar, with a diameter of 9.53 mm, or a CFRP bar, with a diameter of 9.7 mm.
In detail, the reinforcement of the experimental models of beams with the NSM technique was carried out according to the procedure described below:

- first, a piezoelectric strain gauge was applied in the midspan of the FRP bar, to record the deformation during bending test (Figure 4.2),
- execution of the groove in the lower face of the beam specimens for their entire length and cleaning the cut using a metal bristle brush and compressed air (Figure 4.3a),
- preparation of the two-component epoxy resin compound according to the supplier's recommendations (ratio 1: 1), and application of a first continuous layer of the epoxy (Figure 4.3b, Figure 4.3c, Figure 4.3d),
- insertion of the FRP rod inside the groove, exerting a light pressure so as to make part of the resin flow laterally and prevent the formation of internal voids (Figure 4.3e),
- application of a further layer of epoxy resin until the groove is completely covered and the intrados of the reinforced element is reached, removing any excess adhesive if necessary (Figure 4.3f).

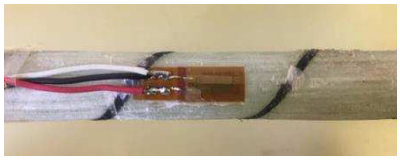

Figure 4.2 – Strain gauges on FRP bar

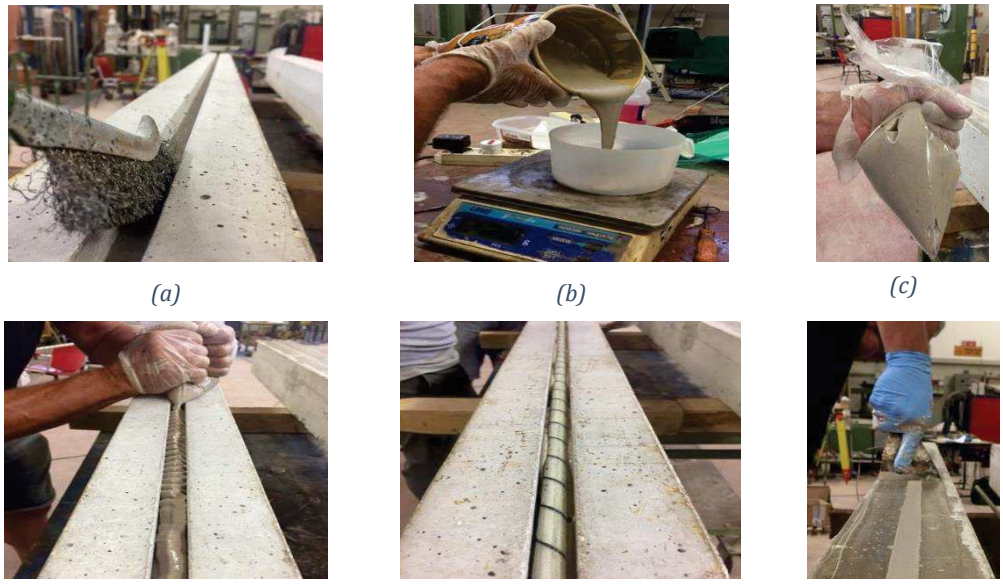

(a) (b) (c)

(d) (e) (f)

Figure 4.3 – Steps for applying the reinforcement bars according to the NSM technique in beam models

As mentioned above the specimen's object of the work are four in total and are described in detail below:

- Specimen CB, un-strengthened, it is a control beam to use as reference,
- B_1, strengthened with NSM GFRP bar,
- B_2, strengthened with NSM GFRP bar,
- B_3, strengthened with NSM CFRP bar.

In Figure 4.4 the strengthened configuration of beam's samples is depicted.

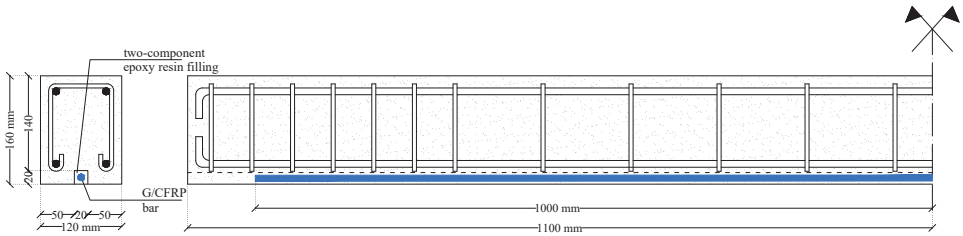

Figure 4.4 – Longitudinal and transverse section of RC beam specimens in the strengthened condition

4.2.2. Mechanical characterization of materials

The characterization of the concrete was carried out through crushing tests, with the use of a hydraulic press, on ten specimens of standard dimensions 150·150·150 mm after 119 days by casting (Figure 4.5).

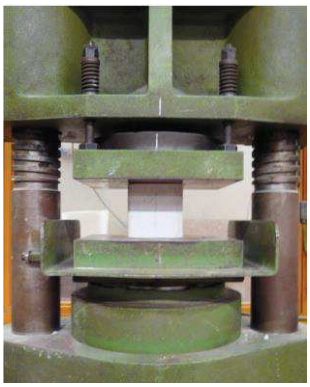

Figure 4.5 – Crushing test on concrete samples

From the tests it emerged that the concrete used in the present experimentation has a characteristic cubic compressive strength (R_{ck}) equal to 44.31 MPa.
Strength results for each specimen tested are shown below (Table 4.1)

Table 4.1 – Results from crushing test on concrete samples

Specimen	**Weight** (kg)	**Area Section** (mm^2)	**Breaking Load** (N)	**Compressive Strength R_c** (MPa)
1	7.6	22500	925000	41.11
2	7.5	22500	945000	42.00
3	7.6	22500	915000	40.67
4	7.7	22500	1080000	48.00
5	7.75	22500	1140000	50.67
6	7.7	22500	1000000	44.44
7	7.5	22500	1045000	46.44
8	7.7	22500	1010000	44.89
9	7.7	22500	815000	36.22
10	7.6	22500	1095000	48.67
Characteristic Compressive Strength R_{ck}			(MPa)	**44.31**

The elastic modulus of the concrete is obtained from the experimental characteristic strength, in accordance with the NTC 2018, at §11.2.10.3 [86].

$$E_{cm} = 22000\left(\frac{f_{cm}}{10}\right)^{0.3} = 34493.7\ MPa \qquad (4.1)$$

Moreover, bending and crushing tests were carried out on three specimens with dimensions of 40·40·160 mm. Tensile strength is obtained from bending tests, carrying the specimen to break, after that the six samples obtained are tested under compression.

Table 4.2 – Results from bending test on concrete samples

Specimen	**Area Section** (mm^2)	**Load** (N)	**Tensile Strength** (MPa)
1	6400	3380	0.528

2	6400	3385	0.529
3	6400	3369	0.526
Average Tensile Strength		(MPa)	0.528

Table 4.3 – Results from crushing test on concrete samples

Specimen	**Area Section** ($mm^{2)}$)	**Ultimate Load** (N)	**Compressive strength** (MPa)
1A	1600	93185	58.241
1B	1600	83385	52.116
2A	1600	89552	55.970
2B	1600	90879	56.799
3A	1600	85556	53.473
3B	1600	89311	55.819
Average Compressive Strength		(MPa)	55.40

The steel bars used for reinforcement of the beams are B450C type. Deformation control tensile tests on three rebars Ø8 of approximately 600 mm length were carried out using the universal testing machine. The results obtained are reported in Table 4.4

Table 4.4 – Results from tensile tests on rebars

Specimen	**Diam-eter** (mm)	**Weight** (kg)	**Yiel load** (N)	**Yield stress** (MPa)	**Initial Length** (mm)	**Elong-ation** (mm)	**Ultimate Load** (N)	**Ultimate stress** (MPa)
1	8	0.235	24710	495.25	600	11.3	29640	594.06
2	8	0.235	-	-	601	9.6	29920	601.95
3	8	0.236	25540	511.65	601	8.4	29810	597.19
Average Yield stress			(MPa)	503.45	**Average Ultimate stress**		(MPa)	597.74

The resin used for the application of the reinforcements is the SEMIFLUID FLK from AhRCOS. It is a two-component fluid epoxy structural adhesive. To determine its characteristics, three specimens of 40·40·160 mm size were subjected to compression tests to determine the mechanical characteristics of adhesive. Each specimen was instrumented with two strain gauges to determine the vertical and horizontal strains. In Table 4.5 the values of Elastic Modulus and Poisson's coefficient determined are shown.

Table 4.5 – Results from tests on resin samples

Elastic Modulus (MPa)	**Poisson's Ratio** -
1597	0.48

The FRP bars used as strengthening are pultruded bars in carbon or glass fibers from the MAPEI company. The one in GFRP is the MAPEROD G glass fiber reinforcement bar with improved adhesion, while the one in CFRP is MAPEROD C carbon fiber reinforcement bar with high tensile strength. The bars have a length

of 2000mm and respectively a nominal diameter of 9.525mm and 9.7 mm. Geometric and mechanical characteristics of the bars, provided by the manufacturer's technical data sheet, are shown in Table 4.6.

Table 4.6 – Characteristics of G/CFRP Maperod bars

		Maperod C	**Maperod G**
Density	(g/cm^3)	1.54	1.995
Fiber Content	(%)	71	75
Transversal Section	(mm)	9.7	9.53
Nominal Diameter	(mm)	73.9	71.26
Tensile Strength	(MPa)	2000	760
Elastic Modulus	(MPa)	155000	40800
Elongation to break	(%)	1.5	2
Thermal expansion coefficient in longitudinal sense	(m/m/°C)	6-10 $x10^{-6}$	6-10 $x10^{-6}$
Thermal expansion coefficient in transverse sense	(m/m/°C)	-	21-23$x10^{-6}$

4.3. Vibrational analysis of RC beams

4.3.1. Continuous systems: bending vibrations of beams

Forced vibration

The solution of the forced vibration equation for beams under bending loads is obtained starting from the Euler-Bernoulli hypothesis, also known as the conservation principle of plane sections (the straight section is kept flat and orthogonal to the deformed geometric axis).

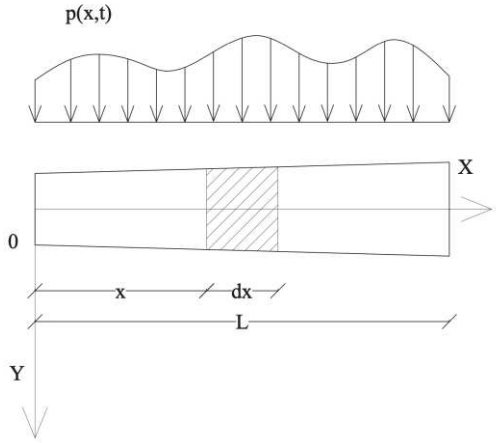

Figure 4.6 – Bending beam with distributed mass and shear load p (x, t)

The beam of Figure 4.6 is given, however constrained at the ends, stressed by the distributed load $p(x,t)$, normally applied to the axis, in the plane of the beam; the

stress of the beam is straight bending with the moment vector orthogonal to the *x*-*y* plane. The load $p(x,t)$ depends on the variables *x* and *t*; Figure 4.6 shows the load profile at the various abscissas *x* for a given instant *t*, as it generally changes as *t* varies, consequently the stress characteristics in the various sections also depend on *t*.

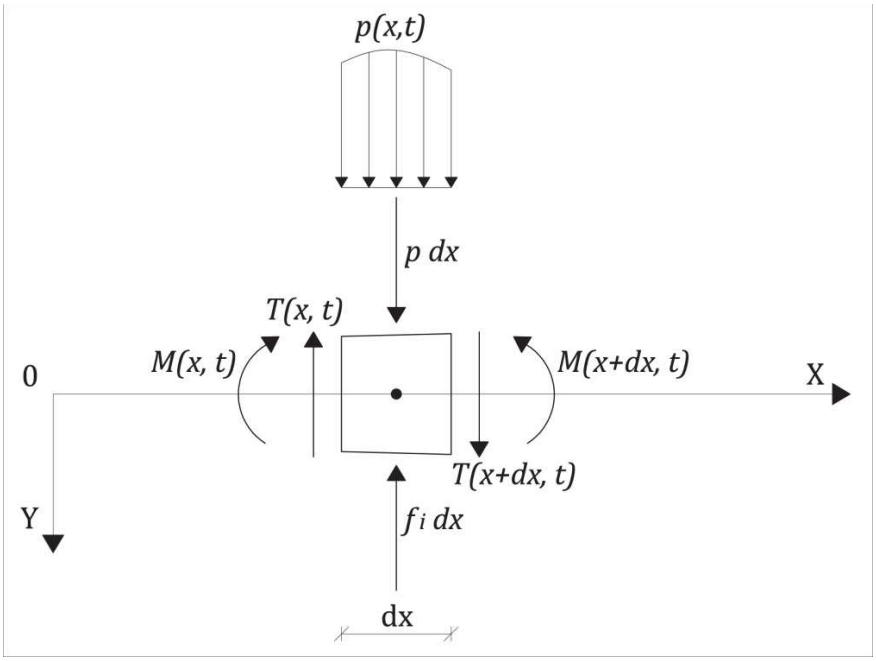

Figure 4.7 – Internal and external forces acting on the trunk of the beam of infinitesimal length right, in dynamic conditions

In Figure 4.7 a portion of the beam of infinitesimal length right is shown delimited by the flat faces and orthogonal to the axis of the beam. The shear $T(x,t)$ and the bending moment $M(x,t)$ act on the face of abscissa *x*. Due to the presence of the distributed load $p(x,t)$, the shear $T(x+dx,t)$ and the moment $M(x+dx,t)$ act along the right portion, on the face of abscissa $x + dx$. The force of inertia is also represented on the portion of the beam.

$$F_i = f_i\, dx = -dm\frac{\partial^2 v}{\partial t^2} = -\mu A\, dx\frac{\partial^2 v}{\partial t^2} \qquad (4.2)$$

with $dm = \mu A\, dx$, μ mass density, *A* cross-sectional area of the beam portion, $v = v(x,t)$ displacement of the geometric axis of the beam in the main *x*-*y* plane in the y direction.
In the hypothesis of small displacements, equating to zero the sum of the forces acting on the portion of the beam, we arrive at the condition of dynamic equilibrium for the forces in the *y* direction:

$$-T + p\, dx - \mu A\, dx\frac{\partial^2 v}{\partial t^2} + T + dT = 0 \qquad (4.3)$$

From which:

$$\mu A\, dx \frac{\partial^2 v}{\partial t^2} - dT = p\, dx \tag{4.4}$$

With:

$$dT = \frac{\partial T}{\partial x} dx \tag{4.5}$$

thus, obtaining *the indefinite equation of dynamic equilibrium:*

$$\mu A \frac{\partial^2 v}{\partial t^2} - \frac{\partial T}{\partial x} = p(x,t) \tag{4.6}$$

Since the beam is an elastic, linear, homogeneous, and isotropic continuum, and since the portion of the beam can be considered cylindrical, given its infinitesimal length, the differential equation of the elastic line from the theory of straight bending of the S. Venant cylinder is applicable

$$\frac{\partial^2 v}{\partial x^2} = -\frac{M}{EI} \tag{4.7}$$

$$M = -EI \frac{\partial^2 v}{\partial x^2} \tag{4.8}$$

with E modulus of normal elasticity and I moment of inertia of the section with respect to the neutral axis.

The condition of equilibrium at the rotation of the portion of the beam around the point of intersection of its axis with the lines of action of the resultants of the external forces $p\ dx$ and of the inertia forces $f_i\ dx$, neglecting the contributions of the infinitesimals of higher order than the first, is

$$T\ dx + M - (M + dM) = 0 \tag{4.9}$$

from which the relationship between bending moment and shear is obtained

$$T = \frac{\partial M}{\partial x} \tag{4.10}$$

Substituting (4.10) and then (4.8) in (4.6), it is possible to obtain the fundamental equation of the forced motion of the straight axis beam with variable section, vibrating in the main plane xy under the action of the transverse load $p(x,t)$:

$$\frac{\partial^2}{\partial x^2}\left(EI \frac{\partial^2 v}{\partial x^2}\right) + \mu A \frac{\partial^2 v}{\partial t^2} = p(x,t) \tag{4.11}$$

If the cross section of the beam is constant, the modulus of elasticity $E = E(x)$ not depending on x, assumes a constant value for the whole length of the solid, and (4.11) becomes

$$EI\frac{\partial^4 v}{\partial x^4} + \mu A\frac{\partial^2 v}{\partial t^2} = p(x,t) \tag{4.12}$$

a partial differential equation, linear, of the fourth order, approximated as it describes the forced vibration neglecting the contribution of the shear deformations and rotational inertia, i.e. those deformations produced by inertial forces, induced by the rotations of the sections terminals of the infinitesimal portions into which the beam can be imagined divided.

Free vibration

In the case of a constant section beam and in the absence of load $p(x,t)$, the fundamental equation is reduced to the homogeneous of (4.13), known as the differential equation of the free oscillations of the beam

$$EI\frac{\partial^4 v}{\partial x^4} + \mu A\frac{\partial^2 v}{\partial t^2} = 0 \tag{4.13}$$

The solution $v = v(x,t)$ of this separable variable equation can be written as the product of two functions, a function of only *x* (called modal form) and only one of time *t*.

$$v(x,t) = V(x)\, g(t) \tag{4.14}$$

Deriving the function $v(x,t)$ (4.14) with respect to the variables *x* and *t* and replacing it in the equation of motion (4.13). Divided by *EI*, we obtain

$$V''''(x)g(t) + \frac{\mu A}{EI}V(x)\ddot{g}(t) = 0 \tag{4.15}$$

$$\frac{EI}{\mu A}\,\frac{V''''(x)}{V(x)} = -\frac{\ddot{g}(t)}{g(t)} \tag{4.16}$$

where the quotes and dots indicate the derivatives with respect to the variables *x* and *t*, respectively.

The first member of (4.16) turns out to be a function of *x* alone, while the second only of *t*. For the identity to exist, both members must be equal to a constant that we will indicate with ω^2, obtaining the two ordinary differential equations

$$V''''(x) - \lambda^4\, V(x) = 0 \tag{4.17}$$

said equation of modal forms and with

$$\lambda^4 = \frac{\mu A}{EI}\,\omega^2 \tag{4.18}$$

from which it is possible to obtain the natural pulsation

$$\omega = \lambda^2\sqrt{\frac{EI}{\mu A}} \tag{4.19}$$

and

$$\ddot{g}(t) + \omega^2 g(t) = 0 \qquad (4.20)$$

said differential equation of harmonic motions, the solution of which can be written in various forms, for example

$$g(t) = G\ cos(\omega t - \varphi) \qquad (4.21)$$

with G the amplitude and φ the phase, which can be obtained through the initial conditions of the system at $t = 0$.

(4.17) can be solved by setting

$$V(x) = Be^{rx} \qquad (4.22)$$

being

$$V''''(x) = r^4 Be^{rx} \qquad (4.23)$$

The (4.17) becomes

$$(r^4 - \lambda^4)\ Be^{rx} = 0 \qquad (4.24)$$

The roots of the characteristic equation $(r^4 - \lambda^4) = 0$ are

$$r_{1,2} = \pm\lambda\ ,\ \ r_{3,4} = \pm i\lambda \qquad (4.25)$$

whose substitution in (4.22) returns four distinct particular solutions of the equation of modal forms (4.17), so its general solution is obtained from the linear combination of the four particular solutions

$$V(x) = B_1 e^{\lambda x} + B_2 e^{-\lambda x} + B_3 e^{i\lambda x} + B_4 e^{-i\lambda x} \qquad (4.26)$$

expressing the exponential functions in terms of trigonometric and hyperbolic functions

$$\begin{aligned} e^{\pm\lambda x} &= cosh\,\lambda x \pm\ senh\,\lambda x \\ e^{\pm i\lambda x} &= cos\,\lambda x \pm\ i\ sen\,\lambda x \end{aligned} \qquad (4.27)$$

(4.26) becomes

$$V(x) = B_1' cos\,\lambda x + B_2' sen\,\lambda x + B_3' cosh\,\lambda x + B_4' senh\,\lambda x \qquad (4.28)$$

The four arbitrary constants that occur in (4.26), the B_j and in (4.28), the B_j' $(j = 1, \ldots 4)$, characterize the modal form and are calculated on the basis of the boundary conditions of the beam (conditions of constraint to extremes).

The boundary conditions allow to determine three of the constants as a function of the fourth and to derive the frequency equation from which the parameter λ is deduced, since these are free vibrations, in fact, it is not possible to determine the fourth constant that defines the amplitude of the motion and depends on the initial conditions.

We therefore have that the stationary solution of the steady-state free motion can be expressed in the form

$$v(x,t) = V(x)\ cos(\omega t - \varphi) \qquad (4.29)$$

with the constant G absorbed by the constants B_j' of (4.28), for which (4.29) describes the transverse motion of a beam for any boundary condition or initial conditions.

The B_j' are determined through the boundary conditions that are satisfied only for particular values of $\lambda_1, \lambda_2, \ldots, \lambda_n$, called eigenvalues, each of which corresponds to

the relative natural pulsation $\omega_n = {\lambda_n}^2 \sqrt{\frac{EI}{\mu A}}$. The eigenvalue λ_n also corresponds to the eigenfunction $V_n(x)$ (spatial function, mode of vibration) which defines the deformation of the beam in correspondence with the natural pulsation ω_n, which can also be defined as the n-th vibration mode of the system.
The solution of the differential equation of harmonic motions corresponding to the eigenvalue λ_n is

$$g_n(t) = G\ cos(\omega_n t - \varphi_n) \tag{4.30}$$

and the general integral of the differential equation of the free oscillations of the beam (4.13) becomes the expression of the deformed geometric axis of the beam in free vibration

$$v(x,t) = \sum_{n=1}^{\infty} V_n(x)\ cos(\omega_n t - \varphi_n) \tag{4.31}$$

In (4.31) the expression relating to the n-th eigenvalue obtained from (4.28) can be assumed for the autofunction $V_n(x)$

$$V_n(x) = B_1' \cos \lambda_n x + B_2' \, sen\, \lambda_n x + B_3' \cosh \lambda_n x + B_4' \, senh\, \lambda_n x \tag{4.32}$$

4.3.2. Classic solution of free beam

The boundary conditions at the free ends of the beam are expressed by annulling the shear and moment values for $x = 0$

$$M(0,t) = 0 \qquad T(0,t) = 0 \tag{4.33}$$

and $x = L$

$$M(L,t) = 0 \qquad T(L,t) = 0 \tag{4.34}$$

For the theory of the straight bending of the S. Venant cylinder (elastic line) and from the equilibrium condition to the rotation of the beam portion, we can express the moment $M(x,t)$ and the shear $T(x,t)$ in terms of shift

$$\begin{aligned} M(x,t) &= -EI \frac{\partial^2 v}{\partial x^2} \\ T(x,t) &= -EI \frac{\partial^3 v}{\partial x^3} \end{aligned} \tag{4.35}$$

The displacement function $v = v(x,t)$, is solution of the differential equation of free oscillations, in the form (4.29), so (4.35) become

$$\begin{aligned} M(x,t) &= -EIV''(x)cos\ (\omega t - \varphi) \\ T(x,t) &= -EIV'''(x)cos\ (\omega t - \varphi) \end{aligned} \tag{4.36}$$

The auto function V (x) is in the form (4.28), deriving it we obtain

$$V'' = \frac{d^2V}{dx^2} = -\lambda^2(B_1' \cos \lambda x + B_2' \, sen \, \lambda x - B_3' \cosh \lambda x - B_4' \, senh \, \lambda x) \quad (4.37)$$

$$V''' = \frac{d^3V}{dx^3} = \lambda^3(B_1' \, sen \, \lambda x - B_2' \cos \lambda x + B_3' \, senh \, \lambda x + B_4' \cosh \lambda x) \quad (4.38)$$

Substituting (4.37), (4.38) in (4.36) and applying the boundary conditions (4.33), we obtain

$$\begin{aligned} M(0,t) &= EI \, \lambda^2(B_1' - B_3') \cos(\omega t - \varphi) = 0 \\ T(0,t) &= EI\lambda^3(B_2' - B_4') \cos(\omega t - \varphi) = 0 \end{aligned} \quad (4.39)$$

From which

$$\begin{aligned} B_1' &= B_3' \\ B_2' &= B_4' \end{aligned} \quad (4.40)$$

Hence the auto function $V(x)$ (4.28) becomes

$$V(x) = B_1' \, (\cos \lambda x + \cosh \lambda x) + B_2' \, (sen \, \lambda x + senh \, \lambda x) \quad (4.41)$$

Deriving it we obtain

$$V'' = \frac{d^2V}{dx^2} = \lambda^2[B_1' \, (-\cos \lambda x + \cosh \lambda x) + B_2' \, (-sen \, \lambda x + senh \, \lambda x)] \quad (4.42)$$

$$V''' = \frac{d^3V}{dx^3} = \lambda^3[B_1' \, (sen \, \lambda x + senh \, \lambda x) + B_2' \, (-\cos \lambda x + \cosh \lambda x)] \quad (4.43)$$

Substituting (4.42), (4.43) in (4.36) and applying the boundary conditions (4.34), we obtain

$$\begin{aligned} M(L,t) &= EI\lambda^2[B_1' \, (-\cos \lambda L + \cosh \lambda L) + B_2' \, (-sen \, \lambda L + senh \, \lambda L)] \cos(\omega t - \varphi) = 0 \\ T(L,t) &= EI\lambda^3[B_1' \, (sen \, \lambda L + senh \, \lambda L) + B_2' \, (-\cos \lambda L + \cosh \lambda L)] \cos(\omega t - \varphi) = 0 \end{aligned} \quad (4.44)$$

from which we obtain the system of equations in B_1' and B_2'

$$\begin{cases} B_1' \, (-\cos \lambda L + \cosh \lambda L) + B_2' \, (-sen \, \lambda L + senh \, \lambda L) = 0 \\ B_1' \, (sen \, \lambda L + senh \, \lambda L) + B_2' \, (-\cos \lambda L + \cosh \lambda L) = 0 \end{cases} \quad (4.45)$$

By annulling the determinant of the matrix of the coefficients of the system (4.45) we obtain

$$det \begin{bmatrix} -\cos \lambda L + \cosh \lambda L & -sen \, \lambda L + senh \, \lambda L \\ sen \, \lambda L + senh \, \lambda L & -\cos \lambda L + \cosh \lambda L \end{bmatrix} = 0$$

$$\Longrightarrow (-\cos \lambda L + \cosh \lambda L)^2 - (sen \, \lambda L + senh \, \lambda L)(-sen \, \lambda L + senh \, \lambda L) = 0 \quad (4.46)$$

$$\Longrightarrow cos^2\lambda L + cosh^2\lambda L - 2cos\lambda L\, cosh\lambda L + sen^2\lambda L - senh^2\lambda L = 0$$

being $sen^2\lambda L + cos^2\lambda L = 1$ e $cosh^2\lambda L - senh^2\lambda L = 1$, from (4.46) the frequency equation is obtained

$$cos\,\lambda L\, cosh\,\lambda L = 1$$
$$\Longrightarrow cos\,\lambda L = \frac{1}{cosh\,\lambda L} \qquad (4.47)$$

Not having a simple solution available, (4.47) it is solved numerically by plotting the graphs of the functions $cos\,\lambda L$ and $\frac{1}{cosh\,\lambda L}$ whose intersections provide precisely the values of λL which verify the equivalence (4.47) as it can be seen in Figure 4.8

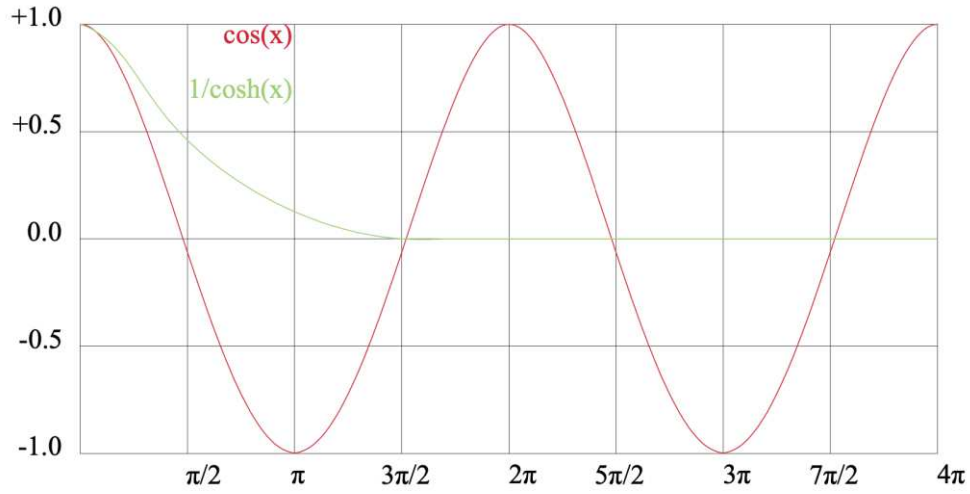

Figure 4.8 – Graph of function cos λL and $\frac{1}{cosh\,\lambda L}$

The first three intersections are for

$$\lambda_1 L = 1{,}506\pi \quad \lambda_2 L = 2{,}5\pi \quad \lambda_3 L = 3{,}5\pi \qquad (4.48)$$

$$\Longrightarrow \quad \lambda_1 L = 4{,}730 \quad \lambda_2 L = 7{,}853 \quad \lambda_3 L = 10{,}996 \qquad (4.49)$$

Since the function $\frac{1}{cosh\,\lambda L}$ rapidly tends to zero, for values of $\lambda_n L$ sufficiently high ($n \geq 4$), the points of intersection correspond to the solutions of the equation $cos\,\lambda L = 0$, or rather

$$\lambda_n L = \left(n - \frac{1}{2}\right)\pi \quad \text{per } n \geq 4 \qquad (4.50)$$

From (4.19) using the values $\lambda_n L$ provided by (4.49) and (4.50) values for natural pulsations can be derived ω_n $(n = 1, 2, 3, ...)$ and the corresponding cyclic frequencies $f_n = \frac{\omega_n}{2\pi}$.

From (4.45) through the values of $\lambda_n L$ provided by (4.49) and (4.50) constants B_1' and B_2' can be determined, which substituted in (4.41), give us the eigenfunctions $V_n(x)$ (deformed of the beam) in correspondence with the natural pulsations ω_n.
The constants B_1' e B_2' are related by the relation

$$B_2' = B_1' \frac{(cos\ \lambda_n L - cosh\ \lambda_n L)}{(sen\ \lambda_n L - senh\ \lambda_n L)} \tag{4.51}$$

Hence the autofunction $V_n(x)$ from (4.41) become

$$V_n(x) = B_1' \Big[(cos\ \lambda_n x + cosh\ \lambda_n x) + \frac{(cos\ \lambda_n L - cosh\ \lambda_n L)}{(sen\ \lambda_n L - senh\ \lambda_n L)} (sen\ \lambda_n x + senh\ \lambda_n x) \Big] \tag{4.52}$$

The first three eigenfunctions $V_1(x)$, $V_2(x)$, $V_3(x)$, corresponding to the natural pulsations ω_1, ω_2, ω_3, are illustrated in Figure 4.9

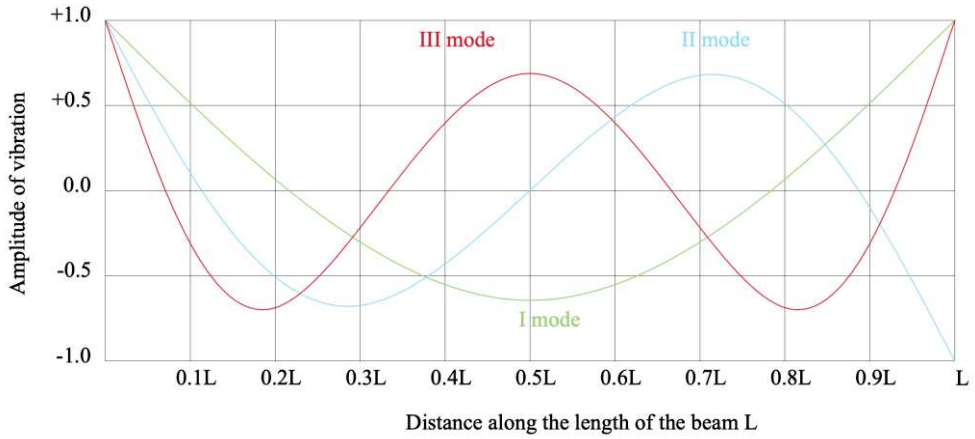

Figure 4.9 – First three natural ways of vibrating of the beam with free ends

4.3.3. Calculation of theoretical frequency values

The theoretical frequencies of vibration of un-damaged un-strengthened RC beams are evaluated following Euler-Bernoulli's theory.
From the previous discussion, assuming a uniform slender beam and neglecting gravity forces, effect of rotary inertia, shear deformation and damping, the equation (4.13) is obtained for free vibration of beam, where:
μ is density of the material of the beam and A is the cross-sectional area.

The eigenvalue relative to r-mode of vibration for free-free ends beam ${\lambda_r}^f$, is determined by the eigenvalue for simply supported beam $\lambda_r = \frac{r \cdot \pi}{L}$ through the expression:

$$ {\lambda_r}^f = \xi_r \cdot \lambda_r \qquad (4.53) $$

where ξ_r is a coefficient depending on r-mode of vibration and boundary condition. Values of the coefficient ξ_r present in literature, relating to first four modes of vibration for different boundary conditions are shown in Table 4.7: in general, depending on the constraint conditions, there are different natural frequencies and, consequently, different modes of vibrating.

Table 4.7 – Coefficients ξ_r relating to the Euler-Bernoulli formula for the calculation of frequencies

Boundary condition	ξ_1	ξ_2	ξ_3	ξ_4
free-free	1.506	1.250	1.167	1.125
hinged-hinged	1.000	1.000	1.000	1.000
fixed-fixed	1.5066	1.5066	1.166	1.122
fixed-hinged	1.249	1.122	1.081	1.063
fixed-free	0.600	0.740	0.830	0.870

The theoretical flexural vibrations of Euler-Bernoulli's continuous beam can be calculated with the following formula, valid for any constraint condition.

$$ f_r = \frac{1}{2\pi} \cdot \left(\frac{r \cdot \xi_r \cdot \pi}{L} \right)^2 \sqrt{\frac{EI}{\rho A}} \qquad (4.54) $$

with r=1,2,3,4.
Table 4.8 and Table 4.9 contains theoretical frequency values obtained applying Euler-Bernoulli's formula for the first four vibration modes, respectively in free-free ends conditions and hinged conditions.
Theoretical values are calculated considering the geometric characteristics and mechanical parameters (elastic modulus, moment of inertia and density) of the experimental model considering only concrete material for the section.

Table 4.8 – Theoretical frequency values for Euler-Bernoulli beam model for the first four modes of vibration in free-free ends conditions

	f_1 (Hz)	**f_2 (Hz)**	**f_3 (Hz)**	**f_4 (Hz)**
Th. Euler-Bernoulli	126.17	347.68	681.84	1126.48

Table 4.9 – Theoretical frequency values for Euler-Bernoulli beam model for the first four modes of vibration in hinged ends conditions

	f_1	f_2	f_3	f_4
Th. Euler-Bernoulli	**(Hz)**	**(Hz)**	**(Hz)**	**(Hz)**
	55.63	222.51	500.66	890.06

4.4. Static behavior of RC beams

The theoretical behavior of the reinforced concrete beam was analyzed also from a static point of view, in fact, we proceeded to calculate the deformations, as well as the ultimate theoretical moments of the RC beam models subjected to an increasing load, applied at midspan section, therefore subject to a bending stress (and shear stress). Theoretical moment-curvature diagrams were built and shown.
The theoretical diagram has been drawn passing through three notable points, therefore the phases analyzed are the following:

- Phase I: Cracking;
- Phase II: Yielding;
- Phase III: Failure.

The hypotheses considered for each phase and the calculated values are briefly reported below.

For phase I, it is assumed to have the concrete section entirely reactive: M_{cr} corresponds to the moment relative to the achievement of concrete tensile strength, therefore it is assumed $\varepsilon_c = f_{ctd}/E_c$.
In this phase, the first section of the curve is straight and passing through the origin, for small load values, the maximum tension in the concrete is lower than the tensile strength, so the part of the stretched section is also reactive. Phase II corresponds to the yield phase, so it is assumed that the deformation in the tension steel reaches the value $\varepsilon_{s,2} = f_{yd}/E_s$. In this second phase, the tensile strength of the concrete is overcome, therefore it is the steel that absorbs the tensile stresses released by the material. Up to the yield point, the behavior of the beam is conditioned by that of the steel still in the elastic phase.
Finally, phase III corresponds to the collapse of the section, therefore it is assumed that the tensioned steel is yielded $\varepsilon_{s,2} \geq f_{yd}/E_s$ and the compressed concrete has reached the ultimate deformation $\varepsilon_c = \varepsilon_{cu} = 3{,}5‰$.
Obviously, for the calculation of the deformation states, the hypotheses of conservation of plane sections is used.

The following tables (Table 4.10, Table 4.11, Table 4.12) show the theoretical values of moment, deformations, curvature, and neutral axis depth calculated for each phase, for the un-strengthened and strengthened beam models.

Table 4.10 – Theoretical deformation states for un-strengthened beam model

Phase I - Cracking		Phase II - Yielding		Phase III - Failure	
M_{cr} (kNm)	1.58	M_y (kNm)	9.21	M_u (kNm)	10.06
χ_{cr} ($mm^{-1}\cdot10^{-6}$)	1.19	χ_y ($mm^{-1}\cdot10^{-6}$)	25.49	χ_u ($mm^{-1}\cdot10^{-6}$)	190.34
x (mm)	79.42	x (mm)	35.95	x (mm)	18.39
$\varepsilon_{c,\,max}$ (‰)	0.095	$\varepsilon_{c,\,max}$ (‰)	0.92	$\varepsilon_{c,\,max}$ (‰)	3.50
$\varepsilon_{s,1}$ (‰)	0.067	$\varepsilon_{s,1}$ (‰)	0.33	$\varepsilon_{s,1}$ (‰)	0.88
$\varepsilon_{s,2}$ (‰)	0.060	$\varepsilon_{s,2}$ (‰)	2.40	$\varepsilon_{s,2}$ (‰)	21.24

Table 4.11 – Theoretical deformation states for strengthened GFRP beam model

Phase I - Cracking		Phase II - Yielding		Phase III - Failure	
M_{cr} (kNm)	1.62	M_y (kNm)	10.33	M_u (kNm)	16.17
χ_{cr} ($mm^{-1}\cdot10^{-6}$)	1.20	χ_y ($mm^{-1}\cdot10^{-6}$)	25.90	χ_u ($mm^{-1}\cdot10^{-6}$)	133
x (mm)	79.93	x (mm)	37.45	x (mm)	26.64
$\varepsilon_{c,\,max}$ (‰)	0.096	$\varepsilon_{c,\,max}$ (‰)	0.97	$\varepsilon_{c,\,max}$ (‰)	3.50
$\varepsilon_{s,1}$ (‰)	0.068	$\varepsilon_{s,1}$ (‰)	0.37	$\varepsilon_{s,1}$ (‰)	0.43
$\varepsilon_{s,2}$ (‰)	0.060	$\varepsilon_{s,2}$ (‰)	2.40	$\varepsilon_{s,2}$ (‰)	13.84
ε_{GFRP} (‰)	0.084	ε_{GFRP} (‰)	2.92	ε_{GFRP} (‰)	16.51

Table 4.12 – Theoretical deformation states for strengthened CFRP beam model

Phase I - Cracking		Phase II - Yielding		Phase III - Failure	
M_{cr} (kNm)	1.73	M_y (kNm)	13.62	M_u (kNm)	25.77
χ_{cr} ($mm^{-1}\cdot10^{-6}$)	1.22	χ_y ($mm^{-1}\cdot10^{-6}$)	27.07	χ_u ($mm^{-1}\cdot10^{-6}$)	94.89
x (mm)	81.38	x (mm)	41.44	x (mm)	36.88
$\varepsilon_{c,\,max}$ (‰)	0.10	$\varepsilon_{c,\,max}$ (‰)	1.12	$\varepsilon_{c,\,max}$ (‰)	3.50
$\varepsilon_{s,1}$ (‰)	0.071	$\varepsilon_{s,1}$ (‰)	0.50	$\varepsilon_{s,1}$ (‰)	1.32
$\varepsilon_{s,2}$ (‰)	0.059	$\varepsilon_{s,2}$ (‰)	2.40	$\varepsilon_{s,2}$ (‰)	8.84
ε_{CFRP} (‰)	0.084	ε_{CFRP} (‰)	2.94	ε_{CFRP} (‰)	10.73

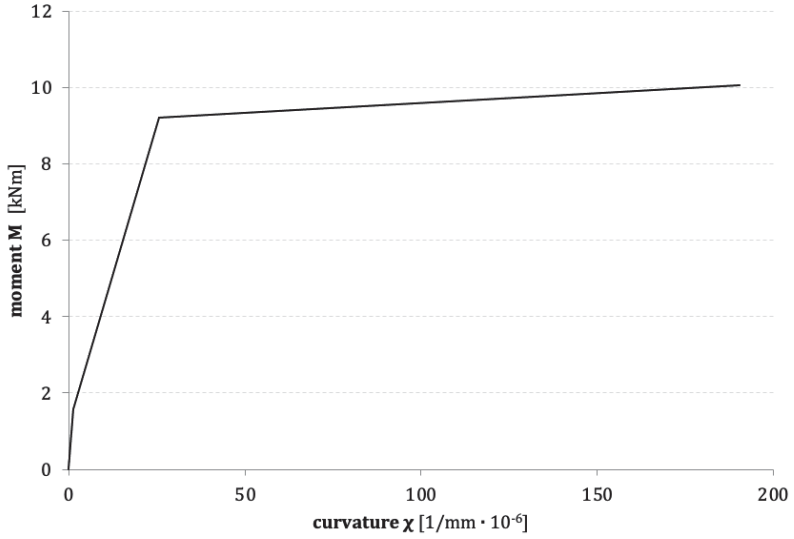
12
10
8
6
4
2
0
moment M [kNm]
0
50
100
150
200
curvature χ [1/mm · 10-6]

(a)

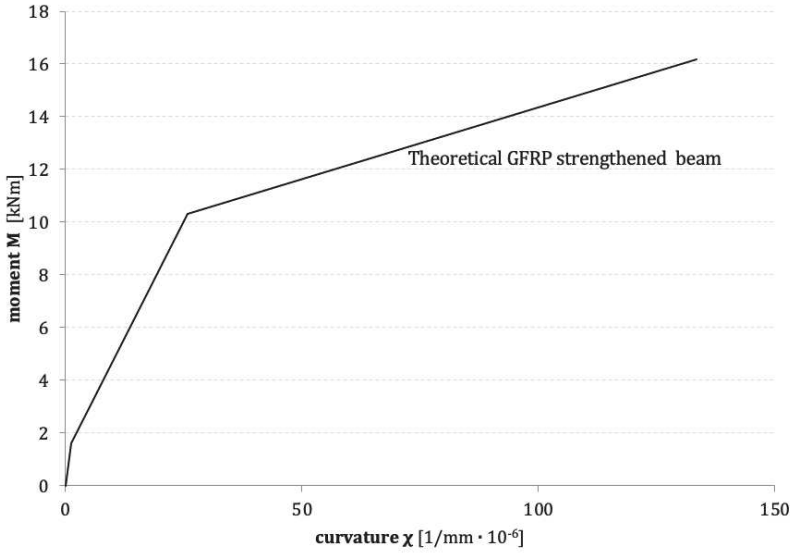
18
16
14
12
10
8
6
4
2
0
moment M [kNm]
Theoretical GFRP strengthened beam
0
50
100
150
curvature χ [1/mm · 10-6]

(b)

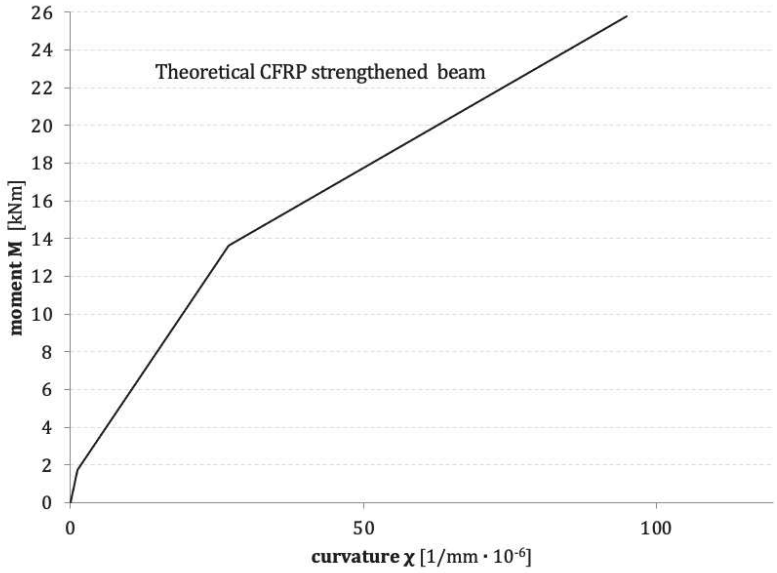

(c)

Figure 4.10 – Theoretical moment vs curvature diagram, (a) for the un-strengthened specimen; (b) for the GFRP strengthened specimen; (c) for the CFRP strengthened specimen

The distribution of calculated theoretical strains for the un-strengthened and strengthened specimens at midspan section, for each phase, are represented, in function of the height of the section, in Figure 4.11.

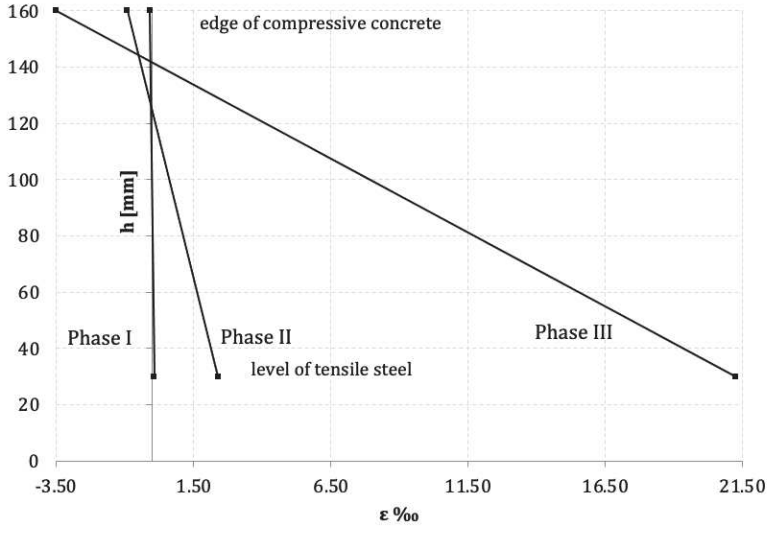

(a) un-strengthened beam model

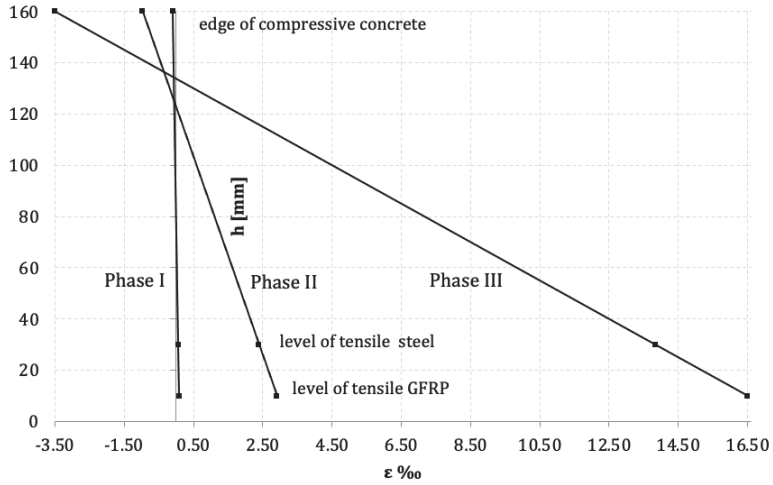

(b) strengthened GFRP beam model

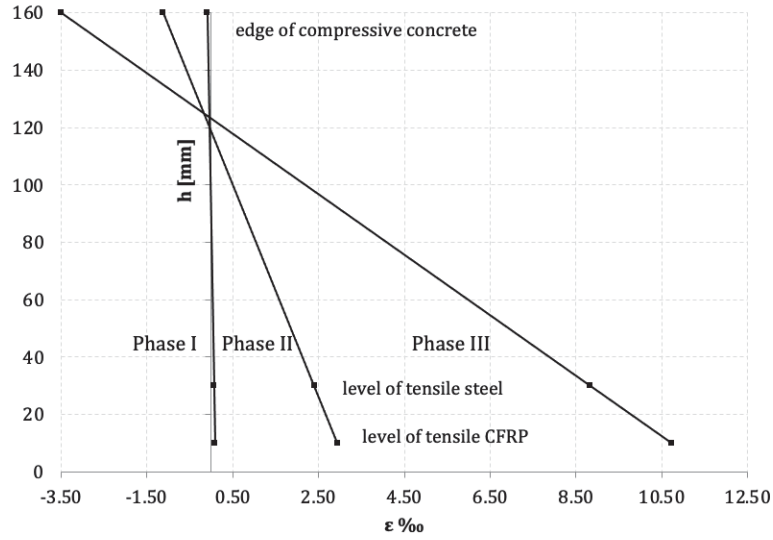

(c) strengthened CFRP beam model

Figure 4.11 – Theoretical strain values vs height, at midspan section, at each phase of RC beams; (a) un-strengthened beam model, (b)strengthened GFRP beam model, (c) strengthened GFRP beam model

Having adopted the hypothesis of conservation of plane sections, the distributions of strains of each material through the full depth of the beam is linear.

Chapter 5. Experimental investigation on NSM strengthened RC beams

5.1. Introduction

In this chapter the experimental work developed during the research activity is presented; the experiments were conducted at the Testing, Materials and Structures Laboratory of the Department of Civil, Building and Architecture Engineering (D.I.C.E.A.) of the Faculty of Engineering of the Polytechnic University of Marche. The four reinforced concrete beam specimens, described in Chapter 4, have been statically and dynamically tested. Static tests are carried out through the application of cycles of bending loading until break. Vibration tests have been adopted as a non-destructive method of control during the experiments to assess the response of RC beams at different damage steps; a brief introduction to experimental modal analysis techniques is also reported in this chapter.
Firstly, all the specimens are tested in their initial conditions, after conducting experimental static and dynamic tests, all the specimens, except one – that remained in the un-strengthened condition – were reinforced with NSM FRP rod and tested again in order to monitor the effectiveness of the reinforcement and the effects of damage.

The adopted procedure for testing and the instrumentation used is described in detail below. In the last section the experimental results are also shown.
About static tests load-deflection, stress-strain of concrete, of steel bars and of FRP bars and moment-curvature diagrams are shown. In this way, the static behavior of each beam model, strengthened and un-strengthened, even in the presence of different level of crack damage is defined. Regarding dynamic tests, frequency response functions (FRFs) in terms of acceleration are shown. The values of the natural frequencies, relating to the first four modes of vibrations, at each damage step are reported.

5.2. Experimental static tests

The four beam models were subjected to static bending tests on four points applying loading cycles until failure, with the aim of defining the behavior of strengthened and un-strengthened specimens.

5.2.1. Test set up and instrumentation

The static test performed on each beam is a four-point load test type: two support points with 2000mm center distance and two load points with 300mm center distance, as depicted in Figure 5.1.

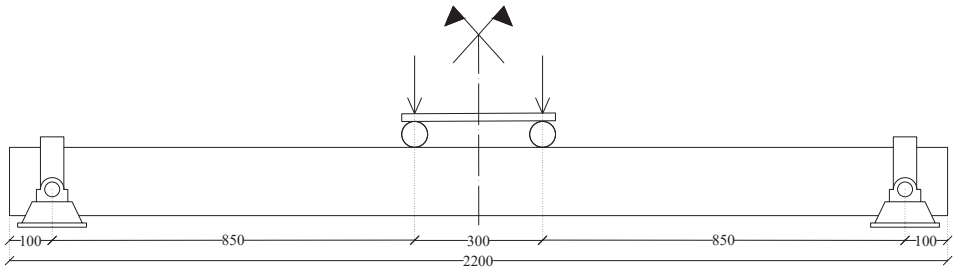

Figure 5.1 – Scheme of the set-up of bending tests

The hinges block the beam trough tightening of three bolts placed on each side. The contact between concrete and the hinge has been regularized using a neoprene rubber.
The load is applied by a hydraulic jack operated by a manual hydraulic pump, positioned above a load divider that distributes the force impressed on two points and contrasted by a rigid steel frame fixed at the ground: the hydraulic jack has a maximum capacity of 500 kN, the hydraulic pump has a maximum exercisable pressure of 700 bar (Figure 5.2).

Figure 5.2 – Set up of bending tests

To acquiring all necessary data about deflection and strain during the tests, suitable instrumentation like piezoelectric strain gauges, mechanical strain gauges and displacement transducers were set up on beams. To record vertical deflection of specimens a Linear Variable Displacement Transducer (LVDT) with a maximum recording capacity of 100mm and a sensitivity of 0.01mm was place at midspan section (Figure 5.3 a); on the lower rebars and, as already mentioned, on FRP bars, at midspan, piezoelectric stain gauges are applied to measure strains[1]. The strain gauges used - produced by the German company HBM s.r.l. - are K-LY41-10 / 120 type, with a resistance of 120Ω (± 0.35%) (Figure 5.3b).

Finally, mechanical strain gauges were placed at extrados of the beams on concrete surface (compressed flap), to measure its deformations. The mechanical strain gauges used can detect maximum strains of 7ηm/m.

[1] for each strain gauge positioned the same number must be prepared with the function of compensators on the same type of material to discard any deformations due to temperature variations.

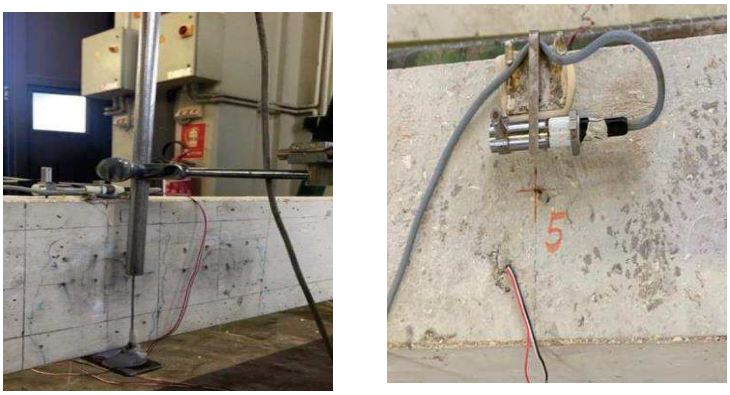

(a) (b)

Figure 5.3 – Instrumentation used during static tests: (a) LVDT placed at midspan section, (b) mechanical strain gauge on concrete surface

The entire layout of instrumentation is depicted in Figure 5.4.

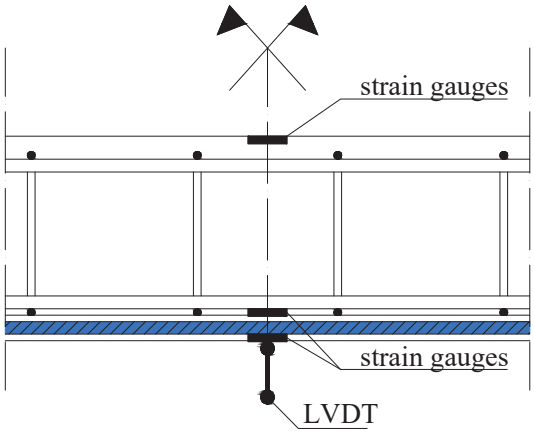

Figure 5.4 – Scheme of instruments location at midspan section

5.2.2. Execution of tests

To determine the values of load steps to which the specimens were subjected, theoretical values of moment and strain related to the main load phases (cracking, yielding and failure) are firstly calculated. The theoretical moment related to the un-strengthened beam model and strengthened beam model were calculated considering the mechanical characteristics of the materials used, determined experimentally and assuming the perfect adherence of the reinforcement to the support and the planarity of the sections until failure.

The static experimental tests on beam specimens were carried out applying loading and unloading cycles up to failure. All beam models in the un-strengthened phase were subjected to four load cycles:
-D_1=4 kN;
-D_2=8 kN;
-D_3=16 or 18 kN.

After strengthening with NSM FRP bar the specimens were subjected to the previous loading cycles, and finally brought to failure. On specimen B_2 an additional loading cycle, was applied, while for specimen B_3, strengthened with CFRP bar, a last cycle of 30 kN was added after applying 24 kN.
The loads applied to each beam are shown in Table 5.1, where D_0 indicates the no-load phase, therefore no crack damage, while D_n indicates the generic load step, until the break load D_f.

Table 5.1 – Loading-unloading cycles applied to each beam specimen

CB		**B1**		**B2**		**B3**	
D_i	P(kN)	D_i	P (kN)	D_i	P(kN)	D_i	P(kN)
D_0	0	D_0	0	D_0	0	D_0	0
D_1	4	D_1	4	D_1	4	D_1	4
D_2	8	D_2	8	D_2	8	D_2	8
D_3	18	D_3	18	D_3	16	D_3	18
		D_f	34	D_4	24	D_4	24
				D_f	38	D_5	30
						D_f	49

5.3. Experimental dynamic tests

In parallel to the static tests, vibration tests adopted as non-destructive method of control were also carried on beam models. The general aspects of experimental modal analysis are addressed in the next paragraph.
After each loading cycle, D_i, the same experimental beam models were subjected to dynamic tests with the aim of experimentally determining the dynamic parameters (natural frequencies), in order to monitoring the effects of reinforcement and of damage on dynamic response.
With an impact hammer an impulse is generated, while with an accelerometer the response of the beam is measured.
The most common technique of hammer impact testing is called *"roving hammer"* test: in this method a single accelerometer is fixed to one position of the structure, which is excited each time at several locations, in order to reproduce the frequency response matrix from which the modal form is obtained.

However, to obviate the drawback of not being able to excite the points of the structure in all directions at the same time, a variant of this method has been used in the present research work. It is called *"roving accelerometer"*: the structure is impacted at a fixed position and move a single accelerometer around several positions. This method is still efficient in terms of transducers and measurement system.

The dynamic test, on all specimens, was carried out recording the response of the structure in nine positions, $Mark_i$, with i=1,…9, to trigger with an impact hammer in a fixed position; recorded frequency values are the average of 10 beats for every location of accelerometer. The tests were carried out considering two constraints conditions: free-free ends and hinged ends.
The experimental modal analysis is carried out after each loading cycle, with the exception of the one at failure of specimens.

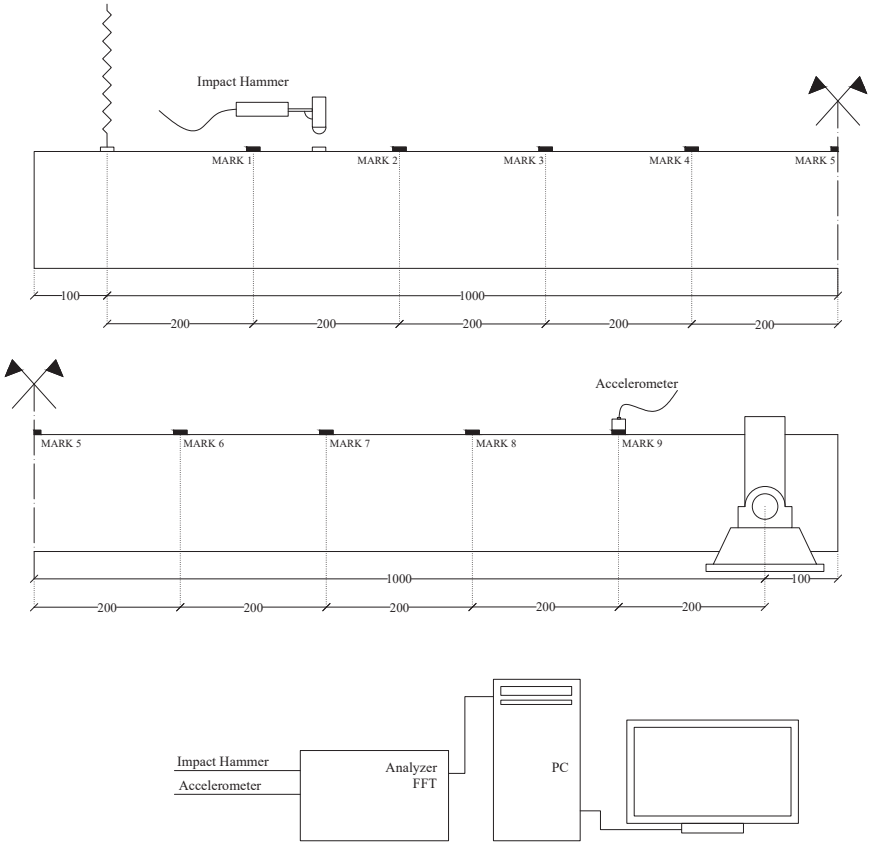

Figure 5.5 – Scheme of set up of vibration tests

5.3.1. Short outline on non-destructive method of control based on vibration

The techniques of dynamic characterization, analytical or experimental, allow to obtain information on the dynamic behavior of a structure in terms of eigen frequencies, modal damping and modal forms.
In the analytical approach or direct problem, starting from the knowledge of the geometry of the structure, the boundary conditions, the characteristics of the materials, the mass, stiffness and damping matrices, solving an eigenvalue problem, it is possible to arrive at the determination of the modal parameters of the system. In the inverse problem experimental approach, on the other hand, starting from the measurement of the dynamic input (cause) and from the acquisition of the structural response in kinematic terms, the frequency response functions are evaluated, then the dynamic parameters of the structure are estimated.

The experimental modal analysis is also known as the “inverse problem”, since it is a problem in which the structural response and the input are known, that is the phenomenon that causes the response, and we want to know the starting configuration of the structure (in contrast, in fact, to the so-called “direct problem”, in which the input and the geometry of the structure are known, and we want to know the answer).

The dynamic behavior of a structure and, in particular, the natural frequencies depend only on its intrinsic characteristics (mass, stiffness, damping, degree of restraint, ...) and not on the entity or type of load applied, or on the position sensor to acquire the response. Therefore, if there are no internal modifications to the structure, such as structural damage, the dynamic behavior of the same remains unaltered; otherwise, it is possible to record variations in frequencies and their own modes of vibration through experimental modal analysis.

For this reason, we speak of non-destructive control techniques, i.e. techniques which, by suitably processing the dynamic response of a structure, are able to verify the state of damage, therefore to correlate the variation of the modal parameters of a structure with the variation the degree of integrity of the same, while maintaining its functionality unchanged.

Considering any damaged structure, it is plausible that, with the same static stressing load, the structure under examination deforms more than the same intact structure; this is equivalent to affirming that the damage has increased the compliance and this increase is only a function of the geometric characteristics of the damage. From the relation:

$$\omega_n = \sqrt{\frac{k_n}{m_n}} \tag{5.1}$$

where k_n is stiffness, ω_n is natural pulsation and m_n is the mass of the structure. Knowing that:

$$k_n = \frac{1}{c_n} \tag{5.2}$$

Where c_n is the compliance.
Substitution (5.2) in (5.1), it gives:

$$\omega_n = \sqrt{\frac{1}{c_n \cdot m_n}} \tag{5.3}$$

Therefore, it is evident that, with the same mass, an increase in the yielding of the structure, caused by damage, manifests itself in a reduction of its natural pulsations. Consequently, the other modal characteristics (damping, proper modes of vibration, ...) also undergo a variation due to the presence of damage. Furthermore, it can also be observed that, under the same load, the difference between the static deformation relating to the damaged structure and that relating to the intact structure is exclusively a function of the increase in compliance; therefore, even in the dynamic field, the difference between the dynamic response of the damaged structure and that of the intact structure depends only on the geometric characteristics of the damage.

In this context, there are some non-destructive dynamic characterization techniques that try to correlate the variation of the dynamic response, due to a variation of the modal parameters (natural frequencies, proper modes of vibrations, modal damping, ...), with the characteristics geometric from damage.

The experimental modal analysis techniques consist in the measurement of the response of a structure to a known excitation, therefore they allow to obtain information on the dynamic behavior of the same, such as the values of the natural frequencies, ω_i, the modal damping factors, ξ_i, and the modal form, ϕ_i. Basically, a pulsating force is applied ω in a point *i* of the structure and the response is measured, understood as displacement, speed or acceleration in a point *j*: thus a complex function is determined H_{ij} (ω), representing the frequency response function at one point (FRF); by repeating the measurements at different points, the frequency response matrix is obtained *H*, from which it is possible to derive the dynamic behavior of the structure.

5.3.2. Test set up and instrumentation

As already mentioned, specimens are tested with two boundary conditions: free-free (Figure 5.6) and hinged ends (Figure 5.7). Free structure means a structure not bound to the ground, but suspended in space: in these conditions, the structure exhibits the rigid body motions, characterized by zero natural frequency, determined exclusively by its mass properties and inertia. In practice, it is impossible to reach the perfectly free test condition, because the object must be supported in some way; however, it is possible to create a suspension system able to approximate the condition of no ground constraints for data acquisition. In the present work to simulate this condition an elastic spring is adopted, which acts as spring with negligible rotational stiffness. These springs are placed 100 mm from the ends of beam models and 2000 mm between them, to be as close as possible to the nodal points, in this way the minimum interference of the suspension system on the constraint conditions of the structure is ensured.
To simulate the simple support points, two steel hinges were used, the same ones used during the static tests. The beam was therefore positioned inside the two hinges, with the aid of a sheet neoprene rubber disc onto which three upper bolts were screwed to hinge it.

Figure 5.6 – Set up of vibration tests with free-free ends

Figure 5.7 – Set up of vibration tests with hinged ends

About the instrumentation, the impact hammer used to generate the impulse is Type 8202 Brüel & Kjær produced; to cover the low frequency range and linearize any non-linear behavior, a random waveform exciter was used. The impact point of the instrumented hammer was fixed 350mm from one end of the specimens. The accelerometer used in the dynamic experiment was a Brüel & Kjær produced Piezoelectric CCLD brand n. 4508; it was moved in 9 different point, $Mark_i$ with i=1, …9. The marks positions have been chosen in order to avoid these coincided with the "modal nodes", where the dynamic characteristics of the system are null, therefore the observability of the analysis is not guaranteed.
Recorded frequency values are the average of 10 beats for every $Mark_i$.
The signals acquired by the accelerometer have been processed and transformed in the frequency domain, with a Fast Fourier Transformation analyzer, a data acquisition system LAN XI TYPE 3050 Brüel & Kjær produced, managed by "BK CONNECT 2018 – PULSE" software, developed by Brüel & Kjær company.

5.3.3. Execution of tests

After each loading step, D_i, that corresponds to different level of damage, the experimental models of beam were tested: ten impacts in the same point for each measurement set are performed with instrumented hammer (Figure 5.8a); the response was acquired with an accelerometer placed each time on one of the nine different measurement points previously provided ($Mark_i$) (Figure 5.8b).

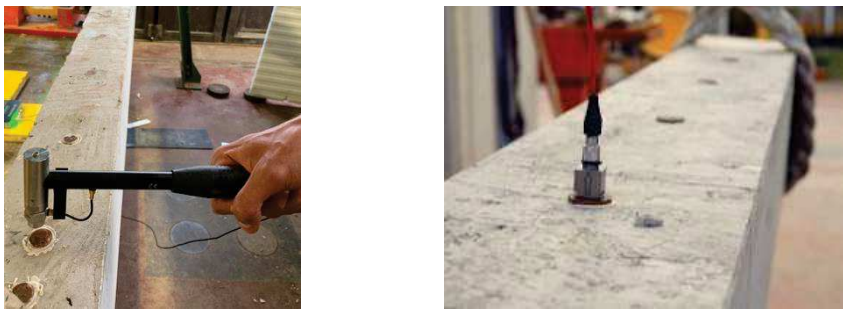

(a) *(b)*

Figure 5.8 – (a) Accelerometer placed on a Mark; (b) impact hammer during dynamic test

The Fast Fourier Transformation analyzer recorded and stored the dynamic responses of the specimens, then the data were transferred to the laptop connected to the acquisition system. Through the BK connect software, it was possible to view the dynamic results, in the form of frequency response functions (FRF), checking the coherence function after each beat. It was also possible to decide whether or not to accept the measurement recorded, as the program is able to signal the goodness of the shot given. Once the set of measurements is completed and the results saved, it is possible to continue with the next accelerometer position.
After completing the test, the data acquired can be exported, in this way they can be processed in tabular form and graphed. In the next chapter, the results of the present experimental work will be reported and analyzed in detail, focusing on the effects of crack damage in concrete, as well as on the effects of the different types of FRP reinforcement.

5.4. Results from static tests

During the static bending tests on four points, instrumentation is prepared on specimens in such a way as to detect the displacements of the beam models and the deformations in the compressed area, in the tension area and in correspondence with FRP reinforcements, as detailed in paragraph §5.2.1.
The results of the static tests allow to define the behavior of beam models strengthened with NSM technique, even in the presence of various states of damage due to cracking.

Table 5.2 shows the values acquired by the instrumentation used and their first reprocessing for each load cycle D_i, considered as a level of damage due to cracking, for the different experimental beam models.
The results of the static experimental tests allow to define the behavior of the reinforced beam models according to the NSM technique with reference to the main phases of load: cracking, yielding and failure.
In some cases, in correspondence with the last load cycles, malfunctions of the measuring instruments have occurred, due to their detachment or breakage, for this reason the inaccurate measurements have not been reported in table and do not appear in diagrams.

Table 5.2 – Experimental results for beam models by static bending test at damage degree D_i

CB			
Experimental data	**D_1**	**D_2**	**D_3**
P - Exp. load (kN)	4.01	7.99	18.03
M - Moment (kNm)	1.70	3.40	7.66
δ - Deflection at midspan (mm)	1.70	5.36	12.62
ε_c - Strain at compressive concrete (‰)	0.22	0.39	0.82
ε_s - Strain at tensile steel (‰)	0.36	1.39	1.62
χ - Curvature of midspan section ($mm^{-1}\cdot10^{-6}$)	4.45	13.71	26.51

B_1				
Experimental data	**D_1**	**D_2**	**D_3**	**D_f**
P - Exp. load (kN)	4.00	8.02	18.01	33.87
M - Moment (kNm)	1.70	3.41	7.65	14.39
δ - Deflection at midspan (mm)	1.95	3.95	9.58	38.30
ε_c - Strain at compressive concrete (‰)	0.25	0.53	1.11	-
ε_s - Strain at tensile steel (‰)	0.48	1.14	2.56	-
ε_{GFRP} - Strain at GFRP rod (‰)	0.37	0.83	1.23	-
χ - Curvature of midspan section ($mm^{-1}\cdot10^{-6}$)	5.65	12.85	28.26	-

B_2					
Experimental data	**D_1**	**D_2**	**D_3**	**D_4**	**D_f**
P - Exp. load (kN)	4.01	8.06	16.02	24.02	38.40
M - Moment (kNm)	1.70	3.43	6.81	10.21	16.32
δ - Deflection at midspan (mm)	1.87	3.69	7.55	12.10	39.70
ε_c - Strain at compressive concrete (‰)	0.14	0.30	0.66	0.99	-
ε_s - Strain at tensile steel (‰)	0.39	0.79	1.69	2.61	-
ε_{GFRP} - Strain at GFRP rod ‰)	0.34	0.72	1.80	3.02	7.86
χ - Curvature of midspan section ($mm^{-1}\cdot10^{-6}$)	4.09	8.35	18.05	27.65	-

B_3						
Experimental data	**D_1**	**D_2**	**D_3**	**D_4**	**D_5**	**D_f**
P - Exp. load (kN)	4.00	8.02	18.01	24.01	30.01	49.06
M - Moment (kNm)	1.70	3.41	7.65	10.20	12.75	20.85
δ - Deflection at midspan (mm)	0.96	0.80	3.29	7.36	9.45	25.35
ε_c - Strain at compressive concrete (‰)	0.09	0.24	0.59	0.83	1.05	20.70
ε_s - Strain at tensile steel (‰)	0.24	0.52	1.42	2.10	-	-
ε_{CFRP} - Strain at CFRP rod (‰)	0.14	0.55	1.50	2.06	2.73	4.33
χ - Curvature of midspan section ($mm^{-1}\cdot10^{-6}$)	2.59	5.78	15.45	22.53	-	-

5.4.1. Load-Deflection

Experimental load-deflection curves for each beam model, related to each loading-unloading cycle are reported and analyzed.
Figure 5.9 shows the total applied load, *P*, versus the average midspan deflection, *δ*; the deflection refers to the midspan of beams, where the vertical displacement transducer has been positioned.

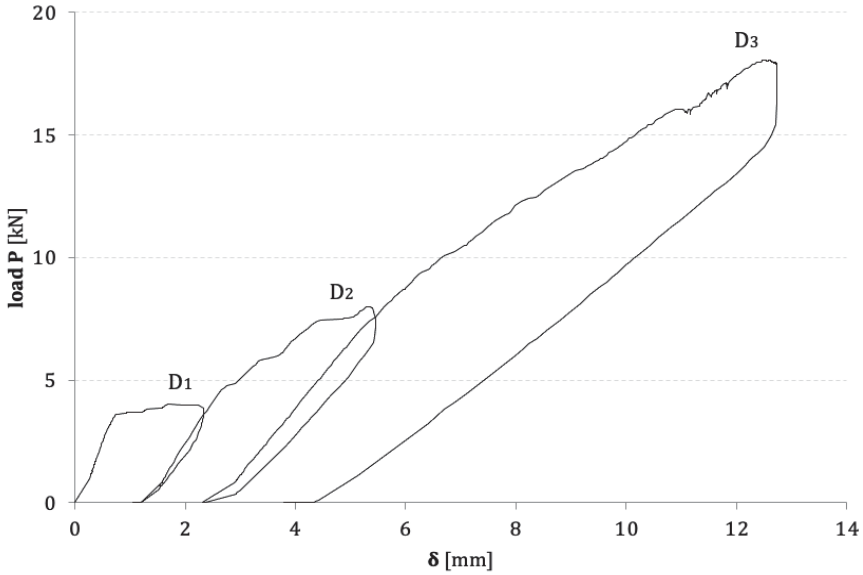
20
15
10
5
0
load P [kN]
D3
D2
D1
0
2
4
6
8
10
12
14
δ [mm]

(a) CB

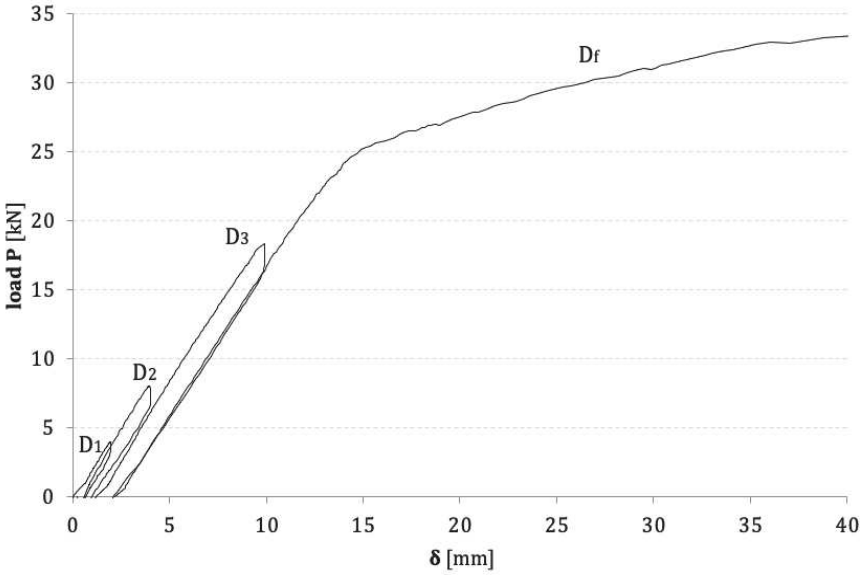
35
30
25
20
15
10
5
0
load P [kN]
Df
D3
D2
D1
0
5
10
15
20
25
30
35
40
δ [mm]

(b) B_1

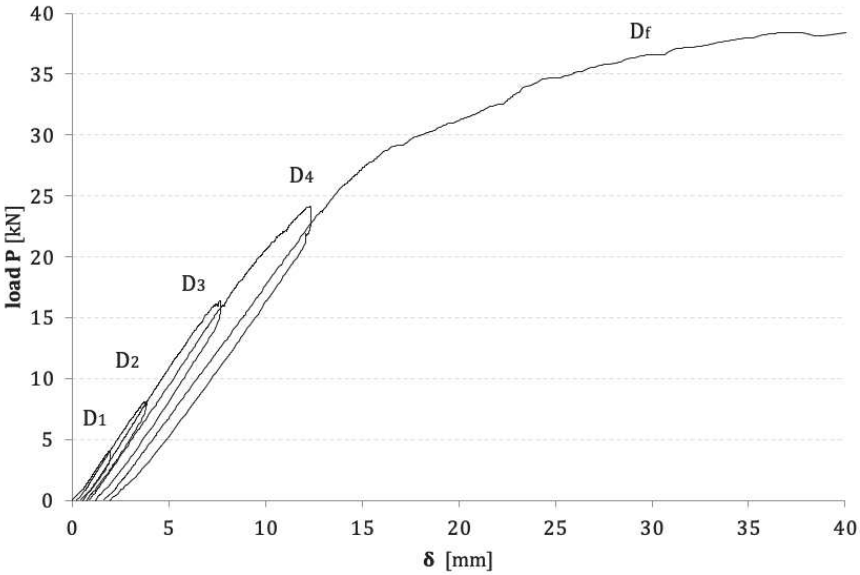

(c) B_2

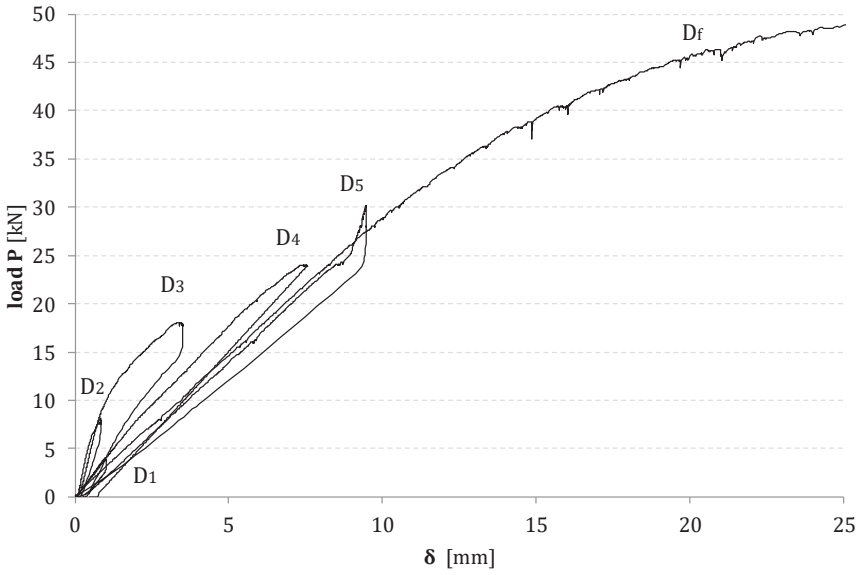

(d) B_3

Figure 5.9 – Experimental diagram load, P, vs deflection, δ, at midspan of RC beams; (a) specimen CB, (b) specimen B_1, (c) specimen B_2, (d) specimen B_3

5.4.2. Load-Strain

The following figure (Figure 5.10) shows the deformations of compressed concrete at extrados, as function of the load, for each loading-unloading cycle.

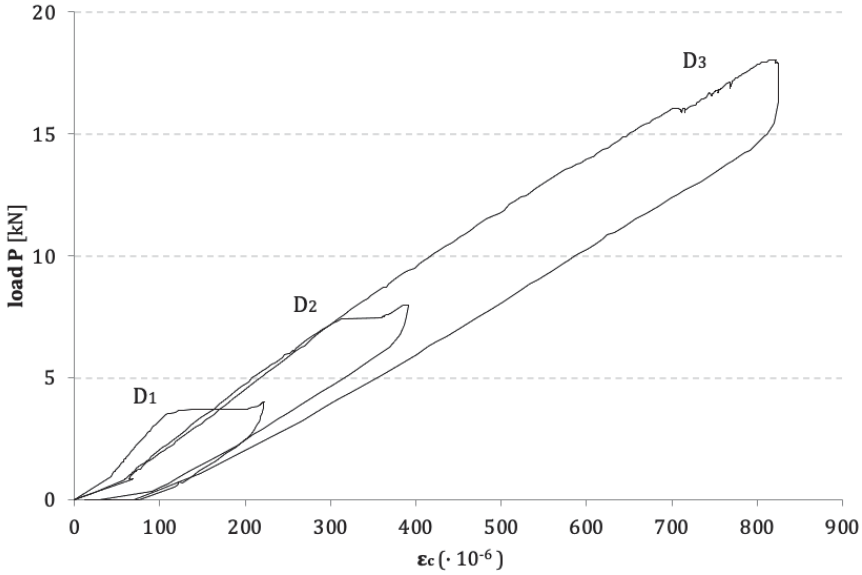

(a) CB

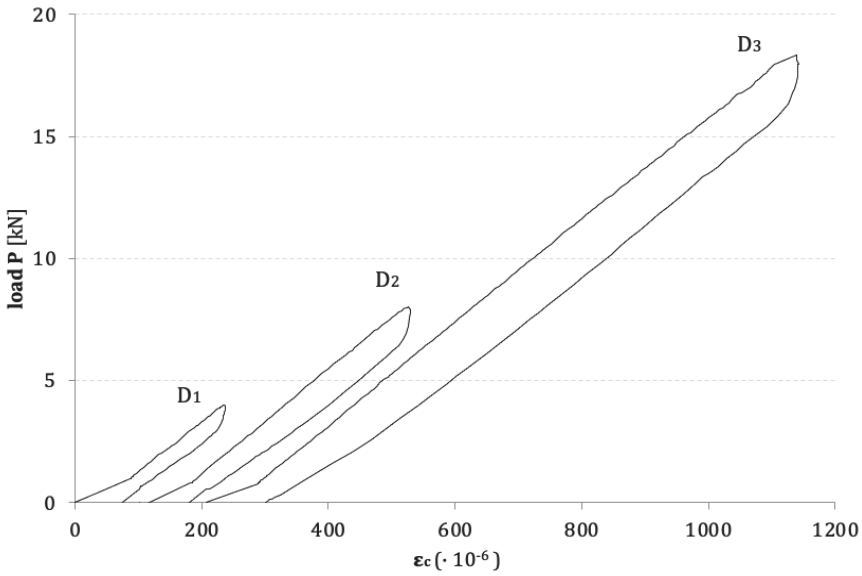

(b) B1

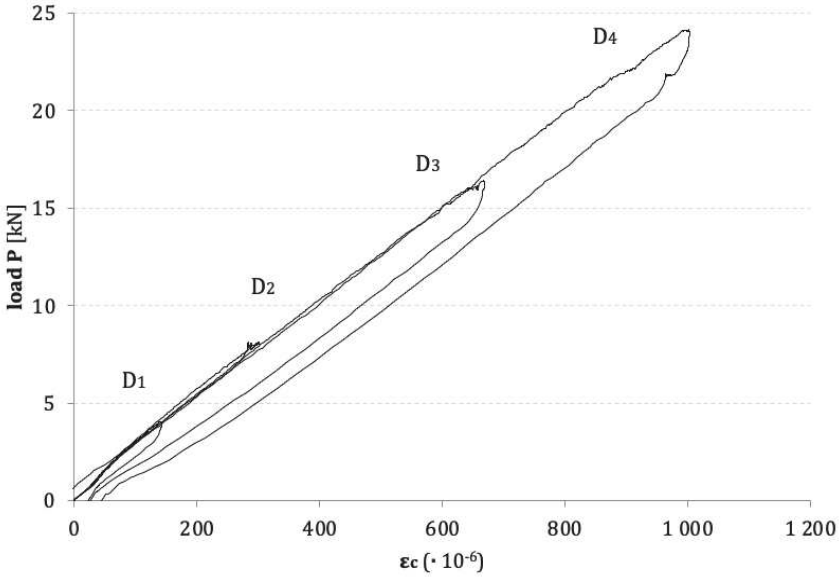

(c) B_2

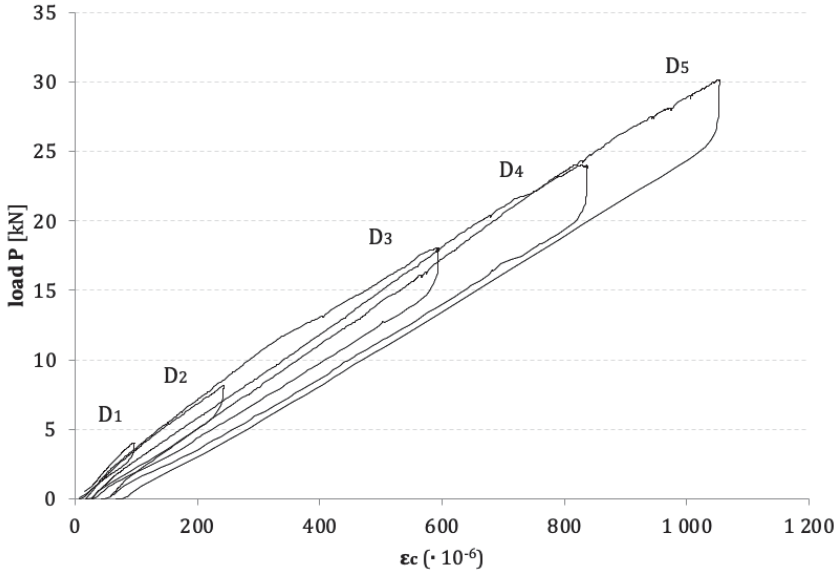

(d) B_3

Figure 5.10 – Experimental diagram load, P, vs strain of concrete, ε_c, at the edge of compressive concrete of RC beams; (a) specimen CB, (b) specimen B_1, (c) specimen B_2, (d) specimen B_3

A close look at the load–strain curves of concrete obtained at midspan indicates that all strengthened beams, exhibited a nearly linear attitude up to the peak load of beam, without clear signs of affection by cracking of concrete or yielding of tension steel.

In Figure 5.11 the trend of tensile steel deformation, as function of load, for each specimen subjected to bending loading is depicted.

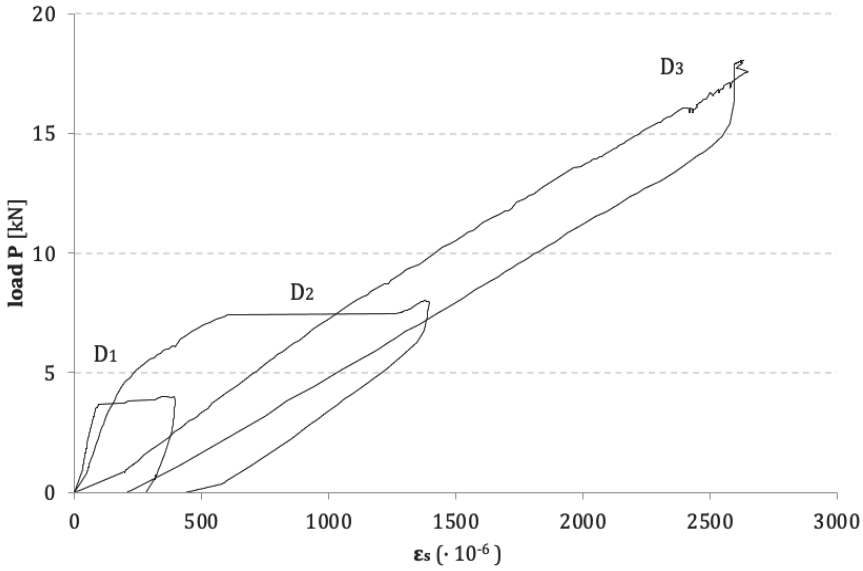

(a) CB

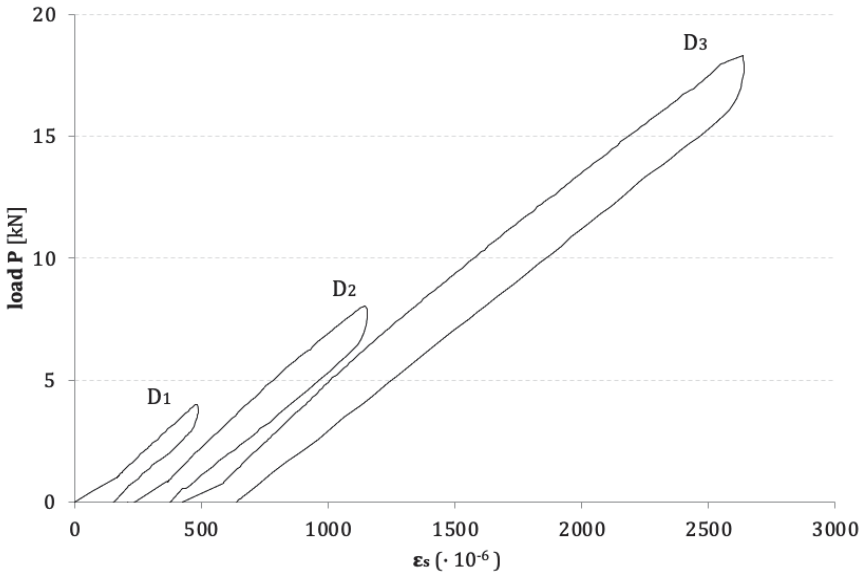

(b) B1

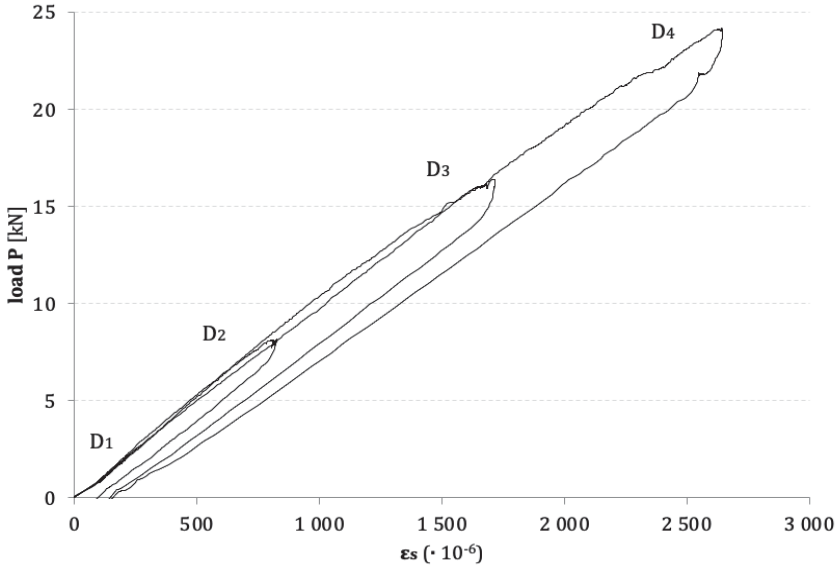

(c) B_2

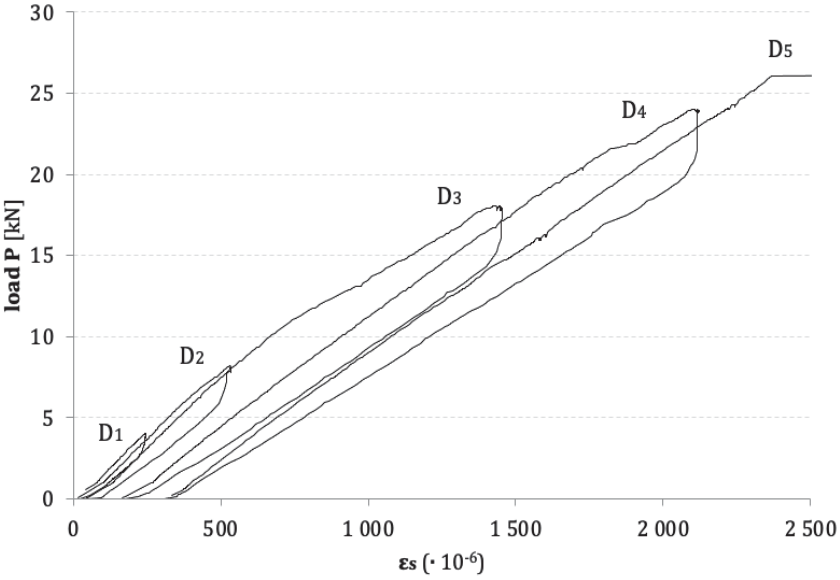

(d) B_3

Figure 5.11 – Experimental diagram load, P, vs strain of steel, ε_s, at bottom of RC beams; (a) specimen CB, (b) specimen B_1, (c) specimen B_2, (d) specimen B_3

Figure 5.12 shows the results from the strain gauges positioned on the FRP rods for the reinforced beam samples, as function of applied load.

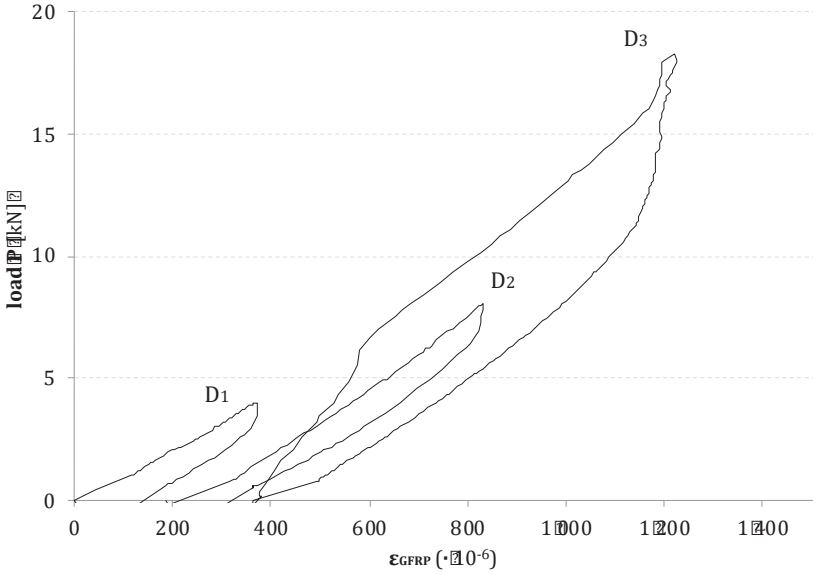
20
15
10
5
0
load P [kN]
D1
D2
D3
0
200
400
600
800
1 000
1 200
1 400
εGFRP (· 10-6)

(a) B1

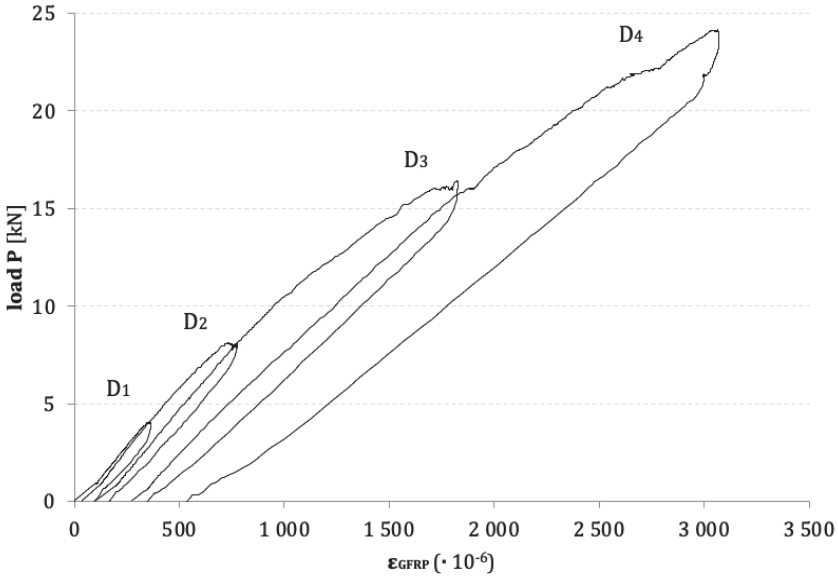
25
20
15
10
5
0
load P [kN]
D1
D2
D3
D4
0
500
1 000
1 500
2 000
2 500
3 000
3 500
εGFRP (· 10-6)

(b) B2

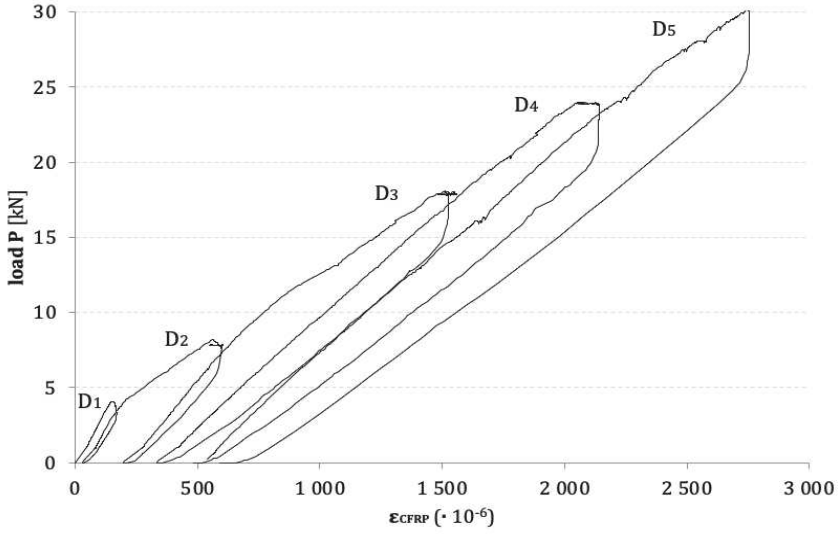

(c) B_3

Figure 5.12 – Experimental diagram load, P, vs strain of FRP bar, ε_{FRP}, of RC beams;(a) specimen B_1, (b) specimen B_2, (c) specimen B_3

5.4.3. Moment-Curvature

Below the experimental diagram moment versus curvature of each beam model are reported (Figure 5.13). The curvature was calculated at midspan section as follows:

$$\chi = \frac{\varepsilon_c + \varepsilon_s}{d}$$

Where ε_c and ε_s are respectively the deformations measured in correspondence with compressed concrete at extrados and tensile steel at intrados, while d represents the working depth of the section, corresponding to the distance between extrados concrete surface and the centroid of lower rebars.
In the diagrams, the tangent to the loading-unloading cycles is also depicted, in red.

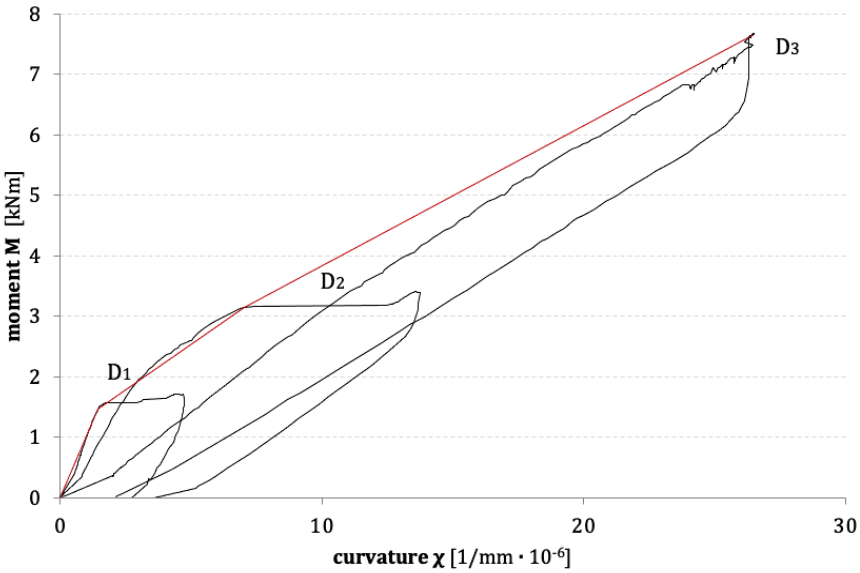
8
7
6
5
4
3
2
1
0
moment M [kNm]
D1
D2
D3
0
10
20
30
curvature χ [1/mm · 10-6]

(a) CB

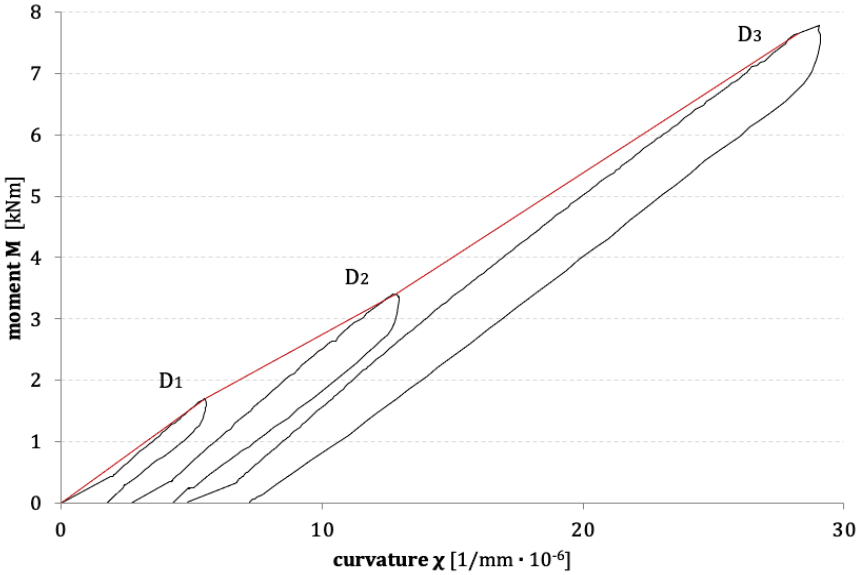
8
7
6
5
4
3
2
1
0
moment M [kNm]
D1
D2
D3
0
10
20
30
curvature χ [1/mm · 10-6]

(b) B1

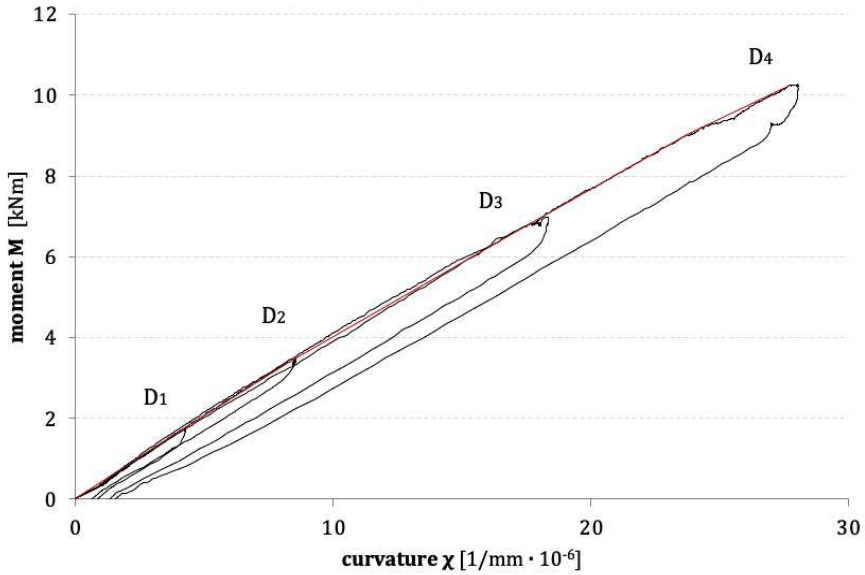

(c) B_2

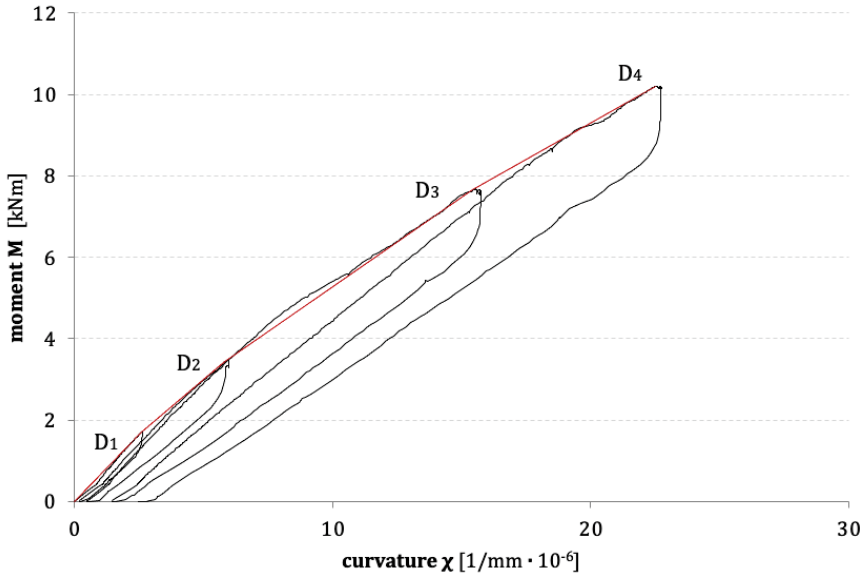

(d) B_3

Figure 5.13 – Experimental diagram moment, M, vs curvature, χ, at midspan section of RC beams; (a) specimen CB, (b) specimen B_1, (c) specimen B_2, (d) specimen B_3

5.5. Results from dynamic tests

At each load step, therefore at each level of damage, the beam models were subjected to dynamic tests, impacting the structure with an instrumented hammer in a fixed point and measuring the response with an accelerometer in nine different positions. The acquisition and analysis of the modal parameters (natural frequencies) allows to evaluate the dynamic response of the experimental beam models at the various levels of damage, therefore, to monitor the effect of FRP strengthening.

The experimental vibration results were obtained through Frequency Response Functions (FRFs), from 9 diagrams, one for each position of accelerometer.
From experimental vibration tests, carried out on all specimens, the natural frequency vibrations for the first four modes of the beams were determined, considering frequency values in correspondence of which a consistent acceleration is recorded, that is in correspondence of peaks.
The program used to record the experimental data is able to identify the most stable frequencies, so you can choose the most correct frequency value.
It is useful to consider a function called "consistency", which allows to control over the results. In order to evaluate the reliability of the measurement it is worth-while to check that the value of the consistency is near one.

5.5.1. Results of beam specimen in free-free ends conditions

The experimental FRF diagrams at different damage state D_i i=0,…,4 with measures of vibration recorded by the accelerometer in chosen points $Mark_i$ for each specimen in free-free ends are contained in Figure 5.14. The *x* axis contains the frequency values in Hertz (Hz), the reported frequency range has been cut to report only the first four peaks for each D_i, in the *y* axis there is the amplitude of FRF (m/s^2) in logarithmic scale.
It is possible to observe the shift of the diagrams at various steps D_i with reduction of the frequency values due to increasing concrete cracking damage.

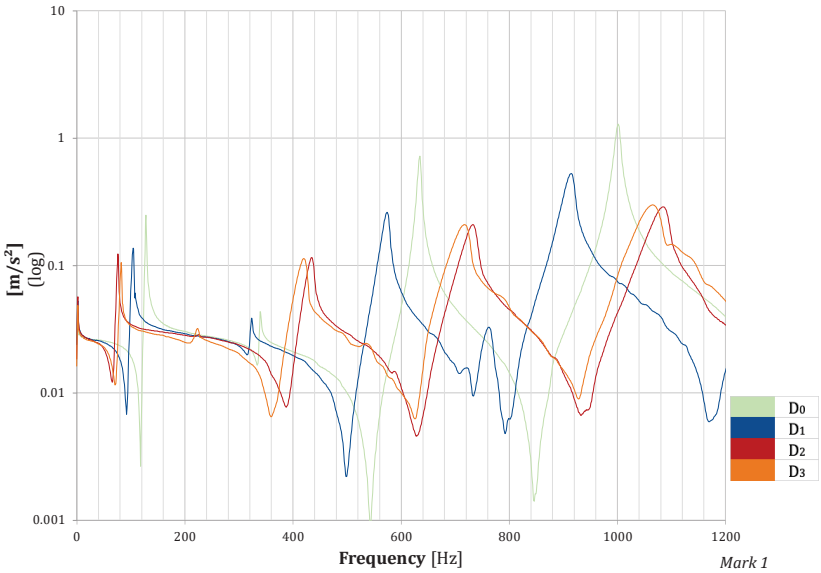
10
1
0.1
0.01
0.001
[m/s²] (log)
0
200
400
600
800
1000
1200
Frequency [Hz]
D0
D1
D2
D3

Mark 1

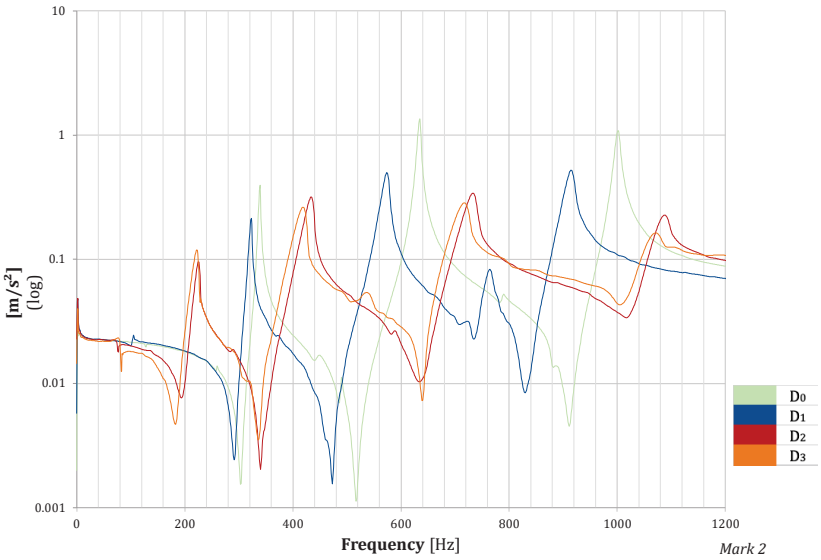
10
1
0.1
0.01
0.001
[m/s²] (log)
0
200
400
600
800
1000
1200
Frequency [Hz]
D0
D1
D2
D3

Mark 2

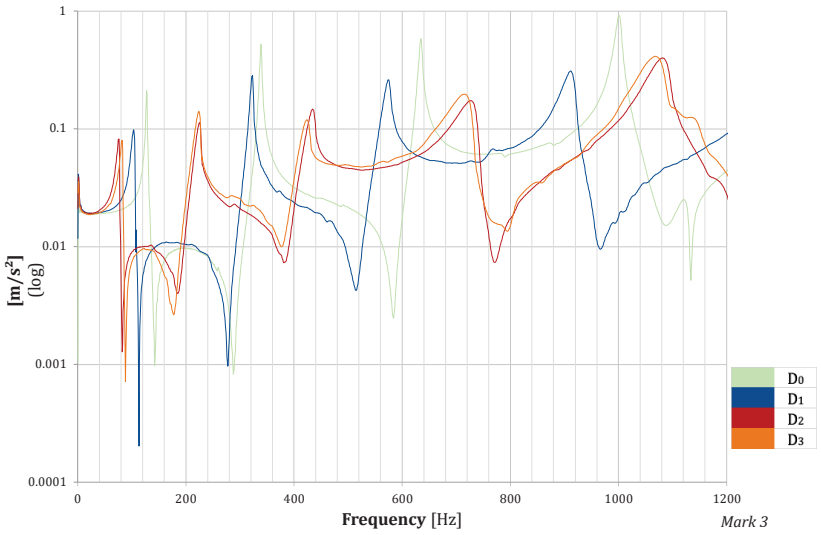
1
0.1
0.01
0.001
0.0001
[m/s²] (log)
0
200
400
600
800
1000
1200
Frequency [Hz]
D0
D1
D2
D3

Mark 3

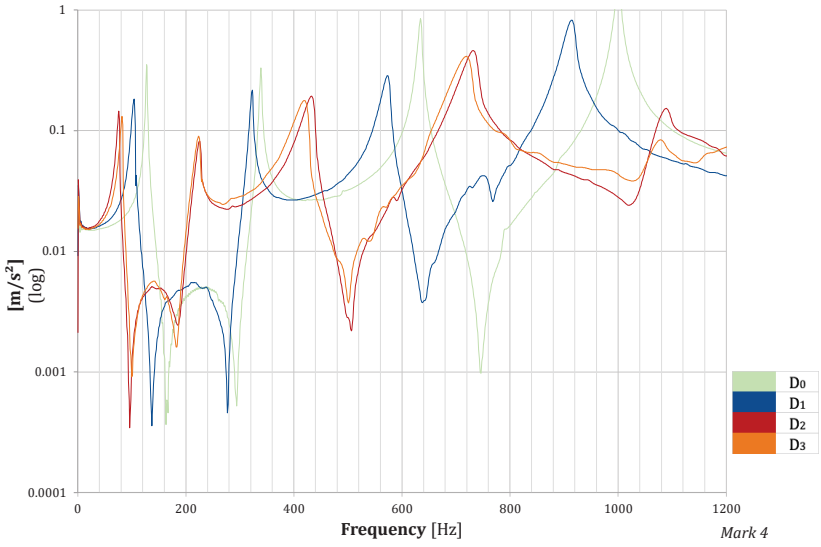
1
0.1
0.01
0.001
0.0001
[m/s²] (log)
0
200
400
600
800
1000
1200
Frequency [Hz]
D0
D1
D2
D3

Mark 4

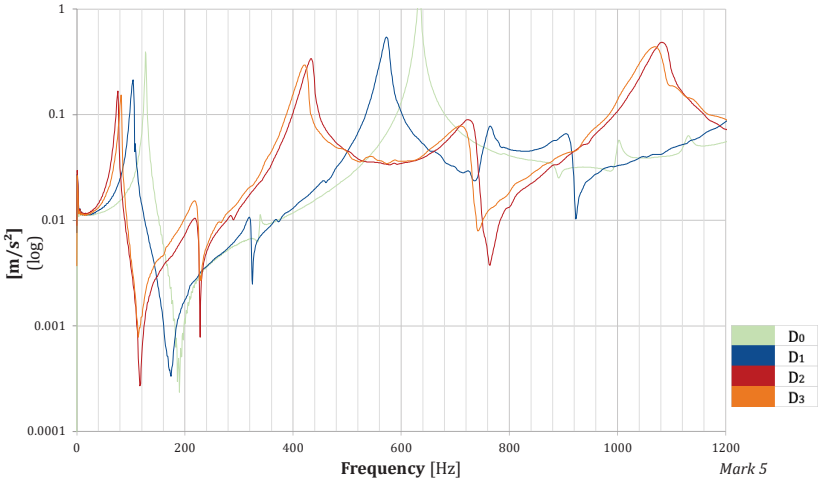
1
0.1
0.01
0.001
0.0001
[m/s²] (log)
0
200
400
600
800
1000
1200
Frequency [Hz]
D0
D1
D2
D3

Mark 5

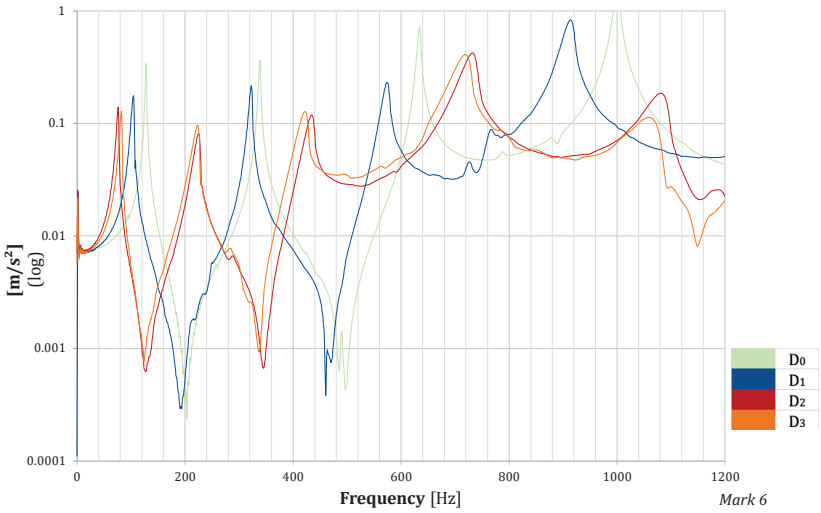
1
0.1
0.01
0.001
0.0001
[m/s²] (log)
0
200
400
600
800
1000
1200
Frequency [Hz]
D0
D1
D2
D3

Mark 6

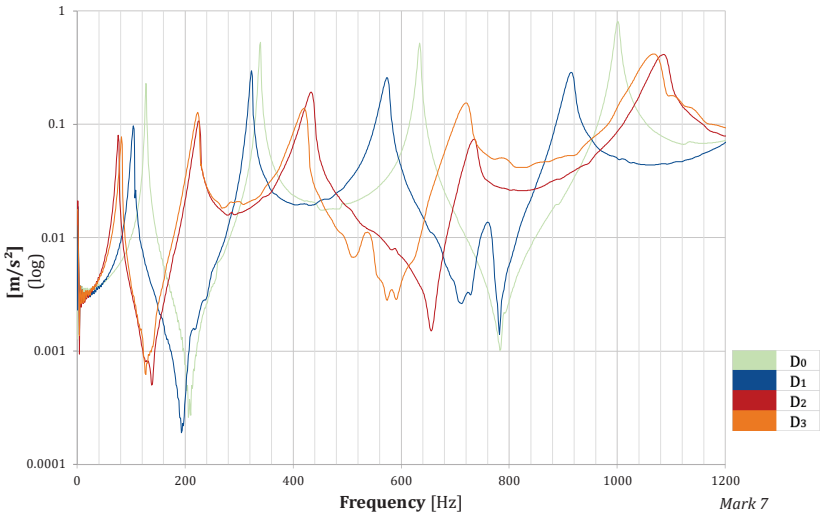
1
0.1
0.01
0.001
0.0001
[m/s²] (log)
0
200
400
600
800
1000
1200
Frequency [Hz]
D0
D1
D2
D3

Mark 7

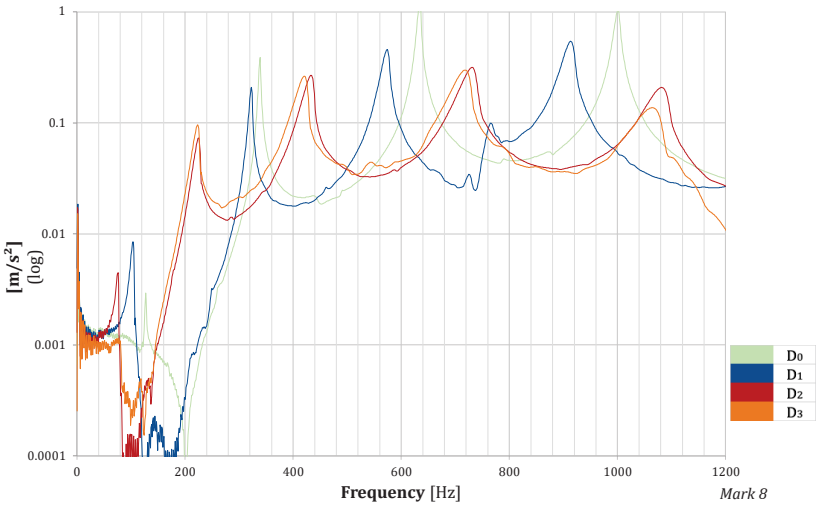
1
0.1
0.01
0.001
0.0001
[m/s²] (log)
0
200
400
600
800
1000
1200
Frequency [Hz]
D0
D1
D2
D3

Mark 8

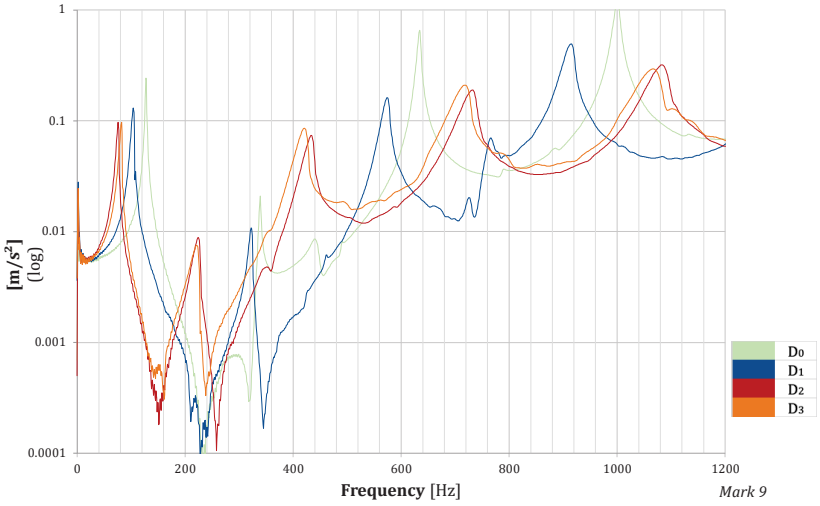
1
0.1
0.01
0.001
0.0001
[m/s²] (log)
0
200
400
600
800
1000
1200
Frequency [Hz]
Mark 9
D0
D1
D2
D3

(a) CB

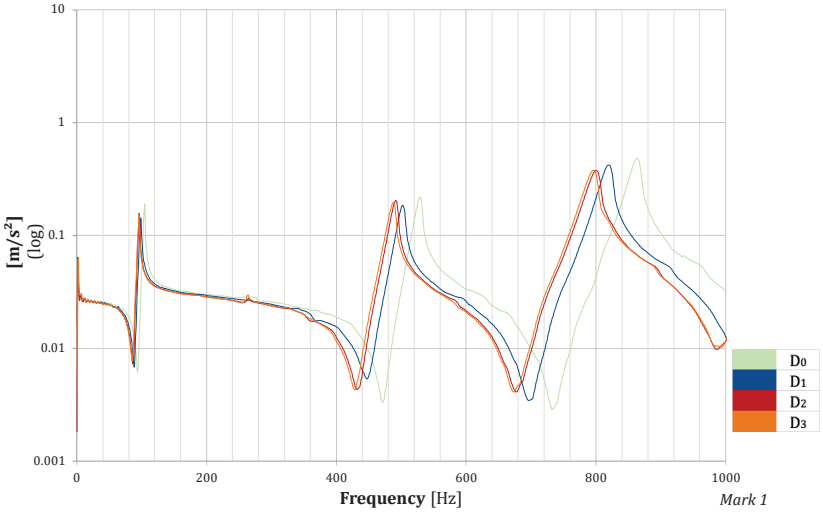
10
1
0.1
0.01
0.001
[m/s²] (log)
0
200
400
600
800
1000
Frequency [Hz]
Mark 1
D0
D1
D2
D3

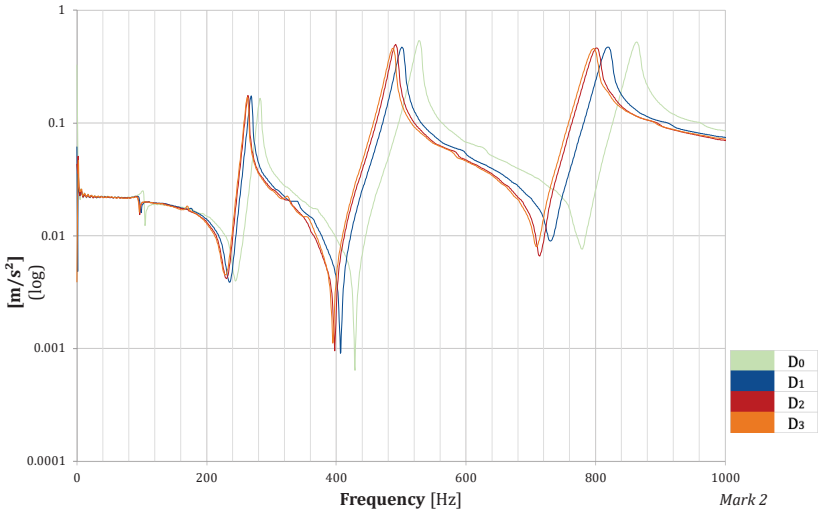
1
0.1
0.01
0.001
0.0001
[m/s²] (log)
0
200
400
600
800
1000
Frequency [Hz]
D0
D1
D2
D3

Mark 2

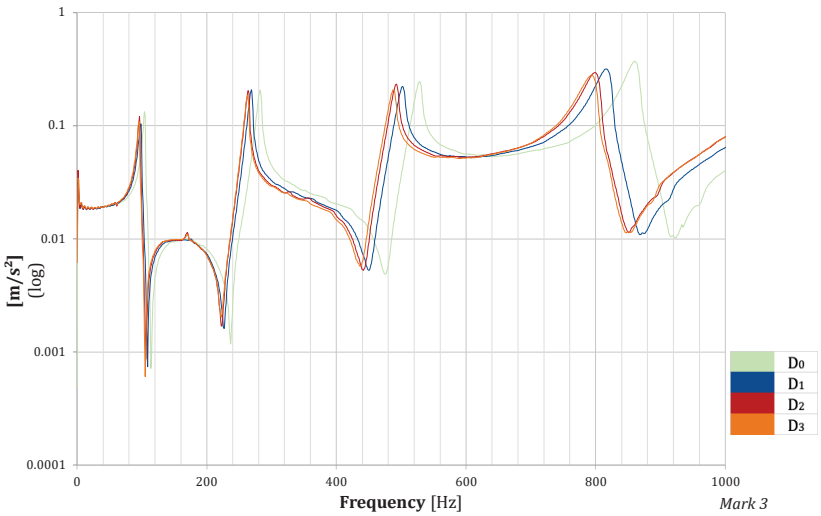
1
0.1
0.01
0.001
0.0001
[m/s²] (log)
0
200
400
600
800
1000
Frequency [Hz]
D0
D1
D2
D3

Mark 3

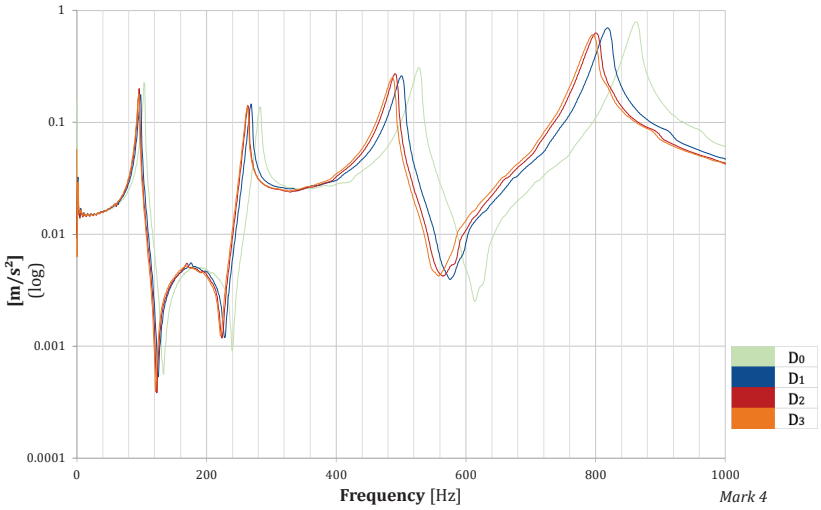
1
0.1
0.01
0.001
0.0001
[m/s²] (log)
0
200
400
600
800
1000
Frequency [Hz]
D0
D1
D2
D3

Mark 4

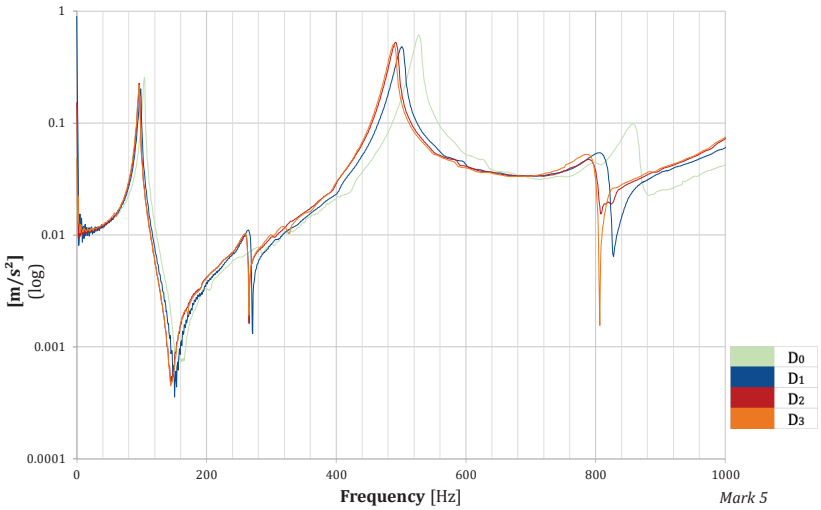
1
0.1
0.01
0.001
0.0001
[m/s²] (log)
0
200
400
600
800
1000
Frequency [Hz]
D0
D1
D2
D3

Mark 5

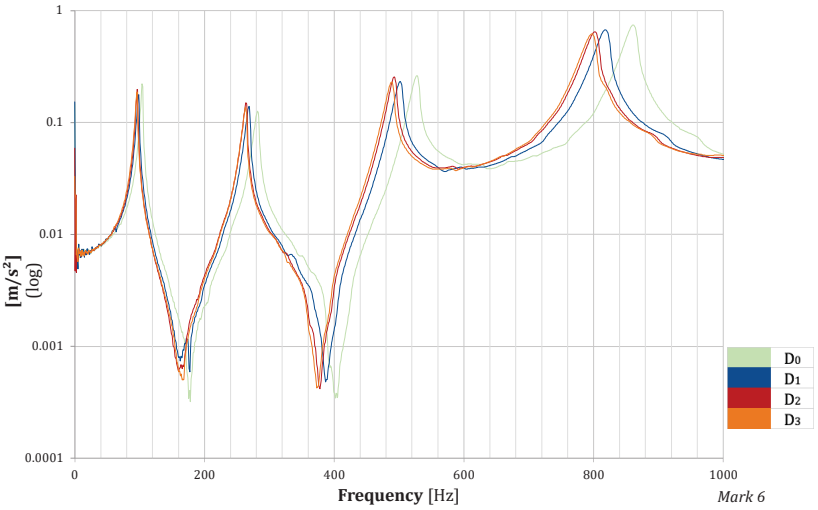
1
0.1
0.01
0.001
0.0001
[m/s²] (log)
0
200
400
600
800
1000
Frequency [Hz]
D0
D1
D2
D3

Mark 6

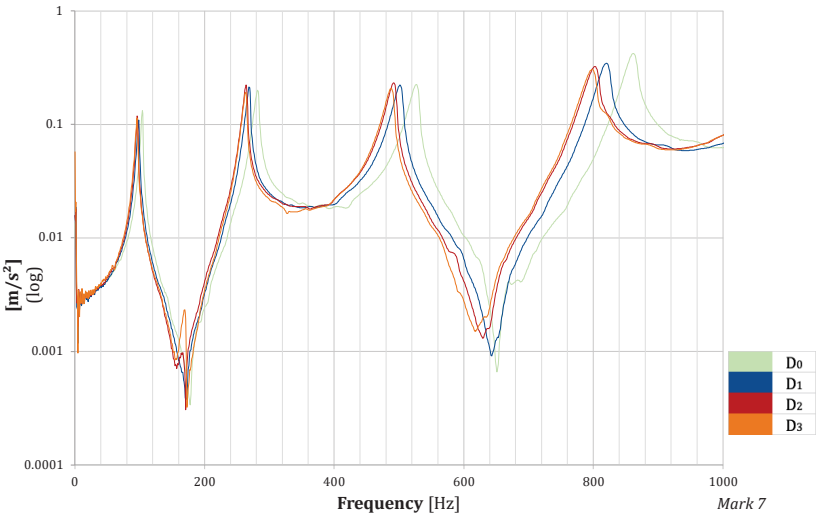
1
0.1
0.01
0.001
0.0001
[m/s²] (log)
0
200
400
600
800
1000
Frequency [Hz]
D0
D1
D2
D3

Mark 7

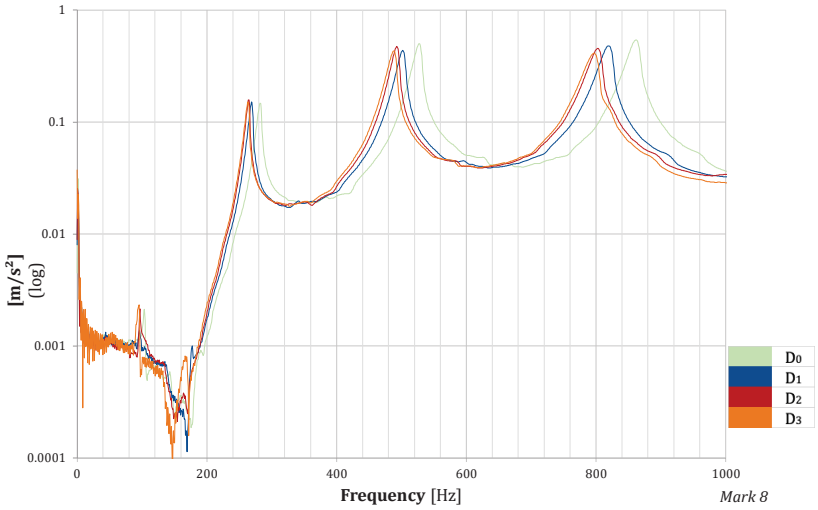
1
0.1
0.01
0.001
0.0001
[m/s²] (log)
0
200
400
600
800
1000
Frequency [Hz]
D0
D1
D2
D3
Mark 8

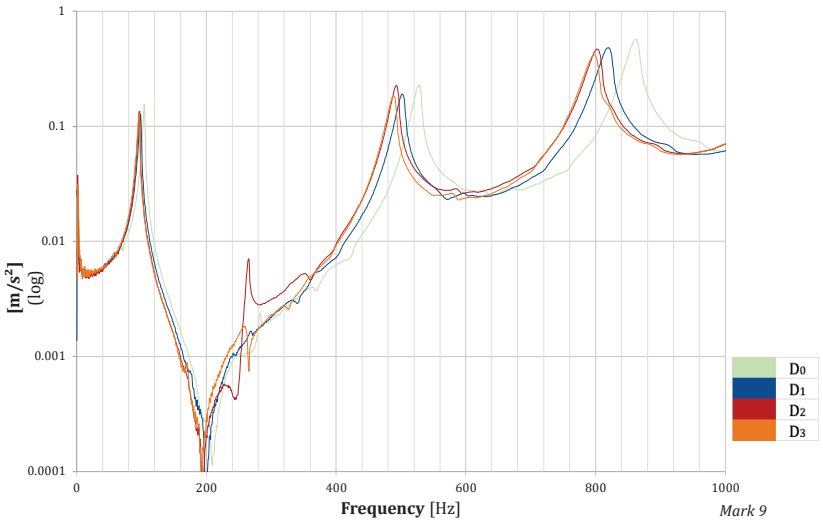
1
0.1
0.01
0.001
0.0001
[m/s²] (log)
0
200
400
600
800
1000
Frequency [Hz]
D0
D1
D2
D3
Mark 9

(b) B_1

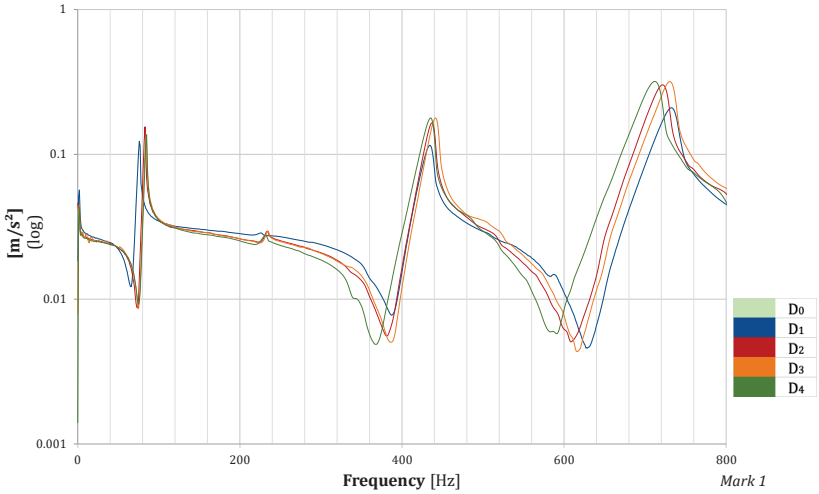
1
0.1
0.01
0.001
[m/s²] (log)
0
200
400
600
800
Frequency [Hz]
D0
D1
D2
D3
D4

Mark 1

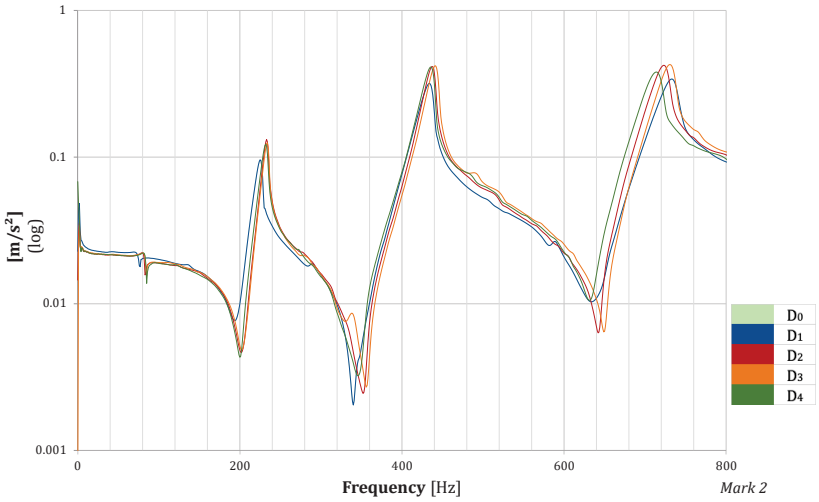
1
0.1
0.01
0.001
[m/s²] (log)
0
200
400
600
800
Frequency [Hz]
D0
D1
D2
D3
D4

Mark 2

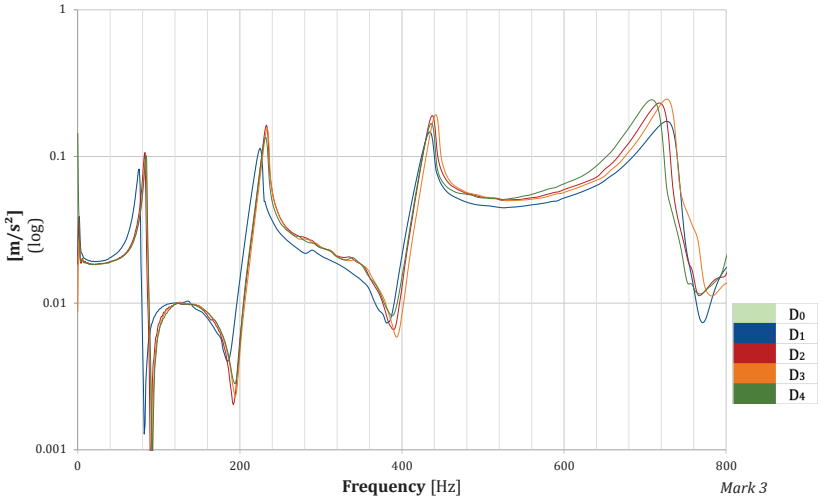
1
0.1
0.01
0.001
[m/s²] (log)
0
200
400
600
800
Frequency [Hz]
D0
D1
D2
D3
D4

Mark 3

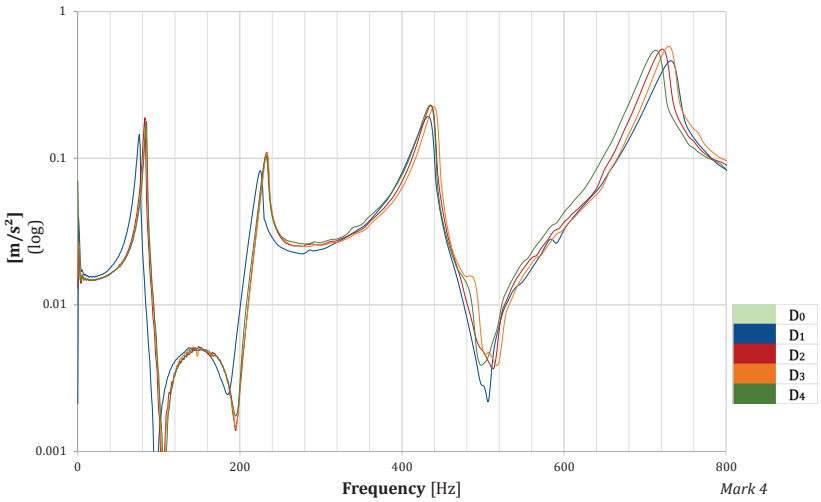
1
0.1
0.01
0.001
[m/s²] (log)
0
200
400
600
800
Frequency [Hz]
D0
D1
D2
D3
D4

Mark 4

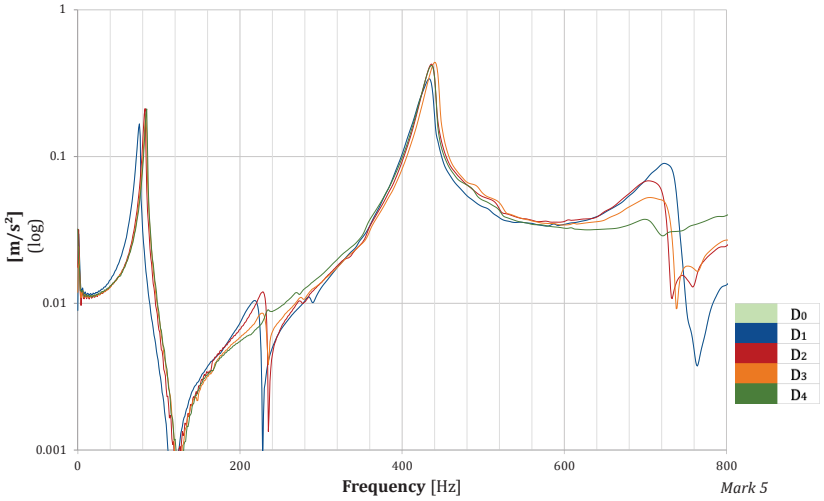
1
0.1
0.01
0.001
[m/s²] (log)
0
200
400
600
800
Frequency [Hz]
D0
D1
D2
D3
D4

Mark 5

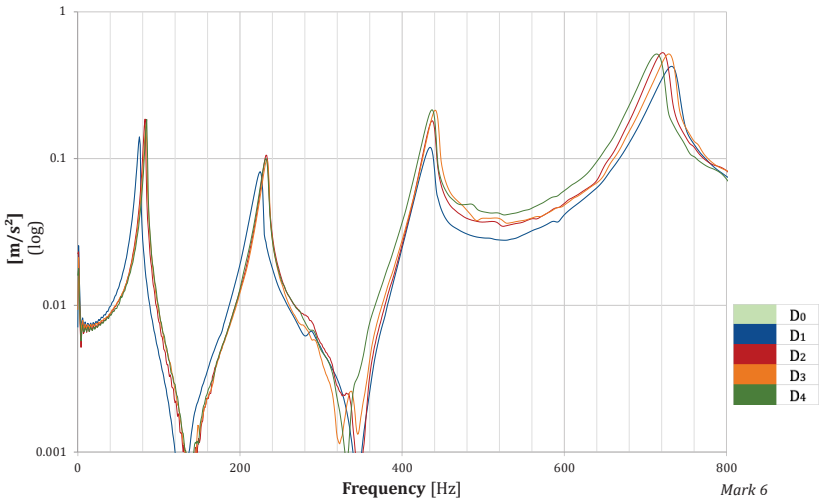
1
0.1
0.01
0.001
[m/s²] (log)
0
200
400
600
800
Frequency [Hz]
D0
D1
D2
D3
D4

Mark 6

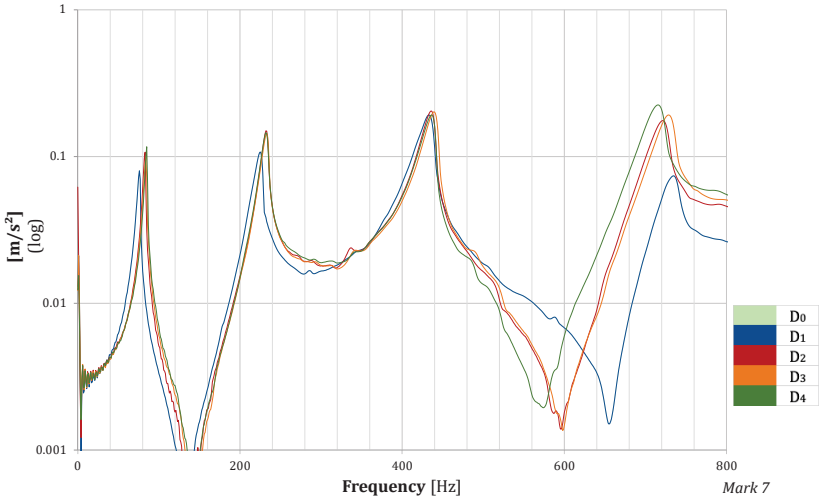
1
0.1
0.01
0.001
[m/s²] (log)
0
200
400
600
800
Frequency [Hz]
D0
D1
D2
D3
D4

Mark 7

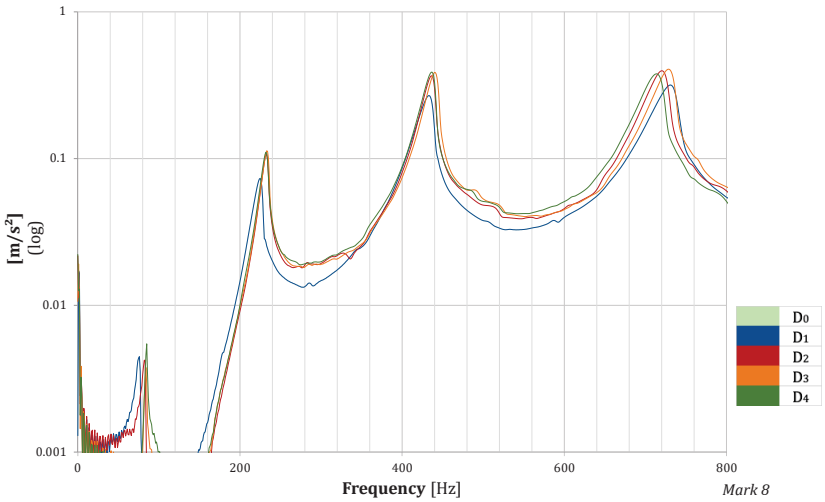
1
0.1
0.01
0.001
[m/s²] (log)
0
200
400
600
800
Frequency [Hz]
D0
D1
D2
D3
D4

Mark 8

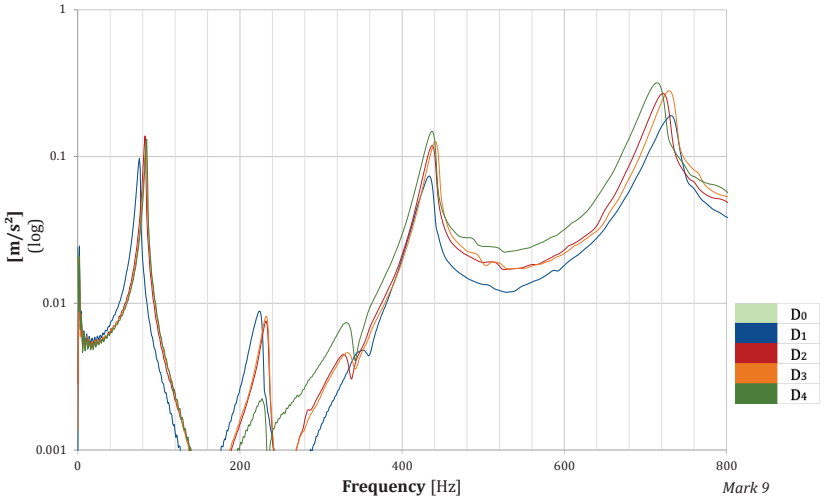
1
0.1
0.01
0.001
[m/s²] (log)
0
200
400
600
800
Frequency [Hz]
Mark 9
D0
D1
D2
D3
D4

(c) B_2

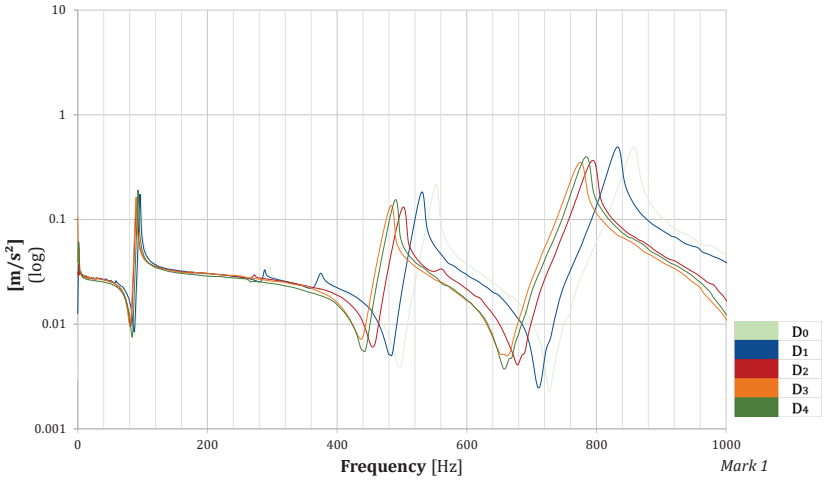
10
1
0.1
0.01
0.001
[m/s²] (log)
0
200
400
600
800
1000
Frequency [Hz]
Mark 1
D0
D1
D2
D3
D4

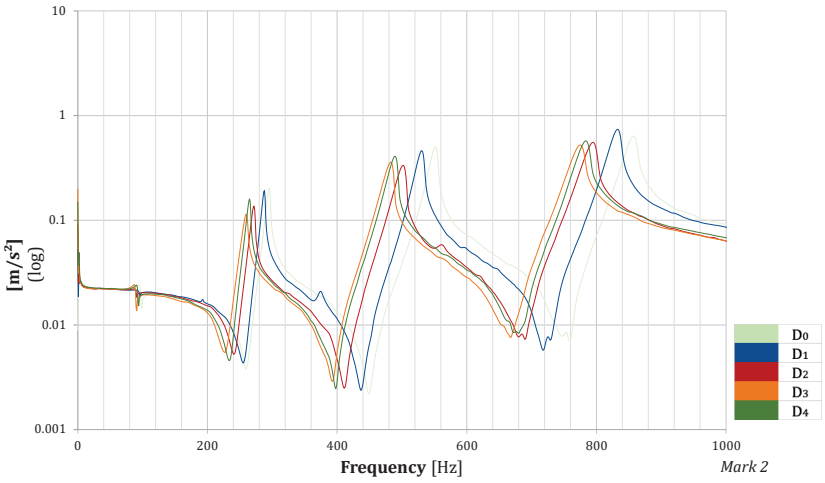
10
1
0.1
0.01
0.001
[m/s²] (log)
0
200
400
600
800
1000
Frequency [Hz]
D0
D1
D2
D3
D4

Mark 2

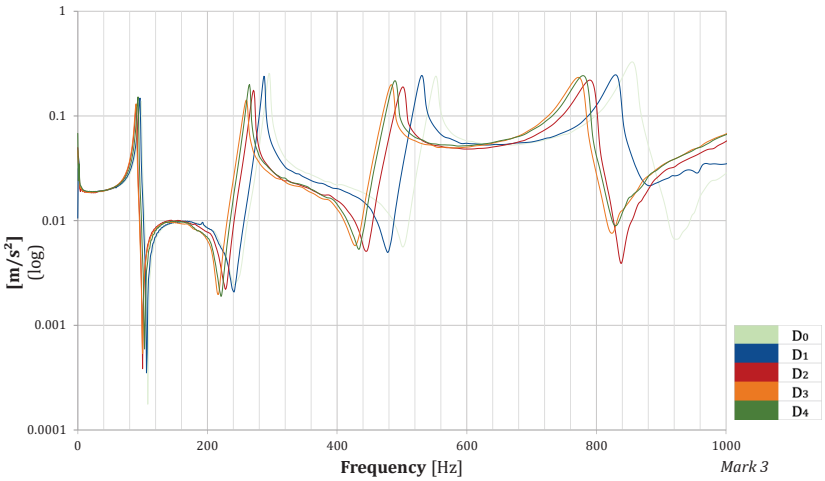
1
0.1
0.01
0.001
0.0001
[m/s²] (log)
0
200
400
600
800
1000
Frequency [Hz]
D0
D1
D2
D3
D4

Mark 3

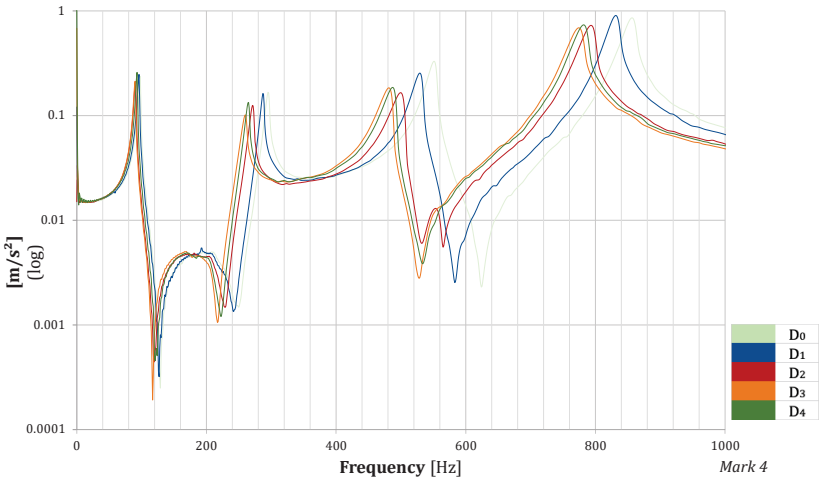
1
0.1
0.01
0.001
0.0001
[m/s²] (log)
0
200
400
600
800
1000
Frequency [Hz]
D0
D1
D2
D3
D4

Mark 4

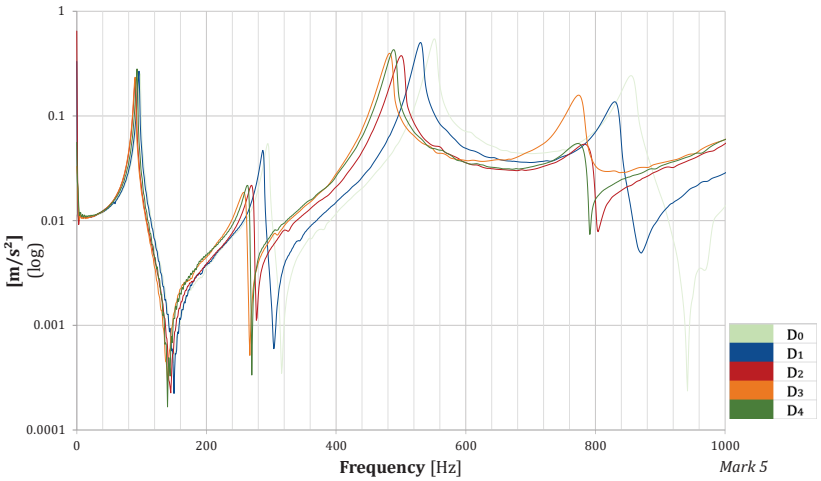
1
0.1
0.01
0.001
0.0001
[m/s²] (log)
0
200
400
600
800
1000
Frequency [Hz]
D0
D1
D2
D3
D4

Mark 5

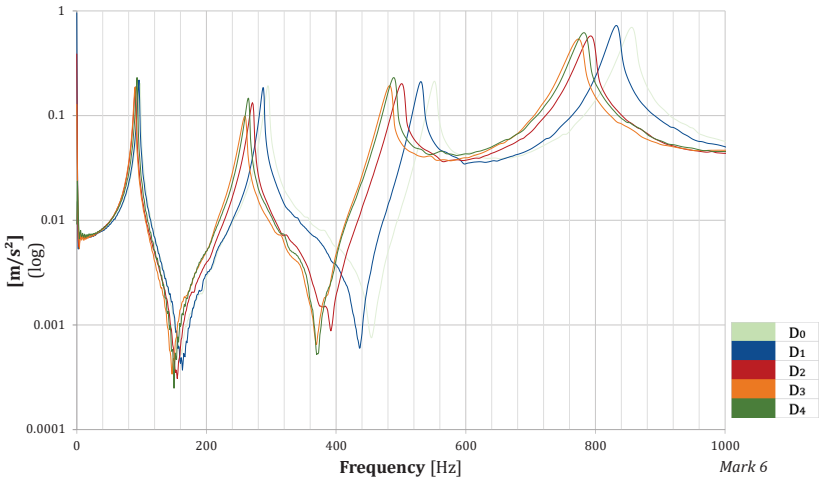
1
0.1
0.01
0.001
0.0001
[m/s²] (log)
0
200
400
600
800
1000
Frequency [Hz]
D0
D1
D2
D3
D4

Mark 6

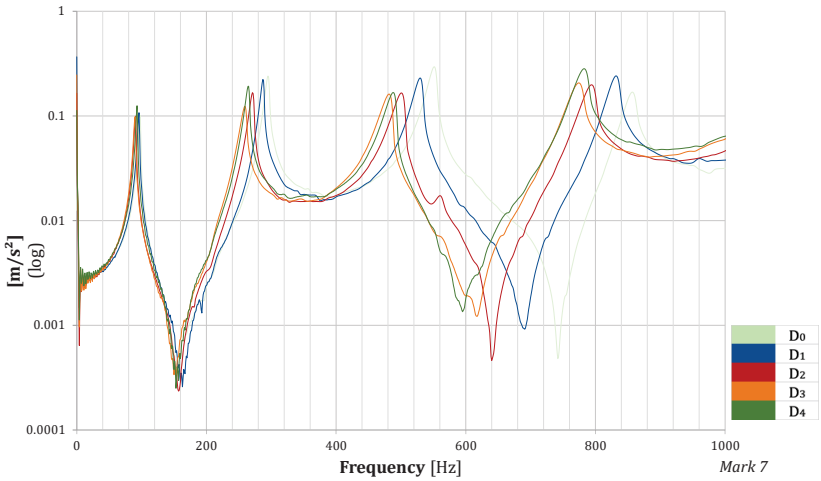
1
0.1
0.01
0.001
0.0001
[m/s²] (log)
0
200
400
600
800
1000
Frequency [Hz]
D0
D1
D2
D3
D4

Mark 7

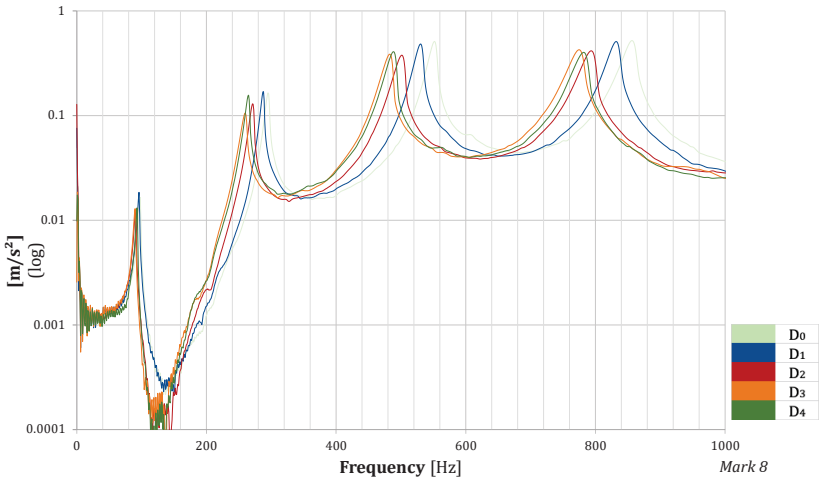

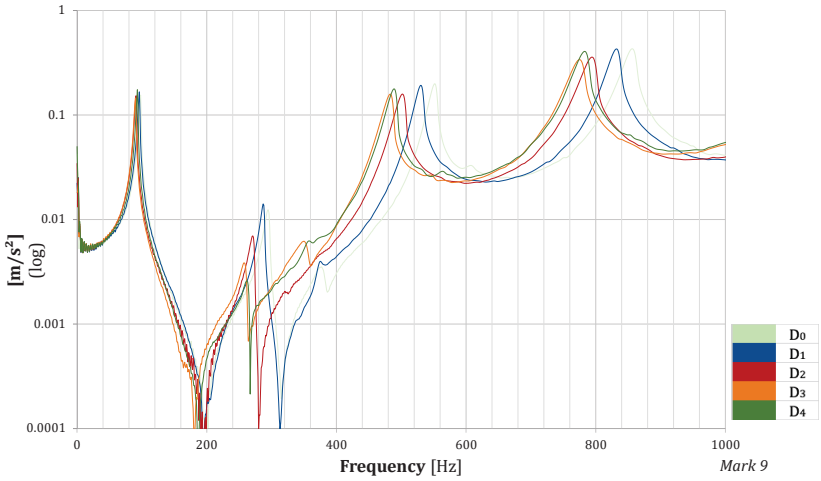

(d) B_3

Figure 5.14 – Experimental FRF diagrams at different damage D_i=0,…,4, at Mark i, for each RC beam; (a) specimen CB, (b) specimen B_1, (c) specimen B_2, (d) specimen B_3 in free-free ends conditions

The main experimental frequency values data obtained from the analysis of free vibration for un-strengthened beam CB and strengthened beams B_1, B_2, B_3 at various damage step D_i are contained in Table 5.3.
Table 5.3 shows the average frequency recorded experimentally at each of the accelerometer positions.

Table 5.3 – Experimental frequency values at different damage degree D_i for each specimen in free-free ends conditions

CB				
Damage degree	**f_1 (Hz)**	**f_2 (Hz)**	**f_3 (Hz)**	**f_4 (Hz)**
D_0	127.13	339.00	634.11	1001.00
D_1	103.50	322.75	573.44	915.25
D_2	75.88	225.14	433.56	731.44
D_3	82.00	222.43	421.33	719.22
B1				
Damage degree	**f_1 (Hz)**	**f_2 (Hz)**	**f_3 (Hz)**	**f_4 (Hz)**
D_0[2]	102.95	275.84	520.17	852.29
D_1	96.35	265.25	502.64	809.60
D_2	95.14	261.02	493.88	790.80
D_3	94.49	258.23	489.14	785.08
B2				
Damage degree	**f_1 (Hz)**	**f_2 (Hz)**	**f_3 (Hz)**	**f_4 (Hz)**
D_0[2]	75.88	224.71	434.56	733.38
D_1	76.00	224.71	433.89	730.33
D_2	83.00	232.60	436.22	721.25
D_3	84.00	233.50	439.78	728.50
D_4	84.86	231.67	436.11	713.75
B3				
Damage degree	**f_1 (Hz)**	**f_2 (Hz)**	**f_3 (Hz)**	**f_4 (Hz)**
D_0[2]	96.56	296.00	554.78	861.67
D_1	94.88	287.88	533.89	836.56
D_2	89.25	274.88	504.33	797.78
D_3	89.00	260.63	485.89	780.33
D_4	92.25	264.88	491.56	787.22

The recorded experimental frequency values for the four examined vibration mode, for each damage state, were plotted in Figure 5.15.

[2] Undamaged condition is at the beginning of vibration test for strengthened beams.

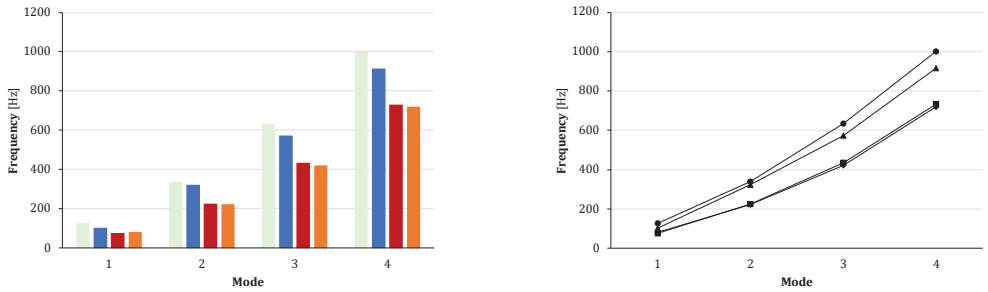

(a) CB

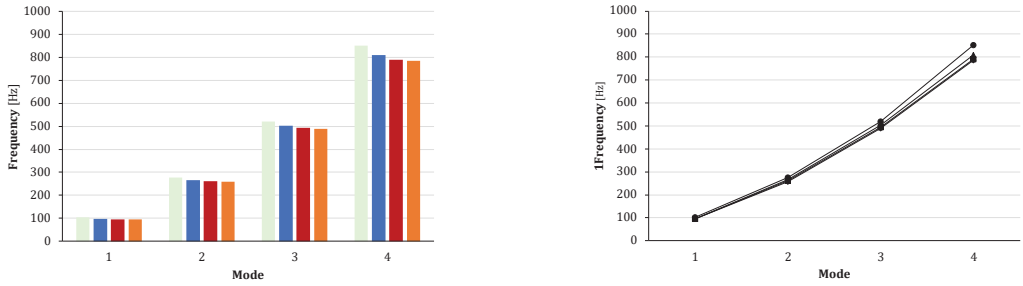

(b) B_1

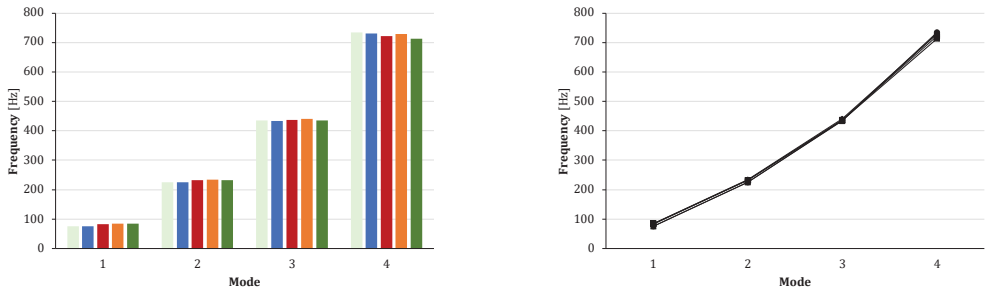

(c) B_2

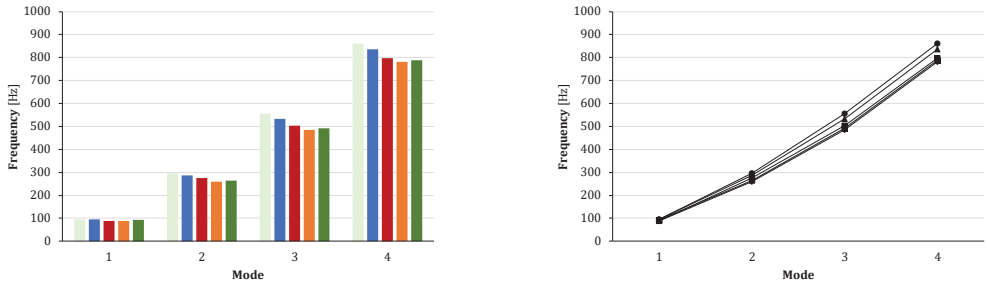

(d) B_3

Figure 5.15 – Graphic representation of the experimental natural frequencies and of their variation for each mode of vibration for each RC beam; (a) specimen CB, (b) specimen B_1, (c) specimen B_2, (d) specimen B_3 in free-free ends conditions

From the observation of the results, it is noted that as the damage state increases, a lowering of the frequencies is recorded; the reduction is accentuated in the un-strengthened CB beam model, while it is less evident in the NSM strengthened beam samples.

5.5.2. Results of beam specimen in hinged ends conditions

The experimental FRF diagrams at different damage state D_i i=0,…,4 with measures of vibration recorded by the accelerometer in chosen points $Mark_i$ for each specimen in hinged ends are contained in Figure 5.16. The *x* axis contains the frequency values in Hertz (Hz), the reported frequency range has been cut to report only the first four peaks for each D_i, in the *y* axis there is the amplitude of FRF (m/s^2) in logarithmic scale.
Numerous peaks can be observed from the diagrams, not always corresponding to the natural frequencies of the tested samples; for the identification of the natural vibration frequencies, the frequency values with greater amplitude were selected, considering those closest to the theoretically calculated values.
It is also clear how the constraint system affects the dynamic response recording: the results are less noticeable and more contaminated.

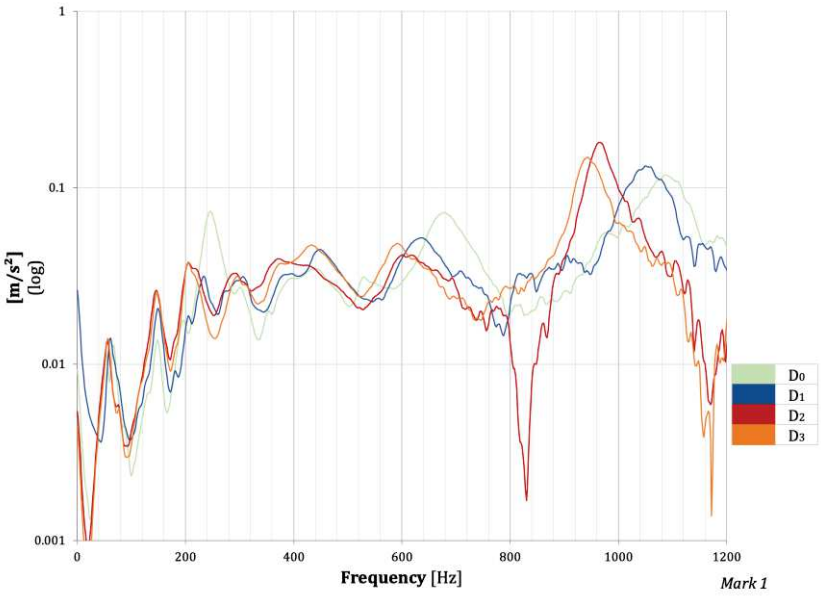
1
0.1
0.01
0.001
[m/s²] (log)
0
200
400
600
800
1000
1200
Frequency [Hz]
D0
D1
D2
D3
Mark 1

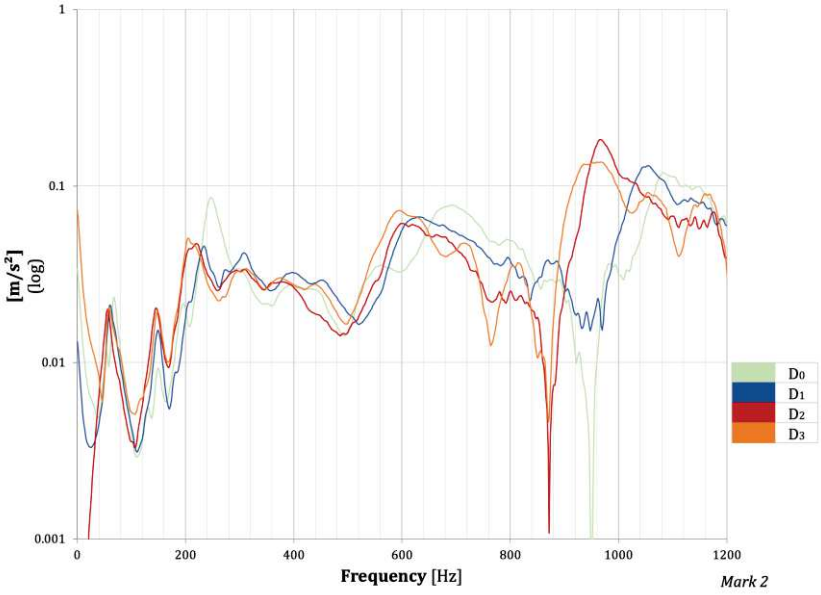
1
0.1
0.01
0.001
[m/s²] (log)
0
200
400
600
800
1000
1200
Frequency [Hz]
D0
D1
D2
D3
Mark 2

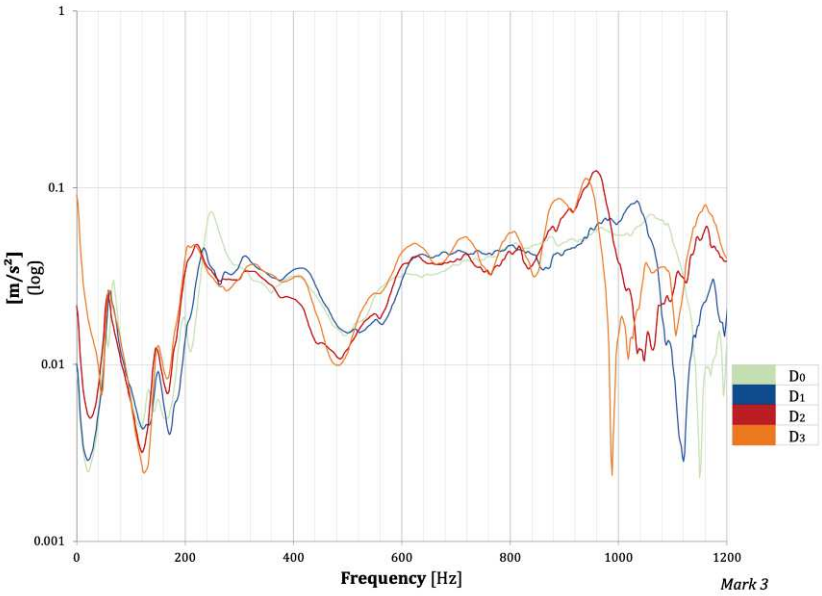
1
0.1
0.01
0.001
[m/s²] (log)
0
200
400
600
800
1000
1200
Frequency [Hz]
D0
D1
D2
D3
Mark 3

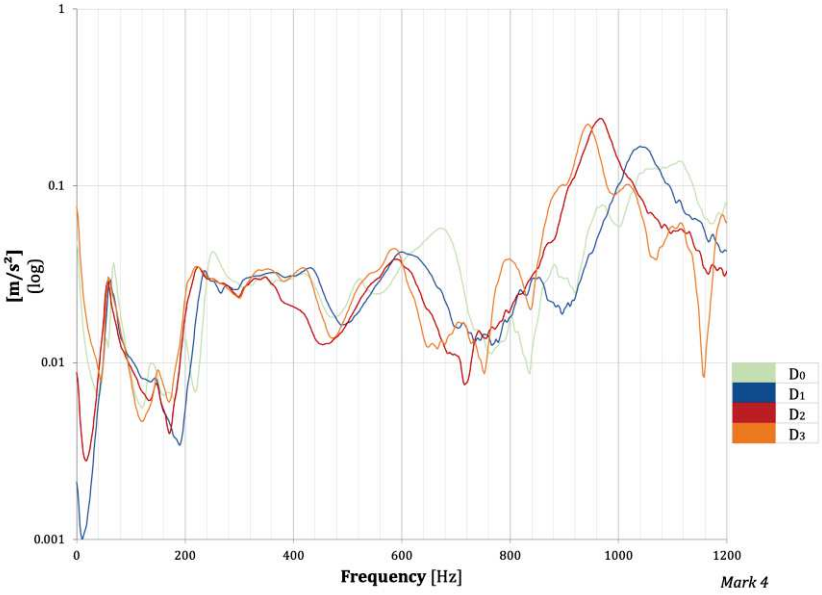
1
0.1
0.01
0.001
[m/s²] (log)
0
200
400
600
800
1000
1200
Frequency [Hz]
D0
D1
D2
D3
Mark 4

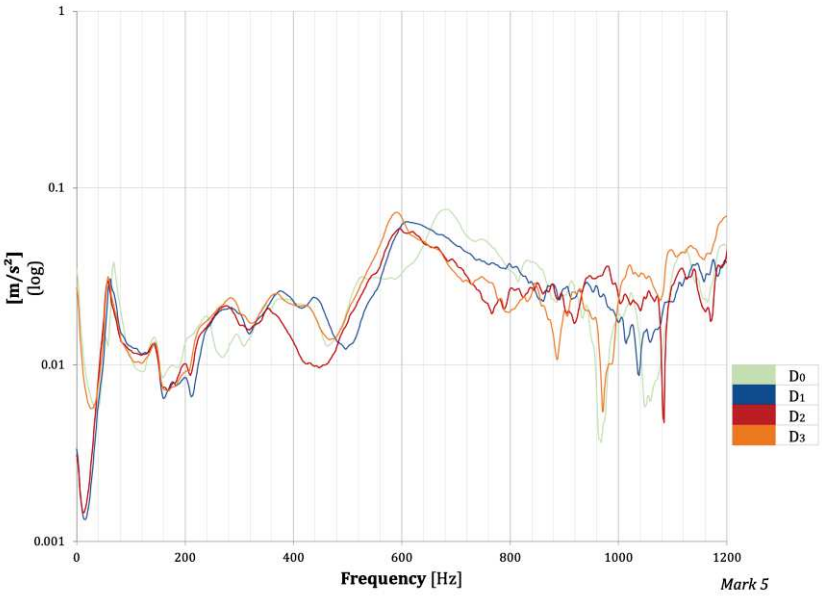
1
0.1
0.01
0.001
[m/s²] (log)
0
200
400
600
800
1000
1200
Frequency [Hz]
D0
D1
D2
D3
Mark 5

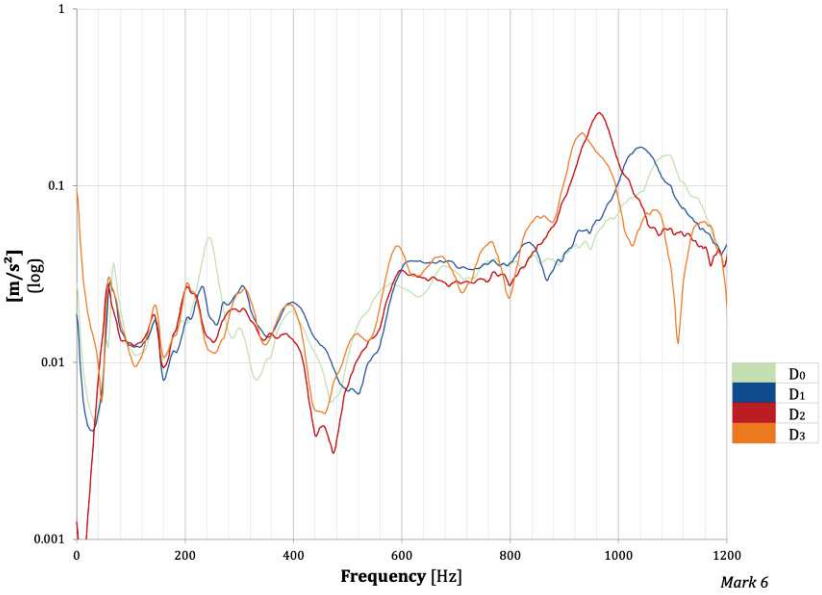
1
0.1
0.01
0.001
[m/s²] (log)
0
200
400
600
800
1000
1200
Frequency [Hz]
D0
D1
D2
D3
Mark 6

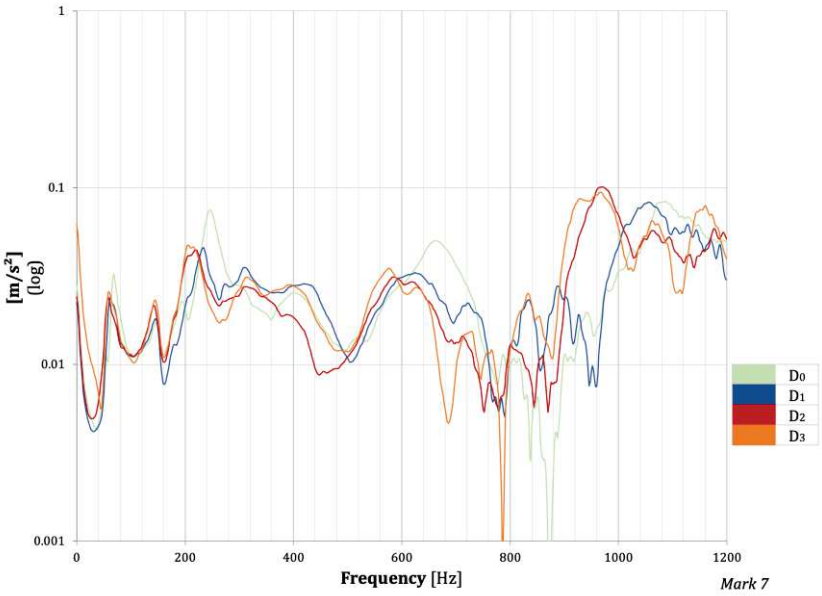
1
0.1
0.01
0.001
[m/s²] (log)
0
200
400
600
800
1000
1200
Frequency [Hz]
D0
D1
D2
D3
Mark 7

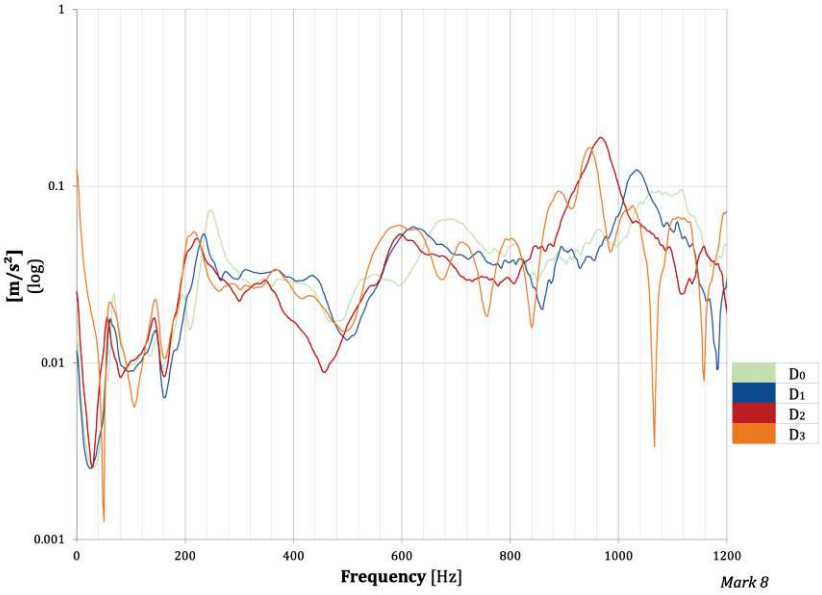
1
0.1
0.01
0.001
[m/s²] (log)
0
200
400
600
800
1000
1200
Frequency [Hz]
D0
D1
D2
D3
Mark 8

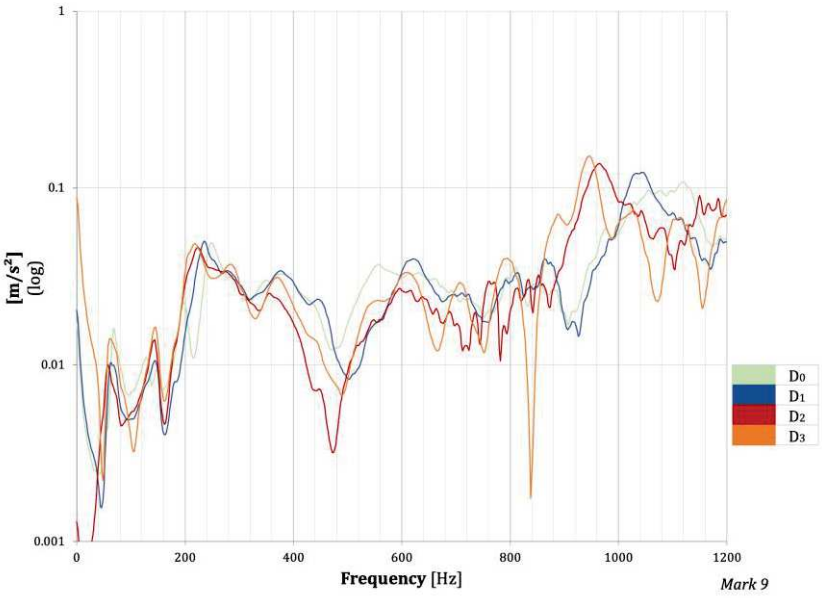
1
0.1
0.01
0.001
[m/s²] (log)
0
200
400
600
800
1000
1200
Frequency [Hz]
Mark 9
D0
D1
D2
D3

(a) CB

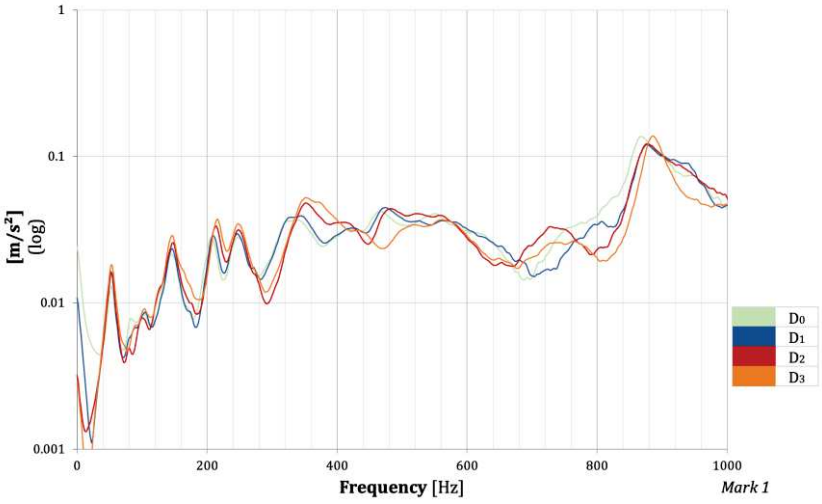
1
0.1
0.01
0.001
[m/s²] (log)
0
200
400
600
800
1000
Frequency [Hz]
Mark 1
D0
D1
D2
D3

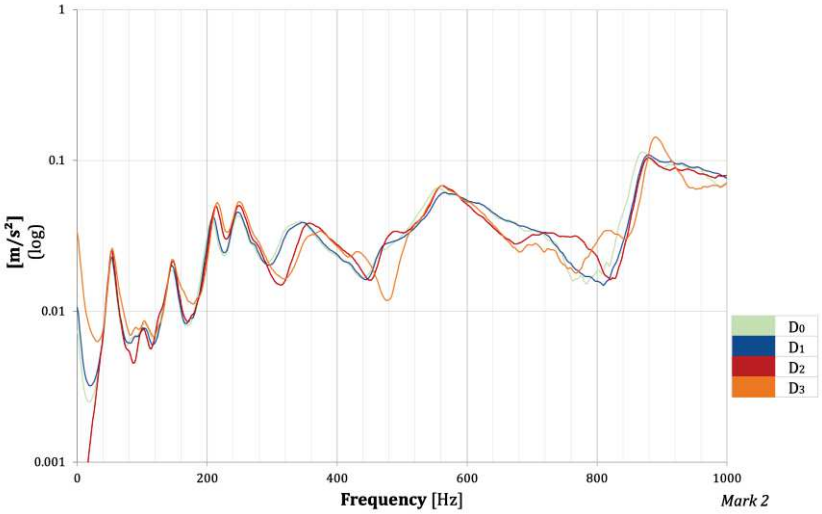
1
0.1
0.01
0.001
[m/s²] (log)
0
200
400
600
800
1000
Frequency [Hz]
Mark 2
D0
D1
D2
D3

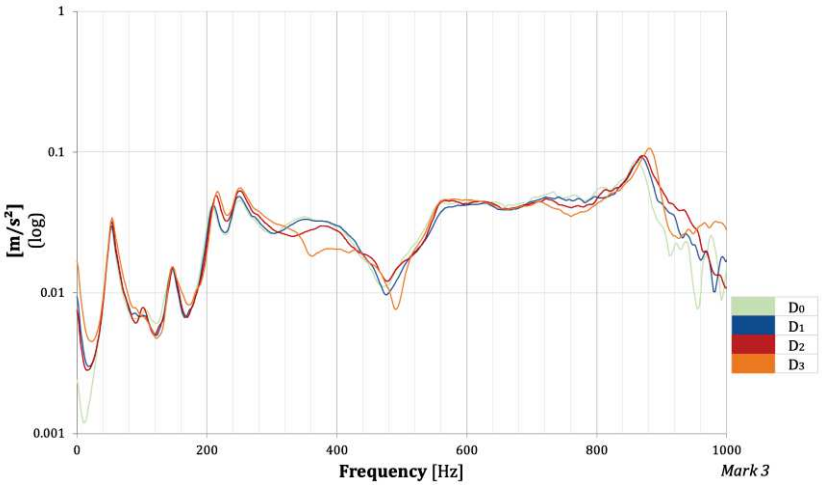
1
0.1
0.01
0.001
[m/s²] (log)
0
200
400
600
800
1000
Frequency [Hz]
Mark 3
D0
D1
D2
D3

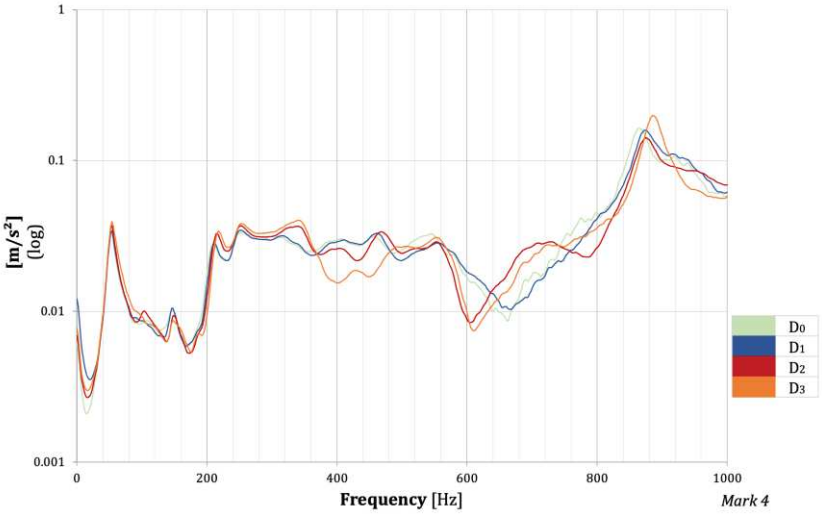
1
0.1
0.01
0.001
[m/s²] (log)
0
200
400
600
800
1000
Frequency [Hz]
D0
D1
D2
D3
Mark 4

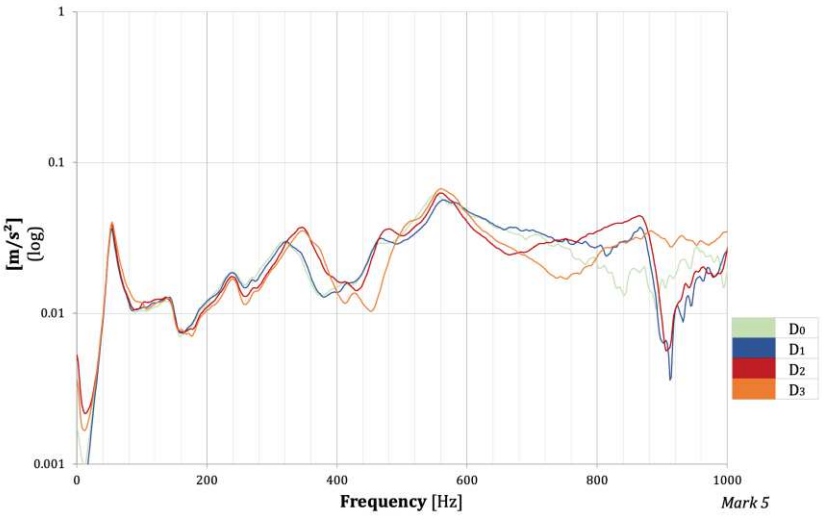
1
0.1
0.01
0.001
[m/s²] (log)
0
200
400
600
800
1000
Frequency [Hz]
D0
D1
D2
D3
Mark 5

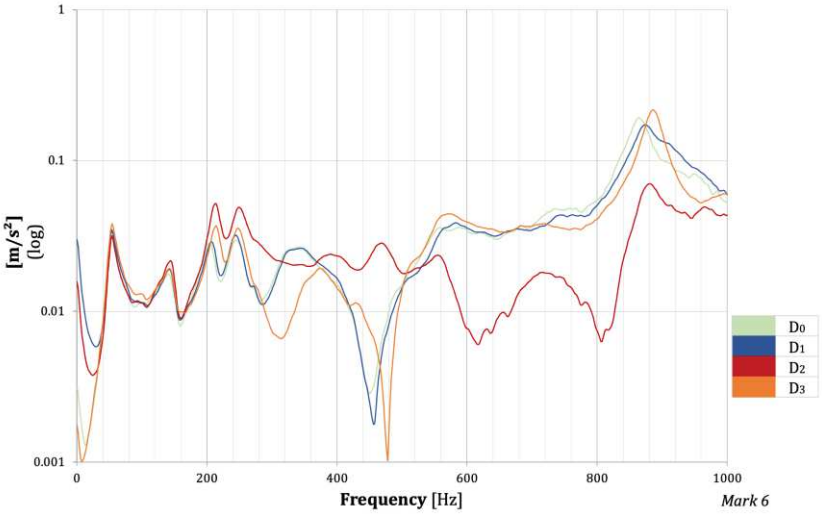
1
0.1
0.01
0.001
[m/s²] (log)
0
200
400
600
800
1000
Frequency [Hz]
D0
D1
D2
D3
Mark 6

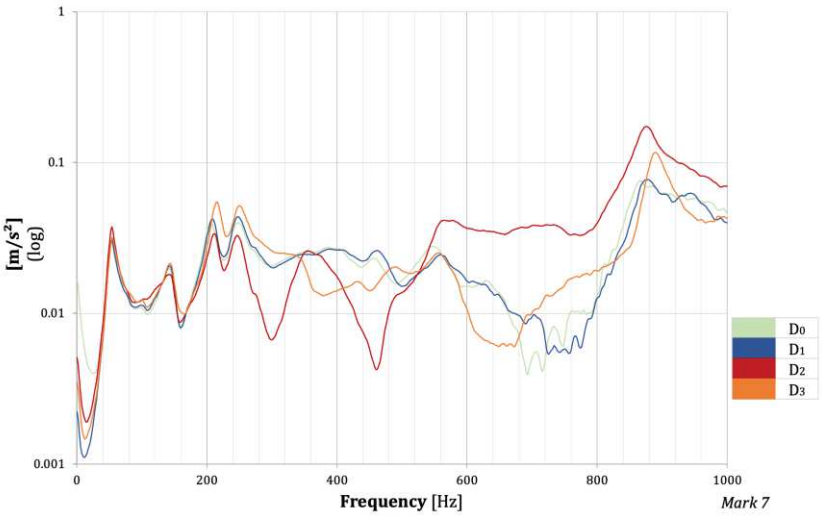
1
0.1
0.01
0.001
[m/s²] (log)
0
200
400
600
800
1000
Frequency [Hz]
D0
D1
D2
D3
Mark 7

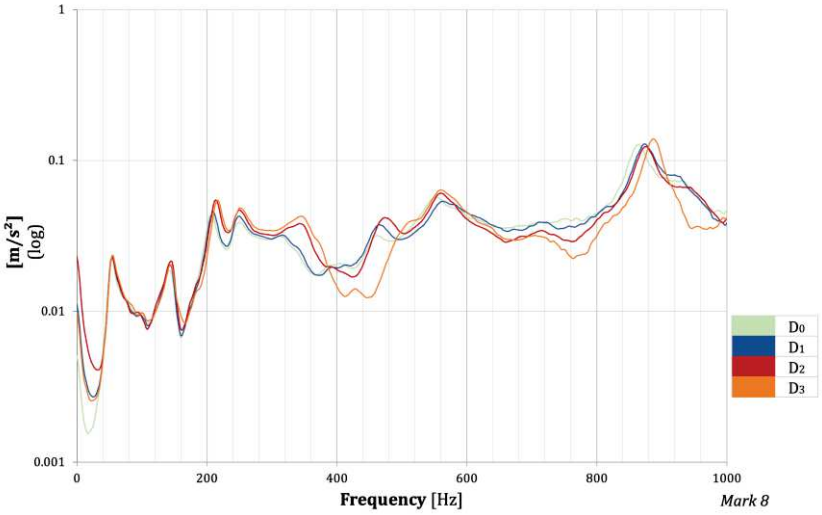
1
0.1
0.01
0.001
[m/s²] (log)
0
200
400
600
800
1000
Frequency [Hz]
Mark 8
D0
D1
D2
D3

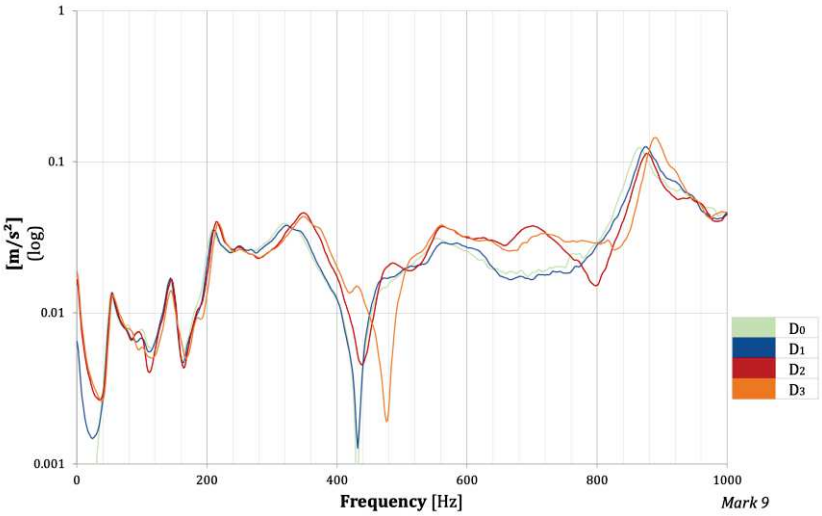
1
0.1
0.01
0.001
[m/s²] (log)
0
200
400
600
800
1000
Frequency [Hz]
Mark 9
D0
D1
D2
D3

(b) B_1

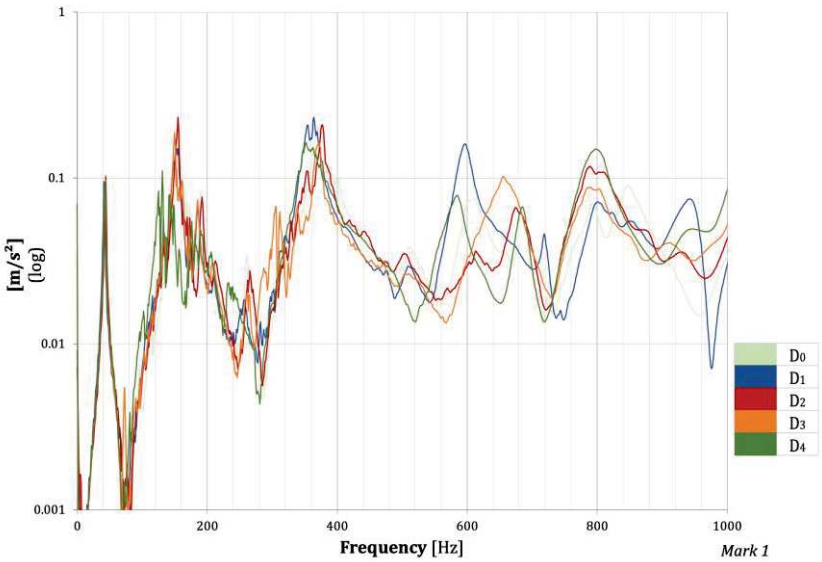
1
0.1
0.01
0.001
[m/s²] (log)
0
200
400
600
800
1000
Frequency [Hz]
D0
D1
D2
D3
D4
Mark 1

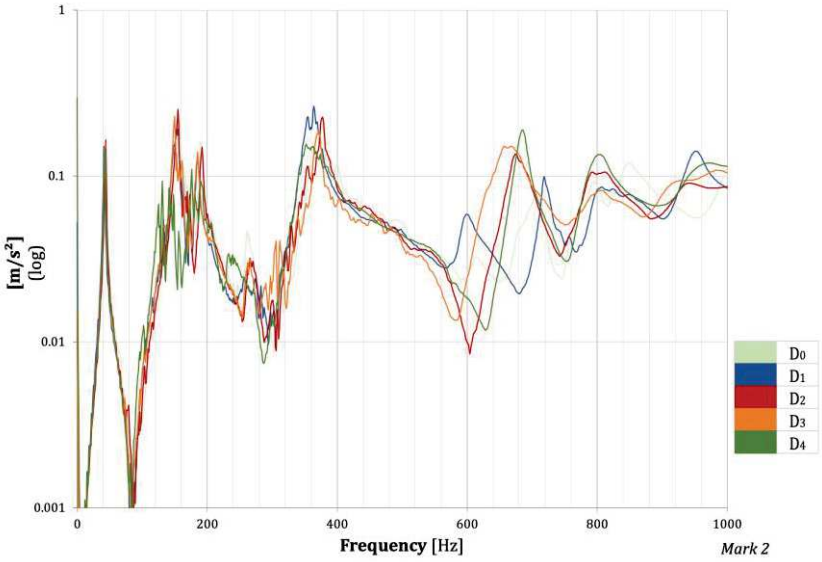
1
0.1
0.01
0.001
[m/s²] (log)
0
200
400
600
800
1000
Frequency [Hz]
D0
D1
D2
D3
D4
Mark 2

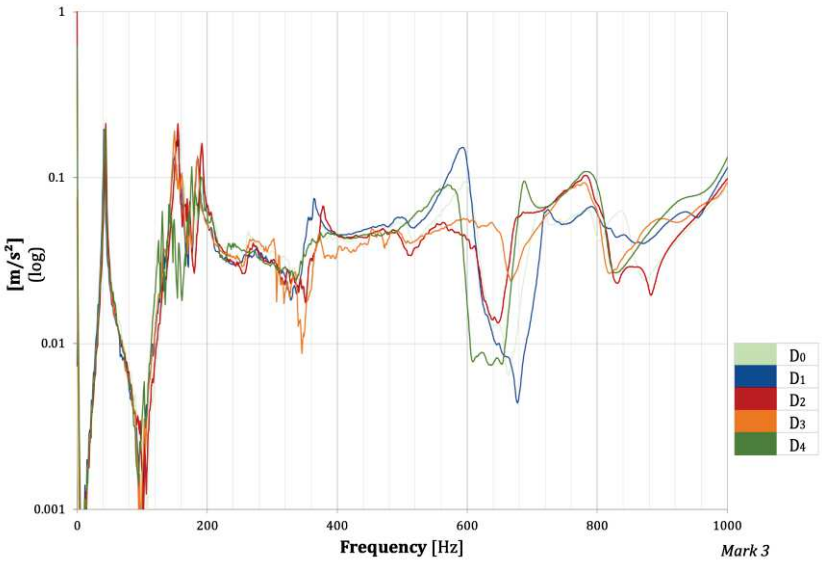
1
0.1
0.01
0.001
[m/s²] (log)
0
200
400
600
800
1000
Frequency [Hz]
D0
D1
D2
D3
D4
Mark 3

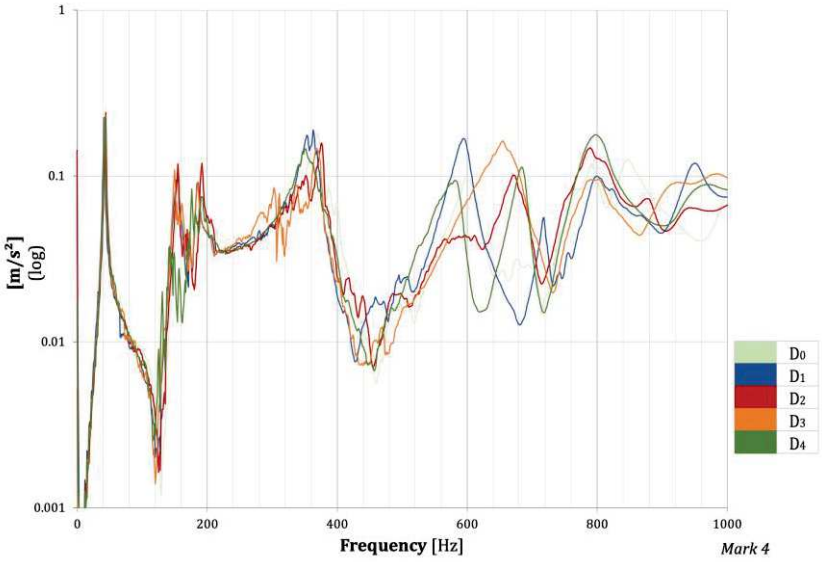
1
0.1
0.01
0.001
[m/s²] (log)
0
200
400
600
800
1000
Frequency [Hz]
D0
D1
D2
D3
D4
Mark 4

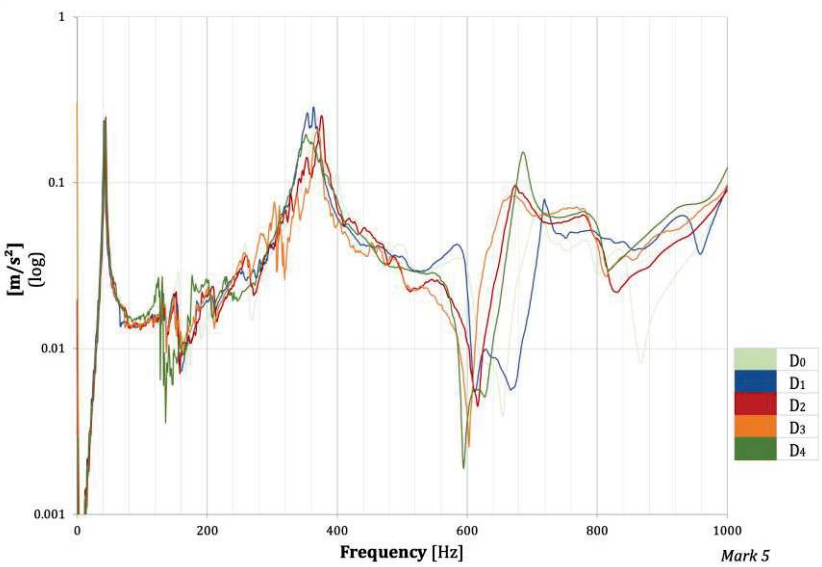
1
0.1
0.01
0.001
[m/s²] (log)
0
200
400
600
800
1000
Frequency [Hz]
D0
D1
D2
D3
D4

Mark 5

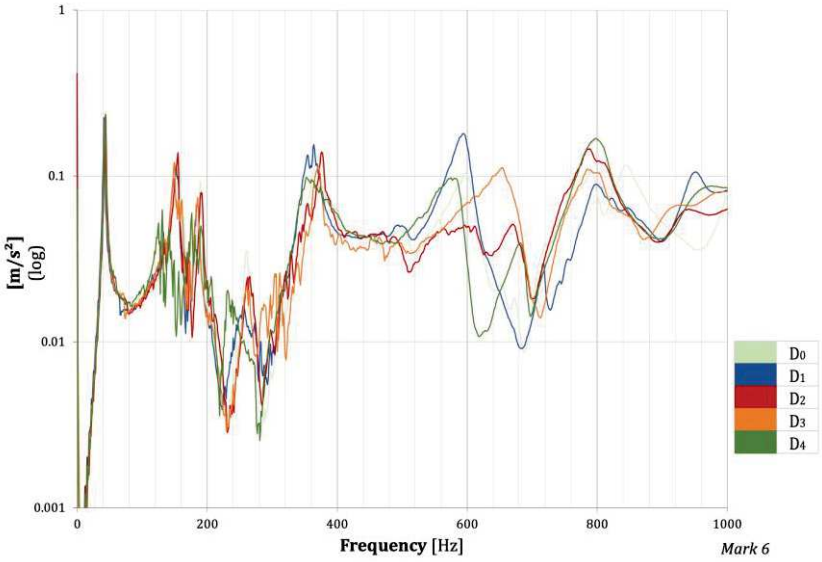
1
0.1
0.01
0.001
[m/s²] (log)
0
200
400
600
800
1000
Frequency [Hz]
D0
D1
D2
D3
D4

Mark 6

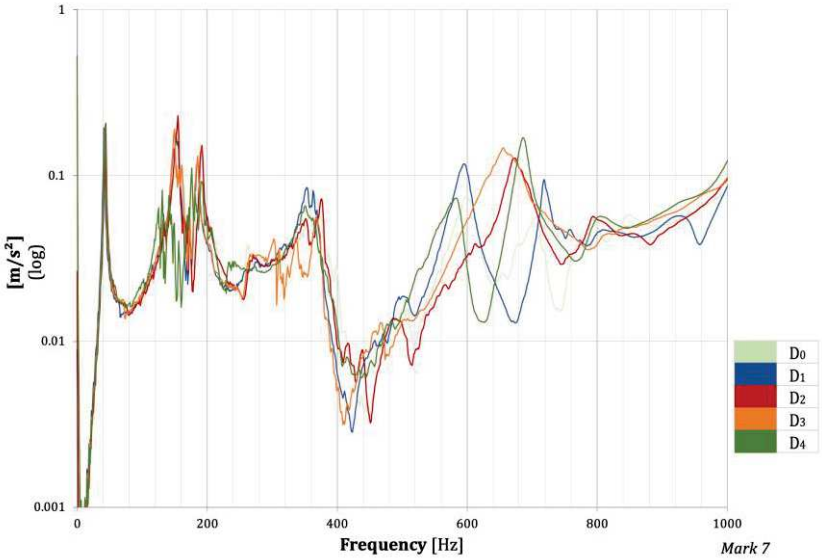
1
0.1
0.01
0.001
[m/s²] (log)
0
200
400
600
800
1000
Frequency [Hz]
D0
D1
D2
D3
D4

Mark 7

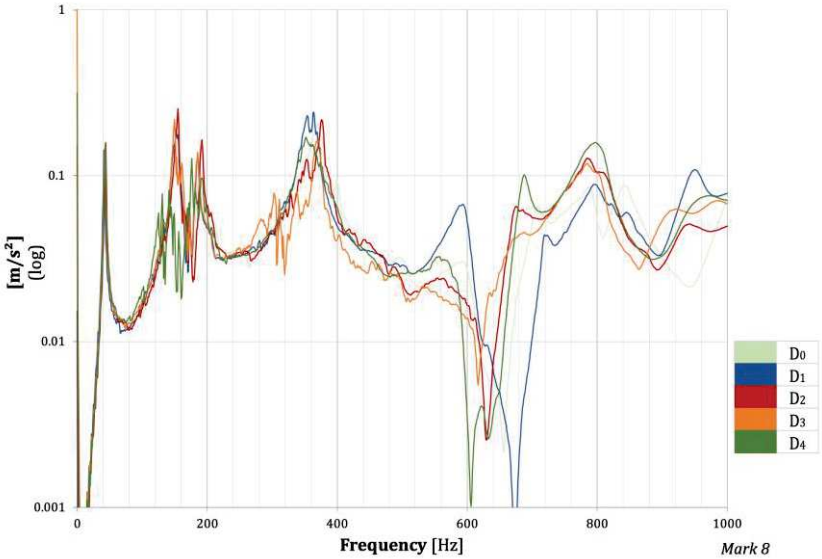
1
0.1
0.01
0.001
[m/s²] (log)
0
200
400
600
800
1000
Frequency [Hz]
D0
D1
D2
D3
D4

Mark 8

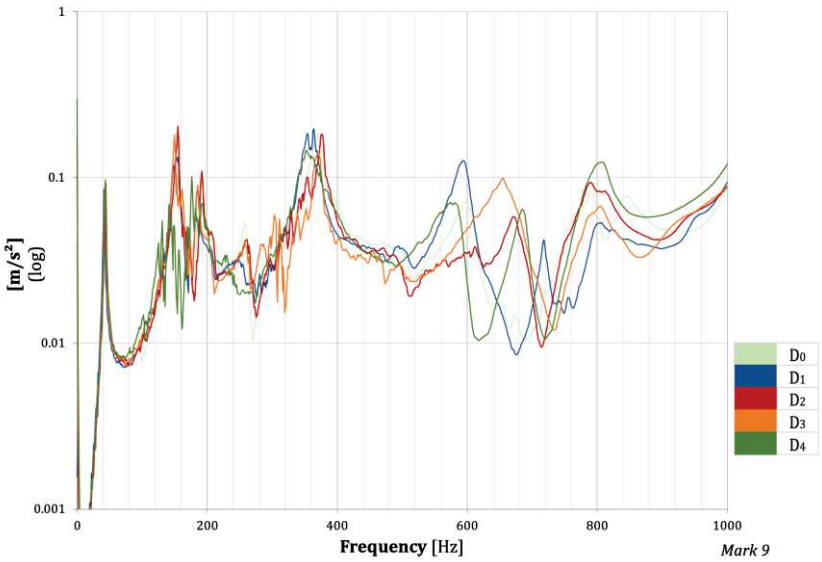
1
0.1
0.01
0.001
[m/s²] (log)
0
200
400
600
800
1000
Frequency [Hz]
Mark 9
D0
D1
D2
D3
D4

(c) B_2

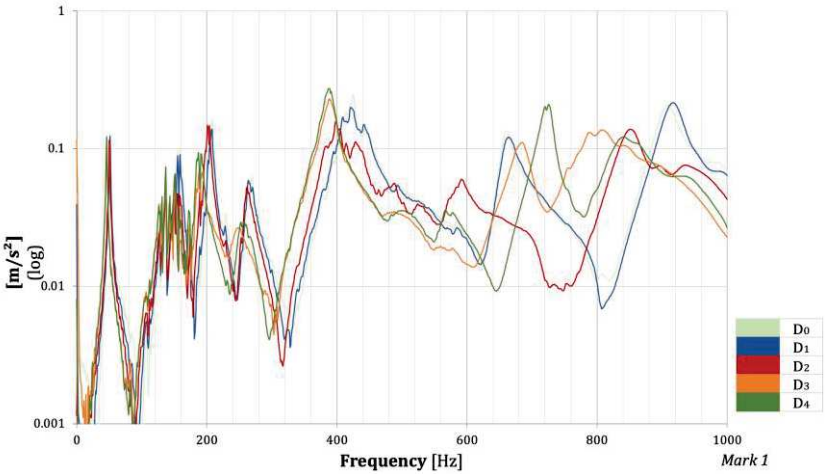
1
0.1
0.01
0.001
[m/s²] (log)
0
200
400
600
800
1000
Frequency [Hz]
Mark 1
D0
D1
D2
D3
D4

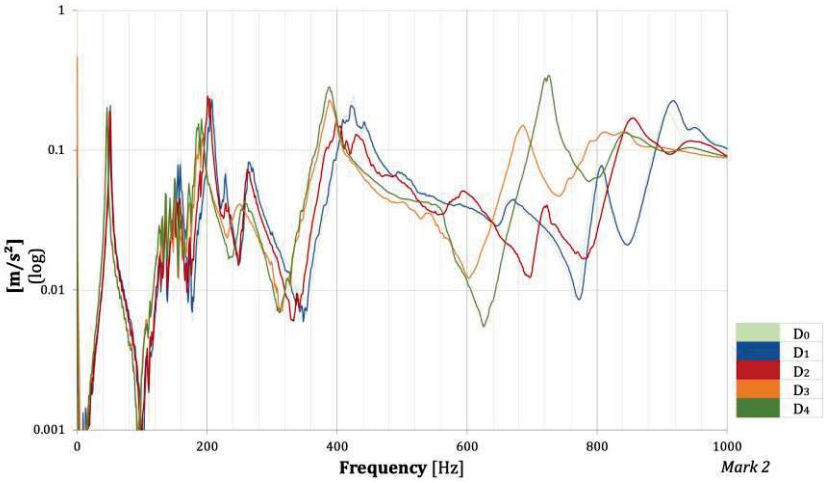
1
0.1
0.01
0.001
[m/s²] (log)
0
200
400
600
800
1000
Frequency [Hz]
D0
D1
D2
D3
D4
Mark 2

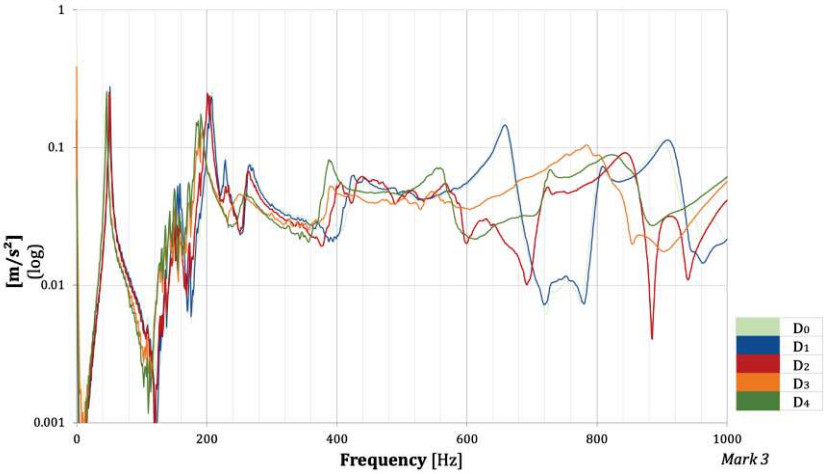
1
0.1
0.01
0.001
[m/s²] (log)
0
200
400
600
800
1000
Frequency [Hz]
D0
D1
D2
D3
D4
Mark 3

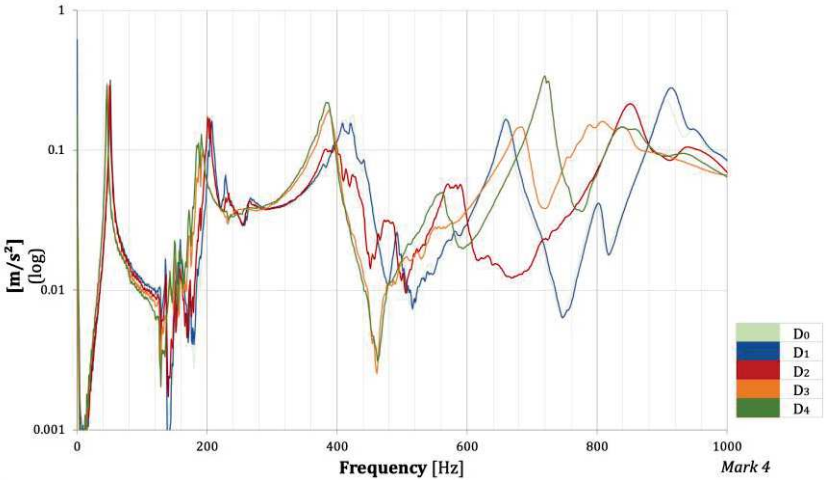
1
0.1
0.01
0.001
[m/s²] (log)
0
200
400
600
800
1000
Frequency [Hz]
Mark 4
D0
D1
D2
D3
D4

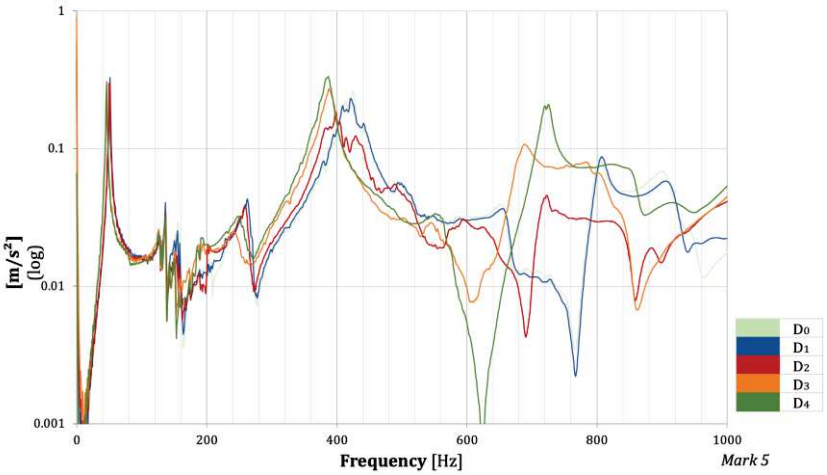
1
0.1
0.01
0.001
[m/s²] (log)
0
200
400
600
800
1000
Frequency [Hz]
Mark 5
D0
D1
D2
D3
D4

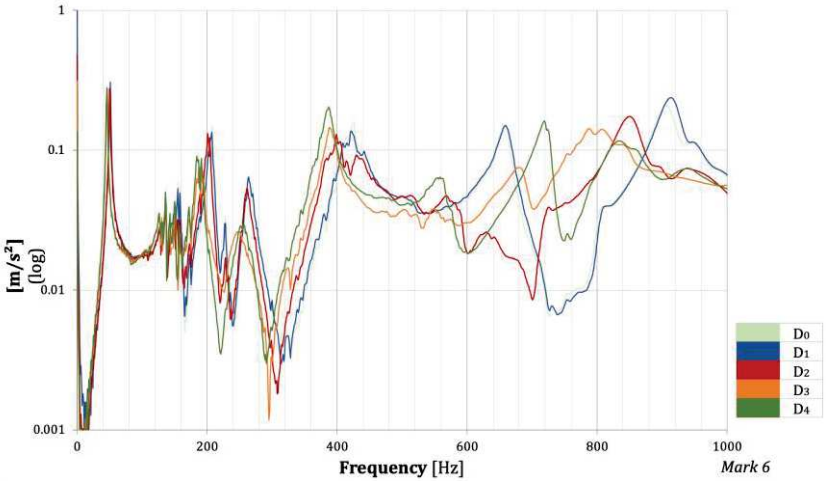
1
0.1
0.01
0.001
[m/s²] (log)
0
200
400
600
800
1000
Frequency [Hz]
D0
D1
D2
D3
D4
Mark 6

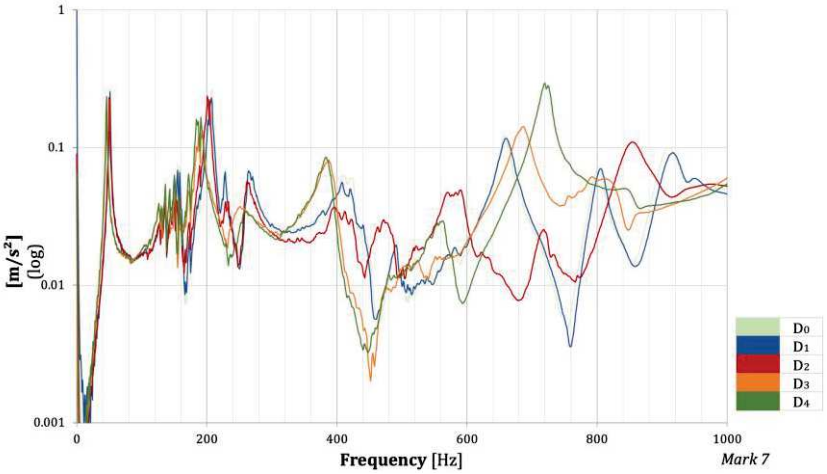
1
0.1
0.01
0.001
[m/s²] (log)
0
200
400
600
800
1000
Frequency [Hz]
D0
D1
D2
D3
D4
Mark 7

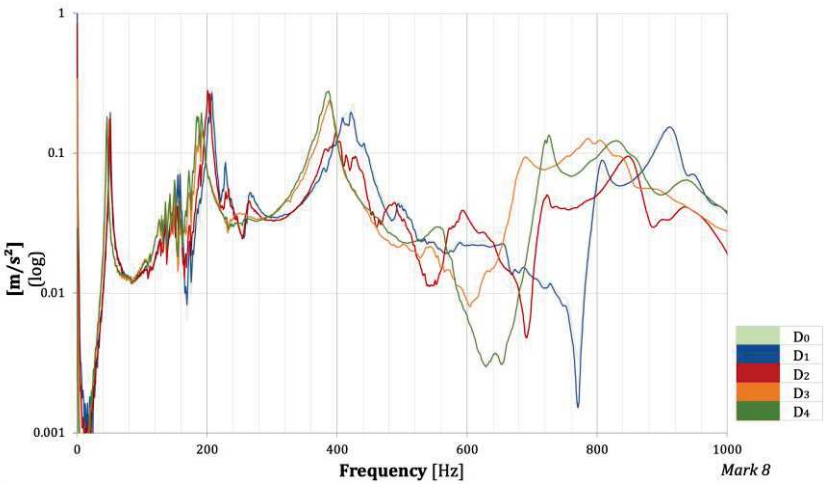

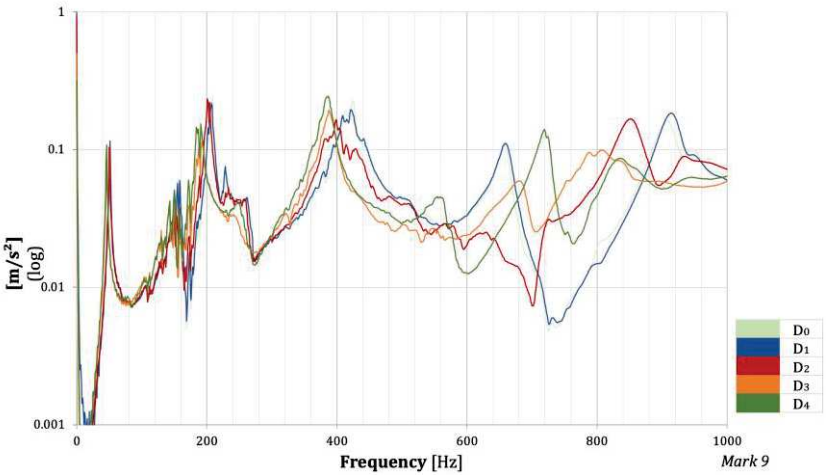

(d) B_3

Figure 5.16 – Experimental FRF diagrams at different damage D_i=0,…,4, at Mark i, for each RC beam; (a) specimen CB, (b) specimen B_1, (c) specimen B_2, (d) specimen B_3 in hinged ends conditions

The main experimental frequency values data obtained from dynamic tests on hinged specimens, for un-strengthened beam CB and strengthened beams B_1, B_2, B_3 at various damage step D_i are contained in Table 5.4.
Table 5.4 shows the average frequency recorded experimentally at each of the accelerometer positions.

Table 5.4 – Experimental frequency values at different damage degree D_i for each specimen in hinged ends conditions

CB				
Damage degree	**f_1 (Hz)**	**f_2 (Hz)**	**f_3 (Hz)**	**f_4 (Hz)**
D_0	68.00	246.44	430.00	1079.20
D_1	61.71	234.57	431.50	1048.00
D_2	57.00	219.71	402.00	966.25
D_3	57.00	212.57	426.00	948.25
B1				
Damage degree	**f_1 (Hz)**	**f_2 (Hz)**	**f_3 (Hz)**	**f_4 (Hz)**
D_0[3]	52.75	227.75	352.00	865.00
D_1	53.56	237.43	345.00	873.56
D_2	53.50	227.25	352.50	875.33
D_3	54.00	227.25	346.40	886.67
B2				
Damage degree	**f_1 (Hz)**	**f_2 (Hz)**	**f_3 (Hz)**	**f_4 (Hz)**
D_0[3]	44.00	159.78	371.11	844.00
D_1	41.00	153.13	362.78	801.00
D_2	44.00	154.63	376.44	789.88
D_3	43.00	147.63	370.44	783.00
D_4	43.00	151.00	352.00	793.14
B3				
Damage degree	**f_1 (Hz)**	**f_2 (Hz)**	**f_3 (Hz)**	**f_4 (Hz)**
D_0[3]	51.11	208.00	427.25	906.00
D_1	51.00	207.13	422.00	912.63
D_2	50.00	201.00	398.38	850.25
D_3	46.00	191.75	388.44	811.00
D_4	46.00	189.63	386.38	835.14

The recorded experimental frequency values for the four examined vibration mode, for each damage state, were plotted in Figure 5.17.

Figure 5.17 – Graphic representation of the experimental natural frequencies and of their variation for each mode of vibration for each RC beam; (a) specimen CB, (b) specimen B_1, (c) specimen B_2, (d) specimen B_3 in hinged ends conditions

[3] Undamaged condition is at the beginning of vibration test for strengthened beams.

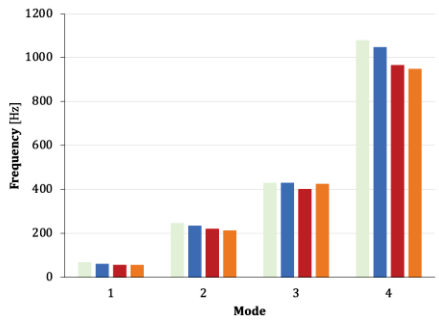

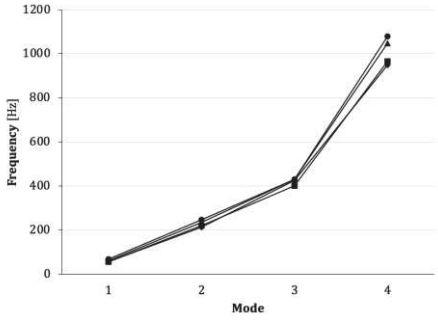

(a) CB

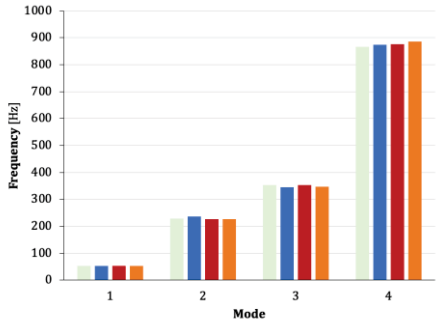

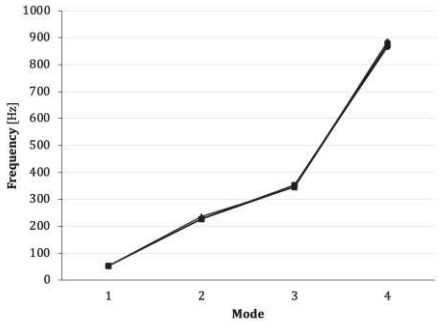

(b) B_1

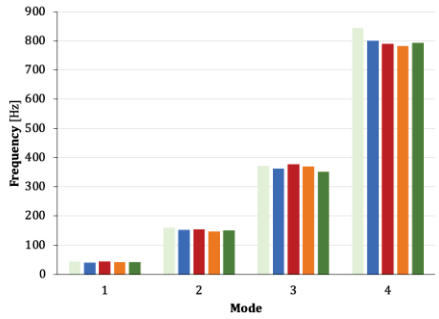

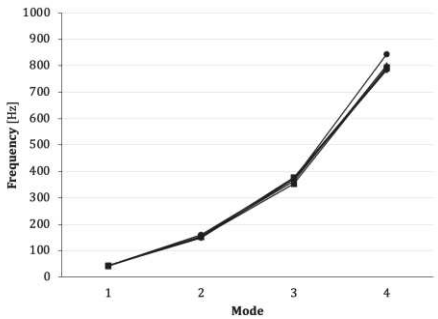

(c) B_2

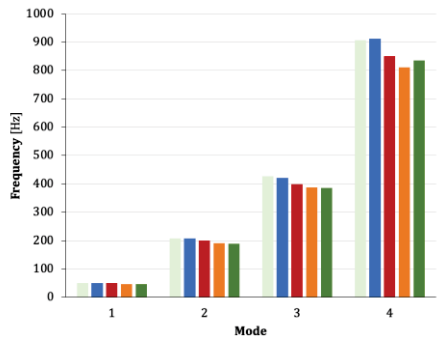

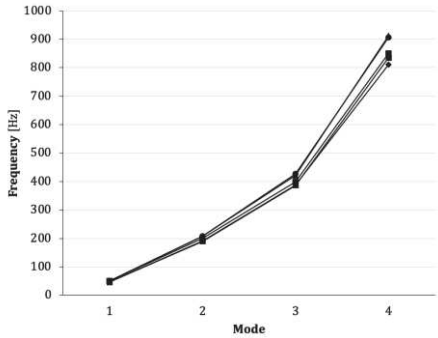

(d) B_3

Chapter 6. Discussion of experimental and theoretical results

6.1. Introduction

In the previous chapter the results obtained from the experimental tests were shown, in this chapter all the necessary re-elaborations and comparisons between the data are carried out.

From the static point of view, the behaviour of the beams subjected to bending is analysed by comparing them with each other in terms of deformations and strains as well as in terms of curvature. A comparison with the theoretical results is also reported.
One of the most immediate results of the static bending test is the observation of the propagation of the cracks and the mode of failure of the samples, in this section are reported images and an analysis of the failure modes.
Another important aspect emerging from experimental campaign, is the impossibility to apply the Bernoulli's hypothesis in the study of RC sections of beams strengthened with NSM FRP rod: this topic is discussed below.

In dynamic terms, comparison of the experimental frequency values as damage proceeds, for the four vibration modes, were conducted, relative to condition D_0 and relative to the immediately preceding state of damage D_{i-1}.
The natural frequencies of undamaged beam have also been evaluated theoretically assuming a uniform slender beam and neglecting gravity forces, following Euler-Bernoulli's model, therefore comparisons between theoretical and experimental results were made.
Finally, it was possible to compare the data obtained for the two different types of reinforcement in order to determine their effectiveness.

6.2. Static results

By comparing the load-deflection curves relating to the different specimens, it is observed that the introduction of the reinforcement involves a considerable increase in resistance compared to the simply reinforced beam model; however, the elastic phase does not undergo any variation in terms of stiffness.
In the elastic stage, the FRP showed marginal contribution in improving the behavior of strengthened beams. All beams displayed approximately same strain values indicating similar stiffness, for the first load cycles. In the subsequent stage, the NSM-FRP beams showed improvement in stiffness and yielding load.
We deduce that the NSM-FRP bars worked effectively as an additional tensile reinforcement, the NSM-FRP bars controlled the flexural performance in the ultimate strength stage increasing flexural stiffness and ultimate capacity of the element and reducing deformation and deflection, therefore reducing ductility.

In terms of ultimate load capacity, for CFRP-strengthened beam B_3 a maximum increasing of 44% compared to the GFRP-strengthened specimens was recorded.
Specimen B_3 strengthened with CFRP bar, shows a deflection reduction in terms of percentage of 43%, 85%, 74% for the first three load cycles compared to the Control Beam, and a reduction of 48%,78%,56%,39% for the first four load cycles compared to the specimen B_2 strengthened with GFRP rod.
$P - \delta$ curves of strengthened specimens have been superimposed in Figure 6.1; points A, B, and C, representing the concrete cracking, steel yielding and ultimate loads of the beams respectively, have been identified. These points were determined based on the slope changes of the $P - \delta$ curves. As can be seen from the $P - \delta$ curves, three distinct stages could be discerned during the loading process, namely the elastic stage (O-A), concrete cracking stage (A-B), ultimate strength stage (B-C).

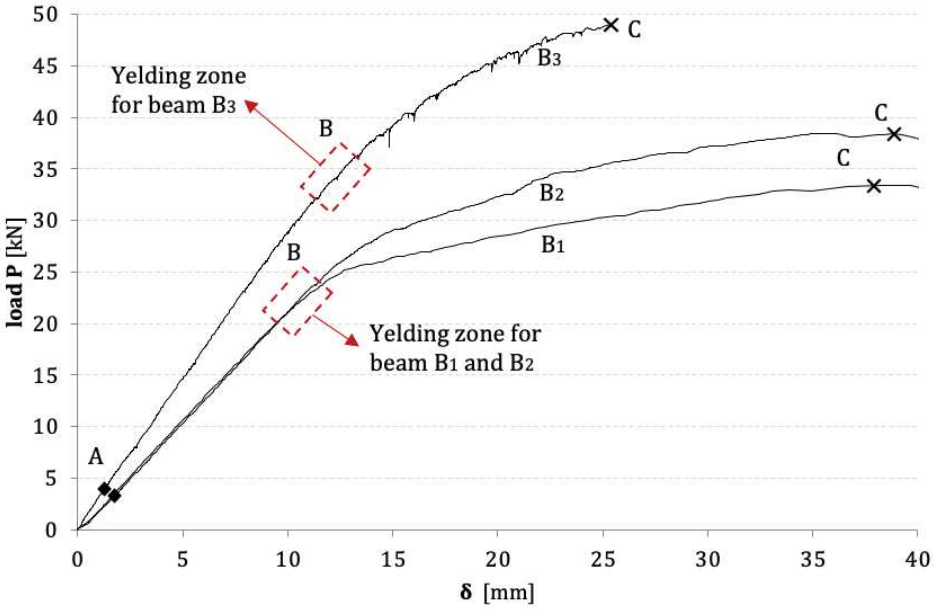

Figure 6.1 – Experimental diagram load, P, vs deflection, δ, at midspan of strengthened beams, with identification of points A, B, and C

As can be seen in Figure 6.1, stiffnesses of beams B_1 and B_2 were lower than that of beam B_3 in the ultimate strength stage, this is a direct result of the mechanical properties of the strengthening bars (CFRP/GFRP). Indeed, the modulus of elasticity of GFRP is much lower than that of the CFRP.

The ductility index (μ) was calculated according to (6.1) in order to measure ductility of the strengthened beam.

$$\mu = \frac{\delta_u}{\delta_y} \tag{6.1}$$

Where δu and δy are the average midspans deflection of beams at ultimate and yielding load, respectively, these deflection values were obtained from the load–deflection response.
Table 6.1 contains the values of ductility index: among the tested strengthened specimens the greater value was found for GFRP-strengthened beams, in particular for specimen B_2.

Table 6.1 – Calculation of ductility index for strengthened beams B_1, B_2, and B_3

	δy	**δu**	**μ**
B_1	10.29	38.30	3.72
B_2	10.40	39.70	3.82
B_3	12.45	25.35	2.04

From the observation of the obtained data in terms of curvature, it can be said the values of curvature, for specimens strengthened with GFRP rod, are comparable or slightly lower to curvature value of the un-strengthened specimen, being equal load values.
For specimen B_3, strengthened with CFRP, the curvature values are approximately halved compared to other specimen, for the first two load cycles.
Analyzing the trend of the tangent, it is noted that no plastic phase is recorded beyond the yielding of tensile steel; in fact, the behavior of specimen is represented by a prevalently linear trend up to failure.
In Figure 6.2 the moment-curvature trends for each beam model are compared.

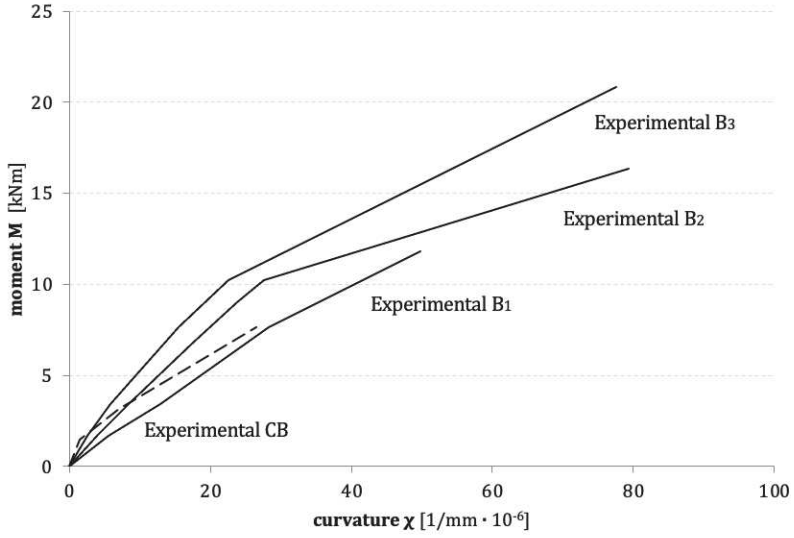

Figure 6.2 – Comparison between experimental moment vs curvature trends of each beam model

In terms of strains, in mid-span regions, the compressive strain of concrete for beams B_2 and B_3 strengthened with NSM-FRP bars was lower than that of the control beam for the same applied load, in particular for beams strengthened with CFRP rods.
A close look at the load–strain curves of concrete indicates that all strengthened beams exhibited a nearly linear attitude up to the peak load of beam, without clear signs of affection by cracking of concrete or yielding of tension steel, the load–strain response remained linear with no visual changes noted in the slopes.

Table 6.2 presents the maximum recorded tensile strain of NSM-FRP bars (ε_{FRP}^{max}) obtained from the experimental investigations conducted on beams. The deformations are the maximum that the instruments were able to measure at the last load cycle before failure. For the B_1 beam it was not possible to obtain an ultimate deformation value, as the strain gauge positioned on the GFRP suffered premature failure.

Table 6.2 – Comparisons between experimental and analytical maximum strain of FRP bars

Specimen	ε_{FRP}^{ult}	experimental ε_{FRP}^{max}	experimental $\varepsilon_{FRP}^{max}/\varepsilon_{FRP}^{ult}$	ACI ε_{FRP}^{max}	ACI $\varepsilon_{FRP}^{max}/\varepsilon_{FRP}^{ult}$
B_2	18.63	7.86	0.42	13.04	0.7
B_3	12.90	4.33	0.34	9.03	0.7

The mobilization levels of NSM-FRP rods ($\varepsilon_{FRP}^{max}/\varepsilon_{FRP}^{ult}$) at peak load of beams B_2 and B_3 were respectively equal to 42%, 34% at mid-span.
According to the American guideline ACI 440.2R [56], the debonding strain of NSM-FRP may vary from $0.6\varepsilon_{FRP}$ to $0.9\varepsilon_{FRP}$, depending on many factors, such as the member dimensions, steel and FRP reinforcement ratios, and surface roughness of the FRP bar. This guideline recommends the maximum strain of NSM-FRP, for beam failed due to debonding, to be equal to $\varepsilon_{FRP}^{max} = 0.7\ \varepsilon_{FRP}^{ult}$ for calculating the nominal capacity of strengthened RC sections.
Comparisons between the values of ε_{FRP}^{max} obtained from the current tests with the above approach is presented in Table 6.2, the debonding strain recommended by the ACI 440.2R guideline is greater than the experimentally measured ones.

6.2.1. Comparison with theoretical results

Having determined, in Chapter 4, the theoretical moment-curvature diagram for each specimen, these are compared with the respective experimental ones in Figure 6.3.

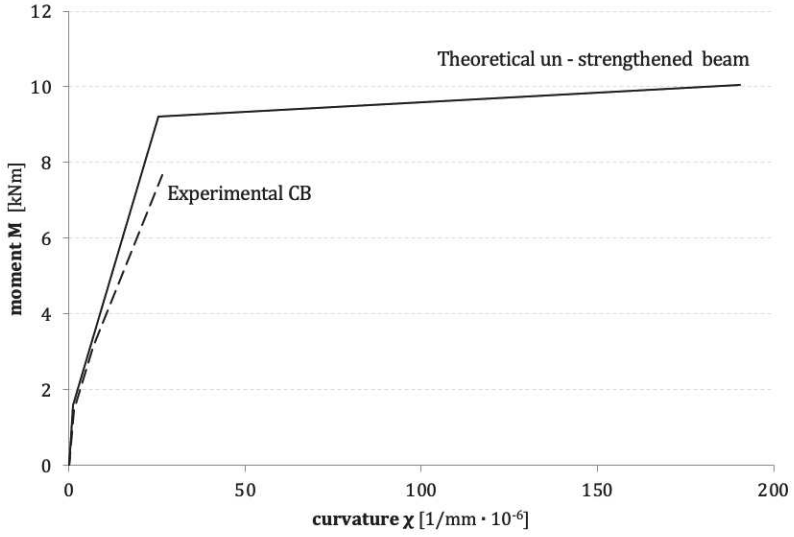
Theoretical un - strengthened beam
Experimental CB
moment M [kNm]
curvature χ [1/mm · 10-6]
0
2
4
6
8
10
12
0
50
100
150
200

(a)

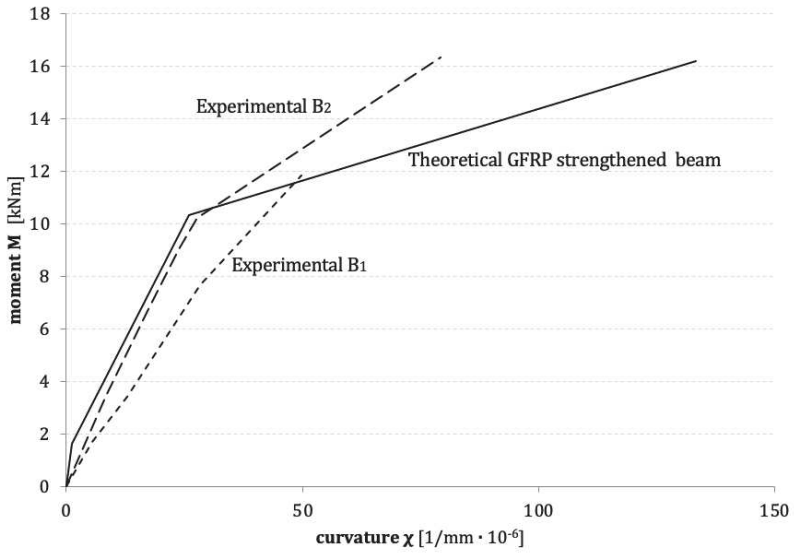
Experimental B2
Theoretical GFRP strengthened beam
Experimental B1
moment M [kNm]
curvature χ [1/mm · 10-6]
0
2
4
6
8
10
12
14
16
18
0
50
100
150

(b)

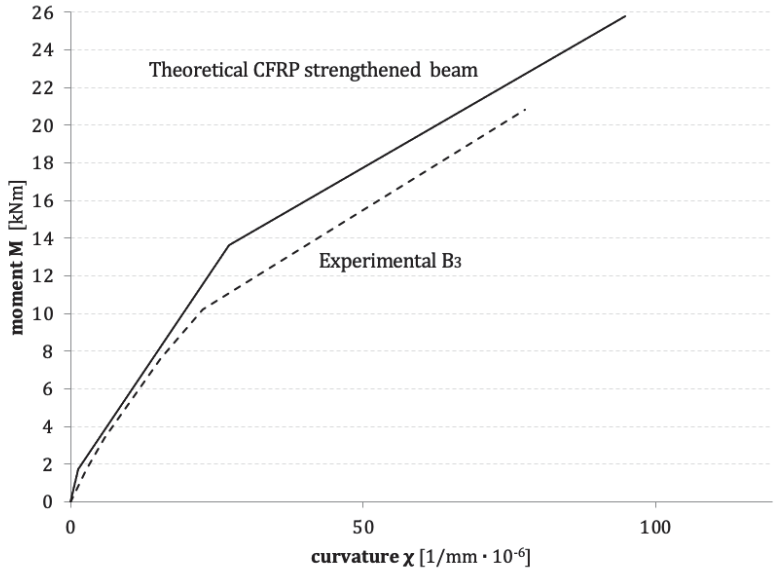

(c)

Figure 6.3 – Comparison between theoretical and experimental moment vs curvature diagram, (a) for the un-strengthened specimen; (b) for the GFRP strengthened specimens; (c) for the CFRP strengthened specimens

From the diagrams it can be observed that the theoretical behavior closely approximates the experimental one especially for the first two phases. For specimen CB, phase III is not experimentally recorded as it was not brought to failure. It wasn't possible to calculate the curvature corresponding to the ultimate moment for beam B_1, due to the premature failure of instrumentation. Specimen B_2, perfectly matches with the theoretical diagram in elastic phase, while shows less ductility than the theoretical section. Experimental behavior of B_3 follows the trend of theoretical one in the I phase but reaches earlier the yielding phase. However, the experimental ultimate moment is comparable with the theoretical one, for each specimen.
The reduction factor ϕ for the section under examination was also calculated: since the section are of ductile type, the ultimate moment should be multiplied by 0.9, Table 6.3 contains theoretical and experimental values of ultimate moment for each section.

Table 6.3 – Summary of ultimate moment

	B_1	**B_2**	**B_3**
$M_{u,exp}$ (kNm)	14.39	16.32	20.85
$M_{u,th}$ (kNm)	16.17		25.77
ϕ $M_{u,exp}$ (kNm)	14.55		23.19

6.2.2. Failure mode of beam specimens

During the static tests, the propagation of cracks and the failure mode was also visually observed.
On the un-strengthened specimen CB, after the first load cycle, with P_1=4 kN, the cracks were almost absent; when the load was increased, the crack pattern followed the trend of a typical RC beam, with vertical cracks in midspan and oblique cracks nearby the supports, as shown in Figure 6.4.

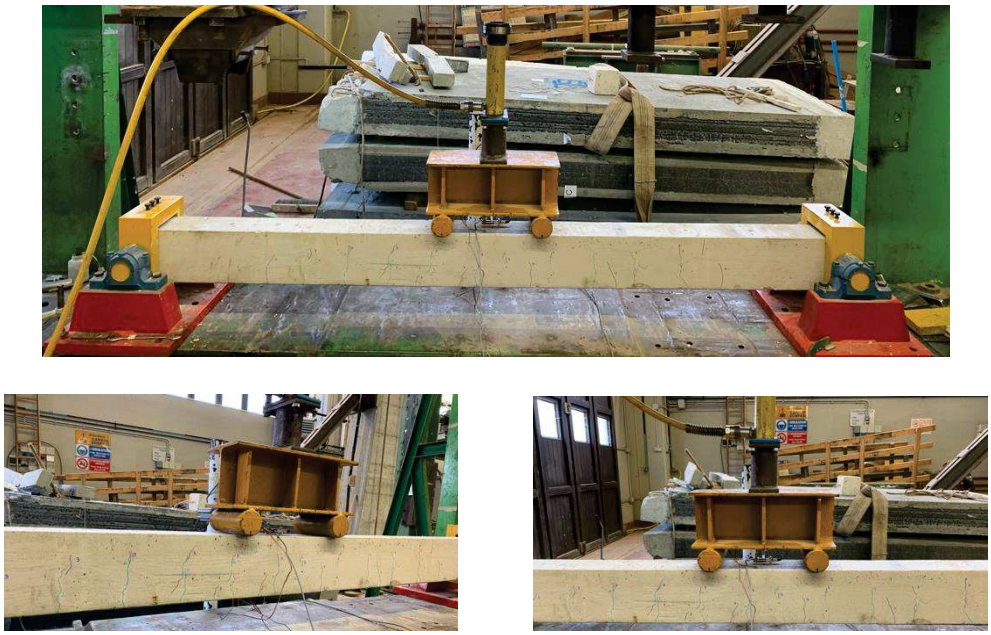

Figure 6.4 – Cracking damage development due to bending test at different damage degrees Di, with i=1,2,3 for specimen CB

In strengthened specimen B_1-B_2-B_3 the crack pattern developed following the fractures occurred during the previous test on the un-strengthened specimen; only for the last loading cycles the cracks increased in depth and width.
In general, all the beam models are joint to failure by crushing of compressed concrete and by cracking of the concrete in the tensioned area with delamination of the FRP reinforcement, the detailed description of failure for each beam is reported below.

In specimen B_1 failure occurs at a load value P_f equal to 34.04 kN. In addition to crushing of compressed concrete, delamination of GFRP bar starting from midspan section is recorded, in this case the detachment involves both the adhesive and the concrete cover (Figure 6.5b).

For specimen B_2, reaching a load value P_f equal to 38.40 kN, break occurs due to crushing of compressed concrete and complete debonding of GFRP rod interesting

the portion of beam from the midspan section to the end section, leading the detachment of the concrete cover (Figure 6.6b).

The failure of beam B_3 strengthened with NSM CFRP occurred due to crushing of compressed concrete and debonding of CFRP rod that started from the region of maximum moment and propagated to an end. In particular, the debonding between adhesive and the surrounding concrete was recorded at midspan; moving away from the midspan section, also part of concrete cover was interested (Figure 6.7b). The maximum load P_f is equal to 49.06 kN.

In general, for strengthened specimens the pull out of FRP rods was sudden and accompanied with an explosive sound; it was followed by the beam failure.

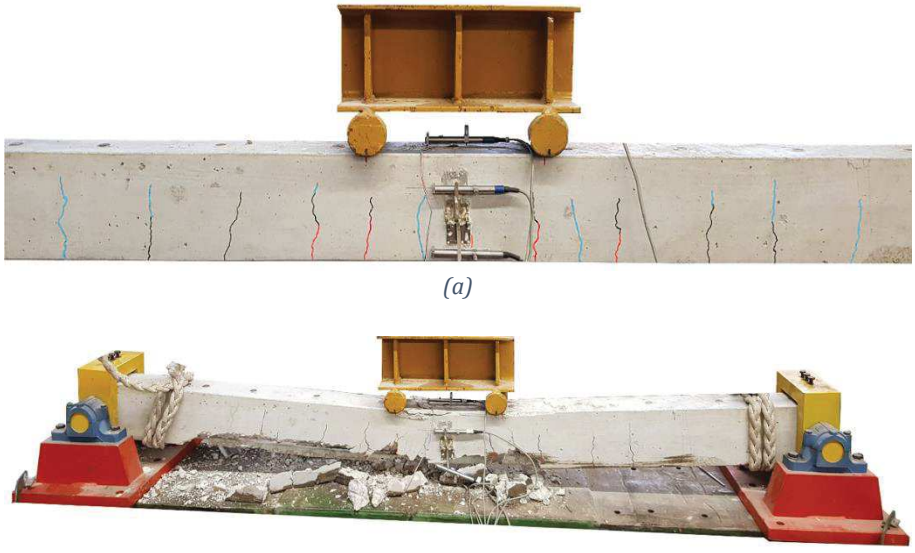

(a)

(b)

Figure 6.5 – (a) Cracking path and (b) failure mode of specimen B_1

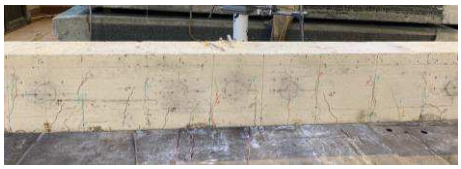

(a)

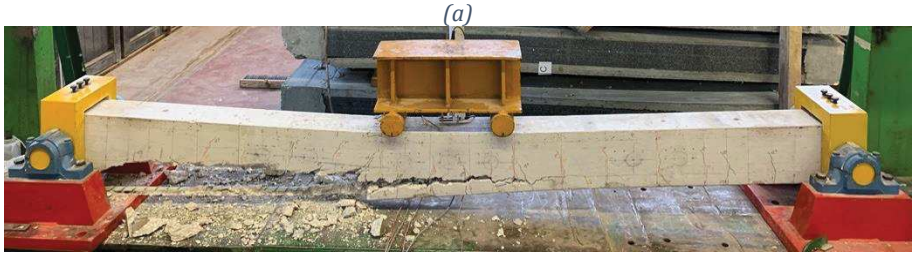

(b)

Figure 6.6 – (a) Cracking path and (b) failure mode of specimen B_2

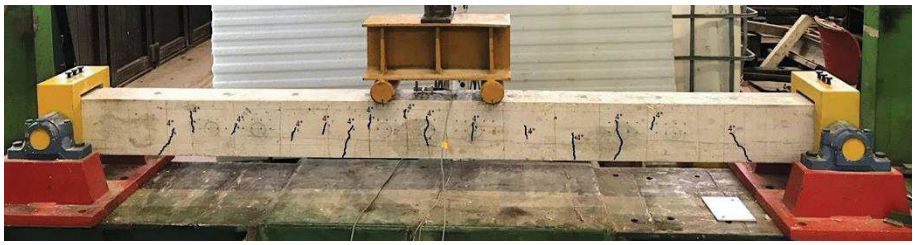

(a)

(b)

Figure 6.7- (a) Cracking path and (b) failure mode of specimen B_3

Table 6.4 summarizes the maximum loads supported by each specimen and the failure modes identified, reported and described in §2.4.1.

Table 6.4 – Maximum load and failure mode of beam specimens

Specimen	**P_f (kN)**	**Failure Mode**
CB	\	\
B_1	34.04	CC + IC-ID
B_2	38.40	CC+EID
B_3	49.06	CC+IC-CS

With
-CC for Concrete Crushing,
-IC-ID for Intermediate Crack with Interfacial Debonding,
-IC-CS for Intermediate Crack with Cover Separation,
-EID for End Interfacial Debonding,
-ECS for End Cover Separation.

For beam B_1 and B_2 we have a bond failure at the bar–epoxy interface, for the first one the failure occurs in mid-span, for the second one at an end. Experimental value of $k = {}^{w_g}/_{d_b}$ is equal to 2.1 for GFRP rods, therefore it exceeds the recommended values by L. De Lorenzis and Nanni [24].

6.3. Calculation of stress-strain lag

The distribution of the experimental recorded strains by bending tests for the midspan section for the un-strengthened and strengthened specimen are represented in Figure 6.8.

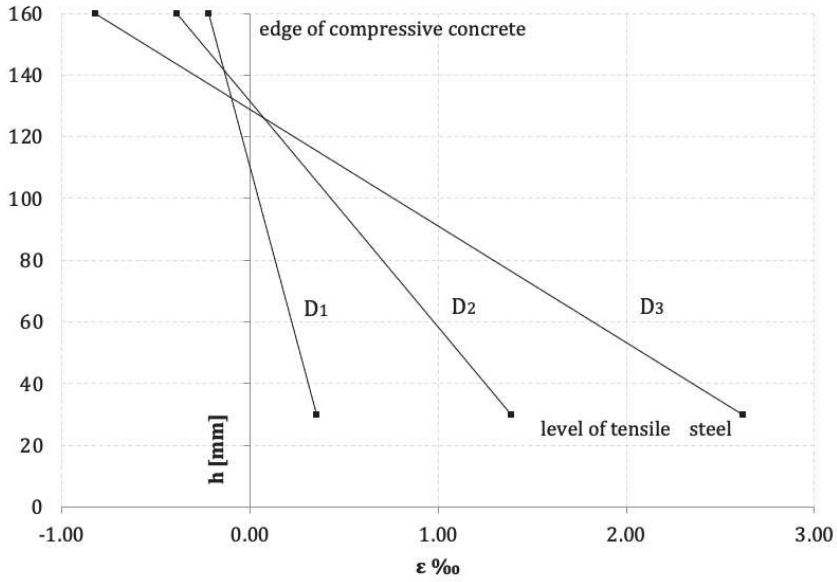
160
140
120
100
80
60
40
20
0
-1.00
0.00
1.00
2.00
3.00
ε ‰
h [mm]
edge of compressive concrete
D1
D2
D3
level of tensile steel

(a) CB

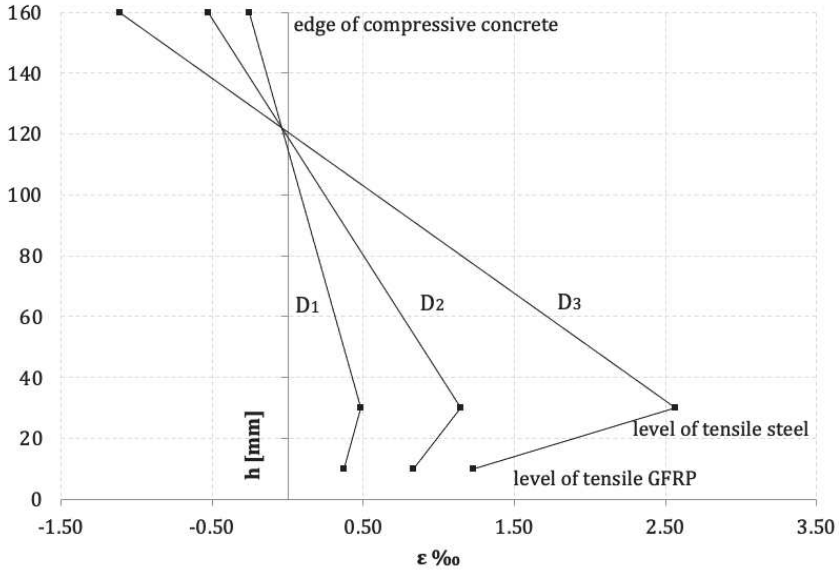
160
140
120
100
80
60
40
20
0
-1.50
-0.50
0.50
1.50
2.50
3.50
ε ‰
h [mm]
edge of compressive concrete
D1
D2
D3
level of tensile steel
level of tensile GFRP

(b) B_1

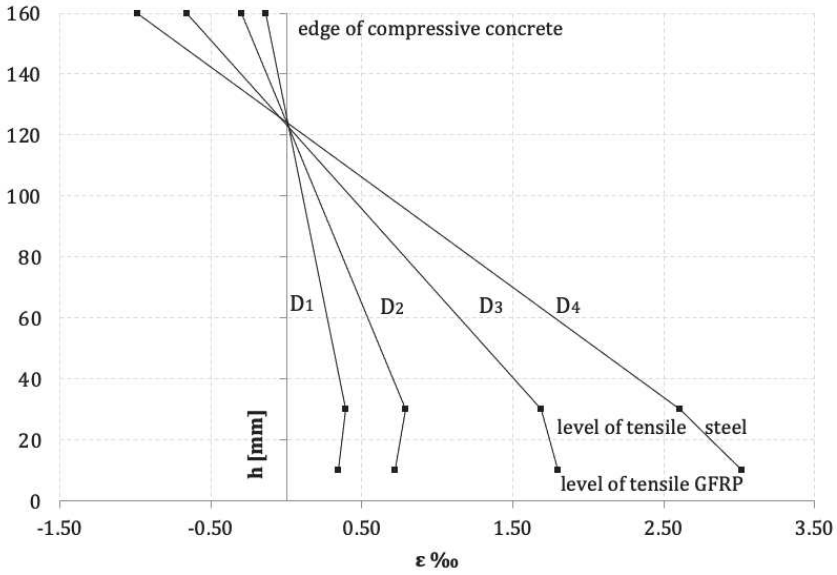

(c) B_2

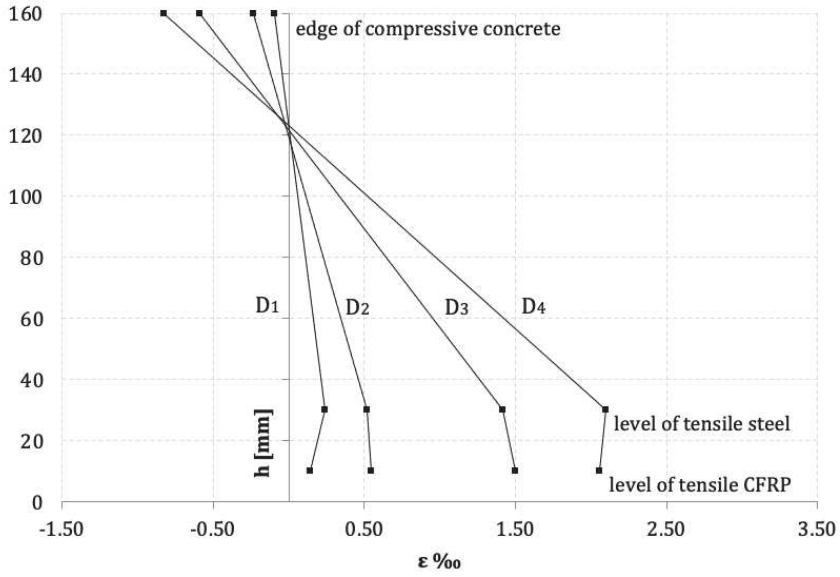

(d) B_3

Figure 6.8 – Experimental strain values vs height, at midspan section, at different loading cycles of RC beams; (a) specimen CB, (b) specimen B_1, (c) specimen B_2, (d) specimen B_3

Experimental results demonstrate that the section's real behavior is not plane, in fact, the strains on FRP aren't linearly congruent with the strains of steel and of compressed concrete and are conditioned by a *stress-strain lag*.

Values of *lag* can be estimated depending on type of strengthening used and on the applied loads. Calculation of *stress-strain lag* values is reported below.

As anticipated, for the strengthened beam model a non-linear distribution of strains through the full depth of the beam is noted; in particular, the strains on FRP rod are affected by a "delay".
The value of this *strain lag* can be calculated in two different ways:

- k_1 is simply the ratio between FRP deformation and that of steel (6.1);
- k_2 it is calculated as a variation in deformation between the one that the FRP should have being valid the hypothesis of conservation of the plane section and the real one (6.2).

$$k_1 = \frac{\varepsilon_{FRP}}{\varepsilon_s} \tag{6.1}$$

$$k_2 = \frac{{\varepsilon_{FRP}}^* - \varepsilon_{FRP}}{{\varepsilon_{FRP}}^*} \tag{6.2}$$

In Table 6.5 the ratios evaluated for each damage degrees for strengthened beam models are shown.

Table 6.5 – Values of lag coefficient k for beams B_1, B_2 and B_3

	B_1		**B_2**		**B_3**	
	k_1	k_2	k_1	k_2	k_1	k_2
D_1	0.77	0.37	0.87	0.28	0.60	0.51
D_2	0.73	0.41	0.91	0.25	1.06	0.13
D_3	0.48	0.61	1.07	0.12	1.06	0.13
D_4	-	-	1.16	0.04	0.98	0.19

In the study of the behavior of RC section with the presence of NSM FRP rods, it can be a good strategy the adoption of one of the coefficient $k_{1,av}$ (or $k_{2,av}$) to prevent overestimation of the beam's strength.
Below the theoretical re-calculation of the NSM FRP beams with the average values $k_{1,av} = 0.83$ and $k_{2,av} = 0.32$ for GFRP and with $k_{1,av} = 0.92$ and $k_{2,av} = 0.24$ for CFRP is shown.

Starting from the calculation made in §4.4, value of ε_{GFRP} (linearly calculated) has been replaced with the one calculated starting from (6.1) and (6.2). In the first case, the deformation value of the FRP does not depend on that calculated in the case of conservation of the flat section but depends only on the deformation on the steel. Therefore, the values adopted are the following:

$$\varepsilon_{FRP} = k_1 \cdot \varepsilon_s \tag{6.3}$$

$$\varepsilon_{FRP} = {\varepsilon_{FRP}}^* \cdot (1 - k_2) \tag{6.4}$$

In Table 6.6 the values of FRP strain and moment obtained for each phase are exposed.

Table 6.6 – Values of FRP strain and moment calculated with the application of k_{av} for each phase

k_1 - GFRP					
Phase I - Cracking		Phase II - Yielding		Phase III - Failure	
ε_{GFRP} (‰)	0.050	ε_{GFRP} (‰)	1.991	ε_{GFRP} (‰)	11.494
M_{cr} (kNm)	1.62	M_y (kNm)	10.02	M_u (kNm)	14.36
k_2 - GFRP					
Phase I - Cracking		Phase II - Yielding		Phase III - Failure	
ε_{GFRP} (‰)	0.057	ε_{GFRP} (‰)	1.988	ε_{GFRP} (‰)	11.257
M_{cr} (kNm)	1.62	M_y (kNm)	10.02	M_u (kNm)	14.28
k_1 - CFRP					
Phase I - Cracking		Phase II - Yielding		Phase III - Failure	
ε_{CFRP} (‰)	0.055	ε_{CFRP} (‰)	2.206	ε_{CFRP} (‰)	8.129
M_{cr} (kNm)	1.71	M_y (kNm)	12.70	M_u (kNm)	22.39
k_2 - CFRP					
Phase I - Cracking		Phase II - Yielding		Phase III - Failure	
ε_{CFRP} (‰)	0.064	ε_{CFRP} (‰)	2.234	ε_{CFRP} (‰)	8.158
M_{cr} (kNm)	1.72	M_y (kNm)	12.74	M_u (kNm)	22.43

It is clear how the moment values are more conservative than those calculated in a linear way. The values obtained with k_1 are very close to those obtained with k_2, these differ by a maximum of 0.6% in the failure phase, in the case of GFRP strengthening.
Furthermore, these values are closer to the experimental ones: for beam B_1 $M_u(k_1)$ differs from $M_{u,exp}$ of about 0.2%, while $M_u(k_2)$ differs from $M_{u,exp}$ of about 1%, in the case of beam B_2 the difference recorded is greater and equal to 14%; for beam B_3 with NSM CFRP rod, the variation between theoretical and experimental moment is about 7%, either applying k_1 or k_2.

6.4. Dynamic results

From a dynamic point of view, the results obtained are compared showing the frequency variations in percentage with respect to the initial condition and with respect to the previous damage condition. The experimental results are also compared with the theoretical ones. The dynamic response of each beam model at different damage step is evaluated, as well as the effect of different type of reinforcement.
In general, from the FRFs diagrams shown in the previous chapter, it was possible to observe a reduction of the frequency values with the increase of crack damage, especially accentuated for the un-reinforced beam and for free-free ends conditions.

6.4.1. Comparison at different damage state

In this section, the frequency values at the initial state D_0 were compared with those relating to subsequent damage levels, for each beam model. The frequency variations were then determined to monitor the frequency trend as the crack progressed.

Figure 6.9 and Figure 6.10 contains the frequency variation in percent $\frac{\Delta f_r}{f_r^{D0}} = 100 \cdot \frac{f_r^{D0} - f_r^{Di}}{f_r^{D0}}$ in reference to the different damage degree for the first four mode of vibration for each beam model in free-free ends condition and in hinged condition.

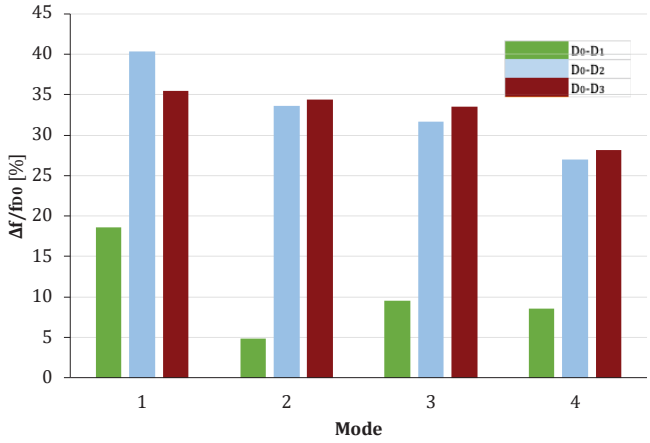

(a) CB

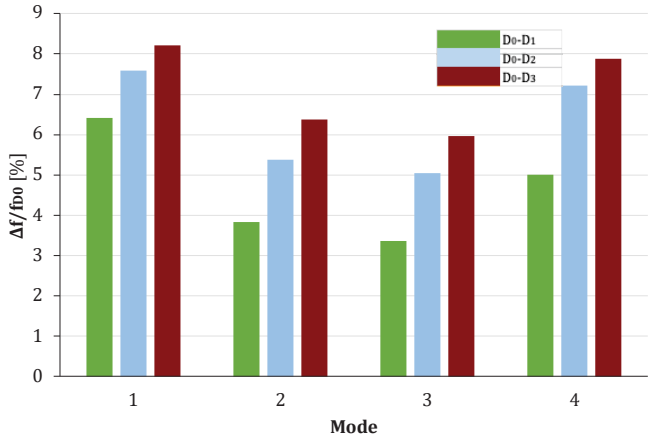

(b) B_1

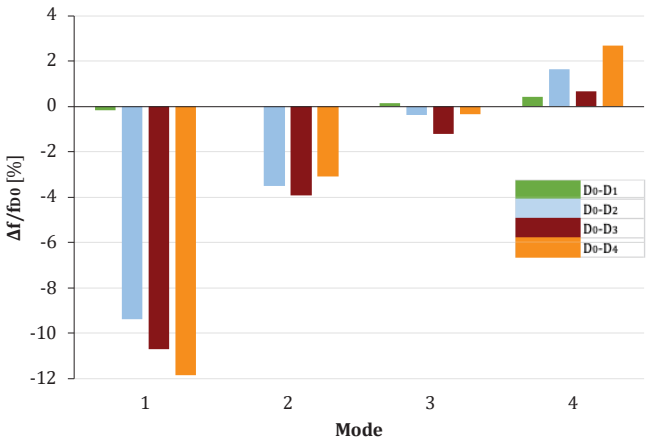

(c) B_2

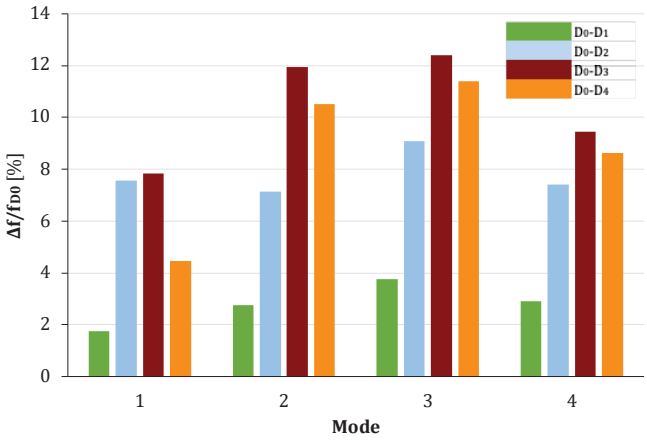

(d) B_3

Figure 6.9 – Variation of frequency values at damage D_i for each RC beam; (a) specimen CB, (b) specimen B_1, (c) specimen B_2, (d) specimen B_3 in free-free ends condition

The diagrams confirm a decrease in the frequency values with increasing crack damage, in some cases higher vibration frequencies are recorded for the penultimate load case, compared to the next one, as in beam B_3.
For sample B_2, on the other hand, an anomalous situation is recorded, that is, a minimal increase of the frequency values, in fact the percentage variations with respect to the initial state D_0 are negative for the first three modes of vibrations. In this case it is evident how the NSM reinforcement in GFRP was able to mitigate the crack damage, as can be seen from Figure 5.15c, the trend of the frequency values is almost indistinguishable between a state of damage and the other.

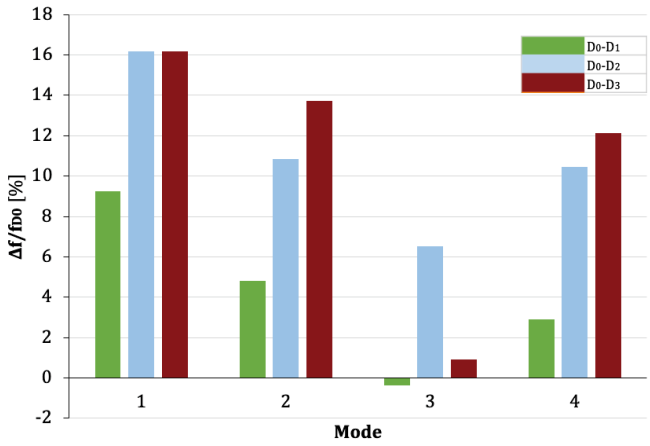
18
16
14
12
10
8
6
4
2
0
-2
Δf/f00 [%]
1
2
3
4
Mode
D0-D1
D0-D2
D0-D3

(a) CB

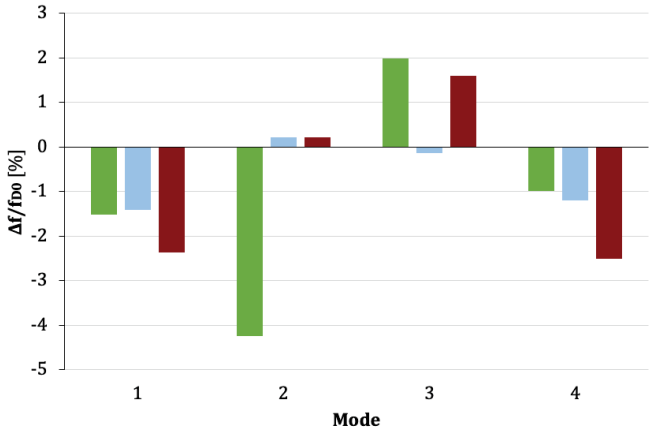
3
2
1
0
-1
-2
-3
-4
-5
Δf/f00 [%]
1
2
3
4
Mode

(b) B_1

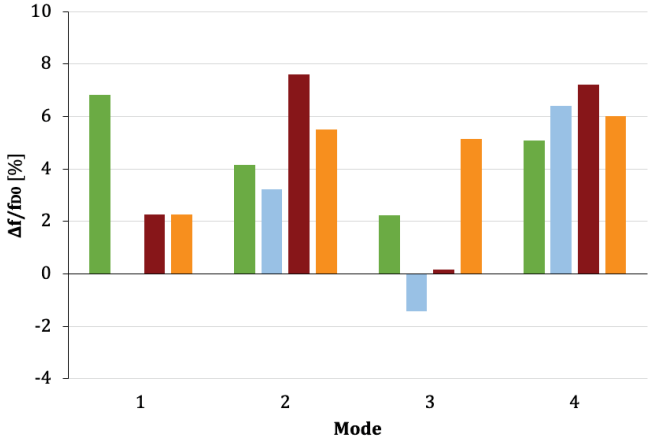
10
8
6
4
2
0
-2
-4
Δf/f00 [%]
1
2
3
4
Mode

(c) B_2

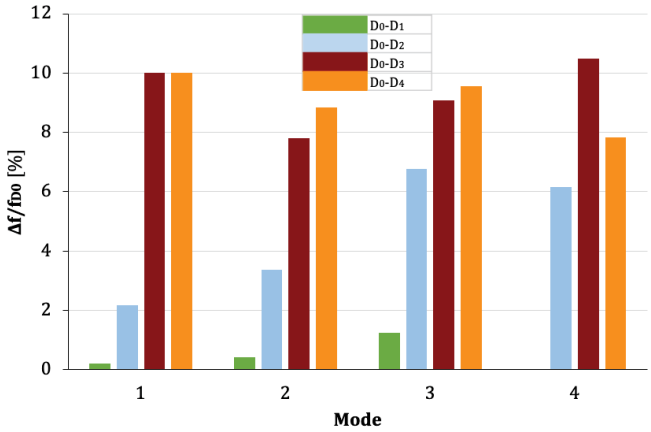

(d) B_3

Figure 6.10 – Variation of frequency values at damage D_i for each RC beam; (a) specimen CB, (b) specimen B_1, (c) specimen B_2, (d) specimen B_3 in hinged ends condition

In hinged conditions, for samples CB and B_3 is recorded a clear decrease in the frequency values as the damage state increases, for samples B_1 and B_2 a more fluctuating frequency trend is noted.

In Figure 6.11 and Figure 6.12 the percent of frequency variations as damage progresses, as compared to the previous damage, calculated as $\frac{\Delta f_r}{f_r{}^{Di}} = 100 \cdot \frac{f_r{}^{Di+1} - f_r{}^{Di}}{f_r{}^{Di}}$, for each of the four vibration modes examined, in free-free ends condition and in hinged condition is shown.

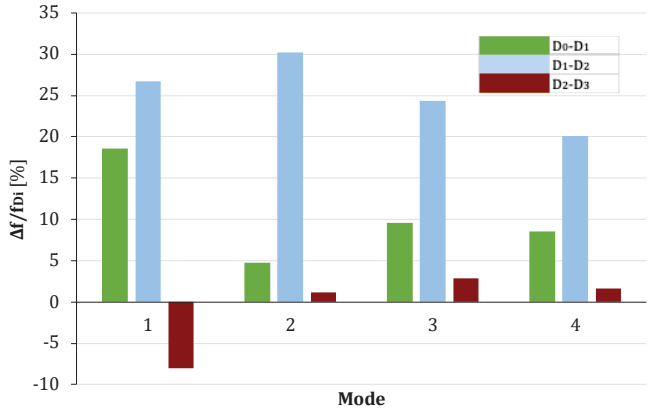

(a) CB

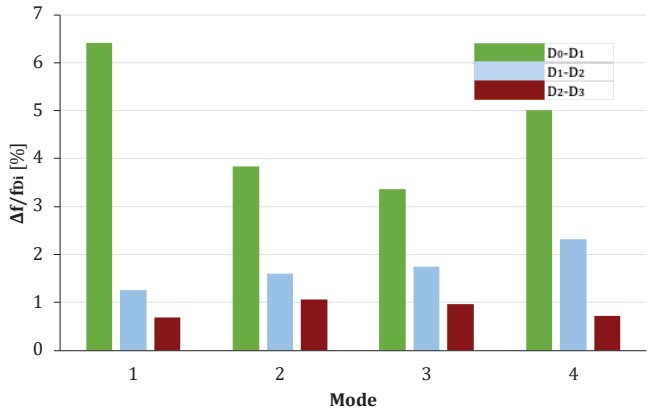

(b) B_1

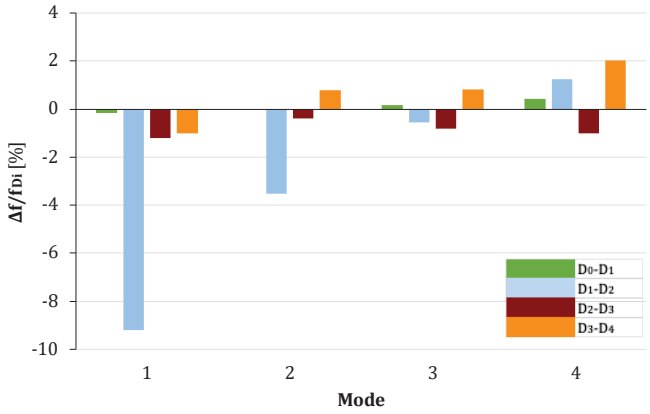

(c) B_2

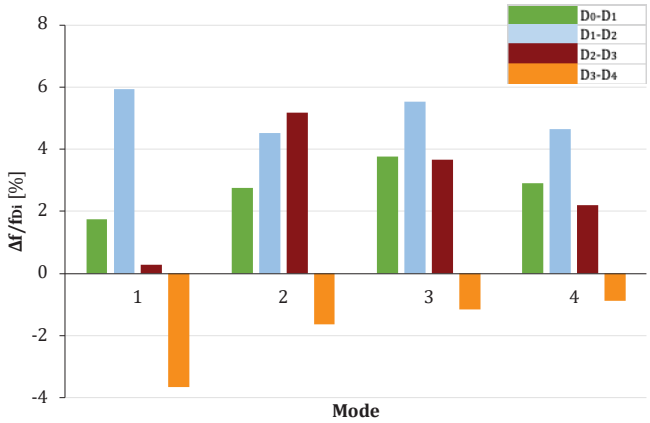

(d) B_3

Figure 6.11 – Variation of frequency values at damage D_{i-1} for each RC beam; (a) specimen CB, (b) specimen B_1, (c) specimen B_2, (d) specimen B_3 in free-free ends condition

Looking at the diagrams in Figure 6.11, it can be concluded that the bending affects the frequency variations especially for the first two load cases, that are the cases during which the concrete begins to crack.
On the other hand, the decrease in the frequency values becomes modest for the last load cases, where in some cases there is even an increase in the values, as previously mentioned.
It can be added that the highest variation values were recorded for the unreinforced CB beam sample, which testifies how the reinforcement is able to mitigate crack damage.

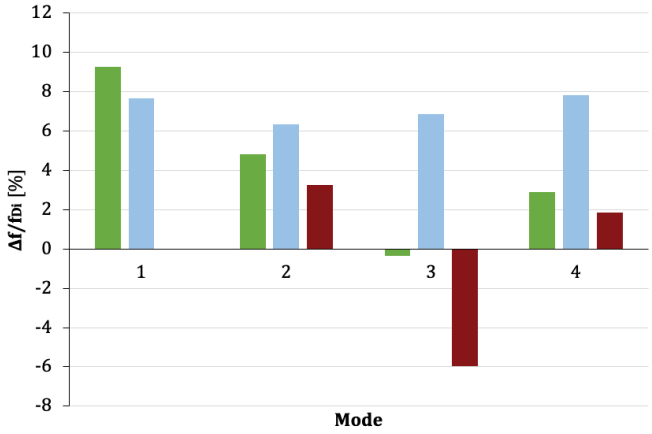

(a) CB

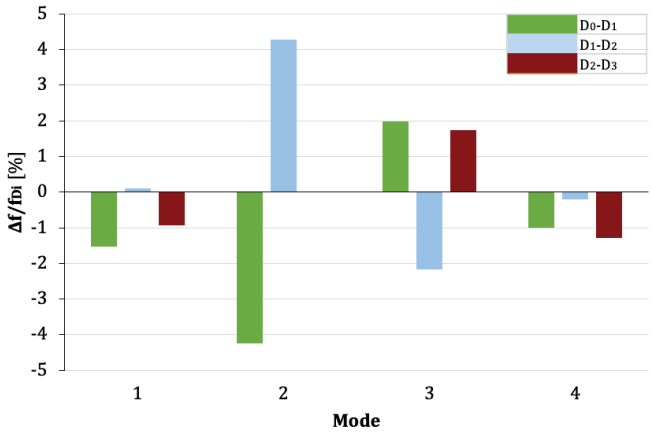

(b) B_1

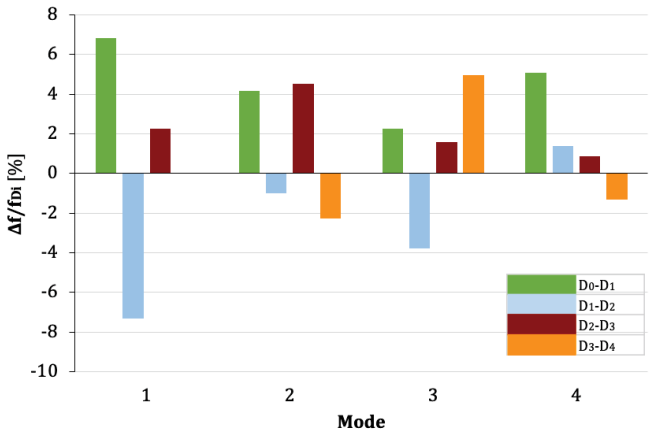

(c) B2

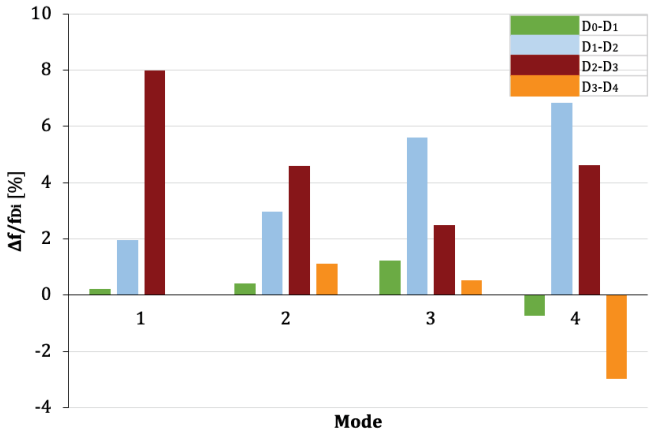

(d) B3

Figure 6.12 – Variation of frequency values at damage D_{i-1} for each RC beam; (a) specimen CB, (b) specimen B_1, (c) specimen B_2, (d) specimen B_3 in hinged ends condition

In this case, the relative frequency variations are noted also for the last load steps.

To complete the diagrams containing the variations in frequency, the following diagrams containing the FRF envelope for different damage degree for each specimen are reported.

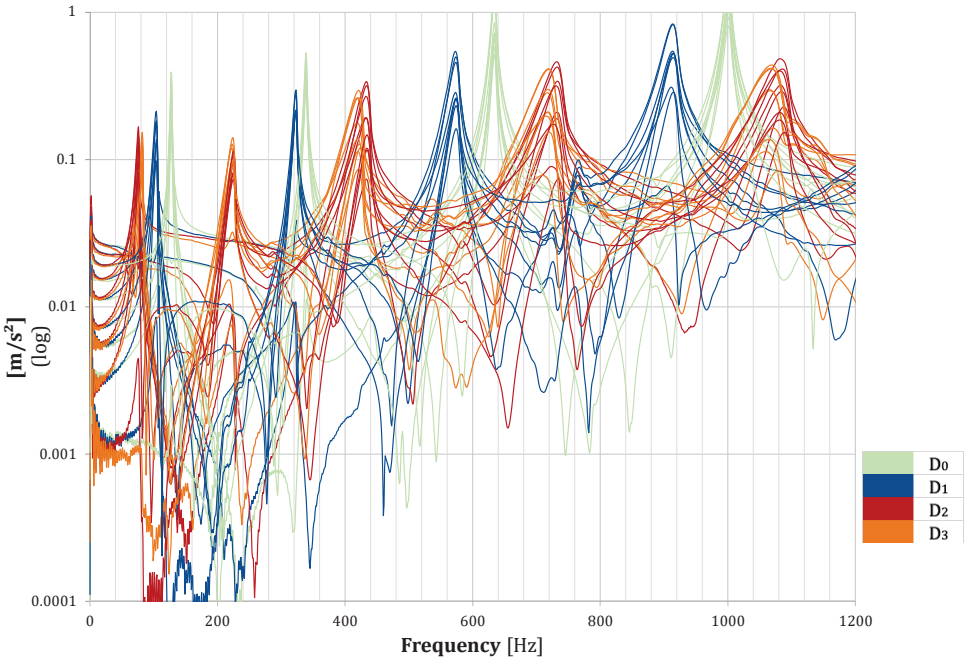
1
0.1
0.01
0.001
0.0001
[m/s²] (log)
0
200
400
600
800
1000
1200
Frequency [Hz]
D0
D1
D2
D3

(a) CB

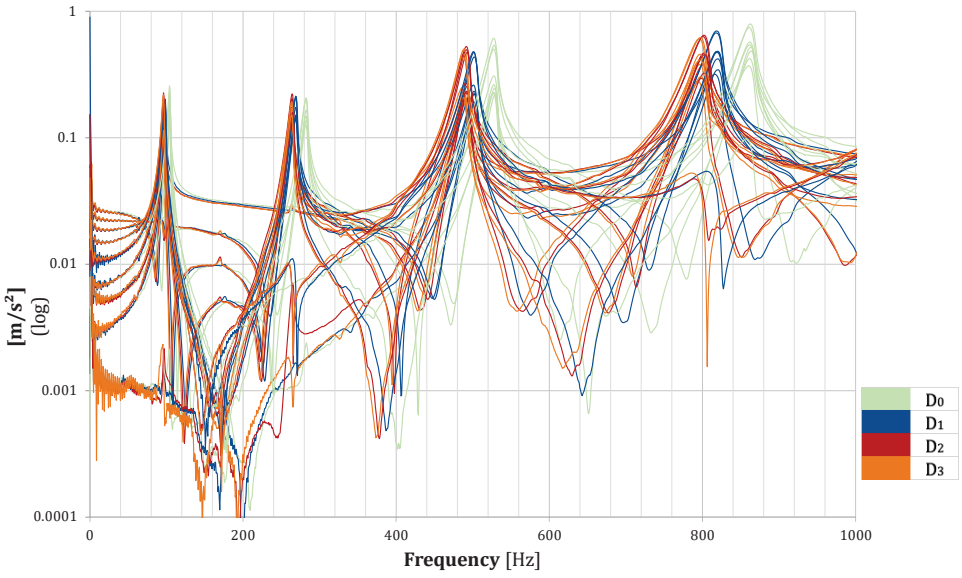
1
0.1
0.01
0.001
0.0001
[m/s²] (log)
0
200
400
600
800
1000
Frequency [Hz]
D0
D1
D2
D3

(b) B_1

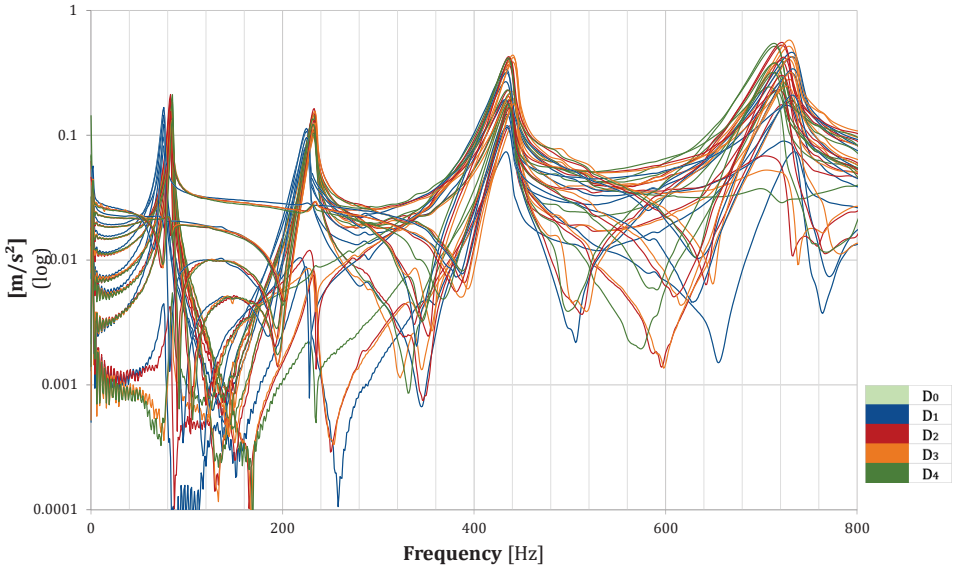

(c) B_2

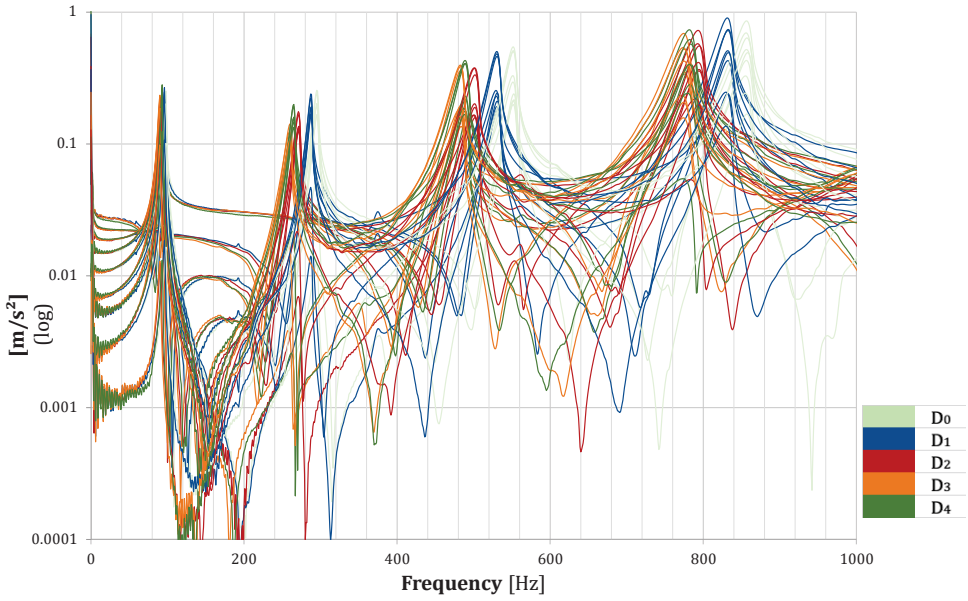

(d) B_3

Figure 6.13 – Envelope of FRFs for damage degree D_i for each RC beam in free-free ends conditions; (a) specimen CB, (b) specimen B_1, (c) specimen B_2, (d) specimen B_3

From the FRF envelopes, it is clear the shift of the frequency values from right to left, except for the sample B_2, where the frequency peaks are for the most part overlapping.

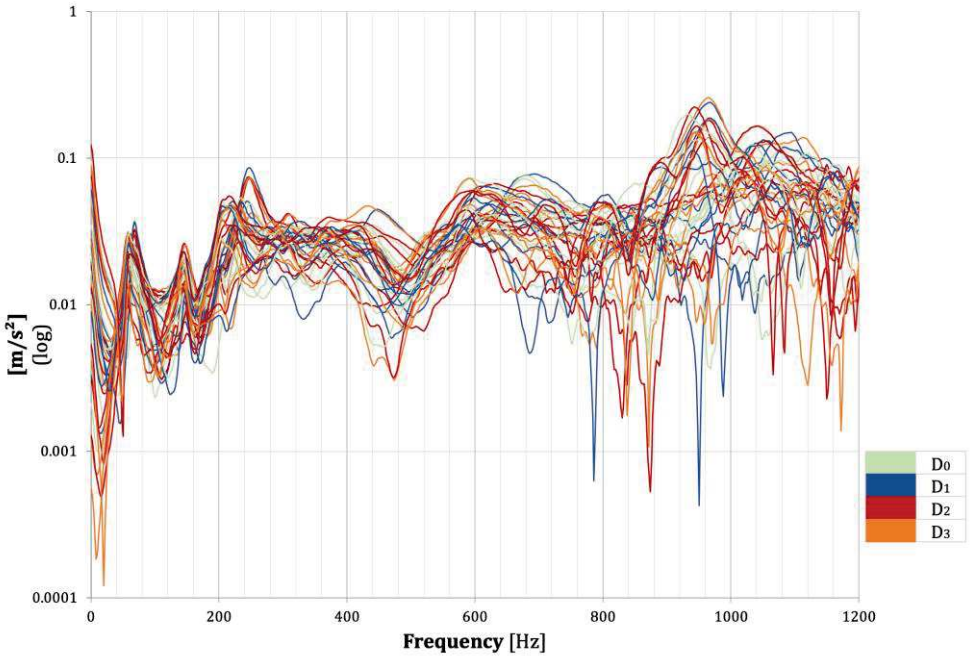
1
0.1
0.01
0.001
0.0001
[m/s²] (log)
0
200
400
600
800
1000
1200
Frequency [Hz]
D0
D1
D2
D3

(a) CB

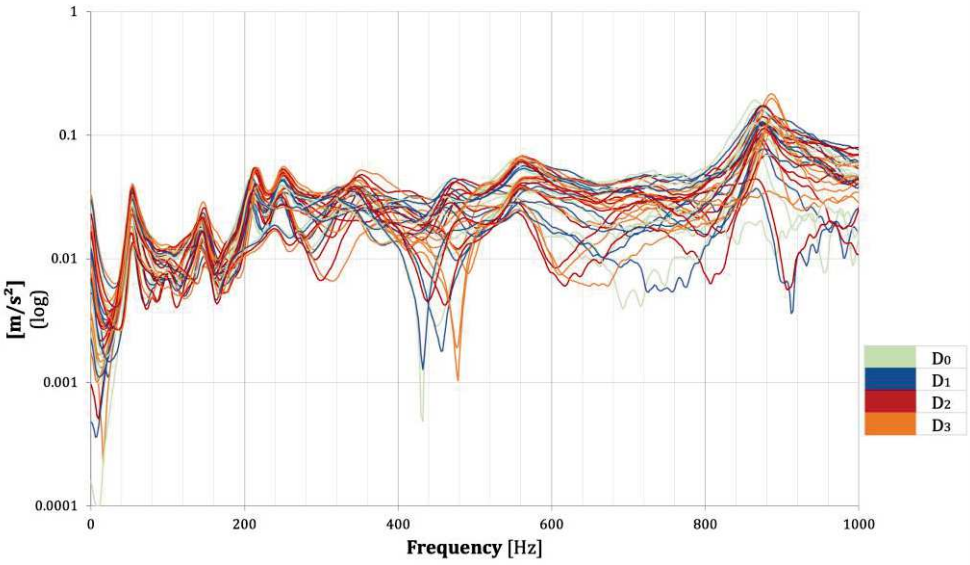
1
0.1
0.01
0.001
0.0001
[m/s²] (log)
0
200
400
600
800
1000
Frequency [Hz]
D0
D1
D2
D3

(b) B_1

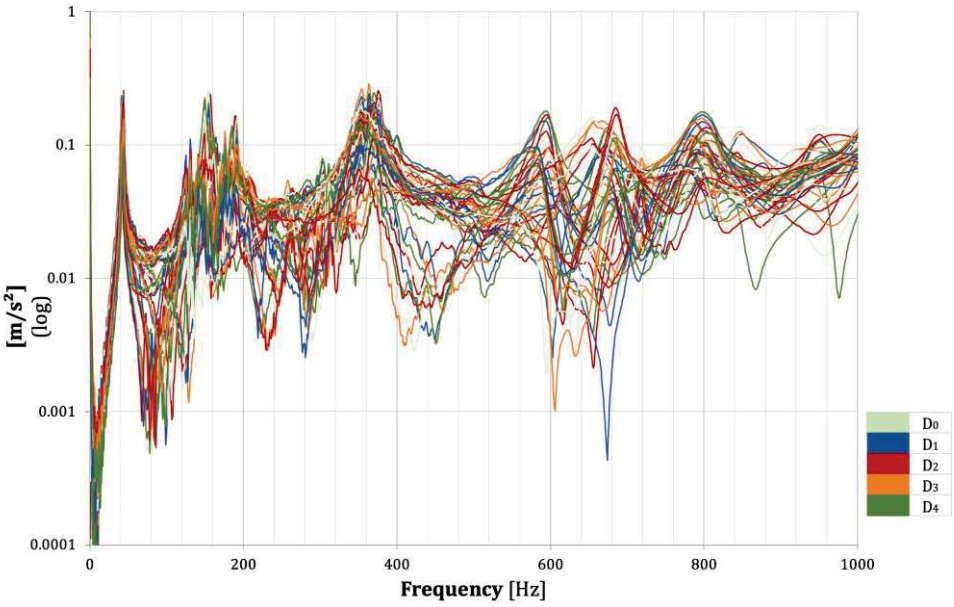

(c) B_2

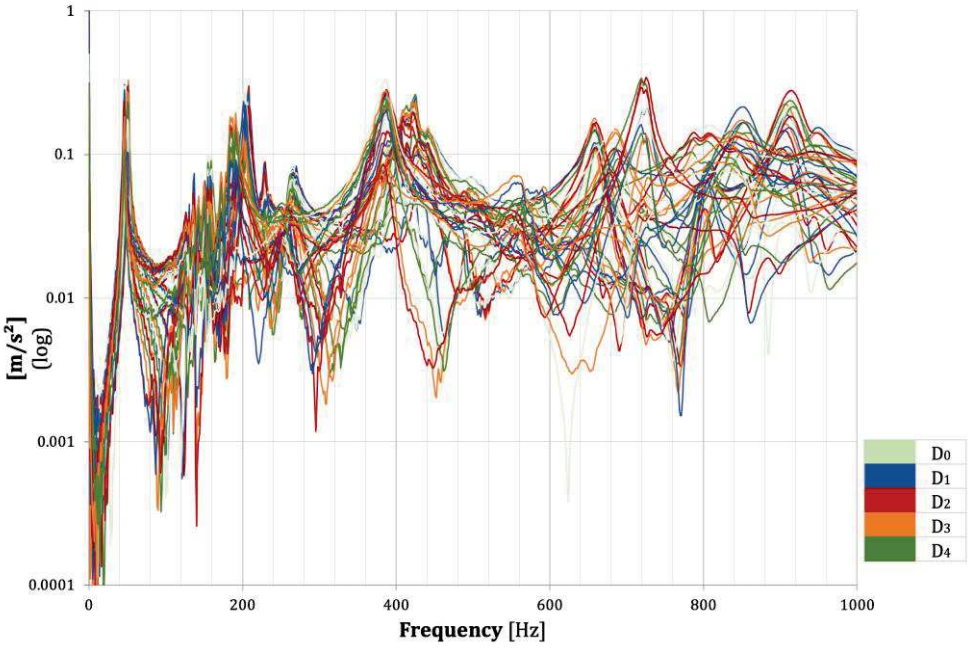

(d) B_3

Figure 6.14 – Envelope of FRFs for damage degree D_i for each RC beam in hinged ends conditions; (a) specimen CB, (b) specimen B_1, (c) specimen B_2, (d) specimen B_3

From the FRF envelopes diagram it is even clearer that for the beam samples tested in a hinged condition there are numerous peaks that do not always correspond to

the natural vibration frequencies; moreover, the results are not easy to understand also due to the reduced frequency amplitude.

6.4.2. Comparison between types of reinforcement

After determining the percentage variations at different damage states, comparisons were made between experimental beam models, to evaluate the incidence of different types of strengthening.

In Figure 6.15 and Figure 6.19 a comparison of absolute frequency percentage variations at damage state D_i in relation to the initial condition D_0 is reported, while in Figure 6.16 and Figure 6.20 a comparison of relative frequency percentage variations at damage state D_{i+1} in relation to the previous damage condition D_i is shown, for each specimen, in both constraints conditions.

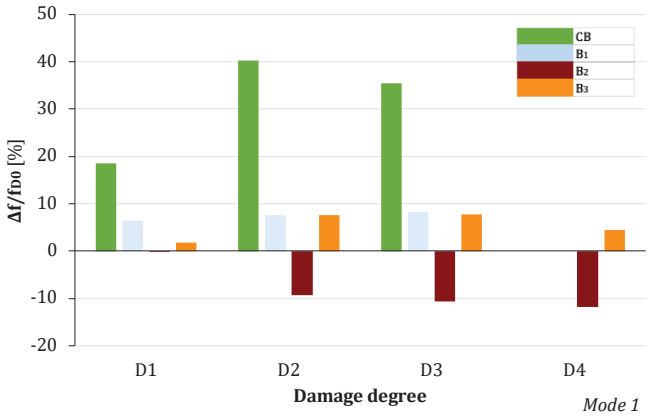

(a)

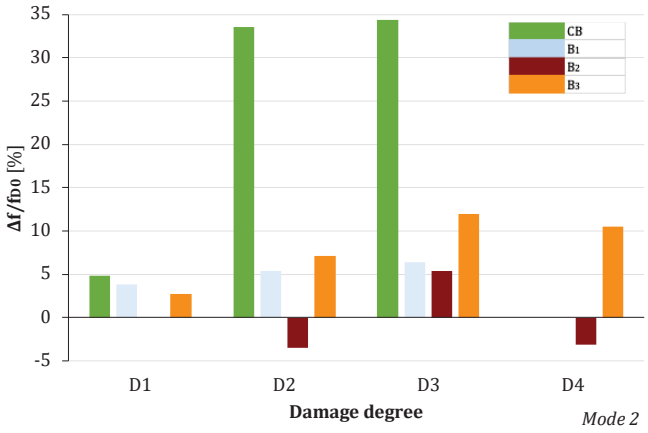

(b)

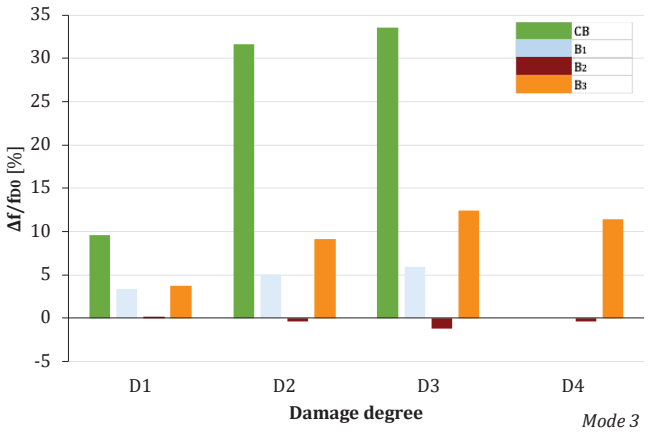

(c)

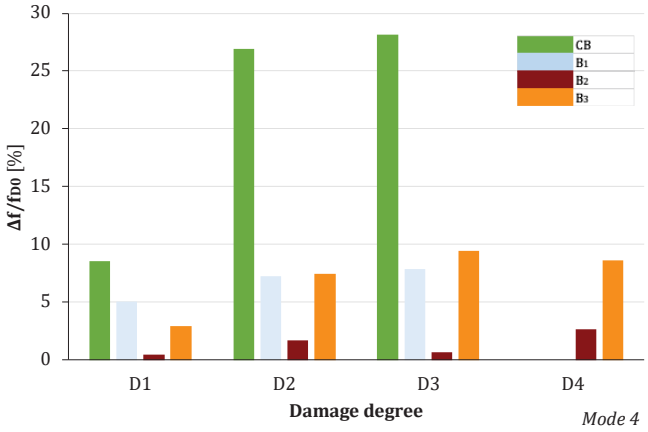

(d)

Figure 6.15 – Comparison between frequency variation of beam models in free-free ends conditions, at damage D_i compared to D_0, for the first four vibration modes: (a) mode 1; (b) mode 2; (c) mode 3; (d) mode 4

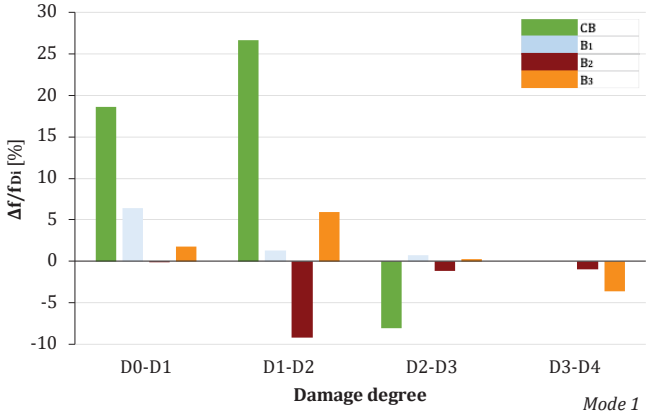

(a)

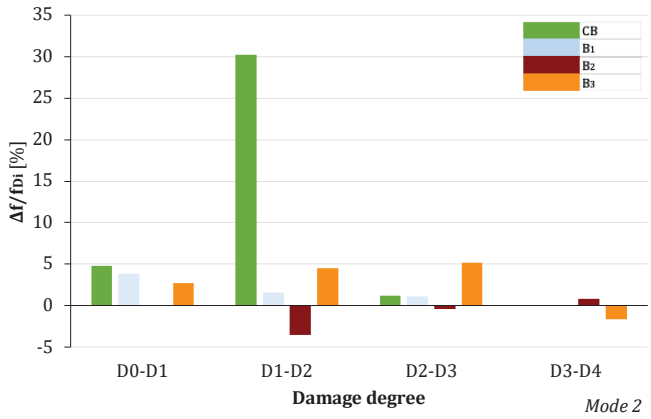

(b)

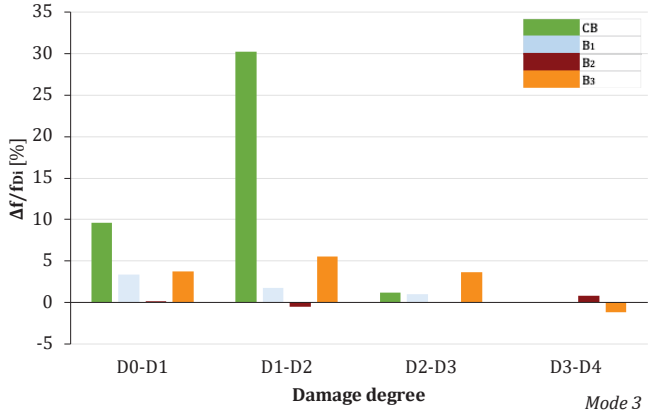

(c)

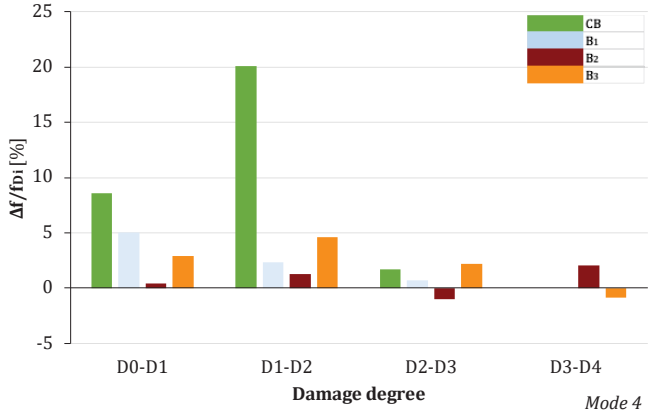

(d)

Figure 6.16 – Comparison between frequency variation of beam models in free-free ends conditions, at damage D_{i+1} compared to D_i, for the first four vibration modes: (a) mode 1; (b) mode 2; (c) mode 3; (d) mode 4

From the data in free condition, it emerges that the absolute variations of frequency are higher in the case of the CB beam, among the strengthened samples, the B_2 beam is the one that records the least variation, therefore where the FRP reinforcement is more effective.

As regards the relative variations, the following is observed:

- the CB beam is more affected by the first cracking that occurs with the load cycle D_2, recording in this phase the maximum frequency variations with respect to the previous cycle;
- for beam B_1 the relative maximum variations are found in correspondence with the first loading cycle D_1, while for samples B_2 and B_3 the cracking seems to be delayed by one loading cycle, as higher variations are recorded in correspondence of step D_2.

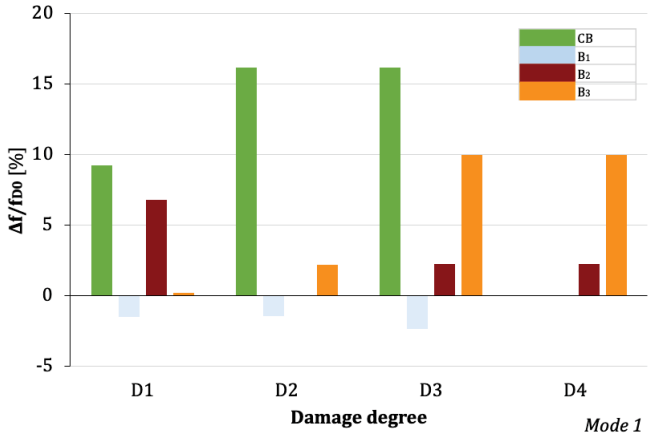

(a)

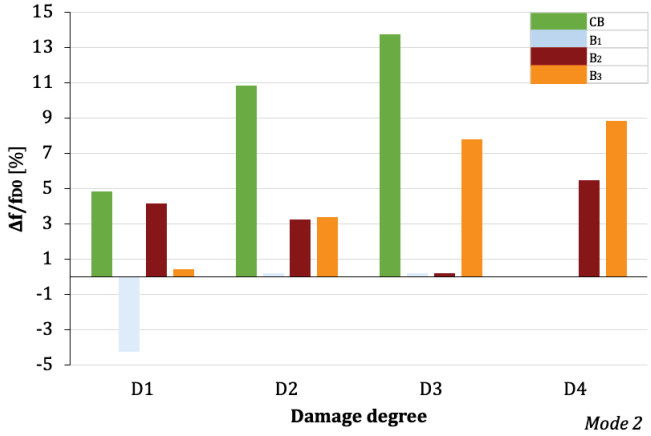

(b)

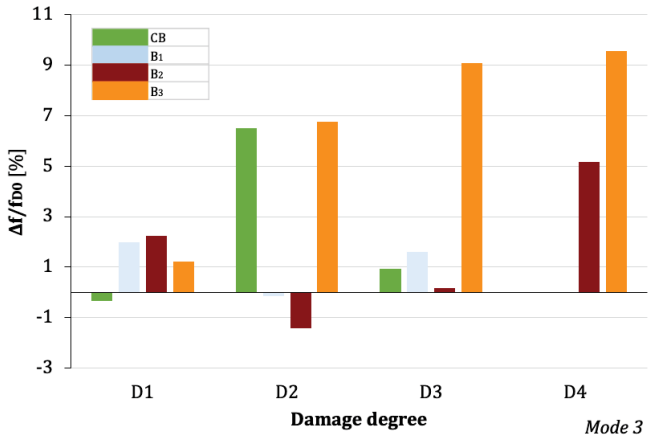

(c)

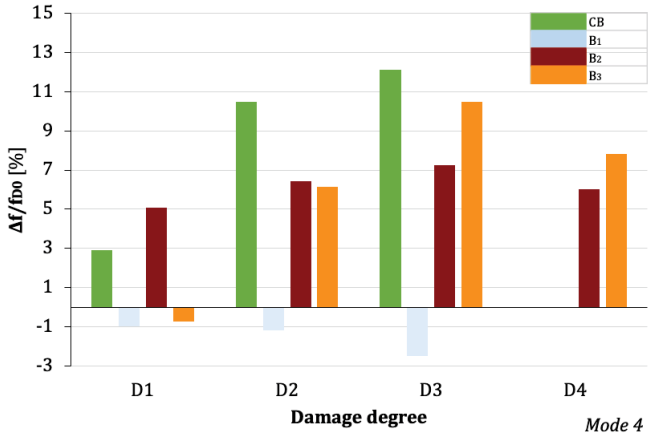

(d)

Figure 6.17 – Comparison between frequency variation of beam models in hinged ends conditions, at damage D_i compared to D_0, for the first four vibration modes: (a) mode 1; (b) mode 2; (c) mode 3; (d) mode 4

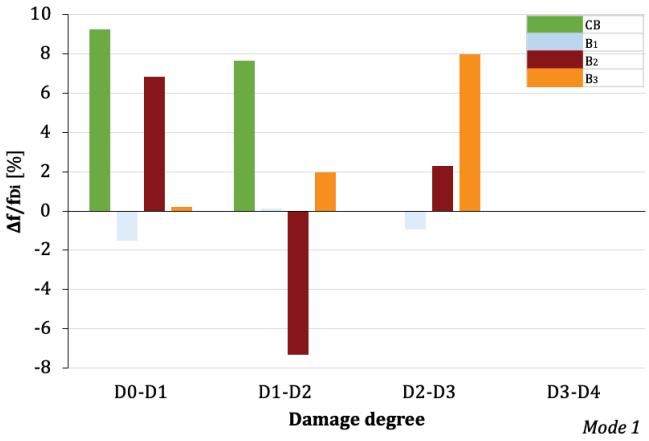
10
8
6
4
2
0
-2
-4
-6
-8
Δf/fDi [%]
CB
B1
B2
B3
D0-D1
D1-D2
D2-D3
D3-D4
Damage degree
Mode 1

(a)

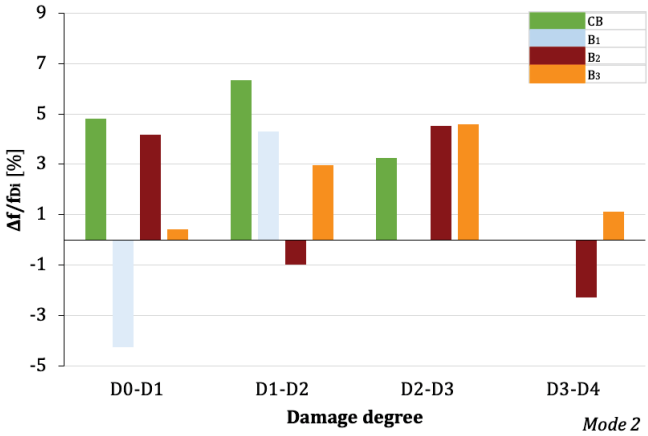
9
7
5
3
1
-1
-3
-5
Δf/fDi [%]
CB
B1
B2
B3
D0-D1
D1-D2
D2-D3
D3-D4
Damage degree
Mode 2

(b)

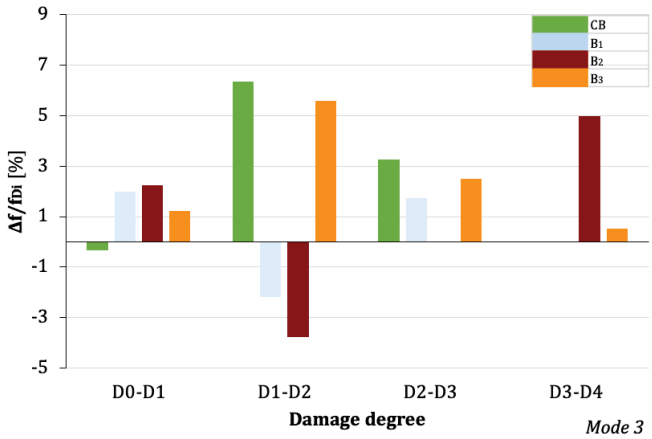

(c)

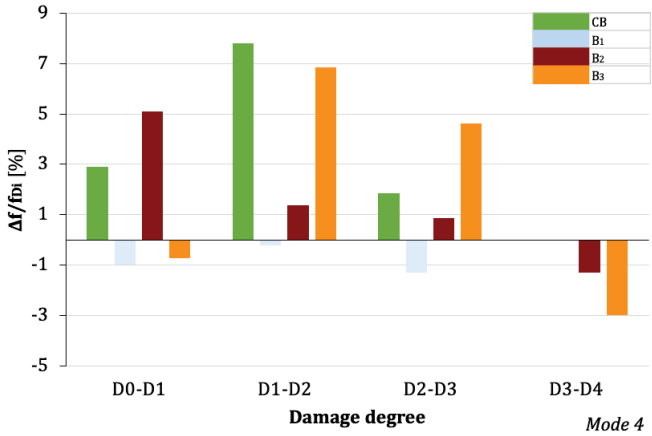

(d)

Figure 6.18 – Comparison between frequency variation of beam models in hinged ends conditions, at damage D_{i+1} compared to D_i, for the first four vibration modes: (a) mode 1; (b) mode 2; (c) mode 3; (d) mode 4

In the hinged condition, beam B_1 is the one that shows the least variations in absolute frequencies, while beams B_2 and B_3 show higher variations especially in vibration modes higher than the first one.
From the relative variation diagrams, it is possible to notice approximately constant values, always slightly higher in correspondence with steps D_2 and D_3, confirming what was previously stated.

6.4.3. Comparison with theoretical results

Table 6.7 and Table 6.8 contain theoretical frequency values obtained applying Euler-Bernoulli's formula and the experimental average frequency values measured for the four specimens in the un-damaged condition D_0, for the first four vibration modes, respectively in free-free ends conditions and hinged conditions.

Table 6.7 – Theoretical frequency values for Euler-Bernoulli beam model and experimental frequency values for undamaged beam specimens (D_0) for the first four modes of vibration in free-free end conditions

Beam Type	f_1 (Hz)	f_2 (Hz)	f_3 (Hz)	f_4 (Hz)
Th. Euler-Bernoulli	126.17	347.68	681.84	1126.48
Exp. CB	127.13	339.00	634.11	1001.00
Exp. B_1	102.95	275.84	520.17	852.29
Exp. B_2	75.88	224.71	434.56	733.38
Exp. B_3	96.56	296.00	554.78	861.67

Table 6.8 – Theoretical frequency values for Euler-Bernoulli beam model and experimental frequency values for undamaged beam specimens (D_0) for the first four modes of vibration in hinged end conditions

Beam Type	f_1 (Hz)	f_2 (Hz)	f_3 (Hz)	f_4 (Hz)
Th. Euler-Bernoulli	55.63	222.51	500.66	890.06
Exp. CB	68.00	246.44	430.00	1079.20
Exp. B_1	52.75	227.75	352.00	865.00
Exp. B_2	44.00	159.78	371.11	844.00
Exp. B_3	51.11	208.00	427.25	906.00

Below there is a comparison between theoretical and experimental frequency values (Figure 6.19 and Figure 6.20).

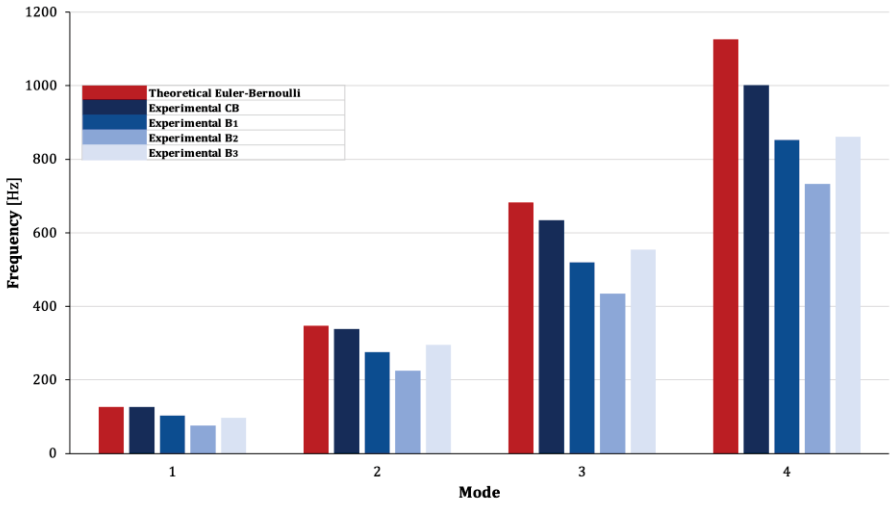

Figure 6.19 – Comparison between theoretical and experimental frequency values relative to un-damaged condition, for specimens in free-free ends

From this comparison it can be seen that the experimental frequencies are lower than the theoretical ones: for the CB beam, which corresponds exactly to the simulated beam in the calculation of the theoretical frequencies, as it is un-strengthened with FRP and not damaged, the experimental frequency values recorded are very similar to the theoretical ones, especially for the first two vibrate modes (average deviation of 5%).

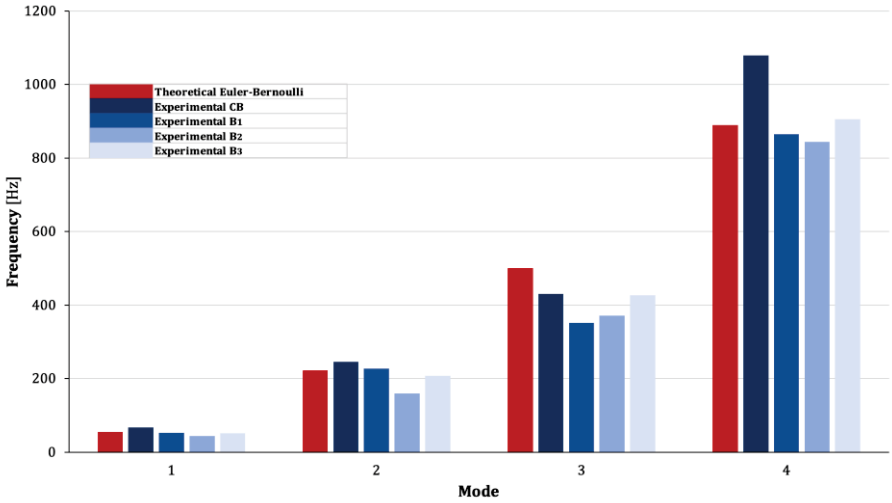

Figure 6.20 – Comparison between theoretical and experimental frequency values relative to un-damaged condition, for specimens in hinged ends

In this case an average deviation of 17% is recorded or the CB beam, for which higher frequency values are obtained for the first, for the second and for the fourth mode than the theoretical ones. The lowest variation among the frequency values is recorded for the second vibration mode and is equal to 11%, the maximum variation

is instead around 22%. However, these values are still acceptable and close to theoretical ones.
This small discrepancy in values can be attributed to the fact that the actual hinge constraint does not too faithfully reproduce the ideal degrees of constraint.

Chapter 7. Numerical modelling of RC beams

This chapter describes the finite element modeling performed for the analyzed beam specimens. A dynamic analysis was carried out on 3D models of reinforced concrete beams, strengthened and not, even in the presence of damage due to cracking of the concrete in order to create a mathematical model capable of comparing and verifying the results obtained from the experimentation.
In particular, the procedure followed for modeling, the creation of the finite element geometry, the choice of the types of elements, material modeling, the definition of the mesh, the application of loads and restraints are described.
From the numerical analysis carried out, the modal forms, the values of the natural frequencies of vibration, the absolute and relative percentage frequency variation are evaluated.
The numerical analysis has been developed only for the free condition beam models. The results of the analysis were then compared with the experimental data.

7.1. Introduction

The calculation software used for the finite element analysis is Ansys v.16. The Ansys software processor is divided into three levels: modeling phase (Preprocessing), numerical solution phase (Solution) and results reading phase (Postprocessing).
The ANSYS calculation code has no unit of measurement; it is therefore up to the operator, during the creation of the model, to insert the values consistently, in order to interpret the results correctly. In the following modeling, the International System (SI) of units is used (the meter for lengths and the Newton derivative for forces).

7.2. Dynamic Analysis

The purpose of the dynamic analysis is to define the dynamic behavior of the elements investigated, i.e., to define the natural vibration frequencies and the modal forms, as the damage degree of the beams increases.
As crack damage causes a reduction in the stiffness of the element, with a reduction in natural frequencies and an increase in modal damping, to correctly determine the

theoretical frequencies of the modeling at the different damage states, a reduced elastic modulus was used, evaluated experimentally.

7.2.1. Geometry

The creation of the geometry was carried out according to the direct approach, that is, by directly entering the coordinates of each node, proceeding in blocks. In this way you have complete control of the geometry and the mesh, but it's a method that takes a long time, especially for large elements such as the one in question.
To reduce computational costs and to make the results more accurate, it was decided to assign different meshes to the blocks and refine the mesh only in some areas, where it's necessary, that are in the stress transmission areas, for example in correspondence with the constraints.
Three-dimensional elements were used to generate the beam and the resin; on the other hand, the FRP rods are modeled as lines, defining the start and end points, to which the relative cross sections were then associated.
Three techniques to model steel reinforcement in concrete by finite element are adopted: the discrete model, the embedded model, and the smeared model. The reinforcement in the discrete model uses beam elements that are connected to concrete mesh nodes. The embedded model overcomes the concrete mesh restrictions although increasing the number of nodes and degrees of freedom. The smeared model assumes that the reinforcement is spread uniformly throughout the concrete elements in a defined region.
Obviously, the interface nodes belonging to different blocks or lines must coincide, so that the transmission of the actions on each of them is guaranteed.

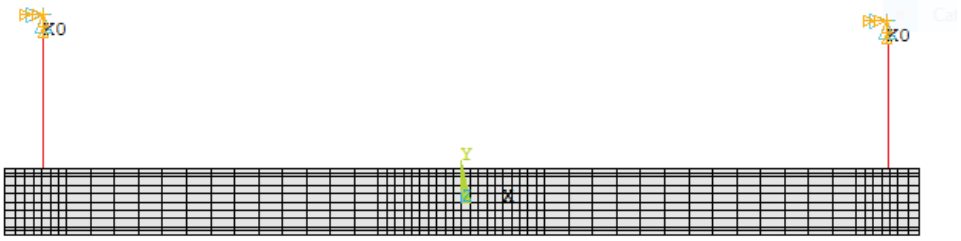

(a)

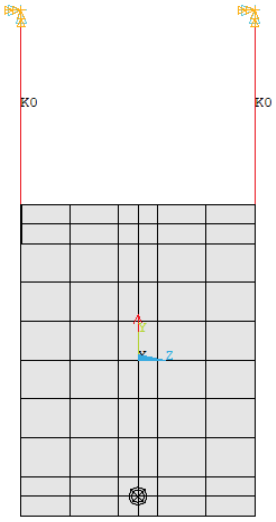

(b)

Figure 7.1 – Typical mesh for FE analysis of RC beam; (a) front view; (b) cross section

7.2.2. Types of elements

Ansys has a library of more than 150 elements; moreover, for many of these it is possible to specify additional options on the behavior and on the definition of the element (keyoptions).
The modeling was carried out using the element called Solid65 for the concrete, the Solid185 for the resin and the Beam188 for the FRP rod.
In those FE models, the straight rebars in the beams are represented using smeared rebar option for the Solid65 elements located closest to the physical rebar positions. Therefore, discrete elements are not required to model the reinforcement. The properties of the smeared rebars are given using element real constants. It is necessary to define a separate real constant for every reinforcement ratio and orientation.
A discrete model, using Link180, was also developed, but it does not bring plausible results.
In addition to these elements used to model the components of the RC beam, Combin14 was used to simulate the elastic springs used during experimental tests.

Table 7.1 – Summary of element type used

Concrete	Solid65	3D 8-node structural solid
Epoxy Resin	Solid185	3D 8-node structural solid
FRP	Beam188	Structural 3D 2-node beam
Elastic Spring	Combin14	Combination Spring-Damper

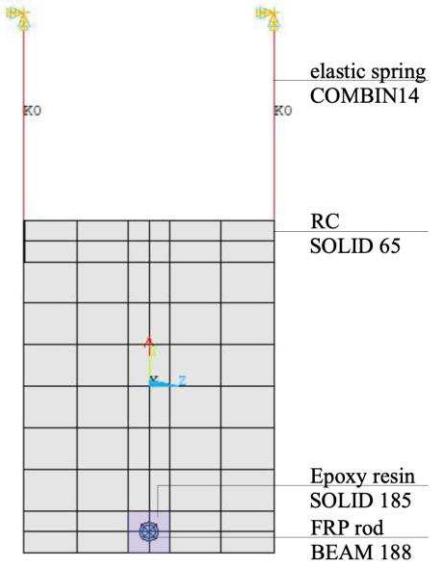

Figure 7.2 – Items of beam section

SOLID65 is used for 3-D modeling of solids with or without reinforcing bars (rebar). The solid is capable of cracking in tension and crushing in compression. In concrete applications, for example, the solid capability of the element may be used to model the concrete while the rebar capability is available for modeling reinforcement behavior. The element is defined by eight nodes having three degrees of freedom at each node: translations in the nodal x, y, and z directions. Up to three different rebar specifications may be defined.
The concrete element is similar to a 3-D structural solid but with the addition of special cracking and crushing capabilities. The most important aspect of this element is the treatment of nonlinear material properties. The concrete is capable of cracking (in three orthogonal directions), crushing, plastic deformation, and creep. The rebars are capable of tension and compression, but not shear. They are also capable of plastic deformation and creep.

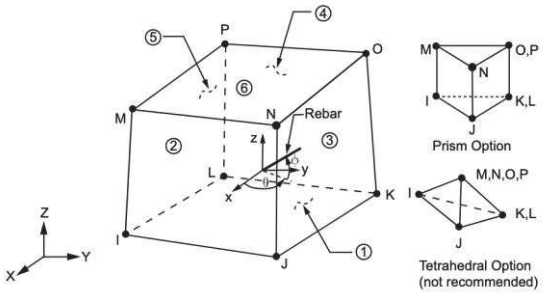

Figure 7.3 – Solid65 element type as defined in Ansys [88]

SOLID185 is used for 3-D modeling of solid structures. It is defined by eight nodes having three degrees of freedom at each node: translations in the nodal x, y, and z directions. The element has plasticity, hyper elasticity, stress stiffening, creep, large deflection, and large strain capabilities. It also has mixed formulation capability for

simulating deformations of nearly incompressible elastoplastic materials, and fully incompressible hyper elastic materials. This structural solid is suitable for modeling general 3-D solid structures. It allows for prism, tetrahedral, and pyramid degenerations when used in irregular regions. Various element technologies such as B-bar, uniformly reduced integration, and enhanced strains are supported.

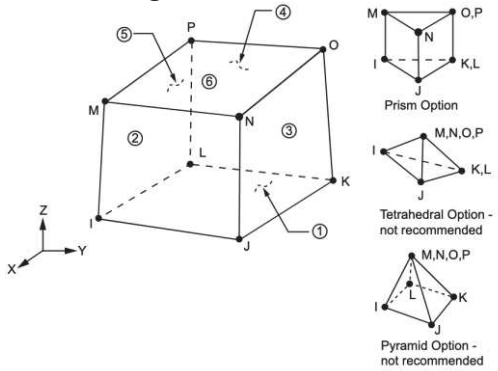

Figure 7.4 – Solid185 element type as defined in Ansys [88]

BEAM188 is suitable for analyzing slender to moderately stubby/thick beam structures. The element is based on Timoshenko beam theory which includes shear-deformation effects. The element is a linear, quadratic, or cubic two-node beam element in 3-D. BEAM188 has six or seven degrees of freedom at each node. This element is well-suited for linear, large rotation, and/or large strain nonlinear applications. A cross-section associated with this element type can be a built-up section referencing more than one material.

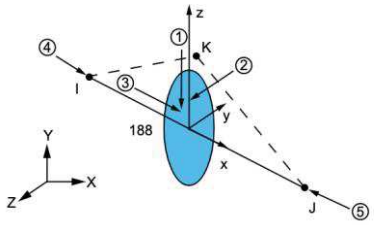

Figure 7.5 – Beam188 element type as defined in Ansys [88]

COMBIN14 has longitudinal or torsional capability in 1-D, 2-D, or 3-D applications. The longitudinal spring-damper option is a uniaxial tension-compression element with up to three degrees of freedom at each node: translations in the nodal x, y, and z directions. No bending or torsion is considered. The torsional spring-damper option is a purely rotational element with three degrees of freedom at each node: rotations about the nodal x, y, and z axes. No bending or axial loads are considered. The spring-damper element has no mass.

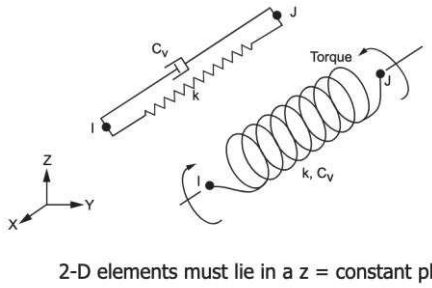

Figure 7.6 – Combin14 element type as defined in Ansys [88]

7.2.3. Material modelling

After the definition of the elements, we proceeded to characterize the models of the constituent materials and their properties: concrete, steel, resin, GFRP and CFRP. These characteristics depend not only on the behaviour of the material, but also on the type of analysis to be carried out.
Having to perform a modal analysis, a linear and isotropic elastic behavior (Linear Elastic Isotropic) has been defined for all material expressed by Hooke's law by defining the two fundamental independent parameters:

- the elastic modulus;
- the Poisson's coefficient.

In addition to these, the density of each material was defined.
For concrete in intact condition, the value of elastic modulus was calculated from the experimental characteristic strength, in accordance with the NTC 2018 [86], using the formula (4.1). The Poisson's coefficient was assumed to be equal to 0.15.
For the steel reinforcement bars the elastic modulus was assumed to be equal to 210 000 MPa, while the Poisson's ratio was assumed to be equal to 0.15.
For the epoxy resin the value of elastic modulus was assumed equal to 1597 MPa, while the Poisson's ratio was assumed to be equal to 0.48 as obtained experimentally.
For GFRP and CFRP Elastic modulus was assumed equal to respectively 40800 MPa and 155000 MPa, reported in data technical sheet, while the Poisson's ratio was assumed to be equal to 0.29, taking values found in literature.
For element COMBIN14, instead, a material with a rather high elastic modulus was defined, in order to represent an infinite stiffness, and a Poisson's ratio equal to 0.1.

Table 7.2 – Parameters used in Ansys model

	Elastic Modulus (MPa)	Poisson's Ratio	Density (N/mm^3)
RC	34493	0.15	$2.43 \cdot 10^{-5}$
Epoxy Resin	1597	0.48	$1.61 \cdot 10^{-5}$
GFRP	40800	0.29	$2.00 \cdot 10^{-5}$
CFRP	155000	0.29	$1.54 \cdot 10^{-5}$
Spring	1000000	0.1	-

Wanting to determine the modal parameters of the beams even in cracked conditions, we worked on the elastic modulus of the concrete.
Since during the static tests there were some cracks spread along the entire length of the beam, the elastic modulus of the concrete was changed from time to time, to simulate the cracking damage caused by load cycles.
The reduced elastic modulus for each damage level was calculated using an experimental law:

$$E = \Gamma(f_r) \tag{7.1}$$

determined starting from the Euler-Bernoulli theoretical formula (4.54) assuming the homogeneous beam in free-free condition and considering the natural frequencies experimentally measured at the different damage states.
Table 7.3 shows the values of the reduced elastic modulus obtained starting from the experimental frequencies relating to the first mode of vibration, used in the modeling.

Table 7.3 – Elastic modulus of beams for numerical model, related to the first mode of vibration, at different damage degree Di

CB		
Damage degree	**f_1 (Hz)**	**E (MPa)**
D_0	127.13	34494[4]
D_1	103.50	23213
D_2	75.88	12477
D_3	82.00	14570
B_1		
Damage degree	**f_1 (Hz)**	**E (MPa)**
D_0[5]	102.95	22966
D_1	96.35	20116
D_2	95.14	19614
D_3	94.49	19347
B_2		
Damage degree	**f_1 (Hz)**	**E (MPa)**
D_0[5]	75.88	12477
D_1	76.00	12516
D_2	83.00	14928
D_3	84.00	15290
D_4	84.86	15604

[4] The value of elastic modulus of CB in the initial un-damaged condition is the real one calculated with (4.1).

[5] Undamaged condition is at the beginning of vibration test for strengthened beams.

	B3	
Damage degree	**f_1 (Hz)**	**E (MPa)**
D_0[5]	96.56	20204
D_1	94.88	19507
D_2	89.25	17261
D_3	89.00	17164
D_4	92.25	18441

7.2.4. Mesh definition

After modeling of beams the next step for finite element analysis is meshing of the model. The model is divided into several small elements termed as meshing. Selection of the mesh density is fundamental for the convergence of the solution. The convergence of results is obtained when an adequate number of elements are used in a model. This is practically achieved when an increase in the mesh density has a negligible effect on the results. To obtain good results from the Solid65 element, the use of a rectangular mesh is selected. Therefore, the mesh was set up such that square elements were created.
As anticipated, the mesh was refined in some areas: in midspan section and at elastic springs. In these areas the mesh size was assumed of 10 mm length, while in the other areas of 60 mm length (x direction).
The mesh in the other two directions is imposed by the size of the groove and the presence of the FRP reinforcing bar, so the cross section of the beam has a mesh of varying sizes.
The lines representing the suspension ropes were also meshed.

7.2.5. Restraints

As already mentioned, the constraints applied to the model are those adopted in the experimentation. To simulate the free condition of the beam, this was hung by means of elastic cords. These ropes were simulated with the Combin14 element and were wedged at the upper ends (Ux=0, Uy=0, Uz=0).

7.2.6. Analysis setup

In the finite element models, a modal analysis was performed, with the aim of determining the dynamic characteristics, therefore the natural frequencies and the vibration modes of the system under examination. Modal analysis ignores any kind of external force; therefore, the characteristic equation valid for discrete domains with n degrees of freedom is given by:

$$[M]\{\ddot{u}(t)\} + [C]\{\dot{u}(t)\} + [K]\{u(t)\} = 0 \quad (7.2)$$

Considering a harmonic elastic behavior of the structure, the response of the system can be approximated to a sinusoidal shape; therefore, the displacement, velocity and nodal acceleration functions of the domain are:

$$\{u(t)\} = \{\phi_i\}\cos(\omega_i t); \quad (7.3)$$

$$\{\dot{u}(t)\} = \omega_i\{\phi_i\}\sin(\omega_i t); \quad (7.4)$$

$$\{\ddot{u}(t)\} = {\omega_i}^2\{\phi_i\}\cos(\omega_i t); \quad (7.5)$$

Where ω_i is the frequency of the i-th node, $\{\phi_i\}$ is the vector of maximum nodal shift, *t* is the time.

Substituting (7.3) (7.4) (7.5) in (7.2) we obtain an eigenvalue and eigenvector problem expressed in the form:

$$([K] + i\omega_i[C] - \omega_i^2[M]) \cdot \{\phi_i\} = 0 \quad (7.6)$$

Whose solution are

$$([K] + i\omega_i[C] - \omega_i^2[M]) = 0 \quad (7.7)$$

Where ω_i is the eigenvalue and represents the natural frequency of the system; $\{\phi_i\}$ is the eigenvector of the equation and indicates the mode of vibration of the structure (modal form).

Hence, from the equation (7.7) we obtain *n* proper solution (ω_1^2, ϕ_1); (ω_2^2, ϕ_2); … ; (ω_n^2, ϕ_n), which represent the natural frequencies and the corresponding modal forms (where *n* indicate the number of degrees of freedom of the system).

In the Ansys finite element computation code, there are five different algorithms to extract the eigenvalues of the problem equation, then to approximate the solution; the use of each technique depends on the size of the model, the computational resources and the specific application.

In the present analysis, the *Block Lanczos* method was used, as it is efficient for the extraction of a considerable number of modes from larger models and can be adopted in mixed models that have different elements used (solids / shell / beams); it is the most used algorithm in most applications. For this it was sufficient to set a number of modes to be extracted (20), so as to be able to determine the first four significant bending modes for the beam models under examination; all other parameters for the dynamic analysis setting have been left at their default value.

Finally, for the purposes of the dynamic analysis, the damping was set equal to 0.04.

7.3. Results of Dynamic Analysis

Below the results obtained from the modal analysis by FEM in terms of frequencies and modal forms, in the various damage conditions, are reported. Also, the comparisons with the experimental results are shown.

7.3.1. Modal forms

The typical modal forms of finite element beam models with free-free constraint conditions are determined. In the proper modes of vibrating the six modes of rigid body are excluded, characterized by natural frequencies equal to 0 Hz.

In Figure 7.7 the first four modes of flexural vibrations are shown, these modal forms are valid for all the beam models investigated.

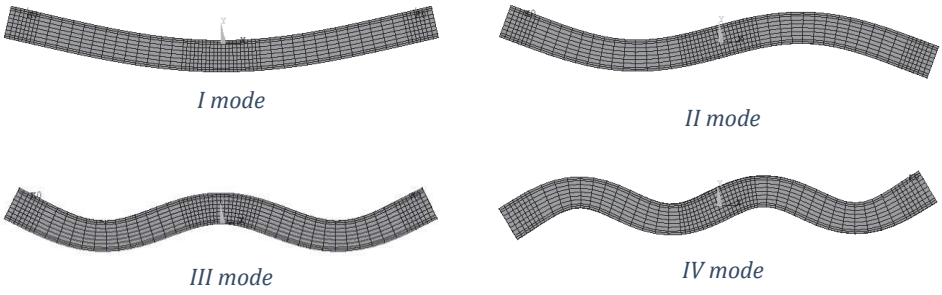

Figure 7.7 – First four flexural vibration modes for beam models obtained with Ansys modeling

7.3.2. Natural frequencies

In Table 7.4 FEM frequencies of vibration calculated for each beam model, at each state of damage, obtained by varying the elastic modulus of the concrete are shown.

Table 7.4 – Proper frequency obtained by FEM for the first mode of vibration for each beam model

CB				
Damage degree	**f_1 (Hz)**	**f_2 (Hz)**	**f_3 (Hz)**	**f_4 (Hz)**
D_0	124.37	333.78	631.18	1000.60
D_1	102.12	274.10	518.38	821.86
D_2	75.06	201.49	381.13	604.48
D_3	81.05	217.56	411.50	652.56
B1				
Damage degree	**f_1 (Hz)**	**f_2 (Hz)**	**f_3 (Hz)**	**f_4 (Hz)**
D_0[6]	102.10	274.11	517.06	816.87
D_1	95.69	256.87	484.42	765.00
D_2	94.51	253.72	478.44	755.50
D_3	93.88	252.02	475.23	750.39
B2				
Damage degree	**f_1 (Hz)**	**f_2 (Hz)**	**f_3 (Hz)**	**f_4 (Hz)**
D_0[6]	75.84	203.58	383.42	604.36
D_1	75.96	203.89	384.00	605.29
D_2	82.73	222.08	418.50	660.18
D_3	83.70	224.69	423.44	661.41
D_4	84.53	226.92	427.67	667.61
B3				
Damage degree	**f_1 (Hz)**	**f_2 (Hz)**	**f_3 (Hz)**	**f_4 (Hz)**
D_0[6]	97.64	261.03	488.62	767.65
D_1	96.03	256.70	480.36	754.46
D_2	90.66	242.21	452.71	710.28
D_3	90.42	241.57	451.47	708.31
D_4	93.52	249.93	467.44	733.82

Observing the frequency values, it is possible to notice a decrease of these as the damage state increases, as for the theoretical values. In some cases, for the last load steps, there is a slight increase in the frequency's values, however this increase has been recorded even during the experimental tests, the model is therefore valid for the dynamic analysis and consistent with the trend of the values of the elastic modules calculated.
Below is reported a graphical representation of the frequencies and their variation as the state of damage increases for each beam model (Figure 7.8).

[6] Undamaged condition is at the beginning of vibration test for strengthened beams.

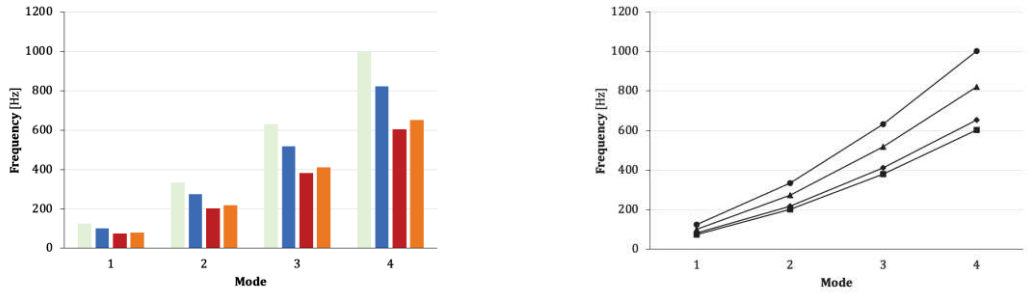

(a) CB

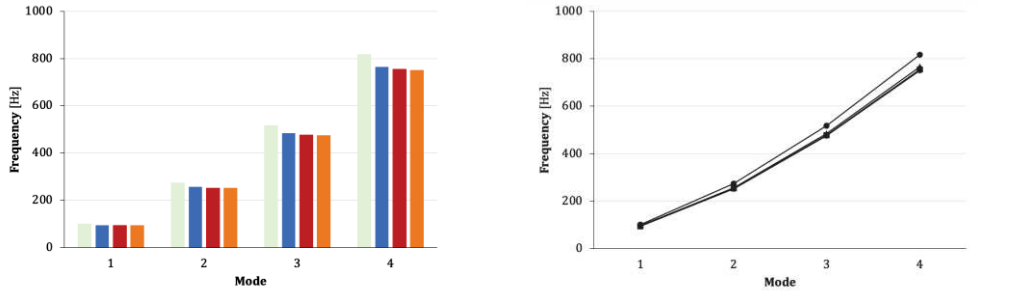

(b) B_1

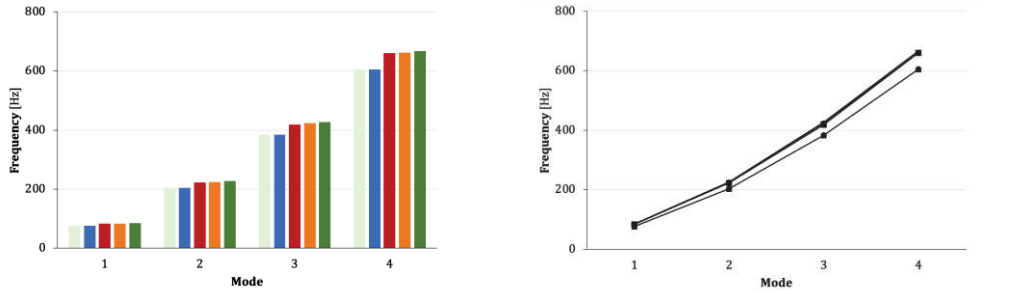

(c) B_2

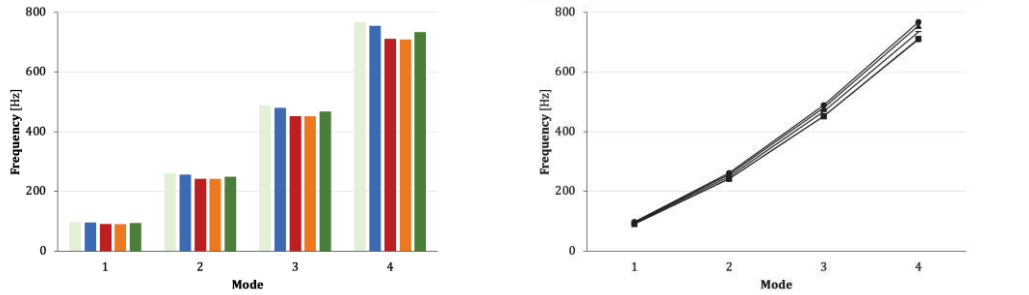

(d) B_3

Figure 7.8 – Graphic representation of the FEM natural frequencies and of their variation for each mode of vibration for each RC beam obtained by varying elastic modulus; (a) specimen CB, (b) specimen B_1, (c) specimen B_2, (d) specimen B_3

7.4. Analysis of variation frequency data

As for the experimentation, after having determined the values of natural frequencies of the finite element beam models, the percentage variations of frequency with respect to the initial condition D_0 and with respect to the previous damage condition D_{i-1} were calculated.

These percentage variations obtained from numerical modeling were then compared with those obtained from experimental data, in Figure 7.10 a comparison between the absolute percentage variations in frequency of the finite element models and of the experimental analysis as the damage state varies for each mode of vibration is shown.

First of all, in Figure 7.9, the trend of the experimental frequency and those obtained from FEM are depicted.

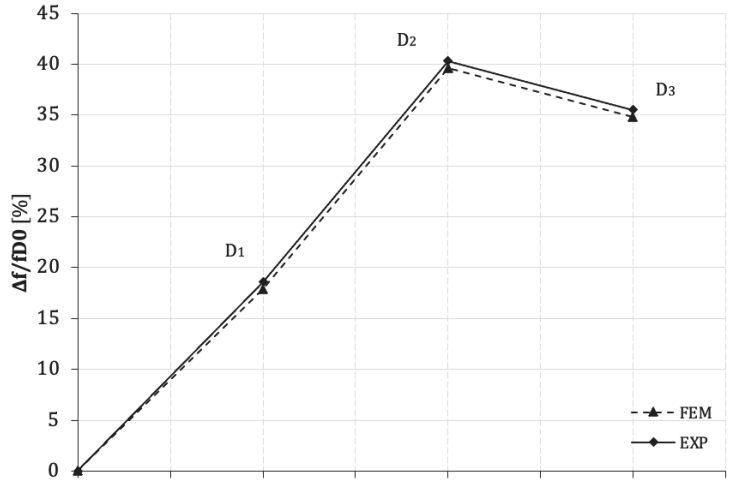
45
40
35
30
25
20
15
10
5
0
Δf/fD0 [%]
D1
D2
D3
FEM
EXP

(a) CB

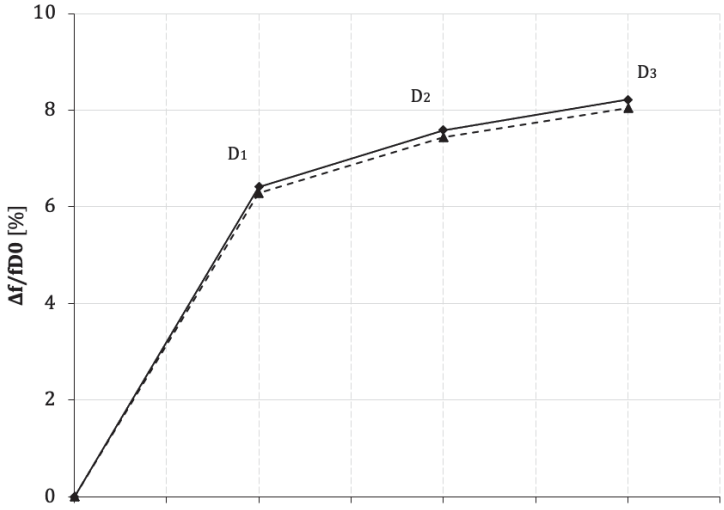
10
8
6
4
2
0
Δf/fD0 [%]
D1
D2
D3

(b) B1

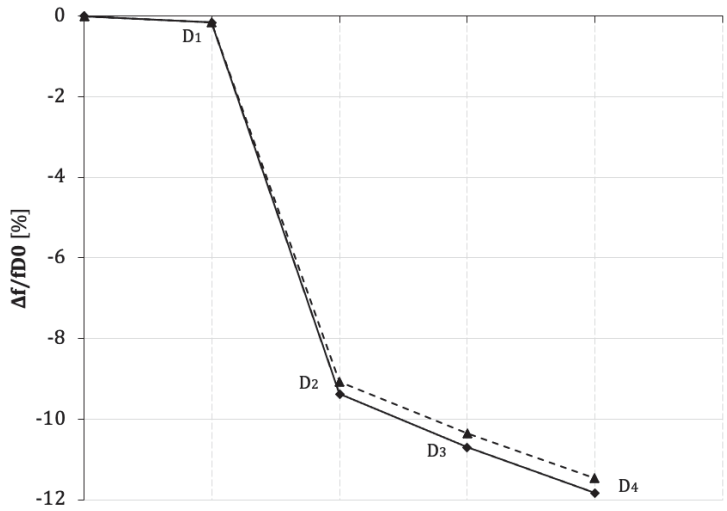

(c) B2

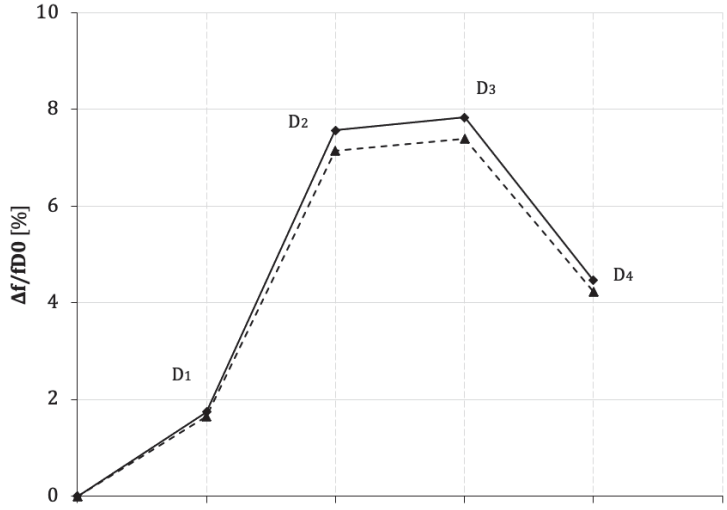

(d) B3

Figure 7.9 – Trend of the absolute percentage variations of experimental and FEM frequency: (a) specimen CB, (b) specimen B1, (c) specimen B2, (d) specimen B3

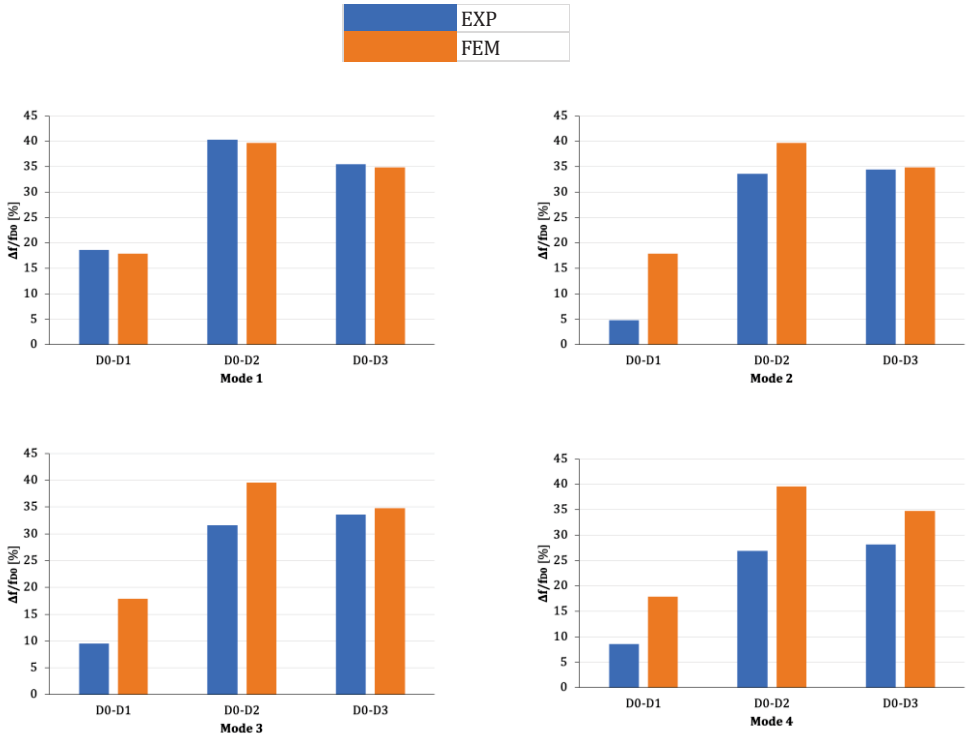
EXP
FEM
Δf/f0o [%]
D0-D1
D0-D2
D0-D3
Mode 1
Mode 2
Mode 3
Mode 4

(a) CB

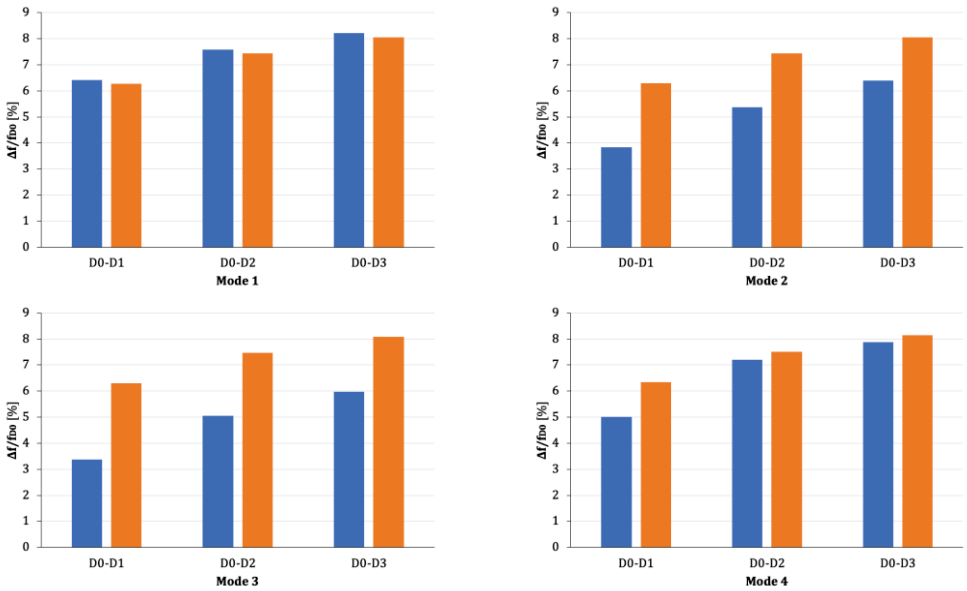
Δf/f0o [%]
D0-D1
D0-D2
D0-D3
Mode 1
Mode 2
Mode 3
Mode 4

(b) B_1

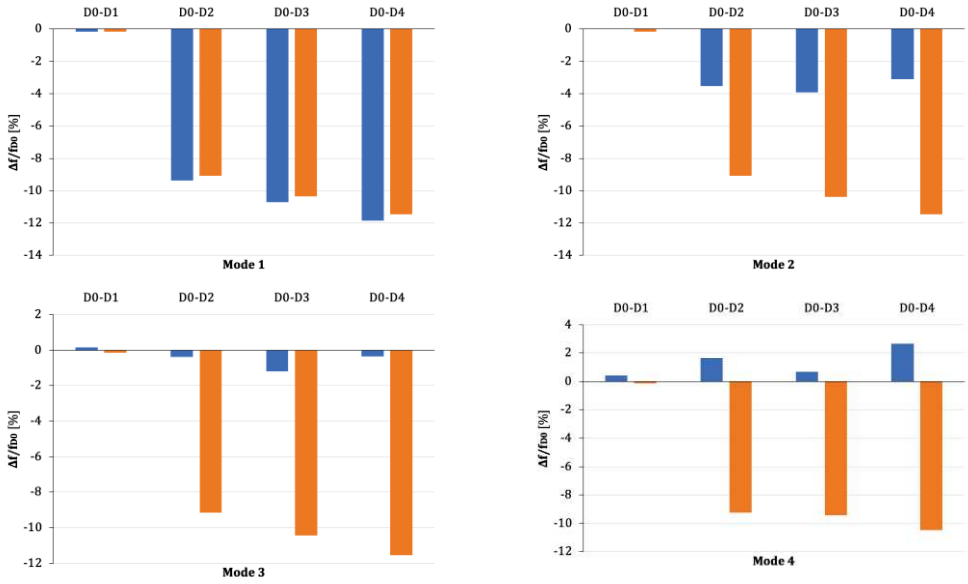

(c) B_2

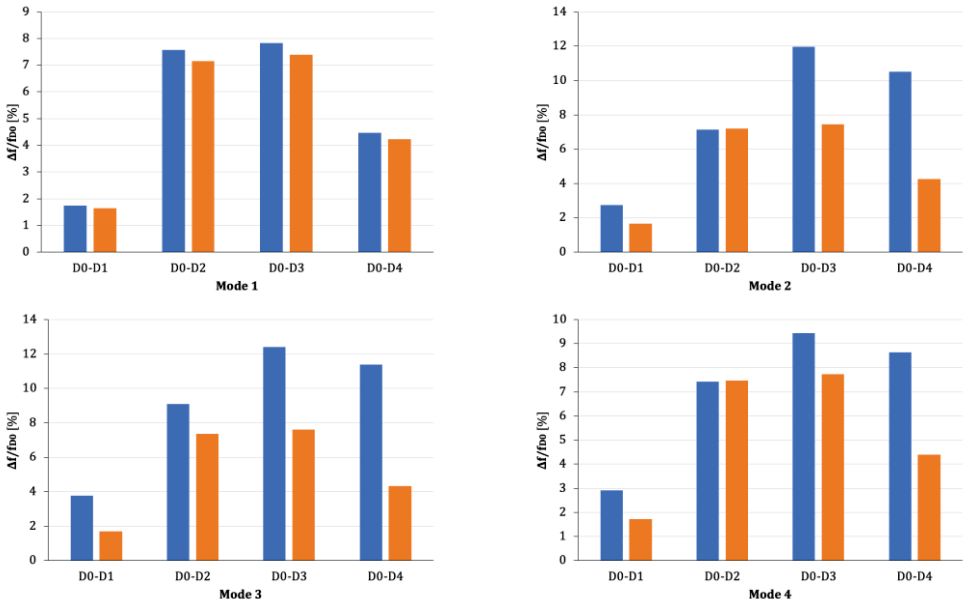

(d) B_3

Figure 7.10 – Comparison between frequency variation of beam models by FEM and by experimental tests, at damage Di compared to D0, for the first four vibration modes: (a) specimen CB, (b) specimen B1, (c) specimen B2, (d) specimen B3

In the same way, the percentage variations in frequency relative to the previous damage condition D_{i-1}, and therefore relative, were calculated, as regards the FEM, and compared with the experimental ones (Figure 7.11).

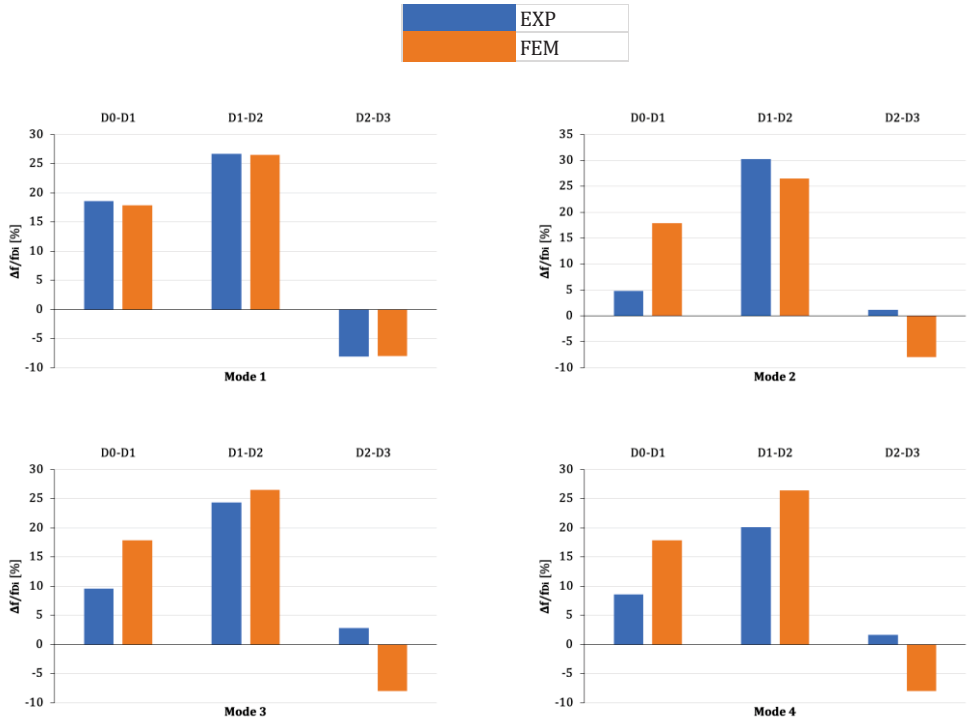
EXP
FEM
D0-D1
D1-D2
D2-D3
Δf/fn [%]
Mode 1
Mode 2
Mode 3
Mode 4

(a) CB

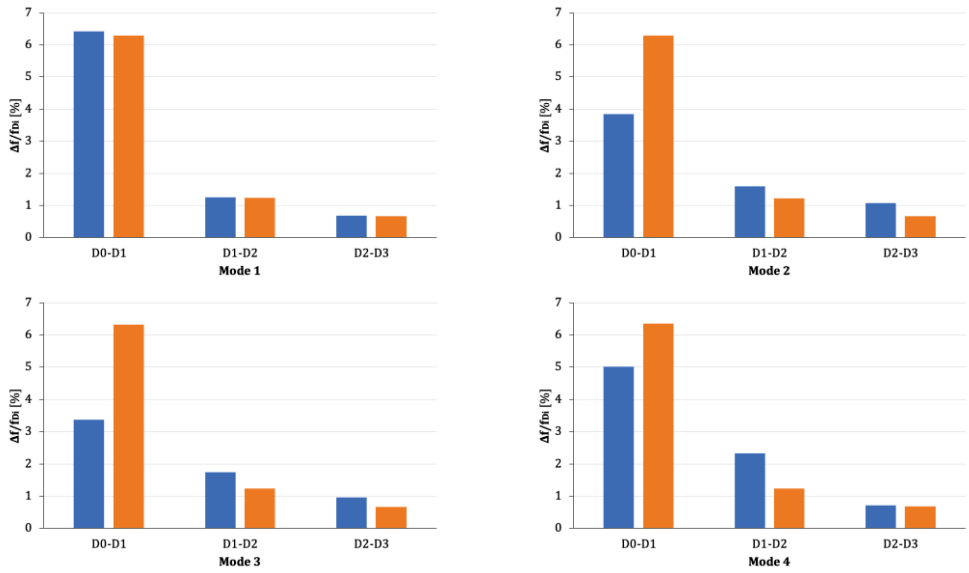
D0-D1
D1-D2
D2-D3
Δf/fn [%]
Mode 1
Mode 2
Mode 3
Mode 4

(b) B_1

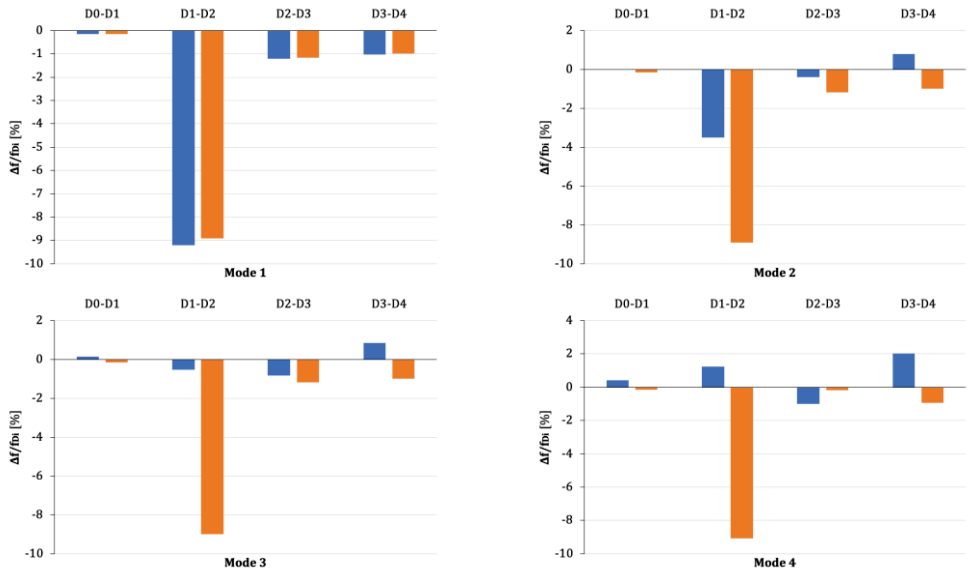

(c) B_2

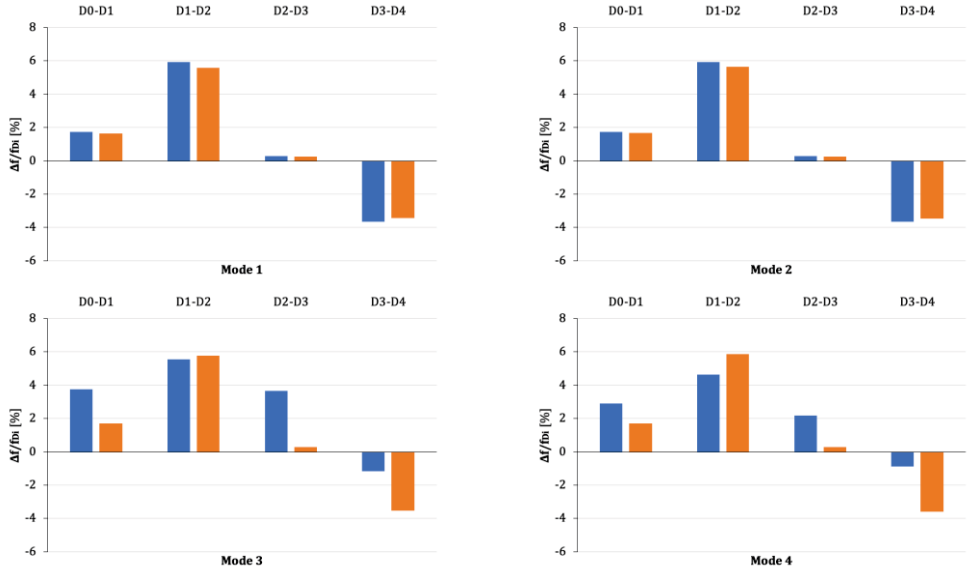

(d) B_3

Figure 7.11 – Comparison between frequency variation of beam models by FEM and by experimental tests, at damage Di compared to Di-1, for the first four vibration modes: (a) specimen CB, (b) specimen B1, (c) specimen B2, (d) specimen B3

In general, it can be observed that deviations between the percentage variations of the finite element models and those of the experimental analysis are less than 15%; for the first vibration mode, on which the theoretical model was calibrated, deviations are less than 1%.

Chapter 8. Concluding Remarks

8.1. Conclusions

In the present research work, a survey campaign was carried out to assess the behavior of RC beams strengthened with FRP rods applied with NSM (Near Surface Mounted) technique. The experimental research included a series of static tests, by means of bending tests on four points with load-unloading cycles until failure, and dynamic tests through the recording of the natural frequencies of vibration.

The first tests made it possible to define the flexural behavior of the reinforced beam models even in the presence of damage, to define the failure modes and to generate the different damage stages; therefore, to define the effects of the different types of reinforcement, as well as to investigate the bond between the reinforcement bar and concrete. The second type of test made it possible to monitor the progression of the damage and monitor the effectiveness of the reinforcement.

The experimental data were compared with those coming from theoretical treatments present in the literature, the dynamic results were also compared with those coming from a finite element modeling developed for the beam models under examination.

Based on the theoretical and experimental results obtained, it is possible to draw the following conclusions:

– The flexural capacity and stiffness of reinforced concrete beams with NSM FRP rods significantly increased in comparison to those of the control beam, while the mid-span deflections of strengthened beams at failure mainly decreased compared to the control beam. The flexural capacity increase consists not only in an increase in terms of ultimate moment and ultimate load but also in an increase of first crack load.
  The failure mode that occurred 2 times out of 3, and only for the GFRP bars, is that due to the delamination between the FRP and the resin, for the CFRP bar, on the other hand, the expulsion of the concrete cover occurred; in all cases the concrete was crushed in the compressed area.

- The ultimate bending moment and stiffness of beams increased with an increase in material strength. By making a comparison between the results of strengthened reinforced concrete beams, the overall efficiency of strengthening techniques on the flexural behavior of models was confirmed for both strengthening materials. In general stiffness of beams with GFRP rod is lower than stiffness of beam with CFRP rod, that is a direct result of the mechanical properties of the strengthening materials. In fact, the elastic modulus of GFRP is much lower than that of CFRP, while the area of section of the rods are almost equal. The ultimate capacity of RC elements strengthened with CFRP rods (beam B_3) in terms of ultimate load P_u, is 31% and 22% higher than ultimate capacity of GFRP strengthened elements, respectively beam B_1 and beam B_2.

- The load-deflection behavior of all strengthened specimens with FRP composites generally had the same trend with an approximate tri-linear response defined by concrete cracking, steel yielding, and post-yielding stages up to the failure mode. In the first stage, before cracking, the strengthened beams followed a linear elastic behavior pattern and the FRP composites had impacts on the concrete cracking moments and deflection at this stage. After this stage, the reinforcement strength of FRP rods was utilized, and the stiffness and load-carrying capacity of the beams gradually increased up to the ultimate bending moment in comparison to the control beam.

- Hypothesis of section planarity (Bernoulli's hypothesis) isn't confirmed by experimental results, for NSM strengthened beams. FRP bar, in fact, exhibits a *stress-strain lag* which makes it impossible to consider the section as plane. Structural design developed on the basis of this usual common hypothesis may overestimate the strength of sections. It can be a good strategy the adoption of one of the coefficient $k_{1,av}$ (or $k_{2,av}$) to prevent overestimation of the beam's strength, in fact the theoretical calculation carried out with the application of the two coefficients k, showed, in both cases, FRP strain values and moment values more conservative and closer to experimental data.

- Concrete cracking reduces the stiffness of beam models, which influences not only its static behavior but also its dynamic response: this is clear by observing the results of the dynamic tests, both in free and hinged conditions, as an effective decrease in the frequency values is recorded. Verified the validity of vibration tests, it is possible to state that the greatest frequency variations occur in correspondence with the un-reinforced beam CB, where in free condition in the case D_0-D_2 a maximum variation of 40% is obtained (I mode); while in hinged condition a maximum value of 17%, for the D_0-D_3 case, is reached (I mode). For the strengthened beam models, the variations between the damage states are considerably lower for the free condition (maximum values are around 10% for the last load cycles with respect to D_0 condition), even for the hinged

condition this result it is confirmed for the B_3 beam only, while for the other two strengthened specimens it is around 5%. These last results underline how the NSM reinforcement is able to mitigate crack damage under bending conditions with limited frequency variations.

– The theoretical model following the Euler-Bernoulli treatment approximates well the behavior of the un-reinforced un-damaged beam and therefore in its initial condition, in the case of a free beam, with a minimum difference of 1% for the first vibration mode, and maximum of 11% for the fourth mode. In the case of hinged beam, the difference is slightly greater, but the values obtained are still acceptable: a minimum difference of 11% (II mode) and a maximum of 22% (I mode) are recorded.

– With the aim of reproducing the dynamic response of un-strengthened and FRP-strengthened RC beams in free conditions, a FE analysis is carried out varying the elastic modulus from time to time. This value was calculated starting from the experimental frequencies obtained, for the I mode of vibration. Frequency data obtained with FEM perfectly match with experimental ones.

References

[1] Hollaway L.C., A review of the present and future utilisation of FRP composites in the civil infrastructure with reference to their important in-service properties. Constr Build Mater 2010;24(12):2419–45.

[2] Teng J.G., Chen J.F., Smith S.T., Lam L., FRP-strengthened RC structures. West Sussex: Wiley; 2002.

[3] Hollaway L.C., Teng J.G., Strengthening and rehabilitation of civil infrastructures using FRP composites, Woodhead; 2008 [Cambridge, U.K].

[4] Zhang S.S., Teng J.G., Finite element analysis of end cover separation in RC beams strengthened in flexure with FRP, Eng. Struct. 75 (2014) 550–560.

[5] Rizzo A., De Lorenzis L., Behavior and capacity of RC beams strengthened in shear with NSM FRP reinforcement, Constr. Build. Mater. 23 (2009) 1555–1567.

[6] Bilotta A., Ceroni F., Di Ludovico M., Nigro E., Pecce M., Manfredi G., Bond efficiency of EBR and NSM FRP systems for strengthening concrete members, J. Compos. Constr. 15 (2011) 757–772.

[7] Hawileh R. A., Nonlinear finite element modeling of RC beams strengthened with NSM FRP rods, Constr. Build. Mater. 27 (2012) 461–471.

[8] Al-Mahmoud F., Castel A., Francois R., Tourneur C., Strengthening of RC members with near-surface mounted CFRP rods, Compos. Struct. 91 (2009) 138–147.

[9] Dias S.J., Barros J.A., Performance of reinforced concrete T beams strengthened in shear with NSM CFRP laminates, Eng. Struct. 32 (2010) 373–384.

[10] Costa I.G., Barros J.A., Flexural and shear strengthening of RC beams with composite materials –The influence of cutting steel stirrups to install CFRP strips, Cem. Concr. Compos. 32 (2010) 544–553.

[11] Al-Mahmoud F., Castel A., Francois R., Tourneur C., Anchorage and tension-stiffening effect between near-surface-mounted CFRP rods and concrete, Cem. Concr. Compos. 33 (2011) 346–352.

[12] Wu G., Dng Z.Q., Wu Z.S., Zhang L. W., Performance and parametric analysis of flexural strengthening for RC beams with NSM-CFRP bars, J. Compos. Constr. 18 (2013), 04013051.

[13] Bianco V., Monti G., Barros J.A., Design formula to evaluate the NSM FRP strips shear strength contribution to a RC beam, Compos. Part B Eng. 56 (2014) 960–971.

[14] Sharaky I. A., Torres L., Sallam H., Experimental and analytical investigation into the flexural performance of RC beams with partially and fully bonded NSM FRP bars/strips, Compos. Struct. 122 (2015) 113–126.

[15] De Lorenzis L., Teng J. G., Near-surface mounted FRP reinforcement: An emerging technique for strengthening structures. Composites Part B: Engineering 2007;38(2):119- 143.

[16] Szabò Z.K., Balazsw G.L., Near surface mounted FRP reinforcement for strengthening of concrete structures. Civil Engineering 2007;51(1):33-38.

[17] Smith S.T., Teng J.G., FRP-strengthened RC beams. I: review of debonding strength models. Engineering Structures 2002;24(4):385-395.

[18] Smith S.T., Teng J.G., FRP-strengthened RC beams. II: assessment of debonding strength models. Engineering Structures 2002;24(4):397-417.

[19] Ceroni F., Experimental performances of RC beams strengthened with FRP materials. Construction and Building Materials 2010;24(9):1547-1559.

[20] Teng J.G., De Lorenzis L., Wang B., Rong L., Wong T.N,. Lam L., Debonding failures of RC beams strengthened with near-surface mounted CFRP strips. J Compos Constr ASCE 2006;10(2):92e105.

[21] Hassan T.K., Rizkalla S.H., Investigation of bond in concrete structures strengthened with near surface mounted carbon fiber reinforced polymer strips. J Compos Constr ASCE 2003;7(3):248e57.

[22] Hassan T., Rizkalla S., Bond mechanism of near-surface-mounted fiber-reinforced polymer bars for flexural strengthening of concrete structures. ACI Structural Journal 2004;101(6):830-839.

[23] Capozucca R., Analysis of bond-slip effects in RC beams strengthened with NSM CFRP rods. Composite Structures 2013; 102:110-123

[24] De Lorenzis L., Nanni A., Bond between NSM fiber-reinforced polymer rods and concrete in structural strengthening. ACI Structural Journal 2002;99(2):123-132.

[25] Hassan T., Rizkalla S., Investigation of bond in concrete structures strengthened with near surface mounted carbon fiber reinforced polymer strips, Journal of Composites for Construction, ASCE 2003;7(3):248-257.

[26] Sena Cruz J., Barros J., Gettu R., Azevedo Á., Bond behavior of near-surface mounted CFRP laminate strips under monotonic and cyclic loading. Journal of Composites for Construction 2006;10(4), 295-303.

[27] Sharaky I.A., Torres L., Baena M., Miàs C., An experimental study of different factors affecting the bond of NSM FRP bars in concrete. Composite Structures 2013; 99:350-365.

[28] Yan X., Miller B., Nanni A., Bakis C.E., Characterization of CFRP rods used as near surface mounted reinforcement. In: Proc 8th int structural faults and repair conference. Edinburgh: Eng. Technics Press; 1999.

[29] De Lorenzis L., Nanni A., Characterization of FRP rods as near surface mounted reinforcement. J Compos Constr 2001;5(2):114–21.

[30] Doebling S.W., Farrar C.R., Prime M.B., Shevitz D.W., Damage identification and health monitoring of structural and mechanical systems from changes in their vibration characteristics: A literature review. Los Alamos Natl. Lab. Rep. 1996, 249299.

[31] Sohn H., Farrar C.R., Hemez F., Czarnecki J. A., Review of Structural Health Monitoring Literature 1996–2001. Los Alamos Natl. Lab. Rep. 2003, 976152.

[32] Kersler S.S., Spearing S.M., Atalla M.J., Cesnik C.E.S., Sontis C., Damage detection in composite materials using frequency response methods. Composites Part B: Engineering 2002; 33:87-95.

[33] Capozucca R., Vibration of CFRP cantilever beam with damage. Composite Structures 2014; 116:211-222.

[34] Cawley P., Adams R.D., The location of defects in structures from measurements of natural frequencies. Journal of Strain Analysis for Engineering Design 1979; 14:49-57.

[35] Salawu O.S., Detection of structural damage through changes in frequency: a review. Engineering Structures 1997; 19:718-723.

[36] Cerri M.N., Vestroni F., Detection of damage in beams subjected to diffused cracking. Journal of Sound and Vibration 2000;234(2):259-276.

[37] Capozucca R., Damage assessment in PRC and RC beams by dynamic tests. Journal of Physics: Conference Series 2011;305.

[38] Hou R., Xia Y., Review on the new development of vibration-based damage identification for civil engineering structures: 2010–2019. J. Sound Vib. 2021, 491, 115741.

[39] Cawley P., Adams R.D., The location of defects in structures from measurements of natural frequencies. Journal of Strain Analysis for Engineering Design 1979; 14:49-57.

[40] Capozucca R., A reflection on the application of vibration tests for the assessment of cracking in PRC/RC beams. Eng Struct 2013; 48:508-18

[41] Gay D., Materiaux composites. Paris. 3e edition Hermes; 1991. p. 564.

[42] Garden H.N., Hollaway L.C., An experimental study of the influence of plate end anchorage of carbon fibre composite plates used to strengthen reinforced concrete beams. Compos. Struct. 1998; 42 (2):175-88.

[43] Burgoyne C., FRP reinforcement in RC structures. Switzerland: International Federation for Structural Concrete (FIB);2007.

[44] Teng J.G., Chen J.F., Smith Schott T., Lam L., FRP: strengthened RC structures. Front Phys 2002:266.

[45] El Hacha R., Rizkalla S.H., Near-surface-mounted fiber-reinforced polymer reinforcements for flexural strengthening of concrete structures. ACI Struct J 2004;101(5):717e26.

[46] Bilotta A., Ceroni F., Nigro E., Pecce M., Efficiency of CFRP NSM strips and EBR plates for flexural strengthening of RC beams and loading pattern influence. Compos Struct 2015; 124:163e75.

[47] Capozucca R., Bossoletti S., Montecchiani S., Assessment of RC beams with NSM CFRP rectangular rods damaged by notches. Compos Struct 2015;128: 322e41.

[48] Hassan T.K., Flexural performance and bond characteristics of FRP strengthening techniques for concrete structures, PhD. Thesis, University of Manitoba, Winnipeg, Canada, 2002.

[49] Sabau C., Popescu C., Sas G., Schmidt J.W., Blanksvärd T., Täljsten B., Strengthening of RC beams using bottom and side NSM reinforcement, Compos. B Eng. 149 (2018) 82–91

[50] Gribniak V., Tamulenas V., Ng P.L., Arnautov A.K., Gudonis E., Misiunaite I., Mechanical behavior of steel fiber-reinforced concrete beams bonded with external carbon fiber sheets, Materials (Basel) 10 (2017) 666.

[51] Kotynia R., Analysis of the flexural response of NSM FRP-strengthened concrete beams. Proceedings of the Eight International Conference on Fibre-Reinforced Plastics for Reinforced Concrete Structures, Patrasso (Grecia); 2007.

[52] Kotynia R., Flexural behavior of reinforced concrete beams strengthened with near surface mounted CFRP strips, Third International Conference on FRP Composites in Civil Engineering (CICE 2006), Miami (Florida, USA), 2006.

[53] Barros J.A.O., Fortes A.S., Flexural strengthening of concrete beams with CFRP laminates bonded into slits. Journal of Cement & Concrete Composites 2005; 27:471-480.

[54] Barros J.A.O., Dias S.J.E., Lima J.LT., Efficacy of CFRP-based techniques for the flexural and shear strengthening of concrete beams. Cement & Concrete Composites 2007;29(3):203-217.

[55] ACI 440 Part 6–8. Specification for carbon and glass fiber-reinforced polymer bar materials for concrete reinforcement. Farmington Hills, MI: American Concrete Institute (ACI); 2008.

[56] ACI 440. Guide for the design and construction of structural concrete reinforced with FRP bars. Farmington Hills, MI: American Concrete Institute (ACI); 2007.

[57] ACI 318. Building code requirements for structural concrete and commentary (ACI 318). Farmington Hills, MI: American Concrete Institute (ACI); 2005.

[58] Al-Saidy A.H., Al-Harthy A.S., Al-Jabri K.S., Abdul-Halim M., Al-Shidi N.M., Structural performance of corroded RC beams repaired with CFRP sheets, Compos. Struct. 92 (2010) 1931–1938.

[59] Costa I., Barros J., Assessment of the bond behavior of NSM FRP materials by pullout tests. Proceedings of the First Middle East Conference on Smart Monitoring, Assessment and Rehabilitation of Civil Structures, Dubai, UAE; 201.

[60] De Lorenzis L., Nanni A., Shear strengthening of reinforced concrete beams with NSM fiber-reinforced polymer rods. ACI Structural Journal 2001;98(1):60-68.

[61] Barros J.A.O., Dias S., Shear strengthening of reinforced concrete beams with laminate strips of CFRP. Proceedings of International Conference Composite in Construction, Cosenza (Italy); 2003. pp.289-294.

[62] Nanni A., Di Ludovico M., Parretti R., Shear strengthening of a PC bridge with NSM CFRP rectangular bars. Advances on Structural Engineering 2004;7(4):97-109.

[63] Dias S.J.E., Barros J.A.O., NSM shear strengthening technique with CFRP laminates applied in high-strength concrete beams with or without pre-cracking. Composites Part B: Engineering 2012;43(2):290-301.

[64] Remennikov A., Goldston M., Neaz Sheikh M., Impact performance of concrete beams externally bonded with carbon FRP sheets, Mechanics of Structures and Materials Adv. Challenges – Proceedings of. 24th Australians Conference. ACMSM24, 2017 2016, pp. 1695–1699.

[65] Gribniak V., Tamulenas V., Ng, P.L., Arnautov A.K., Gudonis E., Misiunaite I., Mechanical behavior of steel fiber-reinforced concrete beams bonded with external carbon fiber sheets, Materials (Basel) 10 (2017) 666.

[66] Adhikary B.B., Mutsuyoshi H., Behavior of concrete beams strengthened in shear with carbon-fiber sheets, J. Compos. Constr. 8 (2004) 258–264.

[67] Yost J.R., Gross S.P., Dinehart D.W., Mildenberg J.J., Flexural behavior of concrete beams strengthened with near-surface mounted CFRP strips. ACI Struct J 2007;104(4):430e7.

[68] Fernandes P.M.G., Silva P.M., Sena-Cruz J., Bond and flexural behavior of con crete elements strengthened with NSM CFRP laminate strips under fatigue loading. Eng Struct 2015; 84:350e61.

[69] Zhang S.S., Yu T., Chen G.M., Reinforced Concrete beams strengthened in flexure with near-surface mounted (NSM) CFRP strips: Current status and research needs. Compos Part B 131(32017) 30-42

[70] Barros J.A.O., Costa I.G., Ventura-Gouveia A., CFRP flexural and shear strengthening technique for RC beams: experimental and numerical research. Adv Struct Eng 2011;14(3):551e73.

[71] Teng J.G., Zhang S.S., Chen J.F., Strength model for end cover separation Failure in RC beams strengthened with near-surface mounted (NSM) FRP strips. Eng Struct 2016; 110:222e32.

[72] Kalfat R., Al-Mahaidi R., Smith S.T., Anchorage devices used to improve the performance of reinforced concrete beams retrofitted with FRP composites: state-of-the-art review, J. Compos. Constr. 17 (2013) 14–33

[73] Adhikary B.B., Mutsuyoshi H., Behavior of concrete beams strengthened in shear with carbon-fiber sheets, J. Compos. Constr. 8 (2004) 258–264.

[74] Baggio D., Soudki K., Noël M., Strengthening of shear critical RC beams with various FRP systems, Constr. Build. Mater. 66 (2014).

[75] Kalfat R., Al-Mahaidi R., Smith S.T., Anchorage devices used to improve the performance of reinforced concrete beams retrofitted with FRP composites: state-of-the-art review, J. Compos. Constr. 17 (2013) 14–33.

[76] del Rey Castillo E., Griffith M., Ingham J., Straight FRP anchors exhibiting fiber rupture failure mode, Compos. Struct. 207 (2019) 612–624.

[77] De Lorenzis L., Strengthening of RC structures with near surface mounted FRP rods. PhD Thesis, Department of Innovation Engineering, University of Lecce, Italy, 2002.

[78] ASTM G115-98. Standard guide for measuring and reporting friction coefficients. ASTM International, West Conshohocken (PA), 2001. 11 pp.

[79] De Lorenzis L., Anchorage length of near-surface mounted FRP bars for concrete strengthening – analytical modeling. ACI Struct J 2004;101(3):375–86.

[80] Blaschko M., Bond behaviour of CFRP strips glued into slits. In: Proceedings FRPRCS-6. Singapore: World Scientific; 2003. p. 205–14.

[81] Cosenza E., Manfredi G., Realfonzo R., Behavior and modeling of bond of FRP rebars to concrete. ASCE J Compos Constr 1997;1(2):40–51.

[82] Sena Cruz J.M., Barros J.A.O., Modeling of bond between near-surface mounted CFRP laminate strips and concrete. Comput Struct 2004;82(17–19):1513–21.

[83] Capozucca R., On the strengthening of RC beams with near surface mounted GFRP rods. Composite Structures 2014; 117:143-155.

[84] De Lorenzis L., Rizzo A., La Tegola A., A modified pull-out test for bond of near-surface mounted FRP rods in concrete. Compos—Part B: Eng 2002;33(8):589–603

[85] Parretti R., Nanni A., Strengthening of RC members using near surface mounted FRP composites: design overview. Adv Struct Eng 2004;7(6):469–83.

[86] D. M. 17 gennaio 2018. Aggiornamento delle Norme Tecniche per le Costruzioni. Ministero delle infrastrutture e dei trasporti, Roma 2018.

[87] Warburton G.B., The dynamical behavior of structures. Oxford: Pergamon Press; 1964.

[88] Programmer's Manual for Mechanical APDL, Ansys manual, United States of America.